Observation and modelling of wave nonlinearities and infragravity waves in the nearshore

Mariana Vieira Lima Matias da Rocha

Communauté
UNIVERSITÉ Grenoble Alpes

universidade de aveiro
theoria poiesis praxis

THESIS

For obtaining the joint degree of

DOCTOR OF THE UNIVERSITY OF GRENOBLE ALPES AND THE UNIVERSITY OF AVEIRO

prepared under the cotutelle of the *Université Grenoble Alpes* and the *Universidade de Aveiro*

Domain: **Coastal Oceanography**

Presented by

Mariana VIEIRA LIMA MATIAS DA ROCHA

Thesis supervised by **Paulo SILVA**
co-supervised by **Hervé MICHALLET**

prepaired at the **Laboratoire des Écoulements Géophysiques et Industriels (LEGI)** and the
Centro de Estudos do Ambiente e do Mar (CESAM)

in the **Terre, Univers et Environnement Doctoral School** and under the **MAP-fis Doctoral Programme**

Observation and modelling of wave nonlinearities and infragravity waves in the nearshore

Thesis publicly presented **the 17th March 2016**
to the jury :

Pr Fernando ROCHA
Professor Catedrático, University of Aveiro, President
Pr Thomas BALDOCK
Professor, School of Civil Engineering, University of Queensland, Rapporteur
Dr Nadia SÉNÉCHAL
Maître de Conférences HDR, EPOC-OASU, University of Bordeaux, Rapporteur
Dr André FORTUNATO
Investigador Principal, LNEC, Lisboa, Member
Dr Paulo VALENTE
Professor Auxiliar, School of Engineering, University of Porto, Member
Dr Hervé MICHALLET
Chargé de Recherche, LEGI, Grenoble, co-supervisor

"Mas quando o Mundo acabar a gente conversa.
Agora, vamos ver o Mar."

— Vergílio Ferreira

Mariana Vieira Lima Matias da Rocha

Observation and modelling of wave nonlinearities and infragravity waves in the nearshore

Observação e modelação das não-linearidades de onda e de ondas infragravíticas na zona costeira

Dissertação apresentada à Universidade de Aveiro e à Universide de Grenoble-Alpes para cumprimento dos requisitos necessários à obtenção dos graus de Doutor em Física e Geofísica, respectivamente, realizada sob a orientação científica de Paulo Manuel da Cruz Alves da Silva, Professor do Departamento de Física da Universidade de Aveiro e de Hervé Michallet, Investigador do CNRS no Laboratoire des Écoulements Géophysiques et Industriels de Grenoble.

This work had financial support from the Foundation for Science and Technology (FCT) of the Portuguese Government Ministry of Education and Science, through the PhD grant with the reference SFRH/BD/80644/2011, funded by the European Social Fund (FSE) through the Human Potential Operational Programme of the National Strategic Reference Framework (QREN); from the Programa de Acções Integradas Universitárias Luso-Francesas with the reference TC-06_12; from the European Community Seventh Framework Programme through the GLOBEX Hydralab IV project, EC Contract 261520; and from the INSU-LEFE, through the BARCAN project.

the jury

president	**Fernando Joaquim Fernandes Tavares Rocha** Professor Catedrático of the University of Aveiro
supervisor	**Paulo Manuel da Cruz Alves da Silva** Professor Auxiliar at the Physics Department of the University of Aveiro
co-supervisor	**Hervé Michallet** Chargé de Recherche CNRS at LEGI, Grenoble
examiners committee	**Thomas E. Baldock** Professor at the School of Civil Engineering of the University of Queensland
	Nadia Sénéchal Maître de Conférences HDR at EPOC-OASU of the University of Bordeaux
	André B. Fortunato Investigador Principal at LNEC, Lisboa
	Paulo A. Valente Professor Auxiliar at the Department of Civil Engineering of the University of Porto

Acknowledgements

A PhD is a very interesting scientific and personal challenge during which we get to extend just a tiny bit further the current knowledge of mankind, preferentially in a subject about which we are passionate, such as, let's say, Coastal Oceanography. In my case, I also have the hope that, somewhere along the line, the world will benefit from the progress achieved.

Behind each author, there are always many people who made him who he is and helped him persist and continue when the path was rougher or the will was weaker. My PhD thesis is no more than another work made by someone who would certainly not have succeeded if it were not for the support of many people along the way. Hence, I wish I could thank individually every single person that contributed, in some measure, to helping me carrying out this work to its end.

Agradeço primeiro ao meu orientador, Paulo Silva, por me ter oferecido a possibilidade de fazer esta tese e, desde o início, ter acreditado que eu seria capaz de a concluir. Obrigada por me ter proporcionado inúmeras oportunidades de desenvolver novas capacidades, pelas boas trocas de ideias e por sempre me ter compreendido e ajudado.

En deuxième, je remercie Hervé Michallet, mon superviseur du côté Français. Je te remercie pour ton énorme patience avec moi, ton partage de connaissance sur la manip et sur notre domaine d'étude en général, ton suivi infatigable et attentif au quotidien. Je te remercie aussi et surtout pour ton côté humain et ton ouverture au dialogue qui ont permis de surmonter les périodes plus compliqués. Je suis bien contente de l'effort que nous avons tous les deux fait pour s'adapter à nos personnalités (très) particulières: celà m'a fait grandir. Si un point hors d'une courbe de tendence ne sera plus jamais dans ma vie juste un point hors d'une courbe de tendance, c'est grâces à toi. Mais si j'ai finis cette thèse c'est aussi, sans aucune doute et en grande mesure, grâces à toi.

Encore dans le cadre de travail de cette thèse, merci aux techniciens qui ont toujours été disponibles pour aider pendant les expériences sur le canal à houle du LEGI. Obrigada também a toda a gente que contribuiu para o bom desenrolar das diversas campanhas de campo em que participei em Portugal. Agradeço ainda à Fundação da Ciência e Tecnologia pelo financiamento da bolsa que me permitiu levar a cabo este doutoramento.

I would like to thank as well the reviewers of this work and all its potential readers, for the time spent reading it and thinking about it. I hope you have enjoyed it.

During my PhD thesis I had the great chance to spend significant periods of time abroad, which I cherished a lot. It is when you get out of your comfort zone that you

evolve, personally, and scientifically as well. However, each time you go abroad, you are far from your home, your routine, your friends, your family. It makes sense to explain this, so that people can understand how much I am thankful to everyone that helped me "to arrive" over and over again, that received me the best way possible and thus undoubtedly contributed to the success of this thesis.

A mis compañeros de carrera y de piso en Santander, que me recibirán tan bien, me acompañaran e hicieran de los tres meses que pasé allí una buena experiencia de inicio de tesis.

To all the GLOBEX team, for the intense month passed in Delft, for sharing your knowledge and giving me the best motivation possible for my first year of PhD. Thank you as well for the interesting exchanges of ideas, the support provided when necessary and the good times spent together.

À tous les gens que j'ai connu en France, que maintenant j'appelle des amis ou famille. Merci Thibaud, pour avoir été le premier à m'ouvrir ta porte en toute confiance, à m'amener de partout parmi tes amis, à me présenter les Alpes. Tu resteras toujours parmi ceux qui m'ont accueilli d'une telle façon que je n'oublierai jamais. Merci Marine aussi et à tout le 123, vous étiez vraiment fondamentaux à mon intégration en France et aux bons moments passés là-bas. Merci à mes premiers colocs, Guillaume, Javi, Rémi, pour avoir toujours rempli mon quotidien de plein de bonnes choses, pour le soutien dans les moments plus difficiles de la thèse et de la vie en France, pour avoir été comme une famille pour moi. Merci à tous ces Saint Hilairois qui me font toujours découvrir le bonheur d'habiter en montagne, même si la mer est bien loin. Spécialement parmi ceux-là, merci à Zélie et Santiago (et Luce!) d'avoir soutenu toujours avec la bonne humeur ma fin de thèse et tout ce qui vient avec. Merci à tous les amis du LEGI pour les discussions philosophiques insolites à midi et pour rendre si agréable l'environnement de travail. Merci Nadia et Jean-Lou, pour avoir fait de chez vous un petit chez moi aussi.

Esta secção de agradecimentos está, de uma certa forma, tacitamente organizada por antiquidade crescente, por imutabilidade crescente, digamos. Assim sendo, bem perto do final, quero agradecer a todos os meus amigos da beira-mar. Obrigada por continuarem a seguir ao meu lado nesta vida e por aceitarem, sem cobrar, a minha ausência intermitente nestes últimos anos. Teria sido bem mais duro o meu tempo de tese se isto fosse de outra forma.

Agradeço ainda, e sobretudo, à minha família. Por me terem sempre apoiado ao longo desta tese (e da vida!), por suportarem, ano após ano, a minha ausência e aturarem os altos e os baixos e me convencerem, uma e outra vez, de que era capaz de chegar ao fim. Aproveito também para vos pedir desculpa, desculpa por todos os momentos

em que não estive presente por estar a construir o meu caminho. Obrigada por sempre me encorajarem a seguir as minhas escolhas e por me apoiarem incondicionalmente nessas escolhas. Sem vocês não seria a pessoa que sou, não teria chegado aqui, não teria havido tese.

Et à toi, Seb, obrigada por tudo.

keywords waves, nearshore, cross-shore profile, hydrodynamics, morphodynamics, wave nonlinearities, infragravity waves, physical modelling, numerical modelling, field data

abstract

Wave nonlinearities have long been recognised as being among the main drivers of sediment transport in the coastal zone. However, there are still significant errors in the prediction of this transport associated, partially due to inaccurate predictions of the velocity nonlinearities. The infragravity waves, which coexist with the short waves in the coastal zone, are long-period waves (with 20-200 s) associated to the short-wave groups. Their generation, propagation and dissipation mechanisms are already reasonably well understood, but their influence on sediment transport is still very poorly characterised.

In order to (i) improve current predictions of velocity nonlinearities and (ii) investigate the role of infragravity waves in sediment transport, new experiments were carried out both in a fixed-bed wave flume and in a light-weight-sediment wave flume. The physical-modelling data set is used in combination with field data and numerical simulations for studying both subjects.

Existing parameterizations of velocity nonlinearities account only for the influence of local wave parameters (e.g. wave height, wave length and water depth), which leads to considerable estimation errors, especially of the maximal values of nonlinearity. This work shows that the velocity nonlinearities depend also on non-local wave parameters: (i) offshore wave steepness, (ii) offshore spectral bandwidth and (iii) beach slope. A new parameterization is proposed, which reduces by about 50% the root-mean-square error relatively to former parameterizations.

The experimental results in the light-weight-sediment wave flume demonstrate that wave conditions with the same short-wave energy, but different low-frequency modulation, shape different equilibrium beach profiles. The influence of the infragravity waves on the sediment transport is confirmed and depends on two different mechanisms: (i) advection of the short-wave suspended sediment by the infragravity-waves, which is dependent on the infragravity-wave height and phasing with the short-wave groups and (ii) modulation of short-wave nonlinearities by infragravity-wave motion, both directly and indirectly, through water-depth modulation.

Changes in the beachface morphology induced by infragravity waves are connected to beach-profile changes in the surf and inner-shoaling zones, highlighting the existent link between the different zones of the cross-shore beach profile.

palavras-chave ondas, zona costeira, perfil transversal, hidrodinâmica, morfodinâmica, não-linearidades das ondas, ondas infragravíticas, modelação física, modelação numérica, dados de campo

resumo As não-linearidades das ondas de superfície são desde há algum tempo reconhecidas como um dos principais promotores do transporte sedimentar na zona costeira. Contudo, existem ainda erros significativos na estimativa do transporte devidos, entre outros, a uma imprecisa descrição das não-linearidades da velocidade do escoamento orbital. As ondas infragravíticas, que coexistem com as ondas curtas na zona costeira, são ondas de longo período (20-200 s) associadas aos grupos de ondas curtas. Os mecanismos de geração, propagação e dissipação destas ondas são actualmente razoavelmente bem compreendidos, mas a sua influência no transporte sedimentar ainda apresenta limitações.

Com o objectivo de (i) melhorar as parameterizações existentes das não-linearidades da velocidade e (ii) investigar o papel das ondas infragravíticas no transporte sedimentar, foram realizadas novas experiências em dois canais de ondas, um de fundo fixo e outro de fundo móvel com sedimentos de baixa densidade. Os dados obtidos nos modelos físicos foram utilizados conjuntamente com dados de campo e de simulações numéricas para investigar ambos os temas.

As parameterizações existentes para as não-linearidades da velocidade têm apenas em conta a influência de parâmetros locais de onda (e.g. altura de onda, comprimento de onda e profundidade de água), o que resulta em erros consideráveis nas estimativas, em particular dos valor máximos de não-linearidade. Este trabalho evidencia que a não-linearidade da velocidade depende também de parâmetros que não são locais: (i) a declividade da onda ao largo, (ii) a largura da banda espectral ao largo e (iii) o declive da praia. Uma nova parameterização que reduz em cerca de 50% o erro dos resultados obtidos com as parameterizações existentes é proposta.

Os resultados experimentais obtidos no canal de ondas com fundo móvel demonstram que climas de agitação marítima com a mesma energia de ondas curtas, mas com diferente modulação de baixa frequência, moldam perfis de praia diferentes. A influência das ondas infragravíticas no transporte sedimentar é posta em evidência e processa-se através de dois mecanismos distinctos: (i) advecção pelas ondas infragravíticas de sedimento colocado em suspensão pela acção das ondas curtas, a qual é dependente da altura das ondas infragravíticas e da sua fase relativamente aos grupos de ondas curtas e (ii) as ondas infragravíticas alteram as não-linearidades das ondas curtas, tanto directa como indirectamente, através da modulação da altura da coluna de água.

As variações morfológicas da face da praia induzidas pelas ondas infragravíticas estão associadas a alterações do perfil de praia nas zonas de surf e de empolamento, evidenciando o elo existente entre as diferentes zonas do perfil transversal da praia.

mots-clés vagues, littoral, profil transversal, hydrodynamique, morphodynamique, non-linéarités des vagues, vagues infra-gravitaires, modélisation physique, modélisation numérique, données de terrain

resumé

Les non-linéarités des ondes de surface, qui se caractérisent par leur aspect dissymétrique, sont reconnues comme l'un des principaux moteurs du transport de sédiments en zone littorale. Cependant, l'estimation du transport reste imparfaite, en partie du fait d'une description inexacte des non-linéarités de la vitesse de l'écoulement orbital. Les ondes infra-gravitaires, qui coexistent avec les ondes courtes en zone littorale, sont des ondes de longue période (20-200 s) associés aux groupes d'ondes courtes. Les mécanismes de génération, propagation et dissipation de ces ondes sont maintenant relativement bien compris, mais leur effet sur le transport sédimentaire est encore mal connu.

Afin (i) d'améliorer les paramétrisations existantes des non-linéarités de vitesse et (ii) d'étudier le rôle des ondes infra-gravitaires dans le transport sédimentaire, de nouvelles expériences ont été réalisées dans deux canaux à houle, l'un avec un fond fixe et l'autre avec un fond mobile constitué de sédiments de faible densité. Les données obtenues avec ces modèles physiques ont été utilisés conjointement à des données de terrain et des simulations numériques pour étudier les deux sujets.

Les paramétrisations classiques pour les non-linéarités de vitesse prennent seulement en compte l'influence de paramètres locaux (la hauteur de vague, la longueur d'onde et la profondeur d'eau), ce qui entraîne des erreurs importantes dans les estimations, en particulier les valeurs maximales de non-linéarité. Ce travail montre que les non-linéarités de vitesse ont aussi une dépendance avec des paramètres qui ne sont pas locaux: (i) la cambrure de vague et (ii) la largeur de la bande spectrale au large, ainsi que (iii) la pente de la plage. Une nouvelle paramétrisation est proposée, qui réduit d'environ 50% l'erreur sur les résultats obtenus avec les paramétrisations existantes.

Les résultats expérimentaux obtenus dans le canal à houle avec un fond mobile montrent que des conditions de vagues avec la même énergie d'ondes courtes, mais avec une modulation basse fréquence différente, modèlent des profils de plage différents. L'influence des ondes infra-gravitaires sur le transport sédimentaire est mis en évidence par deux mécanismes distincts: (i) l'advection par les ondes infra-gravitaires de sédiment mis en suspension par l'action des ondes courtes, qui dépend de la hauteur des ondes infra-gravitaires et de leur phase par rapport aux groupes d'ondes courtes et (ii) les ondes infra-gravitaires modifient les non-linéarités des ondes courtes, que ce soit directement ou indirectement, par modulation de la hauteur de la colonne d'eau.

Les variations morphologiques du haut de plage induites par les ondes infra-gravitaires sont associées à des changements du profil de la plage dans les zones de déferlement et de levée, en mettant en évidence le lien entre les différentes régions du profil transversal de la plage.

Contents

List of Figures

List of Tables

Chapter 1

Introduction

1.1 Research context

According to the United Nations Ocean Atlas, more than 40 % of the population of the world lives nowadays within 150 kilometres of the sea. Coastal cities are usually important ports favouring commerce and fishing. Ocean-related recreation and tourism are rapidly growing, being an important vector of development and economical growth. Most of the megacities of the world with more than 2.5 million inhabitants are located in the coastal area. Unfortunately, the rapid increase of people living near the coast has generated an imbalance of the natural system.

The coastal-erosion problem is a typical example of such an imbalance. Affecting coasts worldwide, it is currently one of the greatest problems of the coastal zones where human occupation is intense. On a geological timescale, the oceans of the world have risen and retreated several times before. Each time, the coast has adapted, advancing or retreating. After the last glaciation, about 20,000 years ago, a fast rise of the mean sea-level of about 8 mm/year was observed, until about 7,000 years ago, slowing down to 1.4 mm/year at present (Komar, 1976). The sea-level rise during the last 20,000 years has left the coast out of equilibrium and the coastline configuration unadjusted to the existing wave climate. Therefore, in the last 7,000 years, the coast has been trying to adapt naturally, eroding capes and filling estuaries, trying to smooth the coastline (Komar, 1976). Furthermore, global warming is nowadays contributing to an expansion of the oceans, which also adds to the sea-level rise (IPCC, 2014). Global warming and associated climate change may further contribute to increase storm frequency and intensity (IPCC, 2014), which is expected to contribute to beach erosion as well. On a shorter time scale, human action has actively contributed to aggravate the problem of coastal erosion, with sand dredging and dam construction in rivers resulting in a decrease of the sediment input to the beaches. Diverse coastal engineering solutions

were built in the last decades (groynes, sea-walls, ...) to help tackling this problem, but unfortunately these frequently end up by solving the problem only locally.

The sea-level rise and the shortage of sediments are only part of the problem. The other part is the intense occupation of the retreating littoral zone. While wild coasts will continuously adjust to sea-level rise and to eventual changes of the wave climate, the wide stretches of coast too intensely occupied by people have to be protected. Since the cost of relocating coastal populations and infrastructures is often too great to be afforded, other solutions must be found.

In order to find solutions for the problem of coastal erosion and thus to help coastal management, the dynamics of the coastal system must be well understood. If accurate predictions of the evolution of the coastline are to be made, all the processes contributing to the sediment transport, and thus to the changing of the beach morphology, must be thoroughly analysed and weighted.

The processes involved in sediment transport are many and complex and act on a wide range of time and space scales, from seconds to millennia, from the tiniest clay grain to an entire delta. Hence, it is a long and ambitious task to achieve a complete understanding of the sediment transport and morphodynamic processes of a coastal system. Since the mid of the twentieth century, many researchers have made their contribution to this task, but many questions remain unanswered.

1.2 Motivation and objectives

Wave and velocity nonlinearities have long been recognised as being amongst the main drivers of sediment transport and have recently started to be incorporated in sediment transport models, which can then be used to simulate real situations. However, there are still significant errors in the prediction of the sediment transport associated, among others, to inaccurate predictions of the velocity nonlinearities. Therefore, one of the aims of this thesis is to improve the comprehension of these nonlinearities, in order to obtain better estimations of sediment transport and thus better predictions of the coastal evolution.

Most damage done by waves on coastal zones and human infrastructure happens during storms, particularly when they occur during spring tides. During the storms, low-pressure systems drive strong winds that can be acompagnied by storm surges (local rise of the sea-level) and big waves that can have an important impact on the coast, either taking offshore important quantities of sediment or promoting overwash and inundation of the upper beach. It is during storms that infragravity waves are more commonly seen to dominate the water motion very close to the shore. These are long

period waves (20-200 s) that are associated to the short-wave groups and modulate the water-depth at the coast, allowing greater short waves to propagate higher up the beach. They can thus have an important role on dune and beach erosion. However, the effect of these waves on sediment transport is still very poorly characterised and quantified. Hence, the other main objective of this thesis is to develop the current knowledge on the sediment transport by infragravity waves, aiming to contribute, once again, to a better comprehension of the sediment transport processes, especially during storm conditions. If wave action and sediment transport during storms are well understood and can be predicted in advance, damage to coastal infrastructures and beaches can ultimately be minimised.

1.3 Organisation of the thesis

This thesis is organised in five chapters. A description of the contents of each chapter is subsequently presented.

Chapter 1 - Introduction - introduces the work developed in the thesis and its context, motivation and general objectives.

Chapter 2 - Fundaments on coastal dynamics - describes the fundamental concepts that constitute the basis of this thesis: the cross-shore beach profile and its hydrodynamic and morphodynamic processes.

Chapter 3 - Wave propagation and nonlinearities - based on the physical model data set of the GLOBEX project, on field data and on SERR1D numerical-model runs, it brings insight on wave and velocity nonlinearities. The chapter starts by an introduction, where the state of the art on wave and velocity nonlinearities is presented together with the organisation of the chapter. Then, the GLOBEX project data and measurements are described and analysed, with a special emphasis on wave nonlinearities and infragravity waves. Field data and SERR1D numerical-model runs are used to extend the results of the GLOBEX data analysis. The discussion of the different results culminates in the improvement of the Ruessink *et al.* (2012) parameterization for the velocity nonlinearities, by the introduction of a dependence on a new parameter and on spectral bandwidth. The chapter draws to an end with the conclusion.

Chapter 4 - The role of infragravity waves on beach morphodynamics- presents the results of a set of experiments performed in the LEGI light-weight-sediment

flume with three different wave conditions, for which short-wave energy was kept constant and IG-wave height was varied. At first, the state of the art of the role of infragravity waves on sediment transport and the organisation of the chapter are presented. This is followed by a methodology section, where the LEGI experimental facility is described, as well as the input wave conditions, instrumentation and associated methods. Subsequently, the evolution of the beach towards equilibrium is analysed and the role of infragravity waves on sediment transport is more thoroughly examined through the analysis of the beach response to two-wave-group runs, in terms of hydrodynamics and morphodynamics. After a discussion of the different mechanisms by which infragravity waves contribute to sediment transport, the chapter ends with the conclusion.

Chapter 5 - Conclusions and perspectives - summarises the work developed and the conclusions of the previous chapters and highlights the existing limitations and possible solutions, together with future perspectives of research.

Chapter 2

Fundamentals of coastal dynamics

2.1 The beach profile

The nearshore ocean starts where the waves first feel the sea bed, and extends all the way to the coast. Many different types of coasts can be found in nature, from high cliffs to gravel or sandy beaches, from coral environments to complex delta systems. The action of the processes driving the dynamics of the nearshore region can be separated in two components: the cross-shore direction and the long-shore direction. In this work, the focus will be on the dynamics of the sandy beaches for processes acting in the cross-shore direction only.

The cross-shore beach profile is one of the most important characteristics of natural sea coasts, since it can be used to evaluate the accretion or erosion of a specific coastal site, as well as the vulnerability of particular regions (Didenkulova & Soomere, 2011). It can be schematically divided in different zones, based on the wave propagation and hydrodynamic and morphodynamic processes, as shown in Fig. 2.1. Each hydrodynamic zone can be further divided into smaller sections, for convenience: the shoaling zone

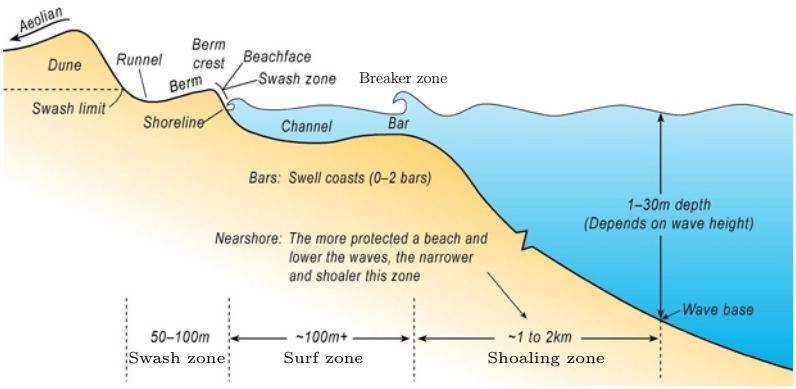

Figure 2.1: Cross-shore beach profile of a barred beach (adapted from Short & Woodroffe, 2009).

into the outer- and the inner-shoaling zones, the surf zone, analogously, into the outer and inner-surf zones and the swash zone into the upper and lower swash zones.

The beach profile shape depends, at each moment, on the balance between the different hydrodynamic and morphodynamic processes at work along its length. However, for study purposes, it is often assumed that a beach profile under constant wave forcing will eventually reach a dynamic equilibrium state, with small variations around a stable equilibrium shape. Dean (1977) modified an empirical equation, initially proposed by Brunn (1954), to describe the shape of an equilibrium profile, which consists essentially on a power law relating the water depth (h) to the offshore distance (x),

$$h = \alpha \left(x_s - x\right)^{2/3}, \tag{2.1}$$

where α is a proportionality constant that depends on the size of the sediment or, alternatively, on the fall velocity (Dean, 1977) and x_s is the position of the shoreline. According to Eq. 2.1, the coarser the sediments, the greater is the value of α and thus the steeper is the beach.

In nature, the wave conditions are constantly changing. Therefore, an equilibrium profile can only be defined as a spatial mean, along a certain coast, or a temporal mean, during a given period of time. Very often this is done to classify beach profiles according to their seasonality: a "summer" profile, associated with mild wave conditions, has generally a large berm and a steep beachface; and a "winter" profile, resulting from highly-energetic wave conditions, has a shorter berm and a mild beachface. Wright & Short (1984) have proposed a classification of the beach profiles according to the Dean number, defined by

$$\Omega = \frac{H_c}{T_c w_s}, \tag{2.2}$$

where H_c and T_c are the characteristic height and period of the incident wave conditions and w_s the fall velocity of the sediment. Wright & Short (1984) have considered H_c and T_c as the breaker wave height and period, respectively, but these variables can also be defined for the offshore wave conditions, as was done by Dalrymple & Thompson (1976).

Fig. 2.2 shows the beach-profile types that can be defined according to the Dean number. For $\Omega < 1$, the beaches are reflective, characterized by a relatively steep and narrow beachface with a berm and a surf zone without bars. Waves are strongly reflected (surging breakers are common), the sediments tend to be coarser and the surf zone is narrow. On the other end, the dissipative beaches, with an $\Omega > 5$, tend to be wide and gently-sloping, with one or more linear bars. These type of beaches are the result of high-energy waves that start breaking far offshore. The intermediate range

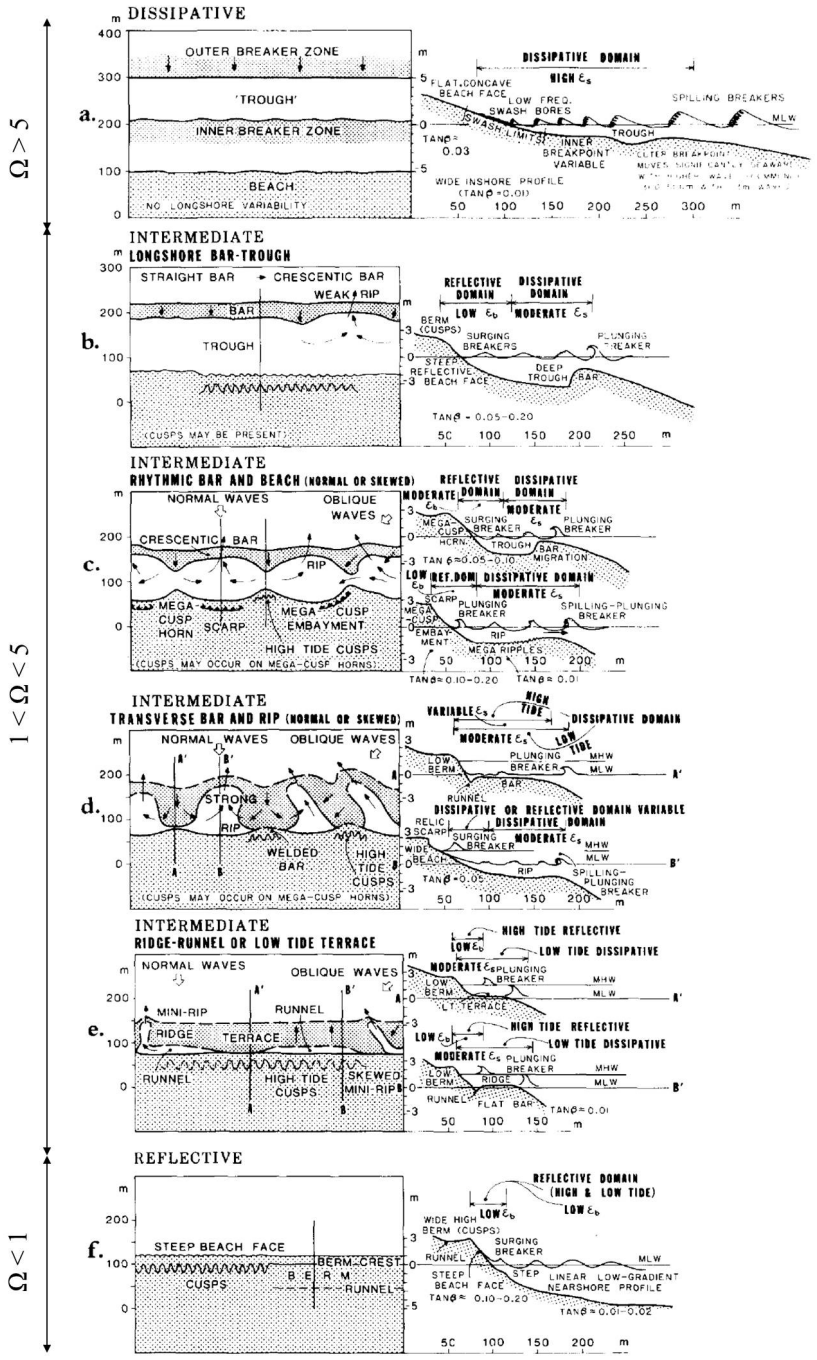

Figure 2.2: Plane (left) and profile (right) configurations of the six beach-profile types that can be defined according to the Dean number (Wright & Short, 1984).

($1 < \Omega < 5$) represents a variety of barred and terraced beaches.

At a given location, the beach is constantly changing its shape. Mild wave conditions will tend to force the beach towards a "summer" (reflective) profile, while storm waves are responsible for driving the sediment fast offshore, changing the beach profile to a "winter" (dissipative) state. In order to perceive the dynamics of the beach profile, the hydrodynamics and morphodynamics processes involved must be understood.

2.2 Hydrodynamics

Fluid motions in the ocean are generated by different phenomena. The wind, pressure differences, the rotation of the Earth and attraction by the moon, seismic and vulcanic activity are some of the phenomena that can generate sea-surface waves and currents. Each different forcing induces motions at a different scale of time and space, which are illustrated in Fig. 2.3.

For describing the beach-profile evolution in the timescale of a day to a year, it is the dynamics of the waves generated by the wind (associated to pressure systems) that must be analysed (see Table 1a of Stive *et al.* (2002)). Waves can be generated locally by the wind, starting as surface ripples, eventually evolving into wind waves. Their characteristics depend on the intensity and duration of the wind and its fetch (distance

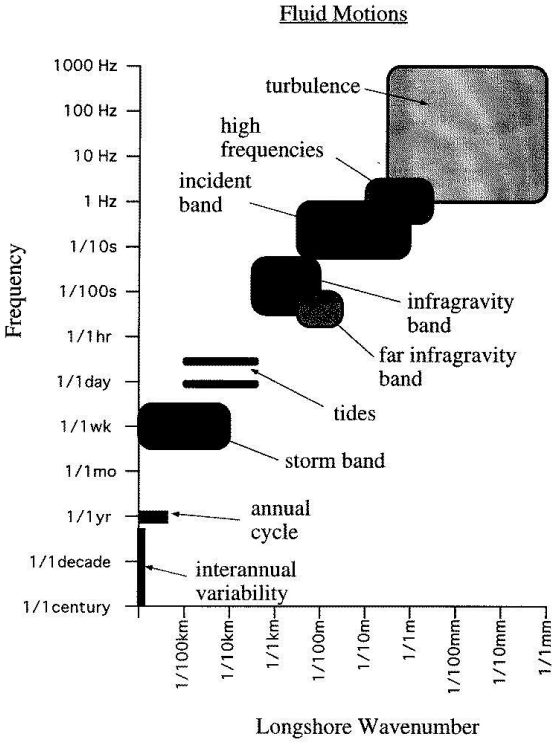

Figure 2.3: Space-time scales of morphology in the nearshore (Thornton *et al.*, 2000).

over which it blows). If the waves then travel a long distance from their generation region, they will tend to organize in groups with similar amplitude and frequency, the swell. Swell waves frequently co-exist with wind waves. Both these types of waves are gravity waves, since the gravitational force is the restitution mechanism acting on the free-surface of the sea when the waves propagate through it.

As the waves propagate from deep waters to the coast, they transform progressively, diffracting, refracting, shoaling, breaking or dissipating their energy through bottom-friction. Diffraction involves a change in the direction of the propagating waves as they pass through an opening or around a barrier in their path and thus allows waves to propagate into the lee zone (the sheltered zone) behind structures or geographical features. The depth-induced refraction is the turning of the direction of wave propagation when, in shallow water, the wave fronts travel at an angle with the depth contours. Since the waves propagate more slowly in shallow than in deep water, the wave fronts tend to become aligned with the depth contours. Wave refraction can also be caused by currents.

Since the waves propagating towards the coast with a certain angle will thus tend to align perpendicularly to the bathymetry, when they leave deep water, the most relevant wave transformations take place along the cross-shore direction. Along this direction, the waves shoal and dissipate their energy, mostly through breaking and bottom friction.

2.2.1 Linear wave theory

In deep water, small-amplitude wave motion ($H << h$) can be thought of as being a pure sinusoidal movement that can be represented by the linear wave theory (Airy, 1845), as shown in Fig. 2.4. According to this theory, a progressive sinusoidal wave can

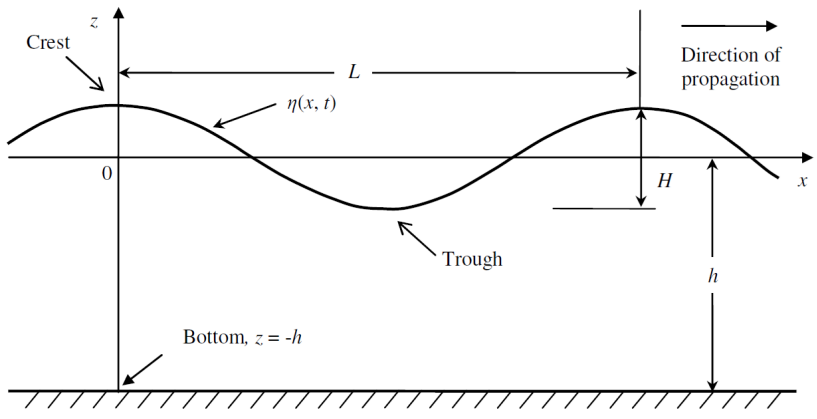

Figure 2.4: Sketch of a progressive sinusoidal wave (Abreu, 2011).

be defined by a sinusoidal variation of the sea-surface η, with a certain wave length L (the horizontal distance between corresponding points on two successive waves), height H (the vertical distance from crest to trough) and period T (the time between the passing of two successive crests at a given point),

$$\eta(x,t) = \frac{H}{2}\cos\left(kx - \omega t\right), \tag{2.3}$$

where x is the spatial coordinate in the direction of wave propagation and t the temporal coordinate, k is the wave number ($k = \frac{2\pi}{L}$) and ω is the wave angular frequency ($\omega = \frac{2\pi}{T}$). In deep water, the particle motion during a wave cycle under a passing linear wave follows circular orbits, whose diameter decreases with depth until the wave base (the limit of fluid motion).

The linear sinusoidal waves are ideal small-amplitude waves that can only exist in deep water ($\frac{h}{L} > 0.5$). As the waves travel towards the coast and the water depth decreases, the shoaling process begins. The waves start feeling the bottom and slow down. This decrease of the phase velocity of the wave ($c = \frac{L}{T}$) implies a decrease of its kinetic energy. In order to maintain the total energy of the wave constant, the potential energy increases and, therefore, the wave height also increases.

As the waves shoal, the particle motion below the free surface also changes, particularly near the bottom. The circular orbits flatten and become elliptical and, in shallow waters ($\frac{h}{L} < 0.05$), the vertical component of the movement becomes negligible. This means that, near the bottom, the horizontal particle displacements and the horizontal velocities become large. Hence, to satisfy the no-slip condition at the seabed, a thin layer where the wave-induced motion is strongly influenced by the bed develops: the boundary layer. This layer is characterized by strong velocity gradients that lead to noticeable shear stresses. This layer is particularly relevant to sediment transport, because it is responsible for the mobilization and transport of the sediment particles. Furthermore, this region is highly turbulent and, consequently, it is where most of the dissipation of the flow energy occurs.

2.2.2 Nonlinear wave properties

Stokes (1847) was one of the first to observe and study the change of the wave shape prior to breaking. He remarked that, as the waves approach the coast and propagate into shallower water (transitional, $0.05 < \frac{h}{L} < 0.5$, and shallow, $\frac{h}{L} < 0.05$ depths), their shape changes, with a gradual peaking of the crests and flattening of the troughs, known as an increase of wave skewness (horizontal asymmetry). At the end of the shoaling zone and throughout the surf zone, the waves start loosing their vertical symmetry as

well, assuming a saw-tooth shape, with a steep front face and a more gently-sloping rear face, increasing their asymmetry (Svendsen & Madsen, 1978; Elgar *et al.*, 1988). This transformation of the free-surface elevation along the cross-shore profile is illustrated in Fig. 2.5.

As they propagate towards the coast, the waves induce a gradient of the excess horizontal-momentum flux, which results in an increase of the mean water level after the breakpoint (the set-up), compensated by a lowering of the mean water level offshore of the breakpoint (the set-down) (Longuet-Higgins & Stewart, 1962). Furthermore, the wave propagation towards the coast may induce an onshore-directed mass flux (a steady second-order drift velocity, known as the Stokes drift, (Stokes, 1847)). In the surf zone, the surf roller adds to the Stokes drift, increasing the mean onshore-directed mass flux. This flux promotes an accumulation of water near the coast, which must then return offshore. This happens by means of an offshore-directed return flow below the level of the wave trough, the undertow. This processes are schematically described in Fig. 2.6.

Near the bed, the flow is affected by the bottom boundary layer. The wave bottom boundary layer is generally a highly-turbulent layer due to the sediment roughness and it has a limited thickness (of the order of 1-10 cm), since it cannot fully develop to a stationary logarithmic flow profile due to the continuously-changing oscillatory flow. Besides the purely oscillatory flow driven by the wave motion near the bed, there is also an onshore mean current, known as the boundary-layer streaming (Longuet-Higgins, 1953).

The linear or small-amplitude wave theory described in the previous subsection provides a useful first approximation to the wave motion. However, ocean waves are generally not small in amplitude and, as they approach the coast and start shoaling and increasing their height ($H/h << 1$ and $H/L << 1$ assumptions become progressively invalid), the linear wave theory no longer provides a sound description. In order to improve the linear theory and to better approach the complete solution of ocean waves, a perturbation solution using successive approximations may be developed (*e.g.* Stokes,

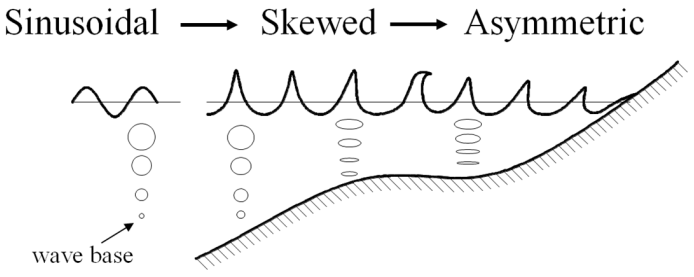

Figure 2.5: Sketch of the wave-shape transformation and corresponding orbital motions as waves propagate from deep to shallow waters (Abreu, 2011).

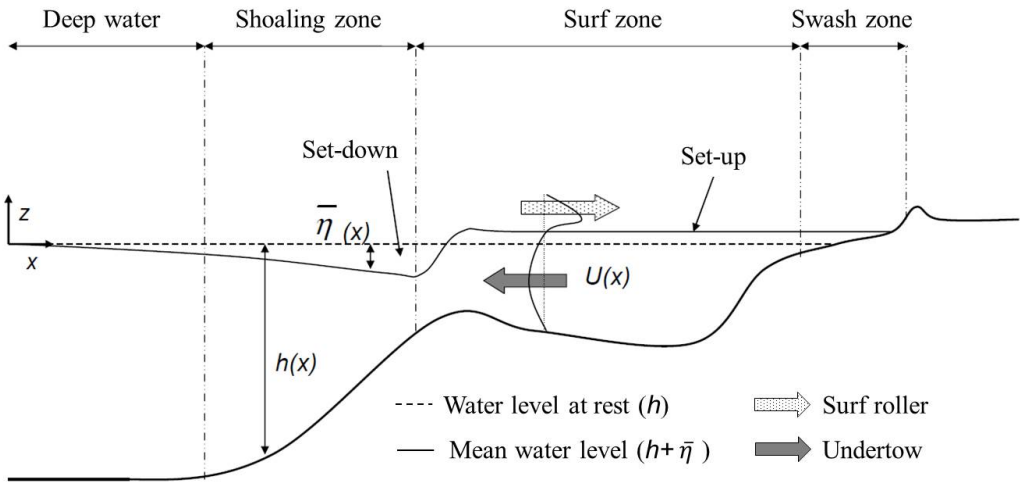

Figure 2.6: Hydrodynamics of a barred beach (adapted from Grasso, 2009).

1847; Boussinesq, 1872; Korteweg & deVries, 1895). The extended theories, often called nonlinear wave theories, have also the advantage of being able of taking into account phenomena associated with the wave nonlinearity, such as the onshore-directed mass transport mentioned before. The cnoidal, solitary and Stokes theories are examples of nonlinear wave theories. Fig. 2.7 shows the wave profile shape as predicted by the different wave theories.

As the the shape of the waves starts changing, with increasing skewness and asymmetry, the corresponding orbital velocity near the bottom follows the variation of the free-surface elevation, and also becomes nonlinear, as depicted in Fig. 2.8.

In the case of a purely-velocity-skewed oscillatory flow, the velocity at the wave crest

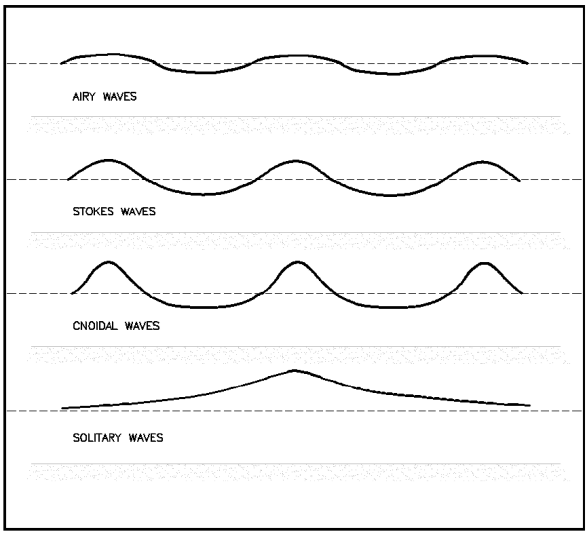

Figure 2.7: Wave profile shape of different progressive gravity waves (U.S. Army Corps of Engineers, 2002).

Figure 2.8: Sketch of a velocity-skewed flow (left) and an acceleration-skewed flow (right) (Abreu, 2011).

is higher, but of shorter duration than at the trough. This induces larger bed shear stresses during the crest than during the trough. When the flow is purely velocity-asymmetric, under the steep front face of the waves, the velocity varies rapidly from a maximum negative (offshore) value to a maximum positive (onshore) value, promoting rapid fluid accelerations. The accelerations induced by the motion of the rear face of the wave are much smaller. This implies that, for velocity-asymmetric flows, acceleration is skewed. Abrupt accelerations are associated with thinner boundary layers and thus higher bed shear stresses for a given velocity magnitude (Elgar *et al.*, 2001).

The near-bed orbital velocity skewness and asymmetry are crucial for sediment transport and are thus important to quantify. In this work, the statistical definitions for velocity skewness (Sk_u) and asymmetry (As_u) are used and calculated, according to Elgar *et al.* (1988), with the following expressions,

$$Sk_u = \frac{\langle (u - \overline{u})^3 \rangle}{{\sigma_u}^3}, \tag{2.4}$$

and

$$As_u = \frac{\left\langle (\mathscr{H}\,(u - \overline{u}))^3 \right\rangle}{{\sigma_u}^3}, \tag{2.5}$$

where u represents the velocity time series, with the angle brackets denoting time-average, σ represents the standard deviations and $\mathscr{H}$ is the imaginary part of the Hilbert transform. The evolution of skewness and asymmetry can then be used to describe the transformation of the near-bed velocity as the waves approach the shore.

Another way of describing this wave transformation along the cross-shore profile is in terms of the energy present at each frequency in the wave spectrum, as is illustrated in Fig. 2.9. Initially, when the waves leave deep water, most of the energy is concentrated near the peak frequency (blue spectrum in Fig. 2.9). Then, as they progress into shallower water, nonlinear triad interactions between the different frequency components start taking place and changing the wave shape (Elgar & Guza, 1985). Energy is first transferred from the primary wave components near the peak (f_1 and f_2, in the case of bichromatic waves), towards secondary components that are multiples of the peak frequency (for bichromatic waves, towards secondary components with the sum $f_1 + f_2$

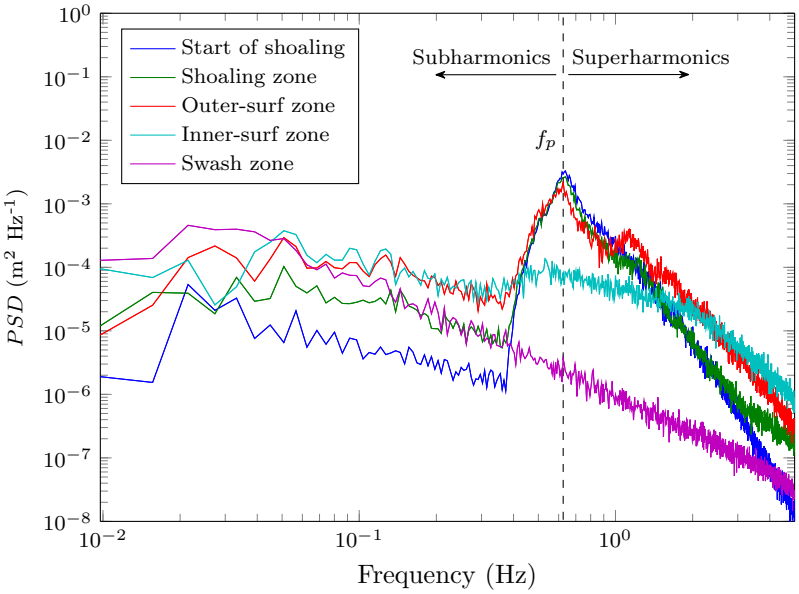

Figure 2.9: Example of the power spectra of free-surface elevation at different cross-shore positions, in a gently-sloping wave flume, for irregular-wave conditions (GLOBEX project, see section 3.2).

or difference $f_1 - f_2$ frequency). These secondary components are called super or subharmonics, if they have, respectively, greater or smaller frequencies than the peak frequency. The nonlinearly-excited secondary wave components are phase-locked to the primary wave components, thus causing deviations from Gaussian statistics, such as steep or asymmetric wave profiles (Norheim *et al.*, 1998). If the harmonics are in phase with the fundamental, this will result in skewed velocity, if they are out of phase, the velocity will be asymmetric. Coincident with the shape transformation of the incident ocean waves, the difference interactions also transfer energy to infragravity waves (Herbers *et al.*, 1994). This is depicted, for irregular waves, by the violet spectrum in Fig. 2.9, which has greater energy in the lower frequencies than in the fundamental-frequency range. This spectrum is typical of the swash zone, as the incident waves and their superharmonics predominantly dissipate in the surf zone and thus infragravity (lower-frequency) waves, even though they may partially reflect at the beach, often dominate the wave run-up at the shoreline. The current state of the art on the understanding of the wave and velocity nonlinearities is summarised in greater detail in chapter 3.

2.2.3 Infragravity waves

Munk (1949) was the first to report low-frequency motions in the nearshore zone, well outside the surf zone, which he called "surf beat", suggesting their origin to be related to the variability of mass transport by the incident waves into the surf zone.

Also known as infragravity waves (IG), subharmonic waves or, simply, long waves, these are waves with longer periods than the gravity (short) waves, of the order of 100 s.

The incident waves propagating towards the coast are organized in groups. The higher waves in each group induce a larger mass transport than the lower waves and hence the difference in the momentum flux causes a transfer of fluid from the higher waves to the lower ones, promoting the development of a "set-down" wave. This wave has the same period and length of the short-wave groups and, for wave groups propagating over a horizontal bed, it is phase-locked and in anti-phase with the short-wave envelope, being thus called bound infragravity wave (Biésel, 1952; Longuet-Higgins & Stewart, 1962, 1964). The irregular waves, their envelope and the bound IG wave are represented in Fig. 2.10.

For shoaling waves, the bound wave travels slightly slower than the wave groups, which causes an increasing phase lag as the depth diminishes, eventually resulting in a phase shift between IG waves and the wave groups. This phase shift (Masselink, 1995; Janssen *et al.*, 2003) is a crucial mechanism of energy transfer from the short waves to the bound IG wave. What happens to the bound waves in the end of shoaling/beginning of breaking is still a current topic of discussion in the research community. Many assume from the theory of Longuet-Higgins & Stewart (1962) that the bound IG waves are mostly released as free waves in the shoaling and breaking processes; others, such as Baldock (2012), argue that the amplitude of the bound IG waves may in fact decay following short-wave breaking, but the former will only be released as free waves when the water is shallow enough for the dispersion relationship to be satisfied for these waves. At the shore, the IG waves can partially reflect off the beach and propagating seawards, as leaky waves, or become trapped at the coastline as edge waves (being either longshore progressive or standing).

A second mechanism of IG-wave generation is also possible, directly related to the variability of the short-wave breakpoint (Symonds *et al.*, 1982). Resulting from the varying amplitude of the incident waves (inducing slow oscillations in the wave setup),

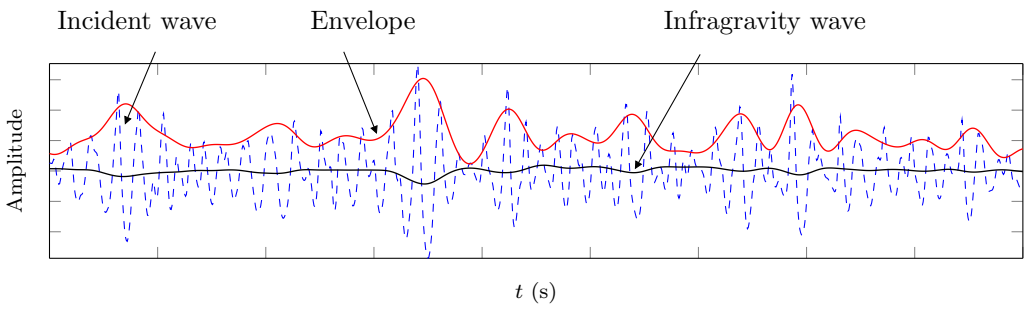

Figure 2.10: Incident irregular waves and associated infragravity wave, in anti-phase with the wave envelope.

the breakpoint changes its location, acting similarly to a wave-maker, radiating free IG waves at the group frequency (and their harmonics), both shorewards and seawards.

Arriving at the shoreline, infragravity waves can either be fully reflected seawards, become trapped at the coastline or dissipate. Battjes *et al.* (2004) found the normalized bed slope parameter, β, to govern dissipation at the shoreline and defined this parameter as

$$\beta = \frac{h_x}{\omega}\sqrt{\frac{g}{h}}, \tag{2.6}$$

with h and h_x the characteristic values of depth and bed slope in the region considered, $\omega = 2\pi f$ the angular frequency (with f the wave frequency) and g the acceleration of gravity. Large values of β imply a nearly-full reflection at the shoreline, whereas for small values of β, reflections at the shoreline are small. When the waves do not fully reflect at the shoreline, part of the energy flux is directed shorewards and ends by dissipating.

The mechanisms involved in infragravity-wave dissipation are not yet a topic of consensus in the research community. Bottom friction (Henderson & Bowen, 2002), nonlinear energy transfers to and from infragravity waves (Henderson *et al.*, 2006; Ruju *et al.*, 2012) and self-self nonlinear interaction of infragravity waves leading to infragravity-wave breaking (van Dongeren *et al.*, 2007; de Bakker *et al.*, 2014) are likely to be significant dissipation mechanisms, with a distinct importance depending on the location along the cross-shore profile.

Even though of much smaller amplitude in deep water than the short waves to which they are associated, the infragravity waves may modulate the propagation of the short waves. They can become particularly important near the coast, where the energy transfer becomes near-resonant and, consequently, infragravity-wave height can augment rapidly to over 1 m (Ruessink *et al.*, 1998a; Sénéchal *et al.*, 2011). In the swash zone, where the amplitude of the short waves becomes very small, the infragravity waves can dominate the hydrodynamics, controlling the water depth.

2.2.4 Swash zone

With a very different hydrodynamics from the rest of the beach profile, the swash zone is the limit between the aerial and the submerged beach areas which is intermittently covered and exposed by wave action. For monochromatic waves this region is well defined, while for irregular waves the maximum run-up (excursion of the waves up the beach above the mean water level), down-wash (excursion of the waves down the beach below the mean water level) and set-up vary constantly in time.

A large range of scales and types of fluid motion may be present in the inner-surf

zone, which subsequently govern shoreline oscillations and swash hydrodynamics. Fig. 2.11 schematically represents the transfer of offshore energy into swash-zone oscillations. If the surf zone is saturated (short-wave heights are depth-limited), the hydrodynamics in the inner-surf zone may be expected to be dominated by infragravity waves and cross-shore standing wave oscillations are usually observed at infragravity frequencies; if it is unsaturated (local wave height independent of depth), short-wave energy dominates the inner-surf zone, with incident bores collapsing at the shoreline and propagating up the beach (Huntley *et al.*, 1977; Guza & Thornton, 1982; Wright & Short, 1984; Raubenheimer *et al.*, 1996). The wave energy dominating the swash zone is thus dependent on the relative magnitudes of short and IG wave energy in the inner-surf zone, that are in turn dependent on the offshore wave groupiness (which can be seen as the offshore short-wave variability). The type of swash motion that prevails is ultimately dependent on the incident-wave conditions and beach morphology.

In natural beaches, high infragravity-energy levels, saturation and dissipation of short-wave energy in the surf zone and saturation of bore-driven swash oscillations at short-wave frequencies contribute to a dominance of IG-wave motion in the swash. For irregular waves, the swash motion at both low and high frequencies is also dependent on the interaction between successive swash events and the interaction between standing waves and incident bores (Elfrink & Baldock, 2002).

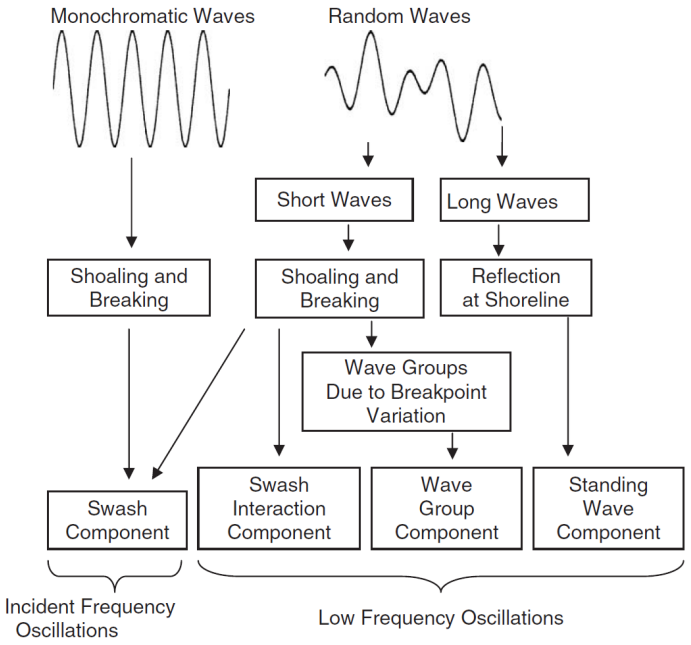

Figure 2.11: Schematic representing the transfer of offshore energy into swash-zone oscillations (Masselink *et al.*, 2006).

2.3 Morphodynamics

Different regimes of sediment transport can be identified, depending on the velocity of the fluid and the characteristics of the sediment (Nielsen, 1992). The sediment can be transported (i) near the bed, as bed load, rolling and sliding, (ii) by saltation, an intermediate mode between suspension and bed load, when the sediments are transported in suspension but impact the bed regularly, or (iii) as suspended load, when particles rest suspended in the water column during the transport and move with the fluid. There is also the sheet-flow regime, a particularly intense mechanism of horizontal sediment transport near the bottom that includes the three modes of transport previously mentioned (bed load, saltation and suspended load) and can be found in different regions of the cross-shore profile, at sufficiently-high bottom shear stresses.

The balance between the different hydrodynamic processes acting over a given beach profile determines the direction of the net sediment transport. Since the beach profile evolves during the action of any given wave climate, it becomes particularly difficult to evaluate the individual contribution of each hydrodynamic process to the sediment transport, as there are ever changing feedbacks between the morphology and the hydrodynamics.

The energetics approach (Bagnold, 1963; Bowen, 1980; Bailard, 1981; Guza & Thornton, 1985; Russell & Huntley, 1999) assumes the sediment transport rate to be proportional to the dissipation of energy near the bed and provides an equation for the total (bed and suspended load) time-averaged immersed-weight sediment transport. This approach can be used to estimate the relative contribution of the different terms containing powers of the instantaneous velocity, which can then be related to different sediment-transport processes. Initially, the instantaneous near-bed cross-shore velocity is decomposed into it mean, short and infragravity wave components, as

$$u = \overline{u} + \widetilde{u}, \tag{2.7}$$

where $\widetilde{u} = \widetilde{u_S} + \widetilde{u_{IG}}$, with u the total cross-shore velocity, $\overline{u}$ the mean flow component and $\widetilde{u}$ the oscillatory component, which can be divided into $\widetilde{u_S}$, the velocity associated with the short waves and $\widetilde{u_{IG}}$, the velocity associated with the infragravity waves. The total-load sediment transport equation can hence be obtained as

$$\langle \vec{q}_t \rangle = \rho C_f \frac{\epsilon_B}{\tan\phi} \left[\left\langle |\vec{u}|^2 \, \vec{u} \right\rangle + \frac{\tan\beta}{\tan\phi} \left\langle |\vec{u}|^3 \right\rangle \hat{i} \right] + \rho C_f \frac{\epsilon_S}{w_s} \left[\left\langle |\vec{u}|^3 \, \vec{u} \right\rangle + \frac{\epsilon_S}{w_s} \tan\beta \left\langle |\vec{u}|^5 \right\rangle \hat{i} \right], \tag{2.8}$$

where ρ is the water density, C_f is the drag coefficient, ϵ_B and ϵ_S are the bed-load and suspended-load efficiencies, respectively, ϕ is the coefficient of internal bed friction, β is the local bed slope, w_s is the fall velocity of the sediment, $\hat{i}$ is the unit vector in the (down-slope) offshore direction and $\vec{u}$ is the total instantaneous velocity vector. The $\left\langle |\vec{u}|^2 \, \vec{u} \right\rangle$ and $\left\langle |\vec{u}|^3 \, \vec{u} \right\rangle$ are the process-related moments and $\left\langle |\vec{u}|^3 \right\rangle$ and $\left\langle |\vec{u}|^5 \right\rangle$ are the gravity terms. The decomposition of the instantaneous near-bed cross-shore velocity will be used later in this work to analyse the theoretical contribution of different mechanisms to the sediment transport.

The distinct hydrodynamic zones of the cross-shore profile are also zones with a different balance between the several sediment-transport mechanisms. Therefore, the sediment transport processes at action in the shoaling zone, in the breaker and surf zones and in the swash zone, are subsequently described.

2.3.1 Shoaling zone

If motions of very long period, such as the tidal currents, are ignored, in the shoaling zone there are two main mechanisms promoting sediment transport. At higher frequencies, skewed waves induce high crest velocities in the onshore direction that mobilize and transport more sediment than the offshore-directed trough velocities (Hsu & Hanes, 2004; Mariño-Tapia *et al.*, 2007). This is due to the fact that the boundary layer has less time to grow during the rapidly-accelerating half-cycle, inducing higher (absolute) velocity gradients and shear stresses than in the half-cycle with less acceleration (Nielsen, 1992). However, under certain circumstances (such as relatively-small wave periods, finer grains, rippled beds) the existence of phase-lag effects may imply that, while the sediment may be put in suspension by the onshore phase of the wave cycle, it may not settle immediately, staying in suspension until the offshore stroke of the wave arrives, which contributes to an offshore transport.

At lower frequencies, even though infragravity waves are probably not capable of suspending sediment, the velocities associated with these waves can advect sediment already in suspension. In that sense, infragravity waves can be considered to behave analogously to mean currents, advecting sediment suspended by short-wave action. In the shoaling zone, the infragravity waves still bound to the wave groups contribute to an offshore transport, as the greater short waves of each group are concomitant with the negative phase of the IG-wave cycle (Osborne & Greenwood, 1992b). This transport is usually an order of magnitude smaller than the onshore-directed transport by the short waves (Baldock *et al.*, 2011) and, in a general way, velocity skewness dominates the shoaling-zone sediment transport, which is mainly induced by bed-shear stresses (Ribberink *et al.*, 2000).

Besides the two main mechanisms mentioned, the boundary-layer streaming and, near the end of the shoaling zone, the wave asymmetry, can also contribute to an onshore sediment transport.

2.3.2 Breaker and surf zones

As the waves approach breaking, new mechanisms start contributing to sediment transport. Besides being skewed, waves become asymmetric as well. The incipient sediment motion can then be induced by fluid accelerations driven by pressure gradients promoted by the steep front faces of asymmetric waves (Drake & Calantoni, 2001; Calantoni & Puleo, 2006; Foster *et al.*, 2006; Silva *et al.*, 2011). Since more sediment is mobilized by the crests than the troughs, free-stream asymmetry possibly triggers a skewed shear stress in the boundary layer (van der A *et al.*, 2010; Ruessink *et al.*, 2011; Berni *et al.*, 2013), further favouring the onshore sediment flux. Short-wave breaking contributes both for picking-up sediment from the bed and to generate wave turbulence, both contributing to picking up, entrainment and suspension of the sediment in the flow. Responding to the wave breaking, the undertow is the main mechanism transporting the suspended sediment offshore (Mariño-Tapia *et al.*, 2007). The direction and magnitude of the infragravity-wave contribution to sediment transport in the breaker and surf zones are still currently under debate.

Infragravity-wave motion in the surf zone can affect sediment transport in different ways. Depending on the phase relationship between the infragravity waves and the short-wave groups, infragravity waves can have an important role modulating the propagation of the short waves. Especially in shallow waters, these long waves can significantly alter water depth, contributing to variations of the short-wave amplitude, which may eventually induce changes in the breakpoint position. A concept of re-suspension maxima (located at x_r) can be defined, corresponding to locations of maximum bed shear stress and maximum suspended sediment concentrations, associated with relative wave height maxima. Fig. 2.12 illustrates this concept. Landward (seaward) of a re-suspension maximum, the net transport by infragravity waves is directed onshore (offshore), responding to the landward (seaward) infragravity-wave stroke (Aagaard & Greenwood, 2008) that "picks up" the sediment at the re-suspension maximum, where the sediment concentration is large, and advects it shorewards (seawards). The infragravity-wave strokes directed towards (and not away from) the re-suspension maximum (both from more seaward or more shoreward positions) do not encounter enough suspended sediment to advect.

Furthermore, if a partially-standing wave is set up by reflection of infragravity waves at the shoreline, a second-order mass transport can be associated with the infragravity-

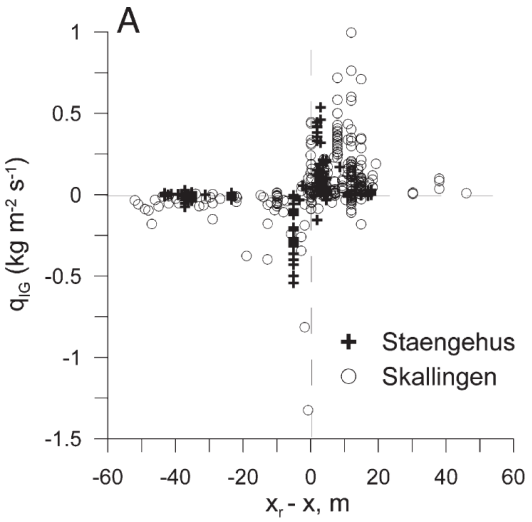

Figure 2.12: Observed net IG sediment fluxes plotted against the measurement position relative to the re-suspension maxima ($x_r - x$) for all experiments at Skallingen and Staengehus. Positive sediment fluxes depict a net onshore sediment transport and positive values of ($x_r - x$) indicate that the measurement position was located landward of the re-suspension maximum (Aagaard & Greenwood, 2008).

wave motion (if the motion is steady and the frequency well defined) (Vicinanza *et al.*, 2011). Therefore, even if short waves are responsible for most gross sediment transport, overall, the morphological evolution depends on gradients in the sediment transport and these can subtly change over the timescales of infragravity waves and wave groups. The current state of the art on the role of IG waves in the sediment transport is described in greater detail in chapter 4.

Nearshore sand bars are a typical feature of the beach profiles which influences the evolution of the shoreline. Two hypothesis are currently proposed for sand-bar formation (Dally, 1987). The first hypothesis proposes that bars may form near the breakpoint of short incident waves, resulting from the convergence of sediment transported onshore in the shoaling zone by the wave asymmetry, and offshore in the surf zone by the bed return flow. In this case, slow bar onshore migration and growth are driven by an asymmetry-induced transport, while mean-current-induced sediment transport (undertow) systematically contributes to offshore bar migration. Skewness-induced transport can either drive onshore or offshore bar migration (Dubarbier *et al.*, 2015). The other hypothesis is that bars may be generated at the antinodes of standing infragravity waves (infragravity-wave velocity nodes), as these represent locations of potential sediment convergence.

2.3.3 Swash zone

An important part of the littoral sediment transport occurs in the swash zone, with sediment concentrations that may typically be several orders of magnitude higher than in the inner-surf zone (Beach & Sternberg, 1991). Offshore and onshore sediment transport in the swash zone thus contribute significantly to shoreline accretion and erosion. The swash zone is characterized by strong and unsteady flows, high turbulence levels, large sediment transport and rapid morphological change (Puleo *et al.*, 2000). In this zone, the net sediment transport is the result of two opposing quantities (the transport during the uprush and the backwash), each of which is several orders of magnitude higher than the resulting net transport, which makes it very difficult to measure and to model.

Sediment transport in the swash zone occurs predominantly under sheet-flow conditions, over a flat bed, with different forcing phenomena acting as sediment-transport controlling mechanisms, such as wave breaking and bore collapse, backwash, sediment advection, infiltration/exfiltration effects, fluid-velocity asymmetries, infragravity waves, wave groups and acceleration asymmetry in the cross-shore flows. Fig. 2.13 offers a schematic summary of the processes at action and modes of sediment transport present during a swash cycle.

The uprush is generally dominated by bore turbulence, especially on steep beaches

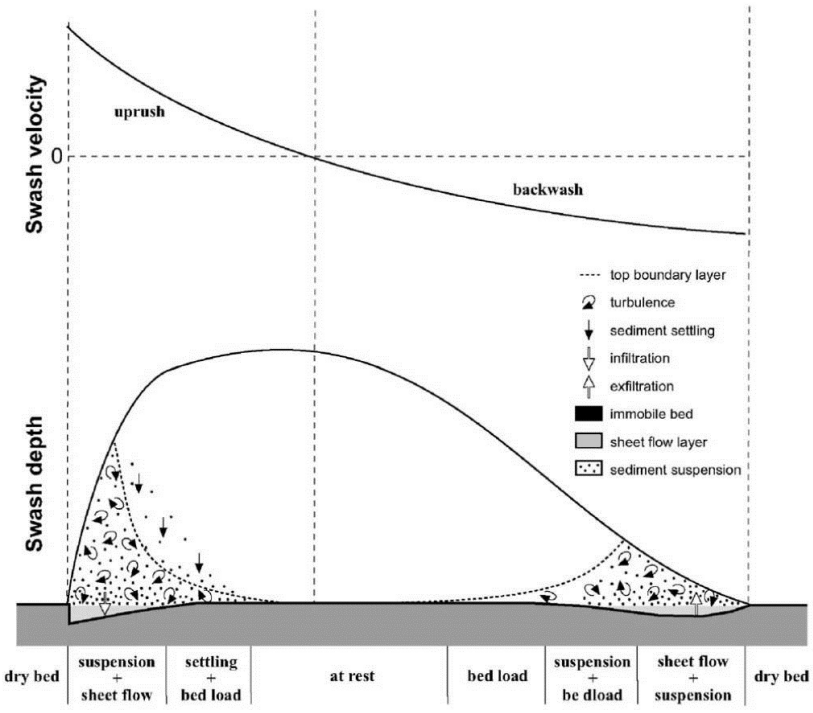

Figure 2.13: Schematic representation of the sediment transport processes during a swash cycle (Masselink *et al.*, 2006).

and in the lower-swash zone, with large shear stresses mixing the sediment higher in the water column, which is then transported as suspended load. The velocity and landward extent of the uprush is controlled by the forcing conditions in the surf zone, beach gradient and sediment characteristics (Inch *et al.*, 2015). Flow velocities are onshore-directed during the uprush, but flow in the lower-swash zone often reverses before the uprush has reached its maximum landward extent (Masselink & Puleo, 2006). Backwash flows are dominated by bed-generated turbulence (Petti & Longo, 2001; Cowen *et al.*, 2003), accelerating under the forces of gravity and offshore-directed pressure gradients (Baldock *et al.*, 2001). Flow velocities are similar for both phases of the swash, but typically of unequal duration, with a longer backwash with slightly weaker velocities (Puleo *et al.*, 2003; Masselink *et al.*, 2005; Aagaard & Hughes, 2006).

The swash motion is inextricably linked to the morphology of the beachface, whose most characteristic feature is its gradient, steeper than the rest of the beach profile. Only when the uprush transports onshore the same amount of sediment that the backwash transports offshore is a dynamic equilibrium reached between the beachface and the swash motion. The equilibrium gradient represents the balance between onshore swash asymmetry and the downslope gravity component (Hardisty, 1986), and the sediment size is the most important factor controlling it. The sediment size influences the sediment fall velocity, but also the permeability of the bed and thus the in/exfiltration effects, which condition the sediment transport during the uprush and backwash phases of the swash motion. For a given sediment size, the equilibrium beachface gradient decreases with the wave height and increases with the wave period (Dalrymple & Thompson, 1976).

The response of the beachface to changing hydrodynamic conditions can be understood in terms of how far the beach profile is, at each moment, from the equilibrium conditions that correspond to the hydrodynamic conditions. A net onshore sediment transport will dominate when the beachface is too gentle, with the uprush moving more sediment than the backwash, eroding the lower part of the beach and depositing the sediment in the upper part. When the beach is too steep, the backwash will transport more sediment than the uprush, eroding the upper part of the beach and depositing the sediment in the lower part. The swash period will also be affected, as a steepening/flattening of the beachface results in a decrease/increase of the swash period. The beach gradient of the lower swash zone further controls the type of breaker or bore, thus playing an important role in the amount of turbulence and sediment suspension. Hence, the processes of beachface steepening or flattening constitute a local feedback between swash hydrodynamics and beachface morphology and evolve continuously until the beachface is in equilibrium with the wave conditions.

Not only do the swash morphodynamics have their own feedback mechanisms, but there also interact with the surf-zone morphodynamics. When the beachface is eroded, sediment is deposited in the surf zone, shifting the location of short-wave energy dissipation from the lower beachface to the surf zone. This results in less short-wave-driven swash dynamics, as less short-wave energy reaches the base of the beachface. If, instead, sediment is transported from the surf zone to the beachface, short-wave breaking may happen closer to the base of the beachface (as the local water depth increases), resulting in a shifting of the short-wave energy dissipation back to the swash zone, which will be exposed to higher short waves and more short-wave-driven swash dynamics. Moreover, a change in the beachface gradient can modify the reflectivity of the beach, particularly for IG waves, changing the amount of reflected infragravity-wave energy in the surf zone. It is overall clear that the beachface cannot be considered in isolation from the surf zone and that the two zones are strongly linked though feedback processes (Masselink *et al.*, 2006).

Chapter 3

Wave propagation and nonlinearities

3.1 Introduction

Understanding nearshore morphodynamics implies a profound knowledge of the hydrodynamics and the complex interaction between motions at different spatial and temporal scales. Along the cross-shore beach profile, as the surface gravity waves propagate from deeper waters to the shore, their shape changes, primarily due to nonlinear wave interactions (Elgar & Guza, 1985; Doering & Bowen, 1995) and further on due to breaking. The nonlinear effects amplify the higher harmonics and cause the oscillatory flow to transform from sinusoidal in deep water, through velocity-skewed in the shoaling zone, to velocity asymmetric in the inner-surf and swash zones. The influence of skewness and asymmetry on sediment transport is hard to study, because it is difficult to isolate those phenomena from other phenomena, such as the breaking-induced turbulence, the undertow, etc. However, these nonlinearities are of paramount importance for understanding sediment dynamics.

In addition to short-wave nonlinearities, the presence of IG waves and wave groups also results in a wave-induced velocity and influences the short-wave hydrodynamics and larger-scale processes, such as the formation of standing waves or cross-shore and longshore nodal structures both inside and outside the surf zone (Baldock *et al.*, 2011). Further, IG waves can themselves contribute to velocity skewness and asymmetry at low frequencies, particularly for very-dissipative mild-slope beach profiles, where IG-wave shoaling and breaking can also occur (van Dongeren *et al.*, 2007; de Bakker *et al.*, 2014).

The role of short-wave nonlinearities on sediment transport has long been recognized. Wave skewness was included in early analytical parameterizations of sediment transport and sand-bar migration numerical models (*e.g.* Stive, 1986). Later on, it was recognized

that, to improve model performance, particularly regarding onshore sand-bar migration, asymmetry should be considered as well. New parameterizations were proposed (*e.g.* Drake & Calantoni, 2001; Elfrink *et al.*, 2006; Abreu *et al.*, 2010; Ruessink *et al.*, 2012) and it became more clear how to include the effects of asymmetry. Finally, the first models capable of better representing onshore sand-bar migration have recently been developed (*e.g.* Dubarbier *et al.*, 2015; Fernández-Mora *et al.*, 2015).

A great effort has been put into finding parameterizations and models capable of correctly representing these nonlinear effects. Currently-used parameterizations still rely mostly on an exclusive dependency of nonlinearity on local wave conditions to describe skewness and asymmetry along the beach profile, even though with the precaution of assuming the parameterizations are only valid for a certain type of beach slope or range of offshore wave conditions. However, applying existing parameterizations to field data, Rocha *et al.* (2013b) have suggested that defining Sk and As from local wave parameters only is not enough, as the history of the wave propagation may also be important. Furthermore, other researchers have already underlined the importance of considering characteristics such as the offshore wave steepness (Dibajnia *et al.*, 2001) and spectral bandwidth (Norheim *et al.*, 1998), as well as the beach slope (Norheim *et al.*, 1998; Dong *et al.*, 2014; Filipot, 2015), in order to correctly describe the wave nonlinearity at a given cross-shore position. There is, hence, a lack of thorough understanding of which factors may effectively condition the evolution of wave nonlinearities besides the local wave parameters (local wave height and period and water depth).

Therefore, the aim of this chapter is to analyse wave propagation and improve its comprehension with respect to wave and velocity nonlinearities. The evolution of the nonlinearities during the wave propagation towards the coast is explored in detail, for a wide range of irregular and bichromatic wave conditions and different beach slopes. The analysis is done for both free-surface elevation and velocity and comprises the entire beach profile, from the shoaling zone until the end of the swash zone. The main research questions explored are the following:

- How do short-wave nonlinearities evolve along the beach profile, for different wave conditions?
- How do infragravity waves influence short-wave propagation and short-wave nonlinearities?
- What is the importance of infragravity-wave nonlinearities?
- Which factors influence significantly wave and velocity nonlinearities?
- How can current parameterizations of nonlinearity be improved?

This chapter is divided into three main sections: physical modelling, numerical modelling and parameterization of velocity nonlinearities. In the first section, a high-resolution data set gathered during the GLOBEX Hydralab IV project, held in the Deltares Scheldegoot in the Netherlands, is analysed. This section starts by describing the experiments and preliminary data analysis. Then, the evolution of free-surface elevation and cross-shore velocity are analysed and compared between conditions, highlighting the particularities of each wave condition and the differences between irregular and bichromatic wave groups. The importance of the lower frequencies is evidenced and thus the IG waves are regarded more thoroughly. The IG-wave separation into incident and reflected components is discussed and a comparison is made between free IG waves and IG waves that propagate associated with short-wave groups. In the last part of this section, the analysis of the nonlinearities is done for free-surface elevation and velocity. From the analysis and comparison of the different wave conditions, it is suggested that the evolution and maximal values of the nonlinearity may depend on certain wave and beach characteristics.

The following section is based on the results of numerical simulations aimed at extending GLOBEX wave conditions, in order to unravel which wave or beach parameters are the most important in determining wave nonlinearities. These results, together with the analysis of several field data sets, present new evidence of the dependence of nonlinearities on offshore wave parameters and beach slope. Hence, in the last section of this chapter, an improvement to the Ruessink *et al.* (2012) parameterization is proposed, which takes into account new parameters and provides a better prediction of the nonlinearities for a wider range of beach slopes and wave conditions. The chapter draws to an end with the conclusion.

3.2 Physical modelling - the GLOBEX project

3.2.1 The experiments

The laboratory data set used in this chapter was collected during the GLOBEX Hydralab IV project (Ruessink *et al.*, 2013; Michallet *et al.*, 2014), held in the Scheldegoot (Fig. 3.1) in Delft, the Netherlands, in April 2012. The aim of this project was to collect a high-resolution (in space and in time) data set of the cross-shore evolution of the short and infragravity waves in a very gently-sloping beach, for a range of wave conditions, including irregular, bichromatic and monochromatic waves. This data set was gathered for the study of infragravity-wave dynamics, wave propagation and boundary-layer dynamics. In the scope of this thesis, the focus of the analysis of GLOBEX data is on the wave propagation (in particular, on the wave nonlinearities) and on the interaction

Figure 3.1: Deltares Shelde flume.

of short waves and infragravity waves.

The GLOBEX beach had an impermeable concrete bed and was 110-m long and 1-m wide, with an initial plain section of 16.57 m, followed by a slope of 1/80 until the end of the flume (Fig. 3.2). The shoreline was located at 84.57 m from the wave-maker position at rest ($x = 0$), corresponding to a mean water depth above the plain section of 0.85 m. The waves were generated by a piston-type wave-maker equipped with Active Reflection Compensation (ARC) to absorb waves coming from the beach and prevent their re-reflection at the wave-maker. All wave-paddle steering signals included second-order wave generation. Table 3.1 presents the characteristics of the 8 wave conditions that were simulated during the experiments.

Series A involved random waves with different H_s and T_p, A1 corresponding to

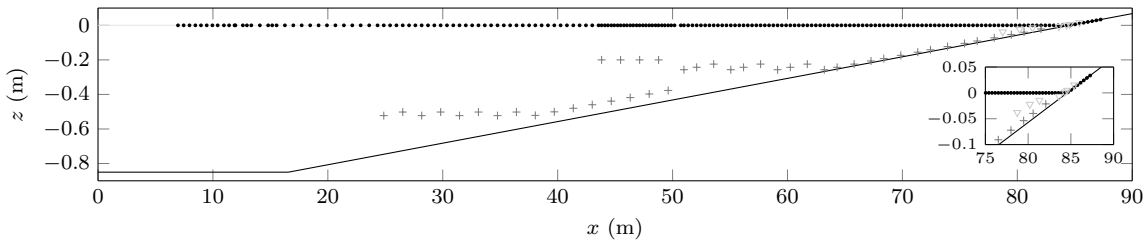

Figure 3.2: Elevation z versus cross-shore distance x of the GLOBEX flume ($x = 0$ is the position of the wave maker at rest and $z = 0$ is the still water level). The dots represent the wave gauges positions, the pluses the ECM positions and the triangles the ADV positions considered in the scope of this paper. The figure in the corner represents a zoomed area near the shoreline.

Table 3.1: Overview of the wave conditions. Hs - significant wave height; T_p - wave peak period; γ - spectral bandwidth parameter; a_1 and a_2 - amplitude of the two primary frequencies (f_1 and f_2) of each bichromatic wave condition; T_{IG} - infragravity-wave period.

	H_s **(m)**	T_p **(s)**	
A1	0.10	1.58	JONSWAP, γ=3.3
A2	0.20	2.25	JONSWAP, γ=3.3
A3	0.10	2.25	JONSWAP, γ=20

	a_1 **(m)**	a_2 **(m)**	f_1 **(Hz)**	f_2 **(Hz)**	T_{IG} **(s)**
B1	0.09	0.01	6/15	7/15	15
B2	0.09	0.01	0.42	0.462	23.8
B3	0.07	0.03	0.42	0.462	23.8

	H **(m)**	T **(s)**	
C1	0.02	23.8	Monochromatic infragravity waves

an intermediate-energy condition, A2 to a high-energy condition and A3 to a more narrow-banded case, similar to energetic swell conditions. Series B consisted of three bichromatic wave cases. For B1 and B2 the amplitudes of the primary components (a_1 and a_2) were the same, and the difference frequency (IG-wave frequency) was different. For B2 and B3, the same frequencies were chosen for the primary components, but the group modulation of B3 was greater. C1 consisted on a monochromatic infragravity wave with a period identical to the period of B2 and B3 IG waves. Each condition of series A and B was run for 75 min, followed by a rest period of approximately 15 min. C1 was run for 30 min.

A suite of instruments was deployed during all runs, including 22 wave gauges (10 of resistive-type and 12 of capacitive-type), sampling at 128 Hz, for measuring free-surface elevation, and 5 Electromagnetic Current Meters (ECM), sampling at 128 Hz as well, and 2 side-looking Acoustic Doppler Velocimeters (ADV), sampling at 200 Hz, for recording flow velocities. After all wave conditions were completed, most instruments were repositioned and the same conditions were repeated with exactly the same wave-board motion. Overall, 10 batches were run, resulting in a total of 190 positions along the flume with free-surface elevation measurements and 47 with flow-velocity data (at 1-30 cm above the bed, obtained with the ECMs). One of the ADVs, positioned near the bottom (at about 6 mm above the bed), was used to extend the ECMs velocity measurements (which ended at $x = 79.48$ m) further into the inner-surf/swash zone for depths shallower than 5 cm, adding 10 more cross-shore positions

of velocity measurements (starting at $x = 78.73$ m), of which at least three were, in average, located in the swash zone (see zoomed region in Fig. 3.2). A more detailed description of the experimental procedure and all the measurement instruments used can be found in Ruessink *et al.* (2013).

3.2.2 Preliminary data analysis

Time series and spectra

The free-surface elevation and flow-velocity time series, of high-resolution in time and in space, allow a clear description and analysis of the wave propagation across the shoaling, surf and swash zones, for both short and IG waves. Figs. 3.3 and 3.4 show an example of the free-surface elevation and cross-shore velocity time series obtained at different positions along the beach profile, for A2 irregular-wave case and B2 bichromatic-wave case, respectively. IG waves are separated from short waves by filtering the full signal at the cut-off frequency (f_c). This frequency is defined, for the A series, by a minimum of the variance density spectrum of the free-surface elevation measured at the wave gauge closest to the wave-maker (de Bakker *et al.*, 2014). For the B series, this minimum is less marked, and thus half the peak frequency is used as f_c (Janssen *et al.*, 2003). Both ways of computing the f_c lead to very similar values. For all conditions, the cut-off frequency separates the range of frequencies that initially have more energy and will tend to loose energy as the waves propagate towards the

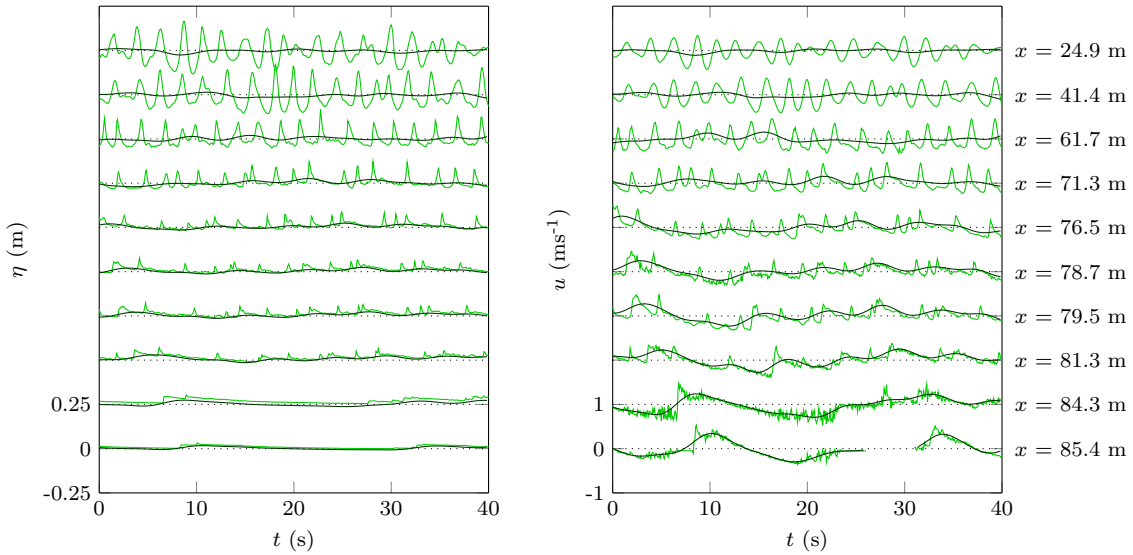

Figure 3.3: Free-surface elevation and velocity time series for the irregular-wave case A2, for different cross-shore positions (top: closer to the wave-maker, bottom: closer to the shore). For each cross-shore position, the scale (of height or velocity) is centered in the dotted line, which represents the zero level, as it is exemplified for the $x = 85.4$ position. The darker lines represent the short waves (high frequencies) and the lighter lines the infragravity waves (low frequencies).

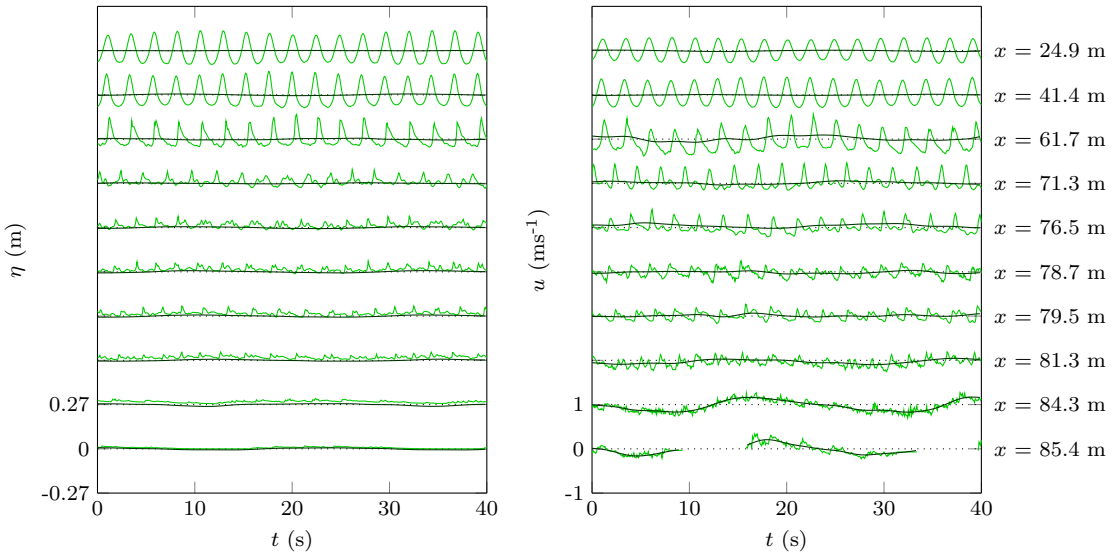

Figure 3.4: Free-surface elevation and velocity time series for the bichromatic-wave case B2, for different cross-shore positions (top: closer to the wave-maker, bottom: closer to the shore). For each cross-shore position, the scale (of height or velocity) is centered in the dotted line, which represents the zero level, as it is exemplified for the $x = 85.4$ position. The darker lines represent the short waves (high frequencies) and the lighter lines the infragravity waves (low frequencies).

shore, from the range of frequencies that have initially less energy and will gain energy closer to the shore (example in Fig. 3.5).

Observing the short waves propagating towards the shore, it is clear their progressive shape change through skewed and asymmetric, finally capturing each other within the same wave group to propagate higher up the beach as bores, associated with the IG-wave motion. This pattern of convergence of multiple waves that can be seen along the time series, reducing the number of short waves as the depth decreases, has been previously described by Sénéchal *et al.* (2001) and van Dongeren *et al.* (2007). The velocity plots reflect the same evolution, with velocity changing from simple orbital motion to swash events with marked uprush and downwash phases. The presence of wave groups and the clear signature of the IG waves are also evident in the free-surface and the velocity time series, for both irregular and bichromatic waves, progressively more marked as the waves approach the shore.

Fig. 3.5 presents the velocity spectra for conditions A2 and B2, at five distinct cross-shore positions. For a beach as dissipative as the one considered in these experiments (1/80 slope), strong infragravity motion is expected to significantly contribute to the energy spectra along the profile, in particular in the swash zone (de Bakker *et al.*, 2015b). The spectra show that, for the two shoaling positions ($x = 30.1$ m and $x = 50.7$ m), energy is concentrated mostly in the high-frequency range, with a clear peak at the peak frequency of the incident waves, for A2, and at the two main frequencies (f_1 and f_2), for B2. In the low-frequency end of the B2 spectrum, at all cross-shore

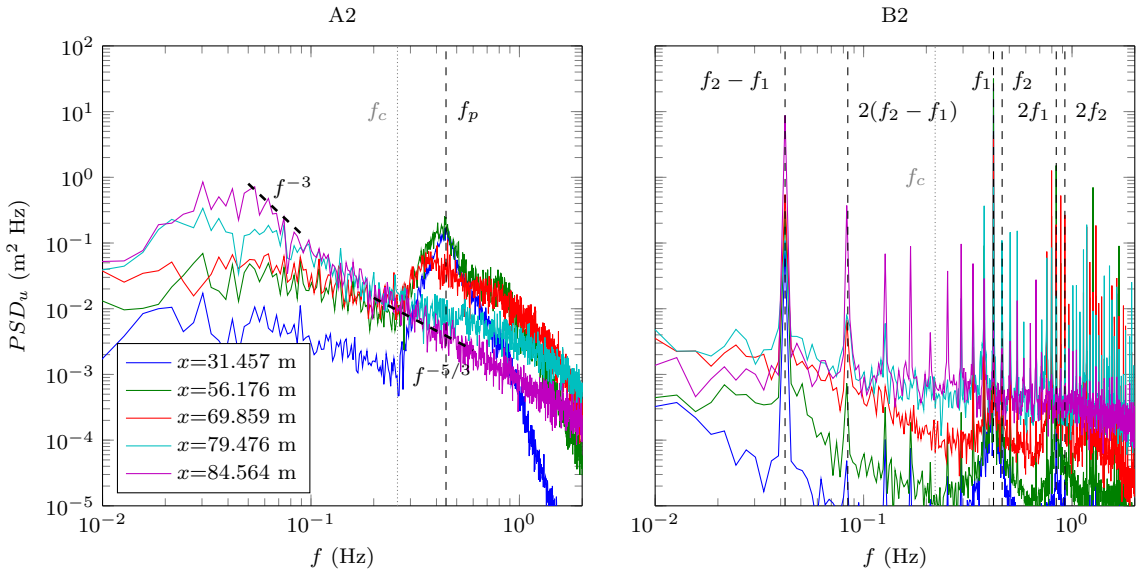

Figure 3.5: Example of the cross-shore velocity spectra obtained for condition A2 (left) and B2 (right) at five different positions along the beach, corresponding to the shoaling (blue), shoaling close to breaking (green), surf zone (red), inner-surf /lower-swash zone (cyan) and upper-swash zone (purple).

positions, there is an energy peak at f_2 -f_1 (0.042 Hz), corresponding to the bound IG wave that is associated to the groups of bichromatic waves.

For A2, the spectrum of the first position after the breakpoint (at x = 68.5 m) shows a strong decay of the incident-frequency component linked to a significant energy transfer to higher frequencies, with a distinct peak around 0.88 Hz (the first harmonic of the peak frequency), following a trend of f^{-3} associated with wave saturation. As waves propagate closer to the shore in the inner-surf/swash zone, the velocity energy levels at frequencies greater than 0.1 decrease approximately as $f^{-5/3}$, which is consistent with an inertial sub-range, and energy is transferred to sub-harmonics, with energy levels peaking at infragravity frequencies. For the position further inshore, the low frequencies in the range of 0.04-0.08 Hz also start decaying following f^{-3}, reflecting the possible saturation and breaking of infragravity waves. For B2, a similar behaviour is observed of energy transfer from the main frequencies to higher frequencies in the shoaling, and to lower frequencies closer to the beach. However, for B2 the energy is preferentially transferred to discrete frequencies, corresponding to multiples of the main frequencies and of their difference (f_2 -f_1) or sum (f_1+f_2), instead of spreading over a wide range of superharmonics and subharmonics.

Overall, both the time series and the spectra depict the importance of IG waves in the GLOBEX gently-sloping beach, particularly in the swash zone. Therefore, understanding infragravity waves implies the analysis and treatment of data collected in the swash zone, an intermittently immersed zone, which is still a challenging issue, especially for flow-velocity measurements.

Analysis of swash velocities

During the experiments, depending on the wave condition, free-surface elevation and cross-shore velocity measurements were performed in three to five cross-shore positions within the swash zone, spanning from the lower to the upper swash: $x = 83.62$ m, $x = 84.29$ m, $x = 84.56$ m, $x = 85.39$ m and $x = 86.51$ m from the wave-maker. The fact that the swash zone is, by definition, a zone which is intermittently covered by water, means that any instrumentation positioned in this zone will be submerged during discrete periods of time. During this periods, the wave gauges will simply register zero values in the time series. Velocity measurements, however, will not be zero and, instead, the parts of the signal corresponding to emersion periods will be noisy and present unrealistic values. It is thus necessary to follow a rigorous procedure in order to define which values are to be considered and which to be excluded from the velocity analysis.

The first step of swash data analysis consisted in synchronizing the cross-shore velocity time series with the free-surface elevation time series measured at the closest wave gauge. The velocity time series were then de-spiked (Mori *et al.*, 2007), as a preliminary way of eliminating spurious data points. Voulgaris & Trowbridge (1998) have shown that accurate ADV measurements can be difficult to obtain within a 1-cm distance of walls. Hence, the purpose of the following method is to evaluate the reliability of measurements performed very close to the bed, in the swash zone.

The first criterion for controlling the output of the ADVs was based on the free-surface elevation relatively to the ADV control-volume height (of 11.8 mm). However, as the wave gauges were not always at the exact cross-shore position of the ADV and also due to the occasional existence of resonant cross-modes in the transverse direction of the flume (van der A *et al.*, 2013), the wave fronts depicted in the free-surface elevation measurements were not always exactly in phase with the sudden onshore-velocity increase associated with the start of the uprush. Therefore, a beam correlation ($Corr$) and a signal-to-noise ratio (SNR) criterion was applied to extend the valid velocity points at the front (backwards in time for each swash event) that would be erroneously excluded if only the water-depth limit was considered. The chosen cut-off values were a minimum $Corr$ of 70% (Puleo *et al.*, 2012) and a minimum SNR of 20 (Aagaard & Hughes, 2006).

The $Corr$ and SNR criterion was not considered appropriate for extending the valid points in the end of the backwashes, as both varied significantly between values above and below the defined cut-off thresholds during this part of the swash events. Even though, the water-depth limit was still allowing part of the backwash velocities to be excluded, thus biasing parameters such as the velocity skewness and asymmetry and the mean discharge. Hence, another criterion was applied to extend the number of valid

measured points at the end of each swash event. The velocity values that had been excluded by the water-depth criterion, but for which the water depth was still greater than 1 mm, were replaced by a mean value obtained from the mean of the last 25 valid points (corresponding to a mean of the last 0.19 s of measurement), and added to the end of each backwash, following the procedure of Raubenheimer *et al.* (2004). Fig. 3.6 shows an example of the application of the method described to a swash time series of A2 wave condition. The mean discharge per run was used to check the validity of the velocity selection method (if the velocity time series is accurate, the mean discharge in the swash zone of an impermeable-bed beach must be the closest possible to zero).

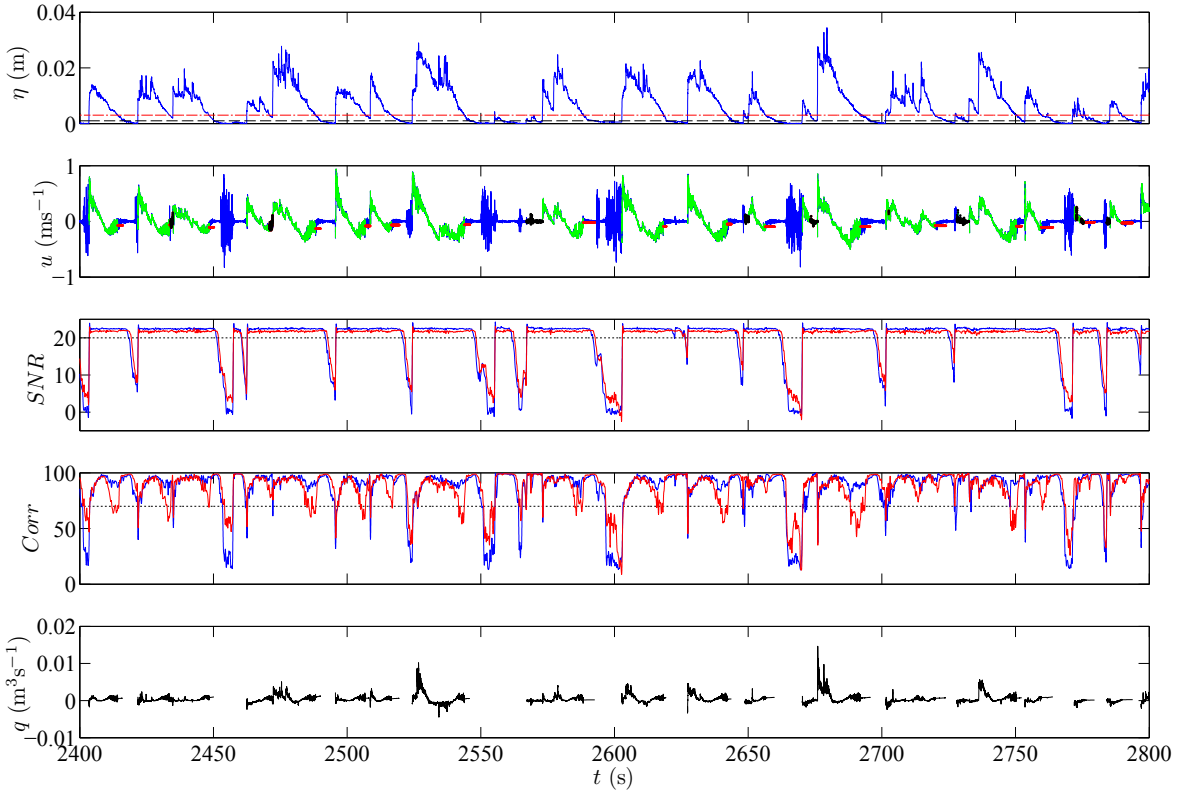

Figure 3.6: Example of the results obtained by the method for selecting swash events at $x = 85.39$ m, for condition A2. In the 1st plot: the red dashed-dotted line represents the water-depth limit, the black dashed line represents the 1 mm limit. 2nd plot: the blue full line is the initial cross-shore velocity time series before the method was applied, the dashed green line are the points considered valid after applying the water depth criterion, the black points are the points added by considering the $Corr$ and SNR criterion, the red points are the points added by the extrapolation of the last 25 values of the backwash. For the 3rd and 4th plots, the blue and red lines correspond to the signal from beams 1 and 2, respectively, and the black lines define the thresholds of $Corr$=70% and SNR=20. The 5th plot represents the instantaneous discharge.

Normalization of wave energy

In order to describe the wave propagation along the beach profile, measures of the wave height, H_{rms}, and of the cross-shore velocity, u_{rms}, can be defined and calculated

$$H_{rms} = \frac{H_s}{\sqrt{2}}, \tag{3.1}$$

where $H_s \approx 4\sqrt{m_0}$, $m_0 = \sqrt{(\sigma_\eta)}$, σ is the standard deviation and

$$u_{rms} = \sigma_u = \sqrt{\langle u^2 \rangle}, \tag{3.2}$$

where $\langle . \rangle$ is the time-averaging operator and u the cross-shore velocity time series. Fig. 3.7 shows an example of the H_{rms} and u_{rms} trends that can be obtained along the beach for A2 and B2, both for the total signal and for IG-frequencies only.

Since the wave height and period are distinct for each wave condition simulated, the waves do not shoal and break at the same cross-shore position for all the irregular and bichromatic wave conditions. Therefore, it is convenient to normalize the data, in order to better compare the results of the different wave conditions. The evolutions of wave height, velocity or nonlinearities along the beach profile have consistent cross-shore structures that depend on the position relatively to the breakpoint, which separates zones of the beach profile with different hydrodynamics. Thus, the breakpoint position is a natural scaling factor for most wave parameters. Wave breaking is also dependent on the energy of each wave condition, and thus scaling the cross-shore position relatively to the breakpoint location is a way of normalizing the wave conditions in terms of energy.

The breakpoint position is considered herein as the mean breaking location around which most waves break. For bichromatic wave conditions, since the waves generated have always the same characteristics, the waves break at a few constant cross-shore

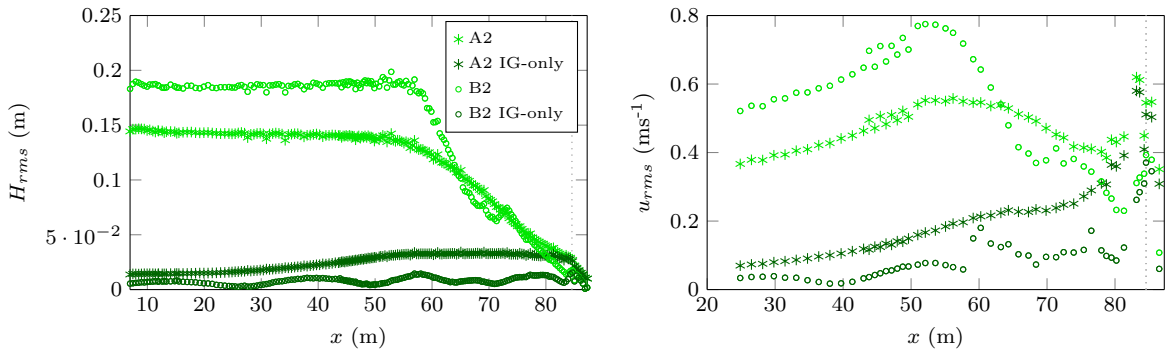

Figure 3.7: Cross-shore evolution of H_{rms} and u_{rms}, for A2 and B2, for the total signal and IG-frequencies only. The dotted grey line represents the position of the still-water shoreline.

positions along the run and the breakpoint position can thus be determined more easily from the maximum wave height measured along the profile (or maximum H_{rms}). However, irregular waves do not always break at the same cross-shore position, depending on the height and period of each individual wave. Larger waves break further offshore than smaller waves and wave breaking occurs over a large region of the domain. This is further enhanced by the very gentle slope of the beach considered. Therefore, the definition of the breakpoint position based on the maximum wave height is less accurate for A conditions and the energy-dissipation rate is used instead, as it is explained below.

First, the energy-dissipation rate is calculated. The energy balance equation can be written as

$$\frac{\partial\left(Ec_g\right)}{\partial x} = -\left\langle\epsilon\right\rangle = -\left[\left\langle\epsilon_b\right\rangle + \left\langle\epsilon_f\right\rangle\right], \tag{3.3}$$

with E the energy density, c_g the group velocity ($= c_p$, the phase velocity, in shallow water), ∂x the cross-shore distance along which the energy dissipates, $\langle\epsilon_b\rangle$ the dissipation by breaking per unit area and $\langle\epsilon_f\rangle$ the frictional dissipation, which is considered negligible when compared with the dominant dissipation by wave breaking. Considering that the waves in the end of shoaling/beginning of breaking are essentially frequency non-dispersive and have a group velocity close to the shallow-water phase velocity, the energy density and group velocity can be calculated following the linear-wave-theory relationships (Thornton & Guza, 1983). Hence, $E = \frac{1}{8}\rho g H_{rms}^2$, and the energy-dissipation rate

$$\left\langle\epsilon\right\rangle = -\frac{1}{8}\rho g^{3/2}\frac{\partial H_{rms}^2 h^{1/2}}{\partial x}. \tag{3.4}$$

Afterwards, the dissipation rate and the maximum wave height ($H_{rms,max}$) were computed for the three bichromatic-waves cases, in order to find a correspondence between both that can be used to define the breakpoint position for the irregular-wave cases. Fig. 3.8 represents the dissipation rates for A and B series. The greatest peak corresponds to the breaking-induced dissipation and, thus, the start of the increase of the dissipation rate towards the maximum value of this peak is linked to the beginning of the breaking process. For B conditions, the cross-shore position of the marked decrease of the H_{rms} trends corresponds to the breakpoint position (x_b). In terms of energy dissipation, this position corresponds (for GLOBEX data set) to two thirds of the distance between the beginning of breaking and the maximum of dissipation. This energy dissipation criterion is then used to define the breakpoint position for A conditions, for which it represents the start of breaking of the greatest waves (which break sooner than the smaller waves).

Having defined the breakpoint position for each wave condition, the cross-shore distance can be normalized by the distance between the shoreline and the breakpoint.

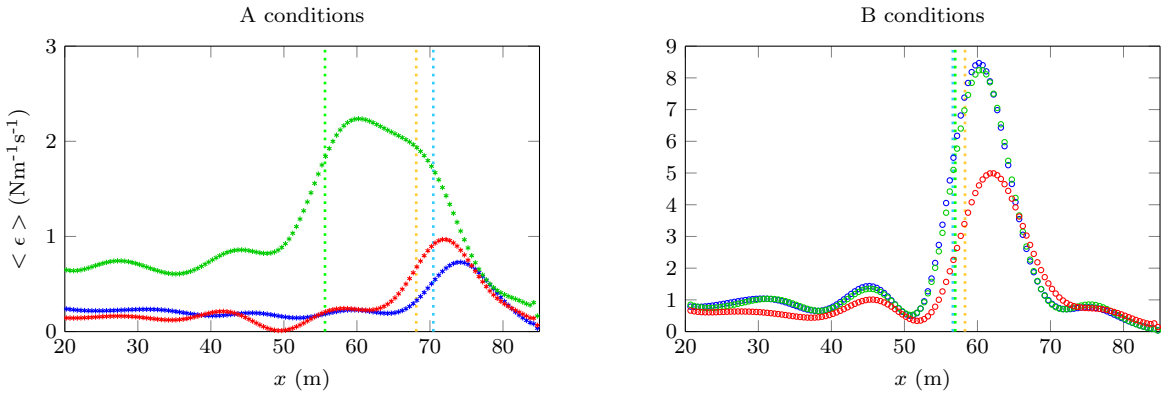

Figure 3.8: Cross-shore evolution of $\langle\epsilon\rangle$ for A and B wave series. Blue, green and red colours represent conditions 1, 2 and 3, respectively. The dotted lines signal the position estimated for the breakpoint of each wave condition. Note: for B conditions, B1 (blue) and B2 (green) breakpoint positions are the same and thus the blue line is not visible.

This can be expressed by the relative depth, h_r which consists of the ratio between the local water depth, measured in still water, at each cross-shore position (h) and the breakpoint depth (h_b). Both water depths are considered at rest. $h_r = 1$ corresponds to the breakpoint position (separating the shoaling and the surf zones), while $h_r = 0$ corresponds to the shoreline position. $h_r = 0.5$ marks the separation between the outer- and the inner-surf zone.

3.2.3 Cross-shore variation of free-surface elevation and velocity

Fig. 3.9 depicts the evolution of H_{rms} and u_{rms} as a function of the relative water depth and highlights the differences between wave conditions. B conditions have greater short-wave height than A conditions, with A2 (the A condition with greater short-wave height) approaching the height of B3 (the B condition with smaller short-wave height). The IG waves have marked wave-height maxima and minima for the B conditions, indicating that part of the energy is reflected at the shoreline. For A conditions, the IG-wave height increases in the shoaling zone until breaking starts and remains approximately constant throughout the surf zone. A2, the wave condition of series A with the greatest H_{rms}, has also the greatest $H_{rms,IG}$. For all conditions, IG-wave height decreases abruptly near the shoreline, mimicking short-wave breaking. Since higher waves induce larger radiation stresses, set-up and set-down are greater for B series, than A series, and for the wave conditions with higher total H_{rms}. IG waves are generally greater for A conditions, with an exception of B3, the B condition with more modulation, which reaches at its maxima a greater height. Larger overall velocity is reached near the breakpoint, but IG-wave velocities are more important near the

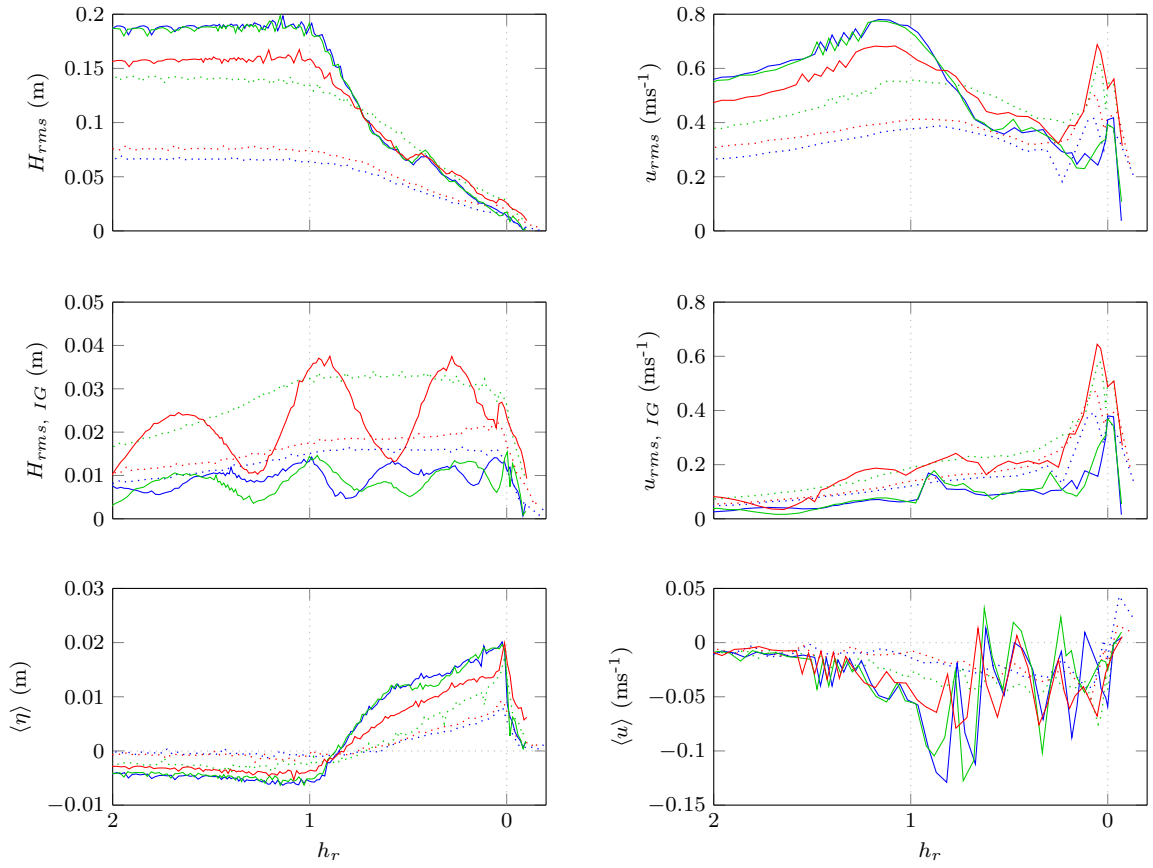

Figure 3.9: Cross-shore evolution of H_{rms} and u_{rms} for the total signal and IG-frequencies only, mean water level and mean velocity. For both A (dotted lines) and B (solid lines) series, the blue, green and red colours represent conditions 1, 2 and 3, respectively. The dotted vertical grey lines mark the location of the breakpoint and the shoreline.

shoreline, in the swash zone. The velocity decrease in the surf zone follows the H_{rms} decrease after breaking, for both A and B conditions. Mean velocity is mostly negative for all conditions, reaching higher values at the end of breaking.

Fig. 3.10 shows the results of normalizing wave height and velocity for all wave conditions, which may reveal some other characteristics of the wave conditions that may be hidden by the disparity in the initial wave height between conditions. For wave height (velocity) and mean water level (mean velocity), the normalization is done by the the H_{rms} (u_{rms}) value measured at twice the breakpoint depth ($h_r = 2$). It highlights the differences in the dissipation of irregular and bichromatic waves. The A conditions show a progressive decrease of H_{rms} that corresponds to the breaking of irregular waves along a wide surf zone. The B conditions present a more marked H_{rms} decrease, with strong energy dissipation, which is linked to the breaking of the waves along a narrow breaking zone. The greater modulation of B3 justifies its slightly gentler decrease of H_{rms}: it has a greater variability of short-wave heights and thus a slightly larger dissipation zone than B1 and B2. These wave conditions have very little modulation and thus their short

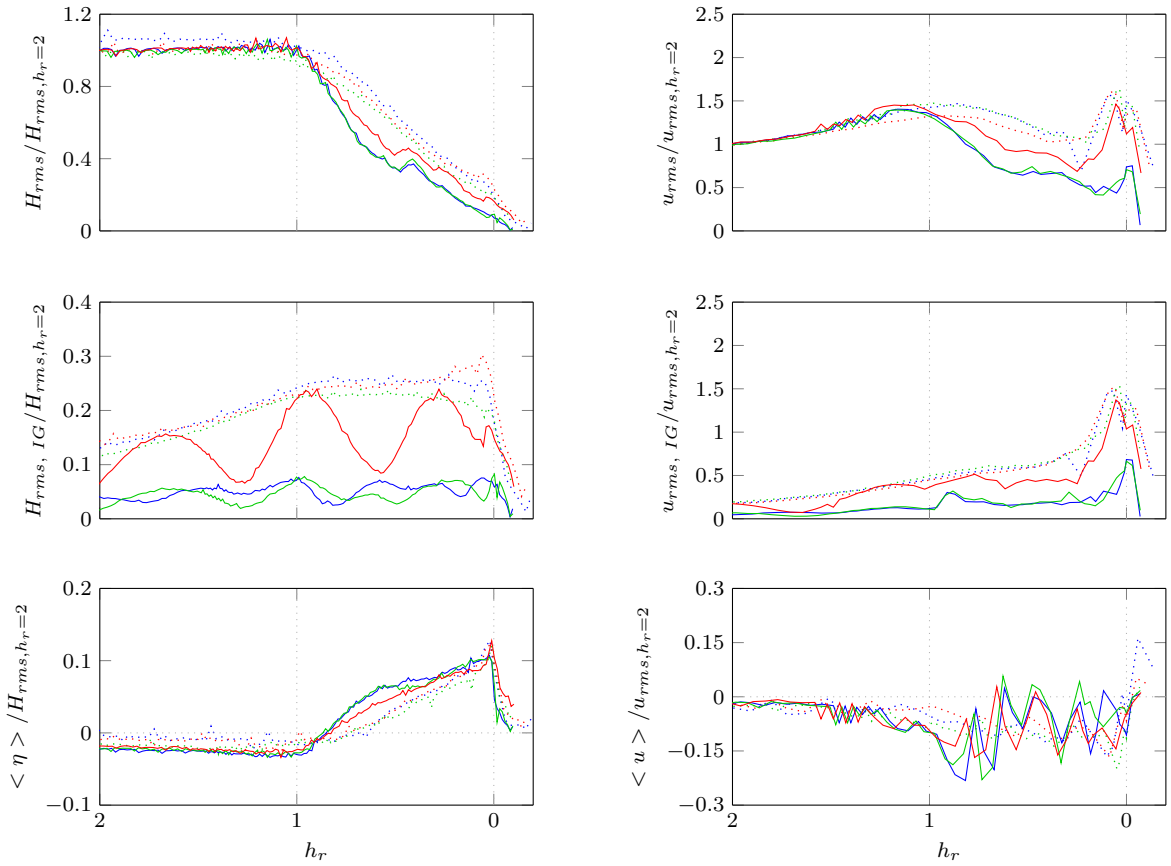

Figure 3.10: Cross-shore evolution of normalized H_{rms} and u_{rms} for the total signal and IG-frequencies only, mean water level and mean velocity. For both A (dotted lines) and B (solid lines) series, the blue, green and red colours represent conditions 1, 2 and 3, respectively. The dotted vertical grey lines mark the locations of the breakpoint and the shoreline.

waves have very similar heights along the groups, which implies that they break almost all at the same cross-shore position. Further onshore, a smaller local maximum of H_{rms} is visible for all B conditions and is associated with the reformation of short waves near $h_r = 0.5$. Near the shoreline, there is again a slight increase of the wave height (further offshore for A than B conditions). It is associated with the great increase of velocity just in the beginning of the swash zone and it represents the change from surf-zone rollers into swash-zone bores, with the water piling up slightly, as several consecutive waves catch each other to form the bores that will break afterwards.

Wave groupiness

In order to better understand how the short-wave groups behave and their link with the IG waves, the variation of the wave groupiness along the beach profile is subsequently analysed. The groupiness factor (GF) can be defined, according to List

(1991), as

$$GF = \frac{\sqrt{2}\sigma_A}{\langle A(t) \rangle}, \tag{3.5}$$

where A is the amplitude of the short-wave envelope, $\langle . \rangle$ represent the time-averaging operator and t the time. GF can be considered as a measure of the variability of short-wave height and has thus, inherently, a link between short and IG waves: greater IG waves induce a greater modulation of the short-wave groups and thus a larger variability of short-wave height and vice-versa. Fig. 3.11 (top) shows the GF calculated for both A and B conditions, which is greater for A conditions: irregular-wave conditions have naturally a larger variability of short-wave heights than bichromatic-wave conditions.

As found by List (1991), it is clear that, in contrast to the near-constant values of GF in deep water, wave breaking rapidly alters the groupiness of the wave-groups. For irregular waves, there is a large decrease in groupiness for depths shallower than

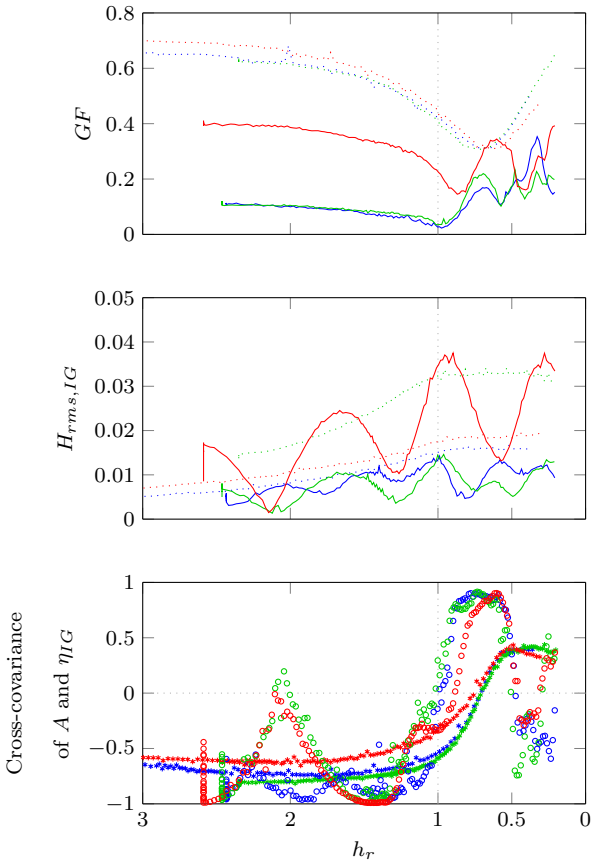

Figure 3.11: Top: Groupiness factor along the beach profile. Cross-shore positions corresponding to $h_r < 0.2$ are excluded from analysis due to the known inaccuracy of the method for very-shallow water depths (List, 1991). Middle: IG-wave height. Bottom: Cross-covariance between the amplitude of the wave envelope and the IG-wave signal. For both A (dotted lines or asterisks) and B (solid lines or circles) series, the blue, green and red colours represent conditions 1, 2 and 3, respectively. The dotted vertical grey lines mark the location of the breakpoint.

twice the breakpoint depth until the approximate limit between the outer and the inner-surf zones ($h_r = 0.5$). Here, all the short waves have finished breaking and have similar heights, thus contributing to a minimum of wave-height variability (and thus of groupiness). GF is higher before breaking, for A conditions, but for B conditions it reaches very similar (B3) and even greater (B1 and B2) values in the surf zone.

A3 has slightly greater groupiness than A1 and A2 until the mid-surf zone. List (1991) found in his data that groupiness seems to be independent of bandwidth. Here, A3 has slightly greater values of GF than the other A conditions, which can either be due to its more narrow-banded spectrum or lower wave steepness. B3 (greater modulation) has, from deep water, a GF more than twice higher than the other B conditions. It also has larger oscillations of the GF values in the surf zone.

List (1991) has suggested a possible model for justifying the existence of significant groupiness within a saturated surf zone, which relates the short-wave interactions with IG-wave induced depth. This concept was also demonstrated earlier on by observations of a positive correlation between local IG oscillations and wave groups in the inner-surf zone (Guza & Thornton, 1985; Abdelrahman & Thornton, 1987). In order to further explore this concept, Fig. 3.11 (bottom) depicts the evolution of the cross-covariance between the amplitude of the short-wave envelope (A) and the IG-wave motion (η_{IG}) along the beach profile.

During most of the shoaling zone, the correlation between the wave envelope and IG-wave motion is near constant and negative, for A conditions, since the bound IG waves are in anti-phase with the short-wave groups. However, for B2 and B3 conditions, the presence of a local IG-wave node (offshore of $h_r = 2$) results in a local de-correlation of IG-wave motion with the wave envelope. When the IG-wave height does not approach zero, the correlation remains high and negative until close to the breakpoint. The change from decreasing to increasing GF values just after the breakpoint, for B conditions, and in the mid-surf zone, for A conditions, is associated to the change of the correlation between A and η_{IG} from negative to positive values (near-zero values). For B conditions, the change to positive values of correlation is done in a shorter distance than for A conditions. As it was observed before, dissipation is greater and happens over a shorter distance for B conditions, which justifies the faster change of correlation. The positive correlation in the surf zone highlights the in-phasing of IG-waves and short-wave groups, previously observed by Guza & Thornton (1985); Abdelrahman & Thornton (1987) and justifies the GF increase in this zone: due to the IG-wave induced depth, the highest short waves can propagate at the crests of the IG waves and the smallest short waves at the troughs, and thus short-wave height variability is promoted. For A conditions, the correlation remains positive and groupiness increases towards the end of the inner-surf

zone. For B conditions, a return to negative values of correlation between the IG-wave motion and the wave groups is observed near $h_r = 0.5$, which is consistent with the wave reformation already mentioned. In the inner-surf zone, correlation between the wave groups and IG waves becomes positive again, as once more short-wave propagation is depth-modulated by the IG waves.

3.2.4 Infragravity waves

Separation of incident and reflected IG waves

The standing IG-wave patterns observed for the bichromatic conditions result from the interference between incident (ingoing) and reflected (outgoing) IG waves. Separating both components helps understanding the contribution of each to the total IG-wave height.

The incident/reflected IG-waves separation methods generally consider the IG waves as free waves. Close to the shore, in very-shallow water, IG waves are essentially free, but in less-shallow water most IG waves are bound. Therefore, it is convenient to first separate bound from free IG waves, and then the incident free from reflected free components.

Ruju *et al.* (2012) described in detail how the free-surface level of the incident bound wave generated by the difference interactions between two short-wave components can be calculated using the formulation of Longuet-Higgins & Stewart (1962). The bound wave component can then be subtracted from the total IG-wave signal, to retrieve the free IG waves. The free IG waves can subsequently be separated into incident and reflected components using different methods.

Guza *et al.* (1984) developed a method for separating the IG-wave components from co-located free-surface elevation and velocity measurements, for which

$$\eta_{IG}{}^{\pm} = \frac{\eta_{IG} \pm \sqrt{\frac{h}{g}} u_{IG}}{2}, \tag{3.6}$$

where η_{IG} is the infragravity free-surface elevation, u is the infragravity cross-shore velocity, h is the water depth and g is the gravitational acceleration. The incident and reflected components of the IG waves are separated based on their propagation direction, which is inferred from the velocity signal, by comparison with the propagation velocity that would be expect considering linear theory. This method assumes that the waves are shore normal and other sources of infragravity energy, such as edge waves, are negligible, which is the case in the experimental flume. Also, it does not account for the nonlinearity of bound waves and the influence of depth changes. van Dongeren

(1997) modified 3.6 to account for the fact that the incoming waves are predominantly forced and thus propagate at the group celerity. ${\eta_{IG}}^{\pm}$ is then defined as

$${\eta_{IG}}^{\pm} = \frac{c(\eta_{IG} + \overline{\eta}) \pm (h + \overline{\eta})u}{c_g + c}, \tag{3.7}$$

with the free IG-wave celerity $c = sqrt(g(h + \overline{\eta_{IG}}))$, $\overline{\eta}$ the steady set-up and c_g the group velocity set equal to the linear group celerity of the primary waves at the peak frequency (Ruju *et al.*, 2012).

The Guza *et al.* (1984) method is the most widely used for separating incident and reflected IG waves: it is simple and gives good results (Sheremet *et al.*, 2002; Ruju *et al.*, 2012; Guedes *et al.*, 2013; de Bakker *et al.*, 2014). However, the need for co-located measurements of free-surface elevation and velocity hinders its application when velocity measurements are not available. This situation is very common, particularly when measurements are made over a mobile bed (with sediments, in experimental wave flumes and or the field) which complicates the obtainment of good and clean velocity data. Since for the GLOBEX experiments high-resolution, in time and space, velocity measurements are available from x=24.87 m until the the shoreline, the Guza *et al.* (1984) method can be used to separate the IG-wave components for the analysis of the IG-wave propagation along most of the profile.

Independently of the method chosen, the first step for separating the different components of the IG waves is to separate the bound waves from the free waves. In theory, the bound-wave solution can only be assumed to work for horizontal beds, since in sloping beds the analytical solution is not known. Nevertheless, if a very-mild slope is considered, it can be assumed that, at the beginning of the slope, the wave shoaling will not be significant, and thus the bound-wave solution can be extended a little further in the cross-shore profile.

Fig. 3.12 shows the separation of B3 IG waves into their different components, following different approaches: (i) the bound wave is subtracted from the total IG-wave signal before separating incident and reflected components (G1) or (ii) the total IG-wave signal is separated into incident and reflected components, considering all IG waves as free waves (G2 and G3).

Even though the initial Guza *et al.* (1984) method (before correction by van Dongeren (1997)) considers all IG waves propagating as free waves, depending on the position along the cross-shore profile, assuming all waves as free may or may not be reasonable. Until close to the breakpoint, bound waves are predominant (left plot in Fig. 3.12). Further onshore, after breaking, IG waves tend to be free, as breaking helps releasing IG waves from the short-wave groups. Moreover, the H_{rms} of the bound waves

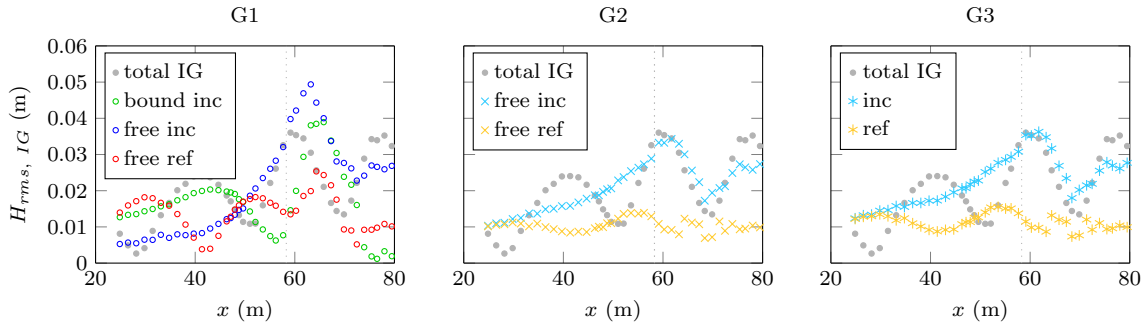

Figure 3.12: Separation of B3 incident and reflected IG-wave components, considering the bound IG-wave component (left plot) and only free waves (middle plot), using the Guza *et al.* (1984) method. The right plot represents the IG-wave separation using the Guza *et al.* (1984) method corrected by van Dongeren (1997). The dotted vertical lines mark the breakpoint position.

cannot be correctly estimated from the bound-wave theoretical solution further onshore than the inner-shoaling zone. The correction of van Dongeren (1997) to the Guza *et al.* (1984) method (G3) accounts for the fact that the group velocity, at which the bound waves propagate, is smaller than the phase velocity, particularly in the shoaling zone (see Fig. 3.13). This correction considers that the incident waves are predominantly forced and thus modifies slightly the calculation of the incident and reflected IG waves, seeking a compromise between G1 and G2 options. G3 is subsequently used to compute IG-wave separation for all the wave conditions, as it is depicted in Fig. 3.14, for A3 and B3. In the surf zone, for B conditions, some scatter is present resulting from the dispersion of the velocity measurements due to the transverse oscillation modes of the flume already mentioned before (van der A *et al.*, 2013).

In the next section, model simulations run for GLOBEX wave conditions are presented. The time series of the free-surface elevation at the first wave gauge was used as input wave condition to compared with the theoretical solution, and thus it was necessary to subtract the reflected IG waves from the total IG-wave signal, since these are not present when the waves are generated by the wave-maker. However, no velocity measurements

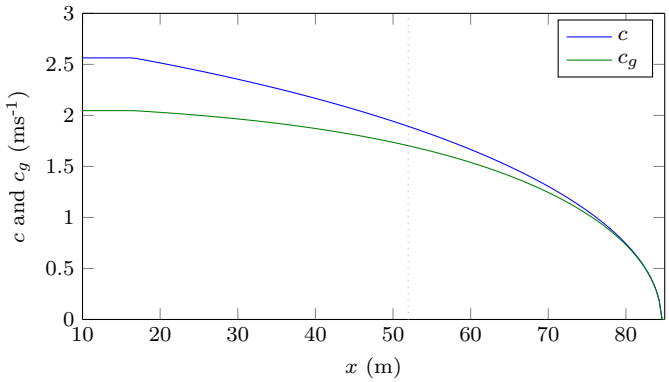

Figure 3.13: Phase (c) and group (c_g) velocities along the beach profile.

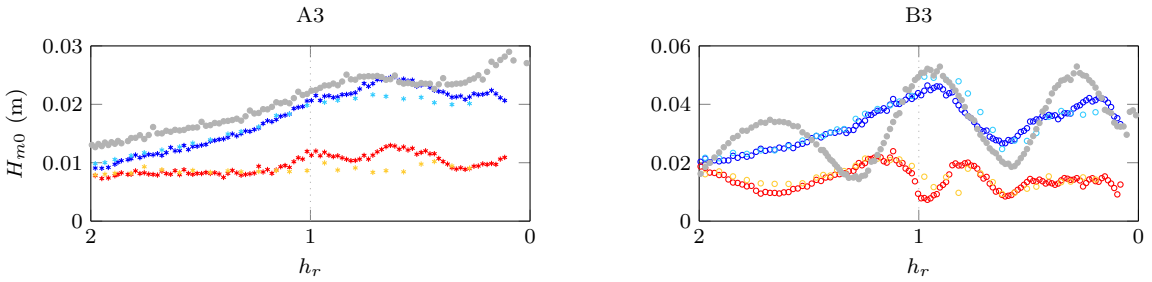

Figure 3.14: IG-wave separation for conditions A3 and B3. In grey, the total IG-wave signal, in blue/cyan and red/orange the incident and reflected components for Battjes *et al.* (2004)/van Dongeren (1997) method.

are available at the first wave gauge ($x = 6.96$ m) and thus Guza *et al.* (1984) method for separating the incident and reflected IG waves cannot be used.

Several authors (*e.g.* Frigaard & Brorsen, 1995; Baldock & Simmonds, 1999; Battjes *et al.*, 2004) have used an array method in which the incident and reflected IG waves at a certain location are estimated using only free-surface elevation measurements at a number of adjacent wave gauges. The amplitude and phase variation of each frequency harmonic between a reference gauge and another gauge is calculated assuming linear propagation and conservation of energy. The phase differences calculated allow the separation of the incident and reflected components. The velocity of propagation is considered as $\sqrt{gh}$ for both incident and reflected (free) IG waves. According to Battjes *et al.* (2004), the low-frequency amplitudes calculated inside the surf zone are not expected to be reliable as: (i) the approximation of the radiation-stress gradient by neglecting the contribution from the amplitude variation compared to that from the phase variation cannot be expected to hold in regions of short-wave breaking (and this also implies that the breakpoint generation mechanism is not modeled); (ii) the energy balance computed for the forced low-amplitude progressive IG waves assumes a steady-state and absence of dissipation, assumption that is *a priori* invalidated by the enhanced low-frequency energy dissipation in the surf and swash zones; and (iii) the use of small-amplitude theory for the translation of short-wave energy into radiation stress may not be accurate in the surf zone. Furthermore, there are conflicting demands on the array length and the number and spacing of the wave gauges considered affect the results. A minimal array length is required to obtain stable estimates and the assumptions of the method introduce larger errors in the separation results for longer arrays. Several authors that have previously used this method do not describe clearly either how many gauges were used (van Dongeren *et al.*, 2007), or why the choice of a defined number of gauges (Dong *et al.*, 2009). Even Battjes *et al.* (2004) do not provide a thorough analysis of the sensibility of the method to wave-gauge number and spacing.

For defining the array length to be used, the results obtained with the methods

of Guza *et al.* (1984), van Dongeren (1997) and Battjes *et al.* (2004) were compared. For A conditions, an array length of about 4.5 m, with four gauges provided the best results. The separation between each two consecutive gauges was taken as 1.5 m, which allows the reduction of noise in the results (stable estimates). For B conditions, as they are repeatable and the low-frequency energy is concentrated essentially at the $f_2 - f_1$ frequency, a smaller array length is sufficient for well resolving the separation of incident and reflected waves and an array of three gauges with a length of 3 m resulted in the best estimation. Since with Battjes *et al.* (2004) method the separation is carried out in the frequency domain, the H_{m0} is computed from the spectra instead of the H_{rms} computed from the time series, and is presented in Fig. 3.14, for one irregular wave condition and one bichromatic. Both methods are expected to present difficulties in the separation of incident and reflected waves in cross-shore positions coincident with nodes (anti-nodes) of the IG waves, as this implies the existence of positions with near-zero free-surface elevation (velocity) values. The similitude of the solutions validates the Battjes *et al.* (2004) formulation for separating IG-wave components offshore of the first velocity measurement available.

Fig. 3.14 illustrates well the differences between A and B conditions in terms of incident and reflected IG-wave components. For A conditions, the incident IG-wave height increases progressively, until the edge of the outer-surf zone, following the total IG-wave signal. This IG-wave height increase is promoted by nonlinear energy transfers from the short waves (de Bakker *et al.*, 2015a). The substantial difference in incident and reflected IG-wave height near the shoreline is indicative of strong IG-energy dissipation in very shallow water (de Bakker *et al.*, 2014). The remaining reflected IG waves decrease as they propagate offshorewards.

For B conditions, there is an abrupt decrease of incident IG-wave height in the outer-surf zone, followed by an increase in the inner-surf zone. The minimum of incident IG-wave height at around $h_r = 0.5$ is coincident with the short-wave reformation observed at this location (see Fig. 3.9). As it was observed for A conditions, B conditions also show a substantial difference between incident and reflected components near the shoreline, but reflected waves do not significantly decrease while propagating offshorewards. Depending on the cross-shore position, the total IG-wave height, for B conditions, has the contribution of both incident and reflected components.

Comparison with the monochromatic IG-wave case

To comprehend how IG-wave motion can correlate and influence short waves, it is important to understand the propagation of the IG waves themselves. In order to do so, the C1 monochromatic IG-wave condition was especially designed to allow the

visualization and analysis of the propagation of free monochromatic IG waves. Fig. 3.15 shows the comparison of the H_{rms} and u_{rms} and also $H_{rms,IGinc}$ and $H_{rms,IGref}$ of the C1 condition with the IG waves of the B2 and B3 conditions (designed to have the same IG wave period as C1). Since the C1 condition does not have a short-wave breakpoint like other conditions, the x axis is not normalized by h_b.

The partially-standing wave patterns observed for the B2 and B3 IG waves are also present for C1 condition. It is notable, however, that whereas C1 wave height progressively increases along the cross-shore profile, reaching a maximum rather close to the shore, B2 and B3 IG waves reach their wave-height maxima sooner in the profile, just after the onset of short-wave breaking.

Separating the incident and reflected IG-wave components helps better understanding the differences between the IG waves associated with the bichromatic waves and the free IG waves of C1. The incident IG waves have a very distinct evolution between the B and the C cases until close to the shoreline. For B conditions, in the shoaling zone, incident IG-wave height markedly increases due to the strong nonlinear coupling with the short waves (and thus, due to the energy transfer to the IG waves) (Sheremet *et al.*, 2002), reaching a maximum height near the shoreward limit of the the outer surf-zone, where the mean radiation stress assumes maximal values (Ruju *et al.*, 2012). As the short waves start breaking, IG-wave energy dissipation starts, which is seen as a decrease of the incident IG-wave height in the outer-surf zone, until the mid-surf zone. As Baldock (2012) proposed, this might be due to the onset of short-wave breaking: as the highest short-waves of the groups break, the short-wave-height variability within the

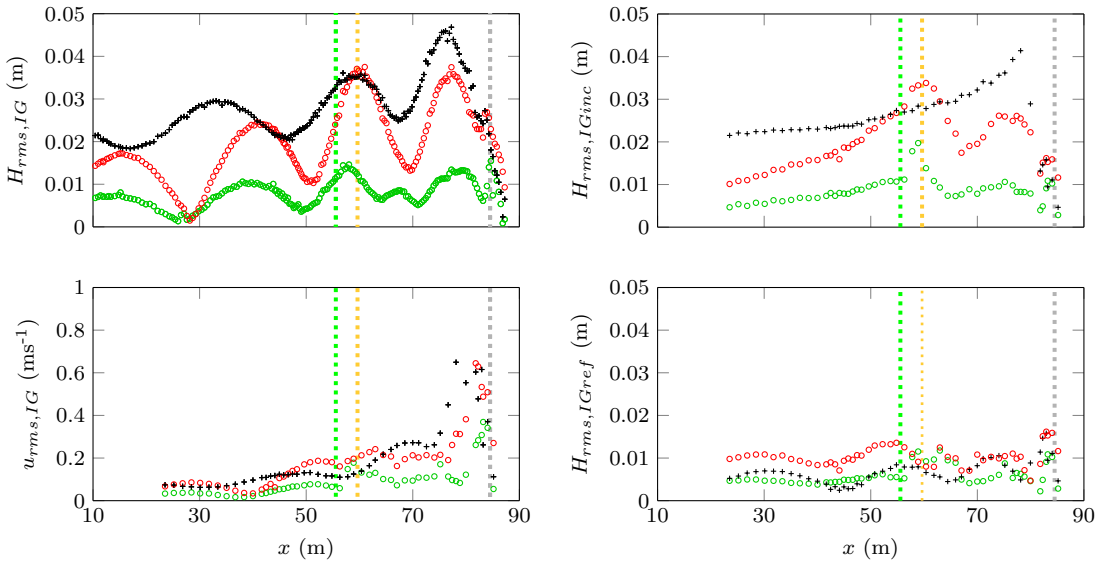

Figure 3.15: $H_{rms,IG}$ and $u_{rms,IG}$ (left), $H_{rms,IGinc}$ and $H_{rms,IGref}$ (right) along the beach profile, for B2 (green circles), B3 (red circles) and C1 (black pluses) wave conditions. Dotted coloured vertical lines mark B2 (green) and B3 (orange) short-wave breakpoints and the dotted grey line, the shoreline.

wave groups is reduced, which implies a smaller difference in momentum flux between the higher and the smaller waves and thus a decrease of the amplitude of the bound IG waves. In the same zone of the beach profile, there is a small reformation of short-waves, which then decrease again towards the shore. In the inner-surf zone, self-self IG-wave interactions develop, dominating the interactions close to the shore (de Bakker *et al.*, 2014). This IG interactions induce higher harmonics that lead to shoaling of the IG waves (which is seen by an increase of the incident IG waves in the inner-surf zone, particularly notorious for B3) and promote a shape transformation of the IG waves to asymmetric (Rocha *et al.*, 2013a). The IG waves thus end up by breaking, which is potentially the dominant mechanism of IG-wave dissipation in this zone of the beach profile (van Dongeren *et al.*, 2007; de Bakker *et al.*, 2014). B3 has greater IG-waves, therefore IG-wave self-self interactions can be expected to be more significant, justifying the larger growth of the incident IG waves in the inner-surf zone comparatively to B2. For both B2 and B3, incident IG waves have a sudden height decrease near the coast (at $x \approx 80$ m), which is accompanied by a significant cross-shore velocity increase. These are trends typically observed for the short-wave height at the end of the shoaling zone, before breaking (Fig. 3.9), which reinforces the idea of IG-wave breaking.

Unlike for B conditions, C1 incident waves grow regularly along the beach, only decreasing near the coast, in the same region where B2 and B3 incident IG waves were shown to break. The wave-height increase for C1 is only linked to the progressive shoaling of the free IG waves. Without a coupling to short-waves, no local increases or decreases of wave height are expected for this wave condition, since no energy transfers from (in the shoaling) or to (in the surf zone) short waves are possible. Nevertheless, C1 incident wave height still decreases abruptly near the shoreline, which is concomitant with a IG-wave velocity increase, like it was observed for B2 and B3 conditions, once again supporting the theory of IG-wave breaking initially proposed by van Dongeren *et al.* (2007).

The reflected IG-wave component of C1 gradually decreases with increasing distance from the shoreline, consistent with both dissipation and refractive trapping (Sheremet *et al.*, 2002). For B conditions, the same behaviour is clear only in deeper waters, beyond the breakpoint. Near the breakpoint there is even a slight increase (especially for B3), which can probably be attributed to the contribution of IG waves generated by the time-varying breakpoint mechanism (Baldock *et al.*, 2000).

3.2.5 Analysis of wave nonlinearities

Evolution of skewness and asymmetry

Analysing the evolution of wave nonlinearities along the beach profile is a way to track the changing of the wave shape during wave propagation. Skewness and asymmetry are essentially a result of the generation of harmonics of the fundamental frequency (or frequencies, for B series), in- or out-of-phase with it, respectively. Therefore, the evolution of skewness and asymmetry values along the beach profile are a proxy of the interactions between frequency pairs.

Skewness and asymmetry of the free-surface elevation can be computed from the wave-gauges measurements as

$$Sk_\eta = \frac{\langle(\eta - \bar{\eta})^3\rangle}{\sigma_\eta^3}, \tag{3.8}$$

where $\langle . \rangle$ is the time-averaging operator and σ_η the free-surface elevation standard deviation. The asymmetry is calculated according to Kennedy *et al.* (2000),

$$As_\eta = \frac{\langle \mathscr{H}(\eta - \bar{\eta})^3\rangle}{\sigma_\eta^3}, \tag{3.9}$$

where $\mathscr{H}$ is the imaginary part of the Hilbert transform. Velocity skewness and asymmetry are analogously calculated (Eqs. 2.4 and 2.5), replacing the free-surface elevation time series by the cross-shore velocity time series.

Fig. 3.16 shows the evolution of Sk and As, for the free-surface elevation and cross-shore velocity, for all irregular and bichromatic wave conditions.

For A conditions, the typical trends of nonlinearity can be observed, with the absolute values of skewness and asymmetry increasing until the middle of the surf zone, where most of the short waves finish breaking and decreasing then towards the inner-surf zone. Near the coast, when the contribution of the IG-waves becomes significant, nonlinearity increases again, responding to the shoaling of the IG waves themselves.

For B conditions, the global Sk and As trends observed for the A conditions are perturbed by multiple local maxima and minima. The cross-shore position of the first local maximum of Sk, corresponds to that of the first breaking of the bichromatic-wave groups and is associated with a return of As values to close to zero, which marks the end of the main breaking region for B conditions. The local maximum of Sk near h_r = 0.5 that is followed by a local maximum of asymmetry is probably linked to the reformation of short-waves observed in Fig. 3.9. The Sk and As increase closest to the shoreline follows the one observed for A conditions and is linked to the IG-wave

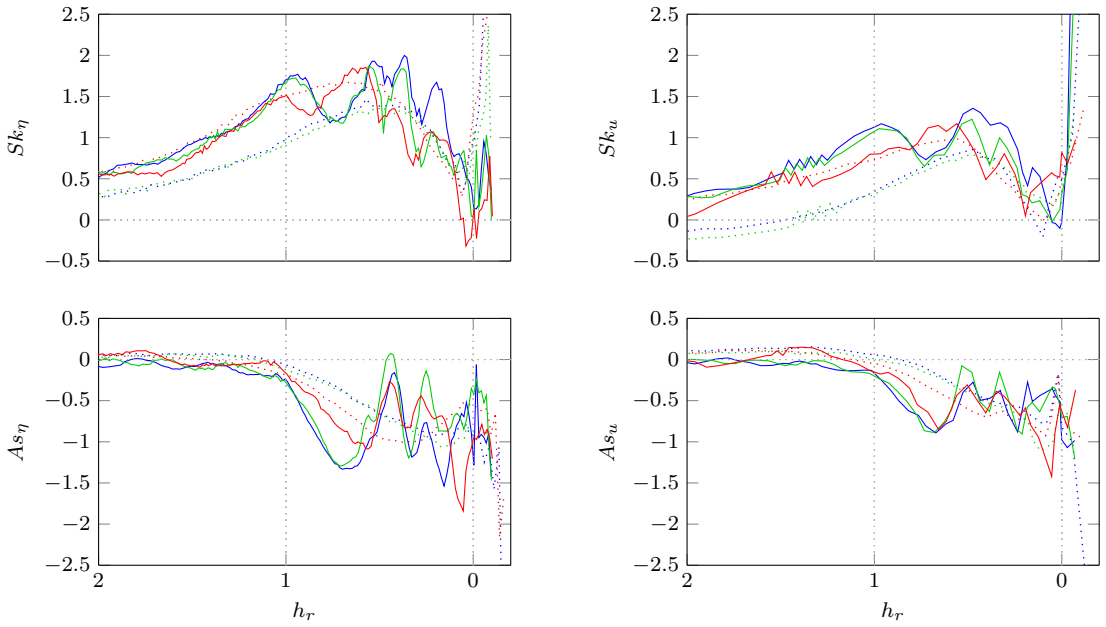

Figure 3.16: Free-surface elevation and velocity skewness and asymmetry for all wave conditions. For both A (dotted lines) and B (solid lines) series, the blue, green and red colours represent conditions 1, 2 and 3, respectively. The dotted vertical grey lines mark the locations of the breakpoint and the shoreline.

shoaling and breaking.

Besides the overall evolution of Sk and As, some aspects can be highlighted:

- B conditions reach, locally, greater Sk and As values than A conditions, although surf-zone minima can be lower for B conditions;
- A3 has greater skewness than the other A conditions, approaching the greater values of the B conditions;
- the multiple Sk and As peaks observed for B conditions have different amplitudes, suggesting different forcing mechanisms;
- the first and third Sk and As peaks of B conditions are related to the first breaking of the short waves and (potentially) to the reformation observed near $h_r = 0.5$, respectively;
- B3 reaches greater absolute As and Sk values than the other B conditions in the inner-surf/lower-swash zones.

For A conditions, the same behaviour and differences between conditions observed for Sk_η and As_η are also present for Sk_u and As_u, although with smaller absolute values. For B conditions the general trends obtained for free-surface elevation are also mimicked by the cross-shore velocity, but the peaks of Sk_η and As_η onshore of the

outer-surf zone are less evident and not always in phase with those of Sk_u and As_u. The larger modulation of B3 promotes a higher correlation between short-wave action and IG wave motion, which affects the evolution of skewness and asymmetry along the beach profile. The conversion from free-surface elevation to velocity skewness and asymmetry is explored in the following subsection.

Retrieving velocity nonlinearities from free-surface elevation nonlinearities

Fig. 3.17 shows the comparison between the Sk and As of free-surface elevation and the Sk and As of velocity for one irregular-wave condition, A1, and one bichromatic-wave condition, B1. Except for some particular peaks for the B conditions in the surf zone, the velocity nonlinearity trends follow the free-surface elevation trends, but with lower absolute values. Particularly for skewness, the difference is of the order of 40%, for A conditions, and 30%, for B conditions. The lower values of Sk_u and As_u result from the attenuation of the high frequencies (and thus of the superharmonics) of the velocity signal throughout the water column, as predicted by the linear wave theory for intermediate depth (Dean & Dalrymple, 1991). The similarity of the trends of free-surface elevation nonlinearities and velocity nonlinearities (Fig. 3.17) suggests that the nonlinearities of the velocity time series may potentially be retrieved (by means of the linear wave theory) from the free-surface elevation time series, in particular for A conditions.

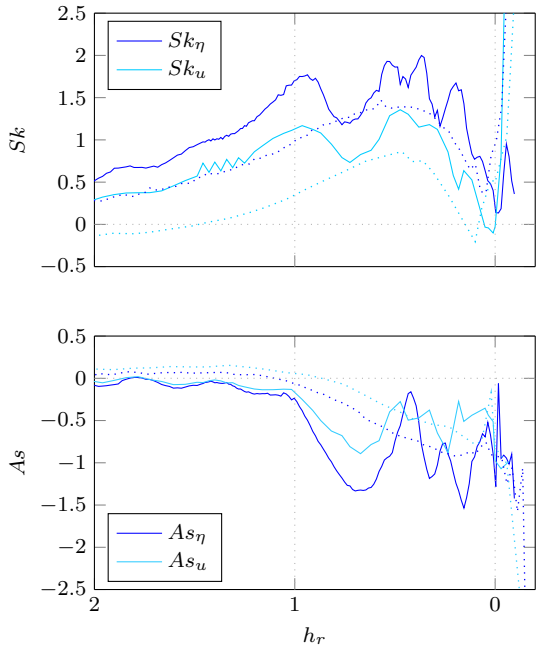

Figure 3.17: Free-surface elevation (blue) and velocity (cyan) skewness (top) and asymmetry (bottom) for A1 (dotted lines) and B1 (solid lines). The dotted vertical grey lines mark the locations of the breakpoint and the shoreline.

Michallet *et al.* (2011) have considered the shallow-water wave theory, corrected to the second-order, to estimate velocity from free-surface elevation measurements. However, they show that, although the trends are well captured, the absolute values of Sk_u and As_u are under- and over-predicted, respectively. The high frequencies, which greatly contribute to Sk_u and As_u, are attenuated with depth. Therefore, an expression aimed at retrieving correctly a velocity time series from free-surface elevation measurements, must include a dependence on the position in the water column at which the velocity is calculated. Hence, instead of considering the shallow-water wave theory, the linear wave theory is considered at intermediate depths, for which a dependence on water depth is included as follows

$$u_\eta = \sum_i u_i = \eta_i \frac{\cosh(k_i z_0)}{\sinh(k_i h)}, \tag{3.10}$$

where the index i represents each of the frequencies that are transferred from the free-surface elevation time series to the velocity time series, k is the wave number ($= 2\pi/\lambda$, with λ the wave length), z_0 is the height above the bottom at which u_η is calculated, and h is the local water depth. k is obtained from the dispersion relation, which can be expressed, for each frequency, as

$$\omega_i^2 = g k_i \tanh(k_i h), \tag{3.11}$$

with g the gravitational acceleration and where $\omega_i = 2\pi f_i$ is the angular frequency and f_i each wave frequency considered. Fig. 3.18 shows the comparison of Sk_u and As_u obtained from the velocity measurements (u_E) and from free-surface elevation measurements (u_η), using Eq. 3.10, for A1, A3, B1 and B3.

For A conditions, the estimated values of Sk_u and As_u are very close to the measured ones until the inner-surf zone, from whereon the linear wave theory fails to predict correctly the velocity from the free-surface elevation measurements. Sk_u is predicted with a very small error of less than 1%, for A1, and less than 5%, for A3, until its maximum value. Beyond that position, u_η overestimates Sk_u. For the As_u of A1 and A3, the trend predicted by u_η is almost totally accurate until near the maximum value. In the case of B1, the Sk_u trend is still fairly well followed until the end of the outer-surf zone, but for B3, u_η does not predict correctly the oscillations of the measured Sk_u in the shoaling zone. This is due to the fact that the presence of reflected IG waves is not accounted for in u_η and for B3 these waves are more important and thus the error in the estimation of Sk_u and As_u is larger.

Overall, u_η can be used to estimate Sk_u and As_u for irregular waves and for bichromatic wave groups with small modulation until the water becomes too shallow (beyond

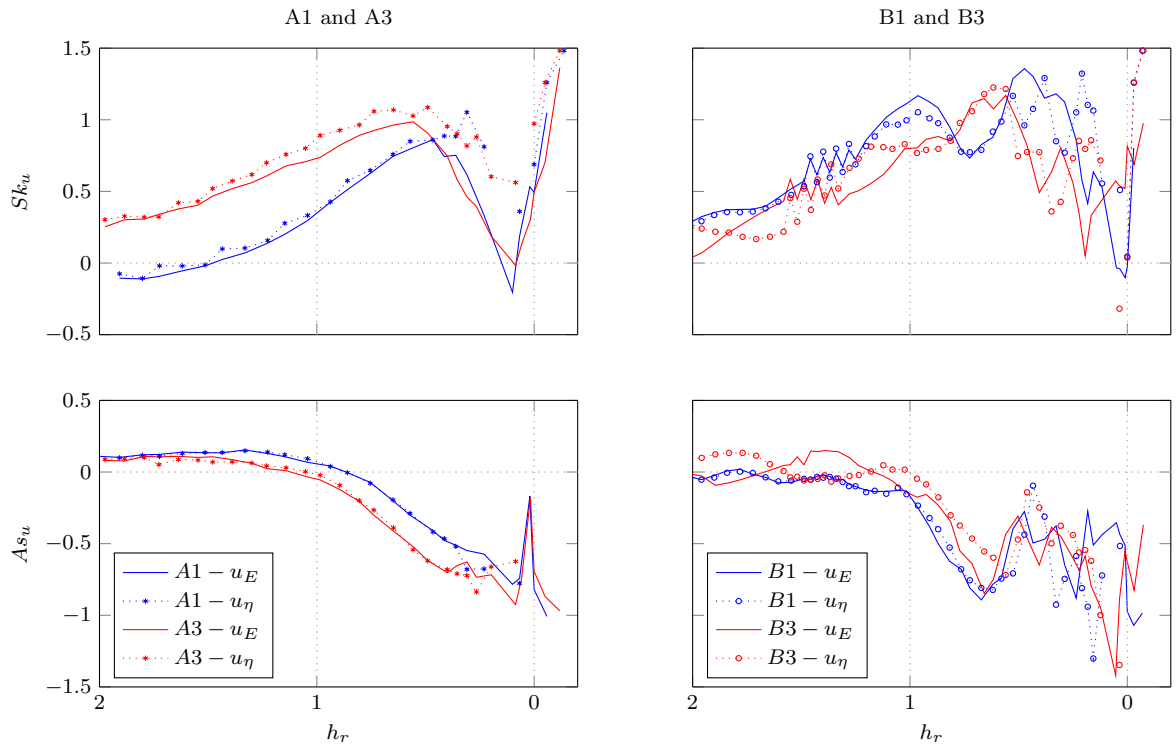

Figure 3.18: Velocity skewness and asymmetry obtained from velocity measurements (u_E, solid lines) and from the free-surface elevation measurements (u_η), using Eq. 3.10 (markers and dotted lines), for A1, A3, B1 and B3 wave conditions. The dotted vertical grey lines mark the location of the breakpoint and the shoreline.

Sk_u and As_u maxima).

Third-order velocity moment

For further exploring the velocity nonlinearities, the third-order velocity moment can be calculated and used to analyse the contribution of different hydrodynamic processes to the total skewness (Mariño-Tapia *et al.*, 2007; Rocha *et al.*, 2013b).

The energetics approach (*e.g.* Bagnold, 1963; Bowen, 1980; Bailard, 1981) is one of the most robust sediment transport formulations for surf-zone conditions. According to this approach, the time-averaged bed-load and suspended-load sediment transports are proportional to four velocity moments: the process-related moments $\langle |u|^2 u \rangle$ and $\langle |u|^3 u \rangle$, and the moments related to the gravity terms $\langle |u|^3 \rangle$ and $\langle |u|^5 \rangle$. The cross shore structure of each velocity moment can thus be used to investigate some of the different processes influencing sediment transport. Guza & Thornton (1985) have shown that the most important terms in the cross-shore transport equation are those included in the third and fourth velocity moments, $\langle |u|^2 u \rangle$ and $\langle |u|^3 u \rangle$, respectively. Russell & Huntley (1999) presented a detailed analysis on the relative contributions of short waves, IG-wave motions and mean flows and interactions between the three to the

total structure of the moments using the normalized third-order velocity moment. This moment was chosen for having a clearer cross-shore structure, being statistically more robust, and its expansion into individual terms being easily coupled with well-known sediment transport mechanisms.

To study the relative importance of short and IG waves on nonlinearity effects, the instantaneous near-bed cross-shore velocities can be split into a mean velocity term ($\overline{u}$) and an oscillatory term ($\widetilde{u}$). The latter can be further separated into high and low frequency components, corresponding to the short ($\widetilde{u}_S$) and infragravity ($\widetilde{u}_{IG}$) orbital motion,

$$u = \overline{u} + \widetilde{u}_S + \widetilde{u}_{IG}. \tag{3.12}$$

The third-order velocity moment can then be computed, resulting its decomposition in ten terms which can be related to different hydrodynamic processes (Table 3.2).

Each term can then be normalized by the velocity variance (wave energy), following

Table 3.2: Terms resulting from the decomposition of the third-order velocity moment.

Sk_0	$\overline{u}^3$	mean velocity
Sk_1	$\langle \widetilde{u}_S^3 \rangle$	skewness of short waves
Sk_2	$3\langle \widetilde{u}_S^2 \widetilde{u}_{IG} \rangle$	correlation of short-wave variance and IG-wave velocity
Sk_3	$3\langle \widetilde{u}_{IG}^2 \widetilde{u}_S \rangle$	correlation of IG-wave variance and short-wave velocity
Sk_4	$\langle \widetilde{u}_{IG}^3 \rangle$	skewness of IG waves
Sk_5	$3\langle \widetilde{u}_S^2 \rangle \overline{u}$	stirring by short waves and transport by mean flow
Sk_6	$3\langle \widetilde{u}_{IG}^2 \rangle \overline{u}$	stirring by IG waves and transport by mean flow
Sk_7	$6\langle \widetilde{u}_S \widetilde{u}_{IG} \rangle \overline{u}$	three-way correlation
Sk_8	$3\langle \widetilde{u}_S \rangle \overline{u}^2$	time-average of short-wave oscillatory component
Sk_9	$3\langle \widetilde{u}_{IG} \rangle \overline{u}^2$	time-average of IG-wave oscillatory component

Wells (1967), Bailard (1981) and Doering & Bowen (1987), enabling the comparison of data collected under different energy conditions (Russell & Huntley, 1999). Fig. 3.19 presents the evolution along the cross-shore beach profile of the six most relevant terms (the mean velocity has already been analysed and Sk_7, Sk_8 and Sk_9 are approximately zero).

A strong dependency of hydrodynamic processes on the distance to breakpoint is evident, with markedly different behaviours offshore and onshore of the breakpoint position. In the shoaling zone, the dominant term is the short-wave skewness (Sk_1), although there is also a contribution from the terms Sk_2 (larger in the outer-shoaling zone) and Sk_5 (larger in the end of the shoaling zone). For A conditions, the greater short-wave skewness of A3 is evident. For B conditions, two Sk_1 local maxima are visible, at the cross-shore positions of the first and third total Sk_η peaks mentioned

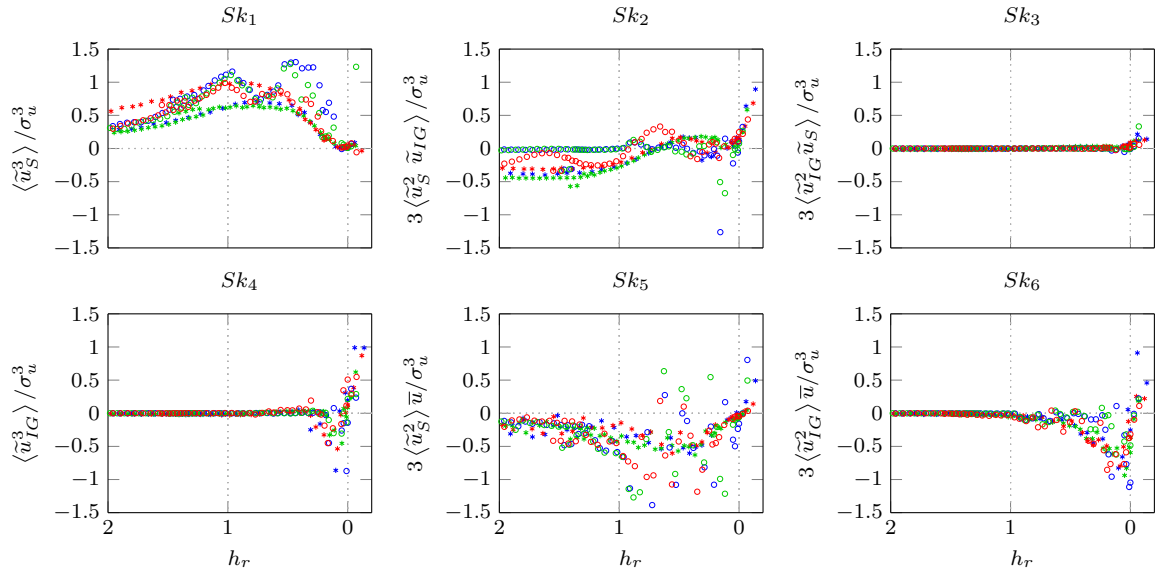

Figure 3.19: The six most relevant terms resulting from the decomposition of the third-order velocity moment, from left to right, bottom to top: skewness of short waves (Sk_1), correlation of short-wave variance and IG-wave velocity (Sk_2), correlation of IG-wave variance and short-wave velocity (Sk_3), skewness of IG waves (Sk_4), stirring by short waves and transport by mean flow (Sk_5) and stirring by IG waves and transport by mean flow (Sk_6). Asterisks represent the A conditions and circles the B conditions. Blue, green and red colours represent conditions 1, 2 and 3, respectively. The dotted vertical lines mark the breakpoint and shoreline positions.

before (and shown in Fig. 3.16) and attributed to the existence of the first breaking and of a short-wave reformation zone in the mid-surf zone. In the case of B3 condition, the second Sk_1 peak is much smaller than for the other two B conditions. For B3, with greater modulation (and thus greater IG waves), the relative contribution of the short-wave skewness to the total skewness is smaller than for the other two conditions. This highlights the fact that, depending on the modulation, the contributions of high and low frequencies to the nonlinearities, at any given cross-shore position, can be different. Still in the shoaling zone, the correlation between short-wave variance and IG-wave velocity (Sk_2) is negative: under non-breaking wave conditions the largest short waves appear under the bound IG-wave trough (see Figs. 3.3 and 3.4). For B3, this correlation is also negative but oscillates responding to the IG-waves maxima and minima.

After the breakpoint and until the end of the surf zone, short-wave skewness (Sk_1) continues to be positive but diminishes, reaching zero values near the shoreline. The term corresponding to the stirring by short waves and transport by mean flow (Sk_5) contributes to negative skewness, with the most negative value at about half the breakpoint depth. This is a result of the negative mean cross-shore velocity in the surf-zone, associated with the undertow (see Fig. 3.9). The correlation of short-wave variance and IG-wave velocity (Sk_2) gradually becomes zero towards the end of the

outer-surf zone and then becomes slightly positive for A conditions in the inner-surf zone, where the short-wave propagation is controlled by the water depth at each moment. For B conditions, the correlation between short-wave variance and IG-wave velocity varies depending on the wave condition and responding to the cross-shore IG-wave height patterns. In the case of B3, the positive correlation maximum observed in the surf zone is located at the cross-shore position of the second total Sk peak depicted in Fig. 3.16.

From the inner-surf to the upper-swash zone, the IG waves start to clearly dominate the hydrodynamics. IG-wave stirring and transport by mean flow becomes increasingly more negative until close to the shoreline (Sk_6). At the transition from surf to swash (around $h_r = 0$), with the formation of IG-wave bores that propagate towards the upper-swash zone, the skewness of IG waves becomes positive (Sk_4) and a weak onshore-directed mean-flow effect is also present (Sk_6). As short waves propagate associated with the IG-wave bores, the correlation of short-wave variance and IG-wave velocity (Sk_2) reaches greater and positive values. A small contribution from IG-wave variance correlation with short-wave velocity also plays a role in the swash zone (Sk_3).

Summing up, in the shoaling zone, Sk_1, Sk_2 and Sk_5 (the terms strongly dependent on short waves) dominate, which is in accordance with the findings of Russell & Huntley (1999) and Mariño-Tapia *et al.* (2007), who also observed the terms Sk_1 and Sk_2 to be positive and negative, respectively, offshore of the breakpoint. However, the positive values perceived by these authors for the term Sk_5 in the shoaling zone, are not found herein, where a negative mean velocity has a stronger signature, leading to negative values. This leads to a distinct behaviour of the overall velocity skewness when compared with the shape function of Mariño-Tapia *et al.* (2007). In the surf zone, the results obtained are also in agreement with previous findings, with a predominance of negative skewness. This is only strictly true when Sk_1 becomes much smaller than Sk_5 and Sk_6, which happens for depths shallower than half the breakpoint depth, for A conditions, and still further onshore, for B conditions. Sk_5 is dominant in the outer-surf zone and Sk_6 in the inner-surf zone. The swash zone is dominated by terms Sk_2, Sk_4 and Sk_6, linked to the IG-wave motion.

Fig. 3.19 further highlights the difference between short-wave skewness for condition A3 and the other A conditions, as well as the significant discrepancy of the correlation between short-wave variance and IG-wave motion, for condition B3, relatively to the other B conditions. Moreover, it underpins the existing link between short waves and IG waves. As Janssen *et al.* (2003) have shown, in the shoaling zone, the correlation between IG and short waves is negative, as the IG waves are in anti-phase with the wave groups. After the breakpoint, this correlation increases to positive values, which are greater in the swash zone, where the water-depth modulation of short-wave propagation

implies a positive correlation between IG-wave crests and the highest short waves of the groups (as shown before in Fig. 3.11).

3.2.6 Summary

Few measurements are currently available from experiments performed on beaches as gentle-sloping as the GLOBEX beach. In this section, a detailed analysis of the wave (and velocity) nonlinearities was carried out, as well as some reflexions on the behaviour of the infragravity waves and their interaction with the short waves. The very-gentle slope makes it possible for wave nonlinearities and infragravity waves to fully develop as the short-wave propagate towards the shore. The comparison between irregular and bichromatic waves has also highlighted some particularities of the bichromatic waves, which merit to be more thoroughly looked at in the future. The main remarks of this section are subsequently presented.

Irregular waves have a broader surf zone than bichromatic waves, for which breaking is stronger and happens over a narrower surf zone. Therefore, bichromatic waves reach a greater maximum energy-dissipation rate than irregular waves. The latter have smaller undertow velocities, but greater u_{rms} and $u_{rms,IG}$.

The wave evolution is influenced by the relation between short-wave groups and IG waves (which can also be seen in terms of wave groupiness). In the shoaling zone, the tendency is for IG waves to be in anti-phase with the short-wave groups. In the inner-surf/swash zones IG-waves are in phase with the short-wave groups, influencing short-wave propagation by depth-modulation of the water level. For A conditions the trends are linear, for B conditions the picture is more complex, due to the existence of significant IG-wave reflection at the shore and of a short-wave reformation zone in the mid-surf zone.

IG waves propagating together with short-wave groups (B conditions) evolve towards the shore differently from free IG waves (C1). This is due to the interactions with the short-wave groups, which are absent for C1 case. It seems likely, for both B and C1 cases, that part of the IG waves shoal and break near the shore.

Few data sets have such a high resolution of velocity measurements as the GLOBEX data set. Frequently, the description along the beach profile of the velocity nonlinearities, which are directly related to sediment transport, is hindered by a lack of velocity measurements. Hence, making use of the high-resolution data set presented, a method to calculate velocity nonlinearities from free-surface elevation measurements was proposed and validated. This method is based in the linear wave theory at intermediate depths and takes into account the attenuation of the high frequencies of the wave throughout the water column.

The evolution of the wave nonlinearities varies depending on the wave condition considered. Irregular waves and bichromatic waves have distinct behaviours along the cross-shore profile. For irregular waves, higher total wave height results in greater cross-shore velocities and IG waves. The largest values of skewness and asymmetry were observed for A3, which has both a more narrow-banded spectrum and a smaller wave steepness than the other A conditions. Modulation of the short-wave nonlinearities by the IG waves is particularly evident for B conditions and more marked for B3, the wave condition with the greatest IG waves. Depending on the cross-shore position relative to the breakpoint, different mechanisms contribute to the wave nonlinearity. Short-wave motion is more important in the shoaling zone, while the mean flow only becomes relevant in the surf zone. The very-gentle slope of the beach promotes the existence of a large surf zone for irregular waves, which can be divided into the outer- and the inner-surf zones, with the maxima of skewness being reached between the two. Asymmetry reaches its highest values closer to the shore. The contribution of the interaction between short-waves and IG-wave motion to the nonlinearity varies along the beach profile. The IG waves dominate the nonlinearities of the inner-surf and swash zones for all wave conditions.

The next two sections of this chapter are dedicated to exploring further the factors influencing the evolution of the nonlinearity of the waves.

3.3 Numerical modelling - SERR1D model

Field data can help identifying the drawbacks of different parameterizations. If the number of instrument is high enough, these data can even be used to follow wave propagation and transformation towards the coast. However, the scarce number of instruments available in most field campaigns often hinders the complete description of the wave evolution, particularly offshore of the surf zone. Furthermore, wave conditions and the beach profile cannot be controlled and data is not always exploitable for a specific purpose. To overcome these difficulties inherent to field work, laboratory experiments can be made, where scaled physical models allow a greater control over the variables aimed to be studied, while representing the most important hydrodynamic and morphodynamic processes as close as possible to nature. Wave conditions can be carefully controlled and the beach can be designed as wished. Notwithstanding, it is a long and expensive process to get accurate and pertinent measurements, and a limited amount of wave conditions can be run, frequently over one single beach profile (the slope remains constant).

Therefore, even though numerical models often present not only numerical limitations

but also limitations related to the state-of-the-art of the knowledge of the processes to be modelled, they are useful tools, as they allow the experimenting of many wave conditions and beach types in less time (and less money!) than physical models or field experiments.

3.3.1 Model description

SERR1D is a fully-nonlinear 4$^{\text{th}}$-order finite-volume Boussinesq-type model (Cienfuegos *et al.*, 2006, 2007). This model is based on the Serre equations, which describe the 2D irrotational and shallow-water flow of an incompressible and inviscid fluid over uneven bottom bathymetries. This set of equations defines the total water depth and the depth-averaged horizontal velocity. The depth-averaged mass and momentum conservation equations can be written in their generic form, according to

$$\frac{\partial h}{\partial t} + \frac{\partial}{\partial x}(hu) - D_h = 0, \tag{3.13}$$

and

$$\frac{\partial u}{\partial t} + \frac{1}{2}\frac{\partial u^2}{\partial x} + g\frac{\partial h}{\partial x} + \Gamma_d - \frac{1}{h}D_{hu} + \frac{\tau_b}{\rho h} = 0, \tag{3.14}$$

where h is the water depth, u is the depth-averaged horizontal velocity, D_h and D_{hu} represent the extra terms that take into account the wave-breaking process, Γ_d groups all the high-order dispersive (non-hydrostatic) terms, g is the gravitational acceleration, ρ the water density and

$$\tau_b = \frac{\rho}{2} C_f u \left|u\right|, \tag{3.15}$$

with C_f the bed-friction coefficient (similarly to that used by Grant & Madsen (1979)); x is the space coordinate, in the cross-shore direction and t is the time coordinate.

For Boussinesq models to represent well the surf zone, breaking criteria must be adopted to turn on/off breaking dissipation. The breaking initiation/cessation criterion is based on threshold values of the breaker front slope, ϕ (Schaffer, 1993). In SERR1D model, the breaking terms are included in both the mass and momentum conservation equations. The breaking term in the mass-conservation equation takes into account the mass deficit induced by depth-integration up to the wave trough, as an attempt to include wave-roller effects. The overall dissipation of organized wave energy is derived using nonlinear shallow-water shock theory, which is corrected to account for dissipation taking place only over a finite cross-wave extent. The breaking-induced terms are thus described as

$$D_h = \frac{\partial}{\partial x}\left[\nu_h \frac{\partial h}{\partial x}\right] \tag{3.16}$$

and

$$D_{hu} = \frac{\partial}{\partial x}\left[\nu_{hu}\frac{\partial hu}{\partial x}\right], \tag{3.17}$$

where ν_h and ν_{hu} are the mass and momentum diffusivity coefficients, written as

$$\nu_h = -K_h \exp\left(\frac{X}{l_r} - 1\right)\left[\left(\frac{X}{l_r} - 1\right) + \left(\frac{X}{l_r} - 1\right)^2\right], \quad \text{for } 0 \leq X \leq l_r \tag{3.18}$$

and

$$\nu_{hu} = -K_{hu} \exp\left(\frac{X}{l_r} - 1\right)\left[\left(\frac{X}{l_r} - 1\right) + \left(\frac{X}{l_r} - 1\right)^2\right], \quad \text{for } 0 \leq X \leq l_r, \tag{3.19}$$

with X a local coordinate system moving with the wave ($X = 0$ is located at the crest and positive shorewards) and l_r the roller length, which is related to local wave properties using Cointe & Tulin (1994) theory of steady breakers calibrated on hydraulic jumps in similarity with surf-zone waves. K_h and K_{hu} are slowly-varying scaling coefficients described as

$$K_h = \delta\frac{cd}{\tan(\phi)} \tag{3.20}$$

and

$$K_{hu} = \kappa\delta\frac{cd}{\tan(\phi)}, \tag{3.21}$$

where c is the wave celerity, d is the mean water depth for a given wave, ϕ is the breaker angle, $\kappa = K_h/K_{hu}$ ($0 \leq \kappa \leq 1.0$) is assumed constant and δ is calculated as

$$\delta = \frac{\alpha_b}{(1+\kappa)}, \tag{3.22}$$

with α_b, which assumes values of the order of $O(1) - O(10)$ in the surf zone, obtained with

$$\alpha_b = \frac{\gamma^3}{4I_{hu}}, \tag{3.23}$$

where I_{hu} is assumed equal to I_h and both are integrals that weakly depend on the breaker index, $\gamma = H/d$ (when referring to the model breaking parameters, γ is the breaker index, in order to follow the definition of the authors of the model; elsewhere in this manuscript, the γ symbol represents the spectral bandwidth parameter). ϕ and γ constitute the two main physical parameters to be set.

The model has been previously validated with laboratory data for short-wave and IG-wave propagation, energy transfers between both frequency bands and short-wave breaking (Cienfuegos *et al.*, 2006, 2007, 2011). In particular, the wave-breaking model was calibrated by Cienfuegos *et al.* (2010) with the case of Ting & Kirby (1994) spilling-

breakers experiments.

Herein, a good compromise between the numerical performance of the scheme and predicted properties of surf-zone waves is achieved by setting: (i) the relative breaking-wave height to 0.8 at the beginning of breaking (γ_b) and 0.7 at the end (γ_f), (ii) the breaker angles (ϕ_b, for breaking initiation and ϕ_f, for breaking cessation) to 26° and 6°, (iii) $\kappa = 0.1$, (iv) $\alpha_b = 5.0$, (v) the empirical parameter for the roller length, to 0.796, (vi) the coefficient for the transitional time scale $T_b = 5.0$, (vii) the friction coefficient $C_f = 0.001$ (calculated with the Grant & Madsen (1979) parameterization) and (viii) the grid resolution parameter $\rho = dx/h_0 = 0.05$ (where dx is the spatial grid spacing, and h_0 the water depth at the wave-maker). The values used for the parameters are within the range proposed by Cienfuegos *et al.* (2010). Since the friction coefficient depends on the bed roughness, this parameter can be changed for data sets obtained on different beaches, as long as it is kept within a reasonable range.

3.3.2 Sensitivity analysis

The sets of parameters chosen for A and B conditions, respectively, were used in all model runs of this section and were chosen as a compromise that works fairly well for both narrow- and broad-banded irregular-wave cases (A1 and A3) and more modulated and less modulated bichromatic wave cases (B1 and B3). Since herein the main focus in on the evolution of wave nonlinearity along the beach profile (accounting for both short- and infragravity-wave propagation), H_{rms} and Sk_η are considered as control variables and calibration was done with a special emphasis on getting the best values simultaneously for both.

The B parameter can be calculated according to Ruessink *et al.* (2012), as

$$B = \sqrt{{Sk_u}^2 + {As_u}^2}. \tag{3.24}$$

Since it combines both velocity skewness (Sk_u) and asymmetry (As_u), this parameter constitutes a measure of the total (non-dimensional) nonlinearity and is thus analysed as well. The emphasis of this analysis is on its maximum value, B_{max}, which represents the maximum value of nonlinearity reached by each condition along the beach profile.

Time-series length

In the case of irregular waves, the time series that are input to the model as boundary conditions need to be long enough to allow the statistical convergence of the results. At the same time, longer input time series imply a longer computation time. Therefore, a compromise must be reached between computation time and statistical convergence. In

order to do so, simulations with different time lengths were run and the sensitivity of H_{rms} of both total and infragravity waves and Sk_η to the length of the run was analysed. Fig. 3.20 shows both variables zoomed at the profile zones where their values are more affected by the run length. The greatest difference observed between the results of the runs with different time lengths is of the order of 6%, for the H_{rms} of the IG waves, and is reduced to less than 1% for the runs with a time length of at least 1500 s. Therefore, we will consider that any run that has a length of more than 1500 s can be used for computing wave statistics for A conditions accurately. Since for B conditions the waves are bichromatic, shorter time series are needed to get statistical convergence: shorter runs, of 500 s, still provide accurate results.

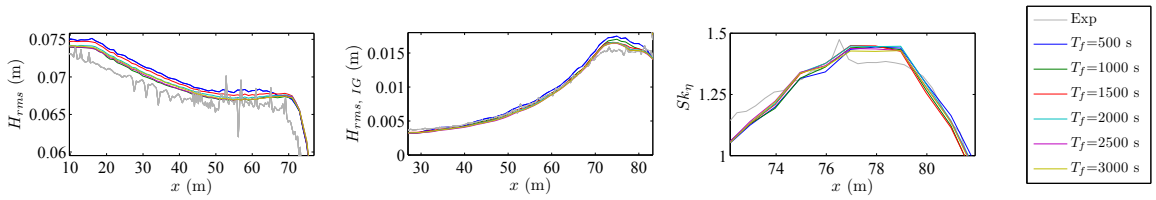

Figure 3.20: Sensitivity of the wave statistics to the length of the runs (A1 example). Spatial distribution off H_{rms}, $H_{rms,IG}$ and Sk_η in the zones of the cross-shore profile where these variables show a greater variation depending on the run length.

Boundary conditions

Two different types of input time series were tested: one obtained experimentally and the other obtained theoretically. From the total free-surface elevation time series measured at the first wave gauge ($x = 6.96$ m), the reflected IG waves were extracted (using the Battjes *et al.* (2004) separation method already described, since no velocity measurements were available at this position), and the input signal arriving from the wave-maker was retrieved. This time series constituted the experimentally-obtained input wave time series (A1E, for condition A1). The theoretical time series were computed using the second-order wave-maker theory for irregular waves (Schäffer, 1996), considering for A conditions both 1000 and 2000 different frequencies (*e.g.*, A1T and A1T2, for condition A1). For B conditions, only the main two frequencies (f_1 and f_2) were considered for computing the bound wave and the higher harmonics (B1T, for condition B1). Figs. 3.21 and 3.22 show the input time series and spectra of A1, A3, B1, B3 wave conditions.

The evolution of different wave statistics along the beach profile, spectra and time series calculate at different cross-shore positions are analysed for both types of input time series. For A conditions, the two theoretical input time series, T (computed with 1000 frequencies) and T2 (computed with 2000 frequencies), are considered in the analysis.

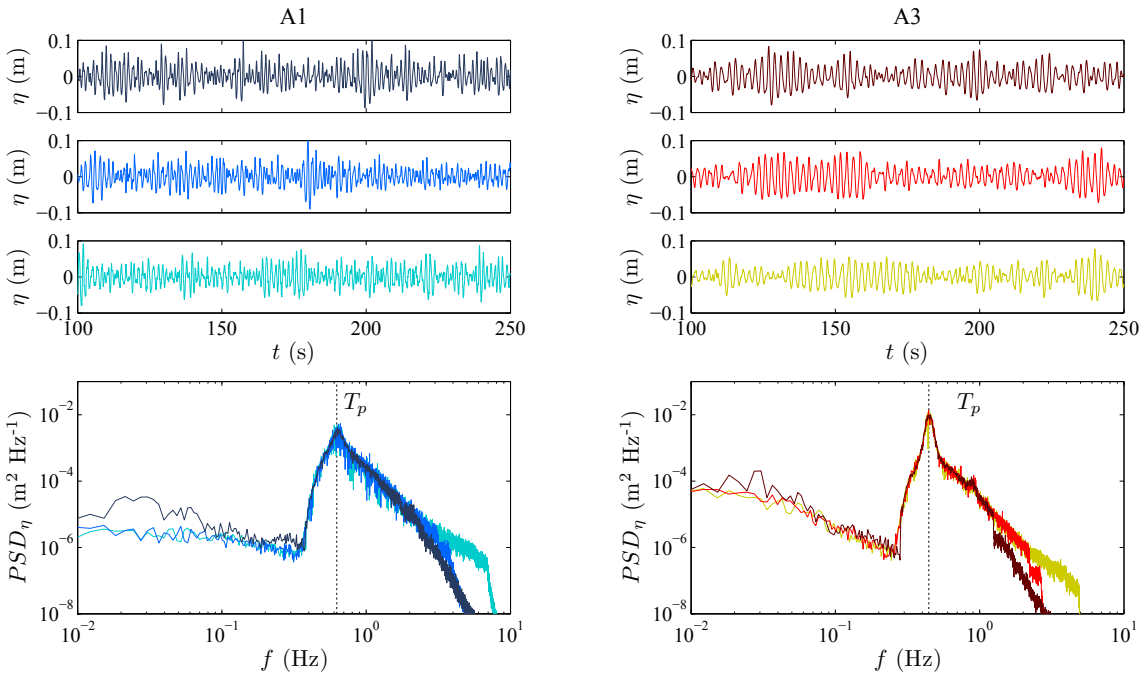

Figure 3.21: A1 and A3 input wave conditions. Dark blue and dark red- A1E and A3E; blue and red - A1T and A3T; cyan and yellow - A1T2 and A3T2.

Figs. 3.23, 3.24, 3.25 show the results obtained for A1 wave condition and in Appendix A equivalent figures are shown for A3 (different spectral width) and the bichromatic wave conditions B1 (smaller modulation) and B3 (greater modulation). SERR1D model was mostly calibrated for GLOBEX data based on A1 and A3 experimental results and

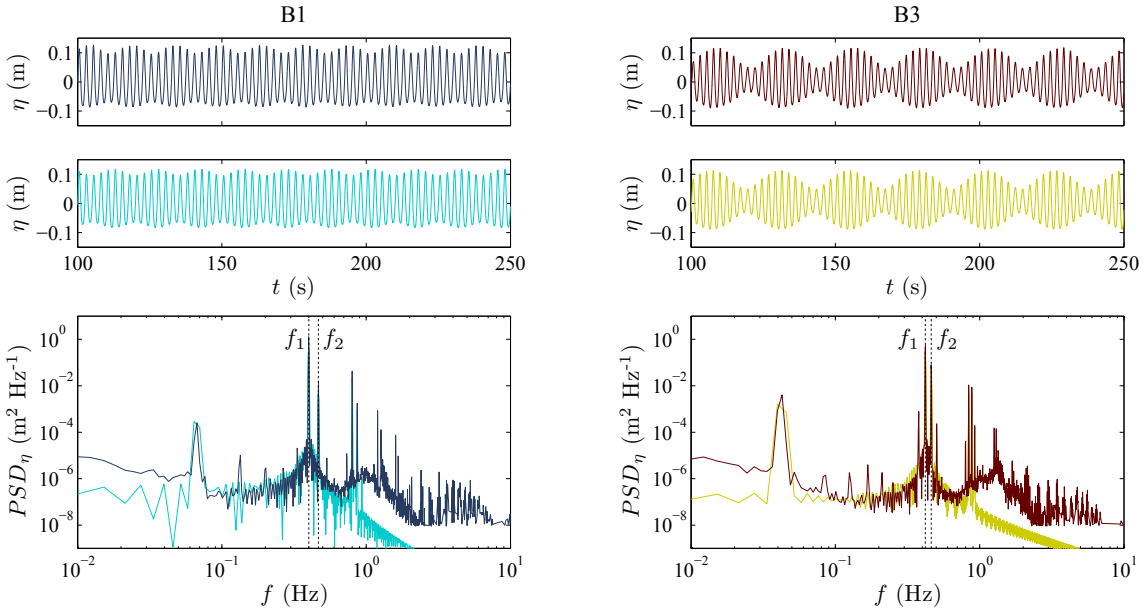

Figure 3.22: B1 and B3 input wave conditions. Dark blue and dark red- B1E and B3E; cyan and yellow - B1T and B3T.

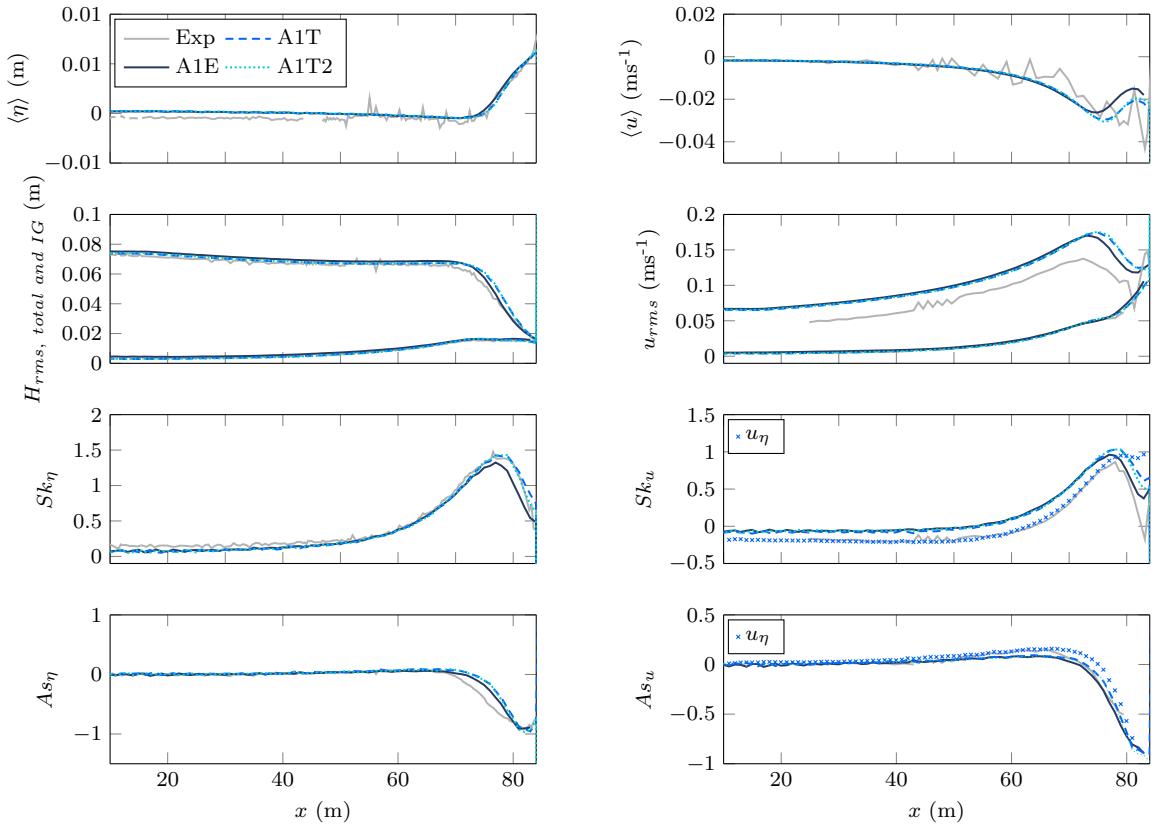

Figure 3.23: Evolution of free-surface elevation and cross-shore velocity statistics along the cross-shore profile, for A1 condition. Grey lines - experimental data; dark blue - A1E; blue - A1T; cyan - A1T2. The blue crosses in Sk_u and As_u figures were calculated from the velocity time series obtained from A1T free-surface elevation time series, with the u_η method (see subsection 3.2.5).

thus it is set up to represent more accurately A than B conditions. Using the same set of wave-breaking parameters for all wave conditions simulated implies the existence of some discrepancies between experimental and numerical results, particularly in what concerns breaking initiation and inner-surf/swash zone nonlinearities.

For A conditions, free-surface elevation trends are well represented by the model, as well as the wave phasing and nonlinearity until the swash zone (Figs. 3.23 and 3.25). Small differences can be seen between the runs forced with theoretical (A1T and A1T2) and experimental (A1E) input conditions, particularly for A1 in the inner-surf and swash zones, a result of the higher IG-wave energy observed for the experimental-input runs, relative to the experimental data (Fig. 3.24).

The three most obvious inaccuracies of the model on the simulation of A conditions can be observed for As_η, u_{rms} and Sk_u statistics (Figs. 3.23). The general shape and maximum of As_η are captured by the model, but in order to represent correctly the H_{rms} decrease due to wave breaking and the Sk_η evolution along the profile, the set of breaking-model parameters chosen delays the beginning of the increase in wave asymmetry. This increase, associated with the breaking process, is reproduced by the

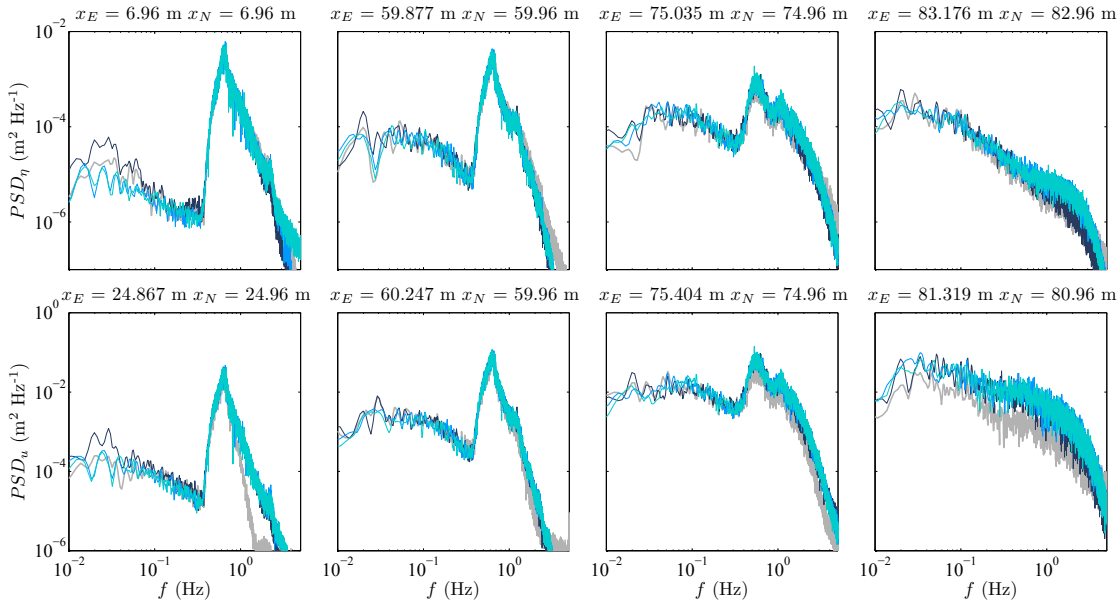

Figure 3.24: Spectra of free-surface elevation (top) and cross-shore velocity bottom) at four different cross-shore positions, for A1 condition. Grey lines - experimental data; dark blue - A1E; blue - A1T; light blue - A1T2.

model about 5 m closer to the beach than expected from the experimental data.

The general trends of velocity statistics are well represented by the model. The overestimation, particularly of u_{rms}, is a consequence of the measurements being made

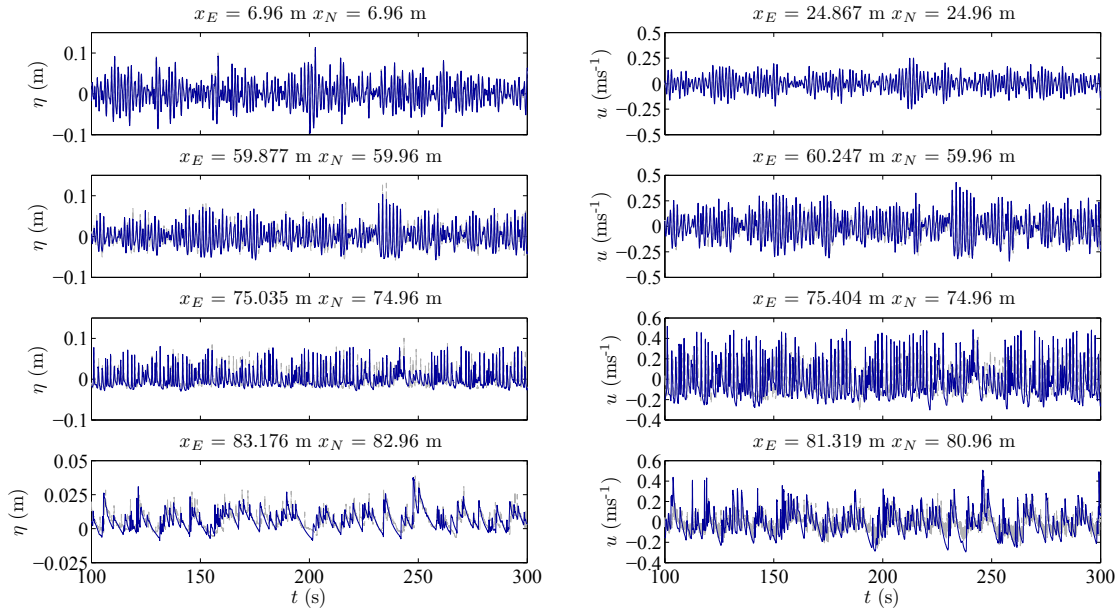

Figure 3.25: Time series of free-surface elevation and cross-shore velocity at four different cross-shore positions, for A1 condition. Grey lines - experimental data; dark blue - A1E. Note: Since A1 is an irregular wave condition, the spectra of theoretical and experimental input conditions is the same, but not the time series and thus the comparison of A1E time series with A1T and A1T2 time series is not showm.

at a certain height above the bed and compared to the model outputs that correspond to a velocity integrated over the entire water column. Near the bottom, the velocity is expected to be lower and less skewed than near the surface. Sk_u is hence overestimated in about 16%, for A1, and 22%, for A3. In the shoaling zone, the model overestimates the energy of the velocity frequencies higher than the peak frequency, but it is accurate further onshore.

In order to overcome the limitation of the model in the simulation of the velocity, the method described in section 3.2.5 for estimating the velocity from the computed free-surface elevation (u_η) can be used to retrieve u_{rms}, Sk_u and As_u, especially for irregular-wave conditions (blue dots in Fig. 3.23).

Computing the theoretical solution with 1000 or 2000 frequencies (difference between T and T2 input time series, Fig. 3.23 and Fig. A.1 of Appendix A), does not improve significantly the statistics. Thus, since computing the theoretical solution with 2000 frequencies is more time consuming, new theoretical irregular-wave conditions defined in this section were obtained using a theoretical solution that considers only interactions between 1000 frequencies.

Keeping the same wave-breaking parameters that were calibrated for the irregular-wave conditions for the bichromatic waves, makes it difficult for the model to accurately simulate all the nuances of the evolution of the nonlinearities of the B conditions (see Appendix A). A small change of ϕ_b (from 26° to 27°) and ϕ_f (from 6° to 9°) helps better represent the existence of a second breaker region, but does not fully resolve the correct representation of skewness and asymmetry trends. The model slightly underestimates set-down and overestimates set-up. It tends to overestimate as well the mean energy level of B conditions and small differences in the $H_{rms,IG}$ at the first wave gauge (around 2% for B1) can increase along the beach and influence the simulation of IG-wave height closer to the coast and the position of the $H_{rms,IG}$ maxima and minima, for the B wave conditions. When the amplitude modulation is greater (the case of B3), these differences affect also the skewness evolution, in particular the skewness peaks that correspond to short-wave modulation by IG waves. Nevertheless, the model represents accurately the energy and frequency of the most important frequencies. This allows it to still represent the general trends of free-surface elevation and velocity sufficiently well, together with the first and second skewness peaks, which are correctly represented in terms of amplitude (only the first one) and cross-shore location (both). The difficulties presented by the model in the simulation of only some of the skewness peaks reinforce, once again, the idea that the various skewness peaks do not have all the same origin.

Friction coefficient

Since the bottom friction is beach dependent, it is difficult to estimate *a priori*, and an adjustment can be made for each beach modelled. Therefore, a sensitivity analysis was performed for a range of resonable values (Grant & Madsen, 1979) for the GLOBEX case. Fig. 3.26 shows the effect of changing C_f on H_{rms} and Sk_η, for both A1 and B1. Keeping the friction coefficient value at a minimum of 0.001 allows a better representation of the onset of wave breaking and thus of the maximum skewness values as well. The value of 0.001 was chosen as a compromise that allows the best representation of the decrease of H_{rms} during wave breaking, the increase of $H_{rms,IG}$ in the inner surf/swash zones, and the shape and maximum value of Sk_η evolution along the profile, for A1. Since it depends mostly on the bottom roughness, which is the same for all runs, the same value was considered for all A and B conditions.

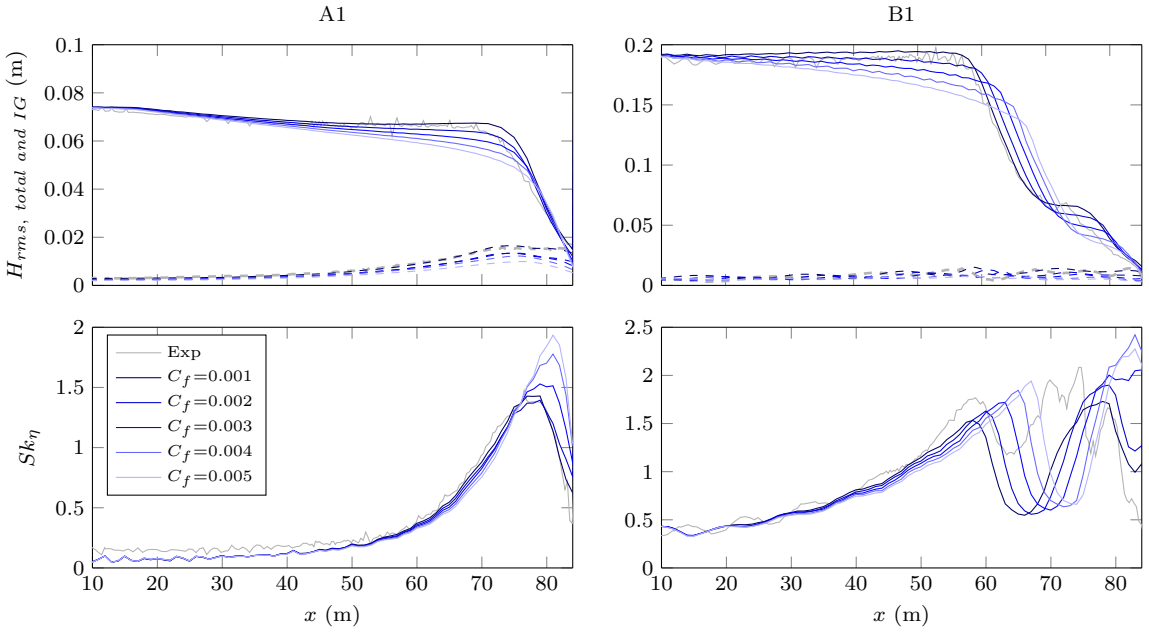

Figure 3.26: Evolution of H_{rms} and Sk_η along the cross-shore profile considering different C_f values. The dashed lines in the H_{rms} plot represent the IG-waves.

Wave-breaking parameters (ϕ_b, ϕ_f, γ_b, γ_f)

As wave nonlinearity and wave breaking are tightly linked, the breaking process (initiation, duration and cessation) must be reproduced by the model as close to the experimental data as possible. The sensitivity of the model to the choice of the breaking parameters is therefore very important and is subsequently analysed. All the sensitivity analysis is presented for A3. A particular attention is paid to the threshold values (corresponding to breaking initiation and cessation) of the two main physical parameters

that can be set in the breaking model, ϕ and γ. H_{rms} and u_{rms} of both all frequencies and IG-waves only, mean water level, mean cross-shore velocity and skewness and asymmetry of both free-surface elevation and cross-shore velocity, as well as Fourier spectral analysis, were used to check the model sensitivity to the choice of the breaking parameters. The analysis presented herein is focused on the control variables mentioned before (H_{rms} of total and IG-waves only, Sk_η and B_{max}), which account for total and IG wave height and nonlinearity.

Each parameter was varied independently, keeping the other three at their default values. The angles for breaking initiation and cessation were varied within a range of $\pm$ 4° around the default values ($\phi_b = 26°$ and $\phi_f = 6°$). The value of γ_b was increased from 0.7 to 1, being 0.7 the default value of γ_f; inversely, the maximum γ_f was defined as the default value of γ_b and the minimum to 0.50. This range of values was chosen for representing breakers of the spilling type in realistic relative water depths (Cienfuegos *et al.*, 2010). The effect of varying the breaking-model parameters on the skewness and H_{rms} of the waves is shown in Fig. 3.27.

As expected, changing the breaking parameters results in no significant changes until the very end of the shoaling zone. In the surf zone, both H_{rms} and Sk_η are more sensitive to the variation of the parameters controlling the start of breaking than the cessation of breaking. However, even in the case of varying ϕ_b (the parameter with a greater effect on the control variables) from the minimum to the maximum value considered, the computed H_{rms} does not change significantly, with the breakpoint position shifting onshore only about 3 m. The skewness is sensitive to the variation of the breaking-model parameters, particularly regarding its maximum value (since the shape is, in all A cases, well modelled); an exception is the variation of ϕ_f, which essentially conditions the Sk_η of the waves in the swash zone, and only when increased beyond 8°.

Fig. 3.28 presents the variation of the B_{max} value as a function of the different values chosen for the four physical breaking-model parameters, ϕ_b, ϕ_f, γ_b and γ_f. Regarding this parameter (B_{max}), varying ϕ_b can result in a change of about 22%, which can be reduced to as little as 4% if ϕ_b is only changed by $\pm$ 1° or to about 11%, for a $\pm$ 2° change. Similarly, B_{max} can oscillate about 11% with γ_b within a range of 0.7 to 1, reducing to 5% if a range of $\pm$ 0.05 around the default value is considered. The Sk_{max} varies only about 11% when γ_f, always assuming inferior values relatively to the default γ_b, is changed between 0.55 and 0.8. However, in the case of B_{max}, the variation of γ_f induces a change of 20%, almost as important as the variation of ϕ_b.

Considering the parameter to which the nonlinearity is more sensitive, ϕ_b, the results show that changing it up to 15% ($\pm$ 2°) around its default value, results in a variation

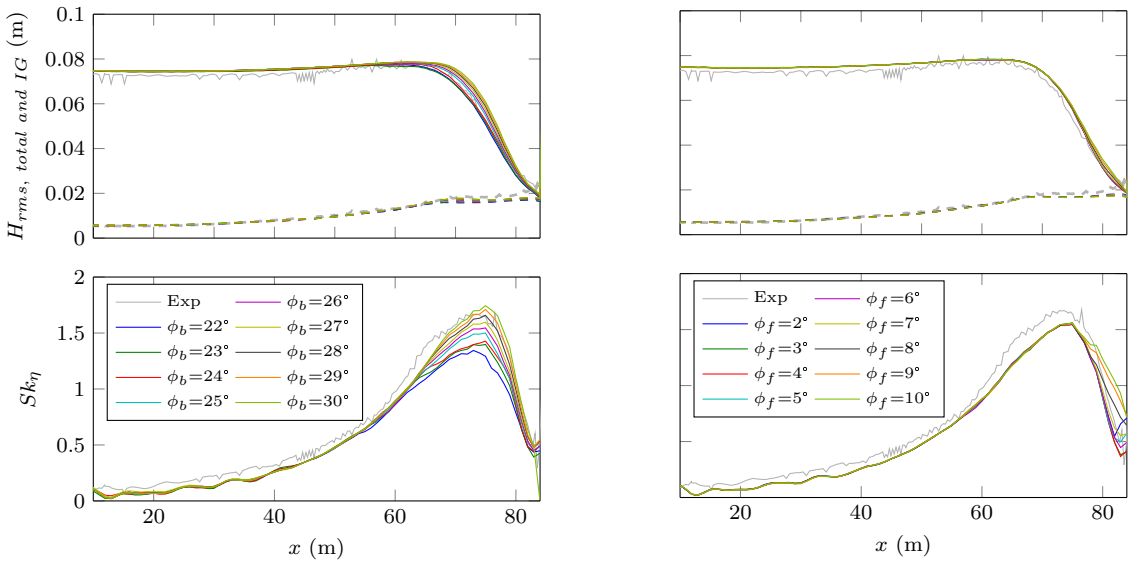

(a) Varying ϕ_b.

(b) Varying ϕ_f.

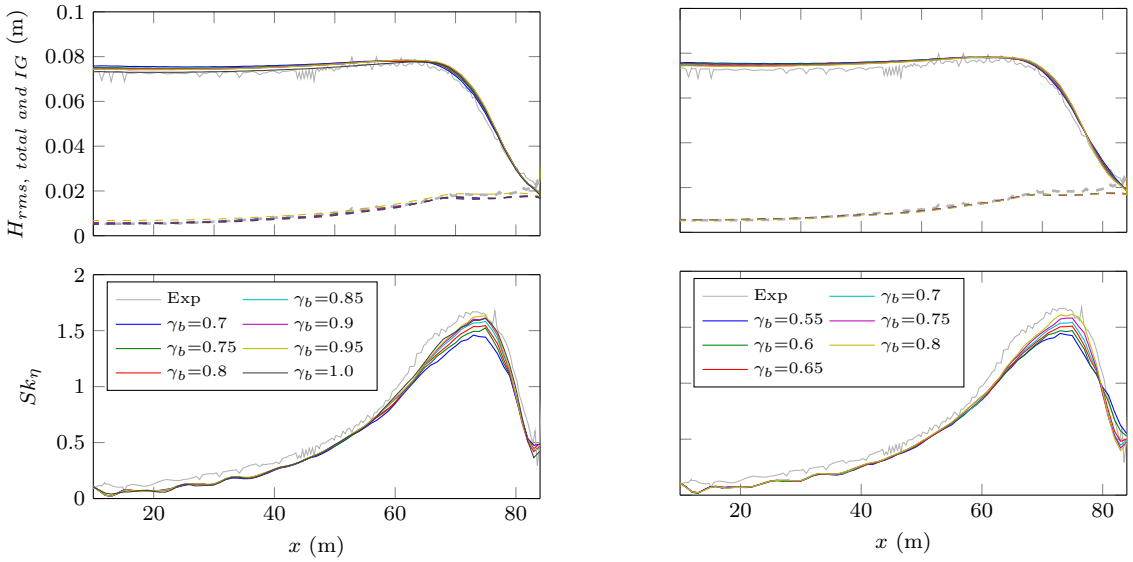

(c) Varying γ_b.

(d) Varying γ_f.

Figure 3.27: Sensitivity of H_{rms} (solid line - all frequencies, dashed line - IG waves) and Sk_η to the main breaking-model parameters.

of B_{max} of less than 11% (a change inferior to the range of variation of ϕ_b itself). It is thus plausible to assume that an increase or decrease in the B_{max} for a given run (specific wave conditions and bed slope) compared to a defined control run (previously validated with experimental data) is significant and independent of the values chosen for the breaking-wave model parameters when greater than 11%. The values chosen for B conditions, ϕ_b=27° and ϕ_f=9° thus imply a very small change to the parameter-set used for A conditions, with the advantage of allowing a better adjustment of H_{rms} and Sk to B-series experimental data.

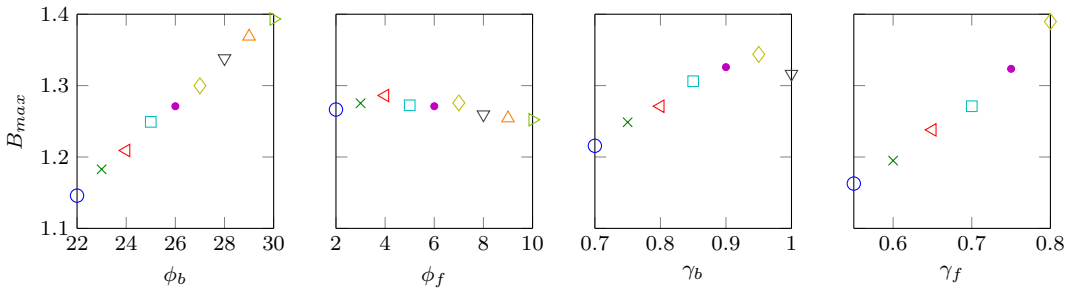

Figure 3.28: Sensitivity of B_{max} to the main breaking-model parameters.

3.3.3 Model validation for vN2003 data set

In the last subsections, the SERR1D model was validated with data from the GLOBEX project. Along those experiments the beach slope was kept constant. Thus, it is convenient to validate the chosen set of model parameters for other experiments run over a different beach. This is particularly important since the model will be used to investigate the influence of the beach slope on wave propagation.

The van Noorloos (2003) experiments (vN2003) consisted of different irregular and bichromatic wave conditions run over a 40 m-long fixed-bed beach with a 1/35 slope starting at $x = 8.5$ m, from the wave-maker. The irregular-wave conditions C-1 ($T_p = 2.0$ s, $H_{m0} = 0.05$ m) and C-3 ($T_p = 2.0$ s, $H_{m0} = 0.1$ m), ran during 40 min, were chosen to validate SERR1D model for four main reasons: (i) most wave conditions simulated with SERR1D are irregular-wave conditions and thus it is more important to validate the model firstly for irregular waves; (ii) the T_p considered is within the range of GLOBEX A conditions tested; (iii) C-3 H_{m0} is the same as for A1 and A3; and (iv) C-1 has a smaller H_{m0} than GLOBEX conditions (and thus smaller steepness than GLOBEX waves), offering an idea of the possible behaviour of SERR1D model when it is forced with wave conditions beyond the range of GLOBEX wave conditions. C-1 condition is particularly useful since some wave conditions that were simulated for highlighting the influence of the different parameters on wave propagation imply forcing the model with wave conditions significantly different from the conditions for which it was calibrated in this work (GLOBEX A1 and A3 conditions). The wave-breaking parameters were kept equal to GLOBEX runs and only the friction coefficient was increased from 0.001 to 0.002 to better represent IG-wave energy in the beach of vN2003. For C-1 condition, two input time series were considered: one obtained directly from the wave gauge measurements (C-1E) and another obtained theoretically (C-1T). As the wave-maker of vN2003 experiments did not have the capacity to absorb IG waves coming from the beach, IG-wave height is enhanced from the beginning until the end of the experiments. Thus, C-1E input time series provides more accurate results than

C-1T, as it includes the enhanced IG waves.

Fig. 3.29 shows that, with no change of the wave-breaking parameters, SERR1D represents sufficiently well the mean water level and the wave height (both of total and IG waves only) of vN2003 C-1 and C-3 experiments. The small differences found between the measured and the simulated skewness maxima for C-3 (already visible for A3 GLOBEX condition relatively to A1 GLOBEX condition) can be halved by changing ϕ_b by only 2° (shown in Fig. 3.29, similarly to what was shown for GLOBEX B conditions). The free-surface elevation asymmetry maximum is found around 2 m further onshore for numerical results than for experimental data, which was already seen to be a limitation of the model with GLOBEX data as well.

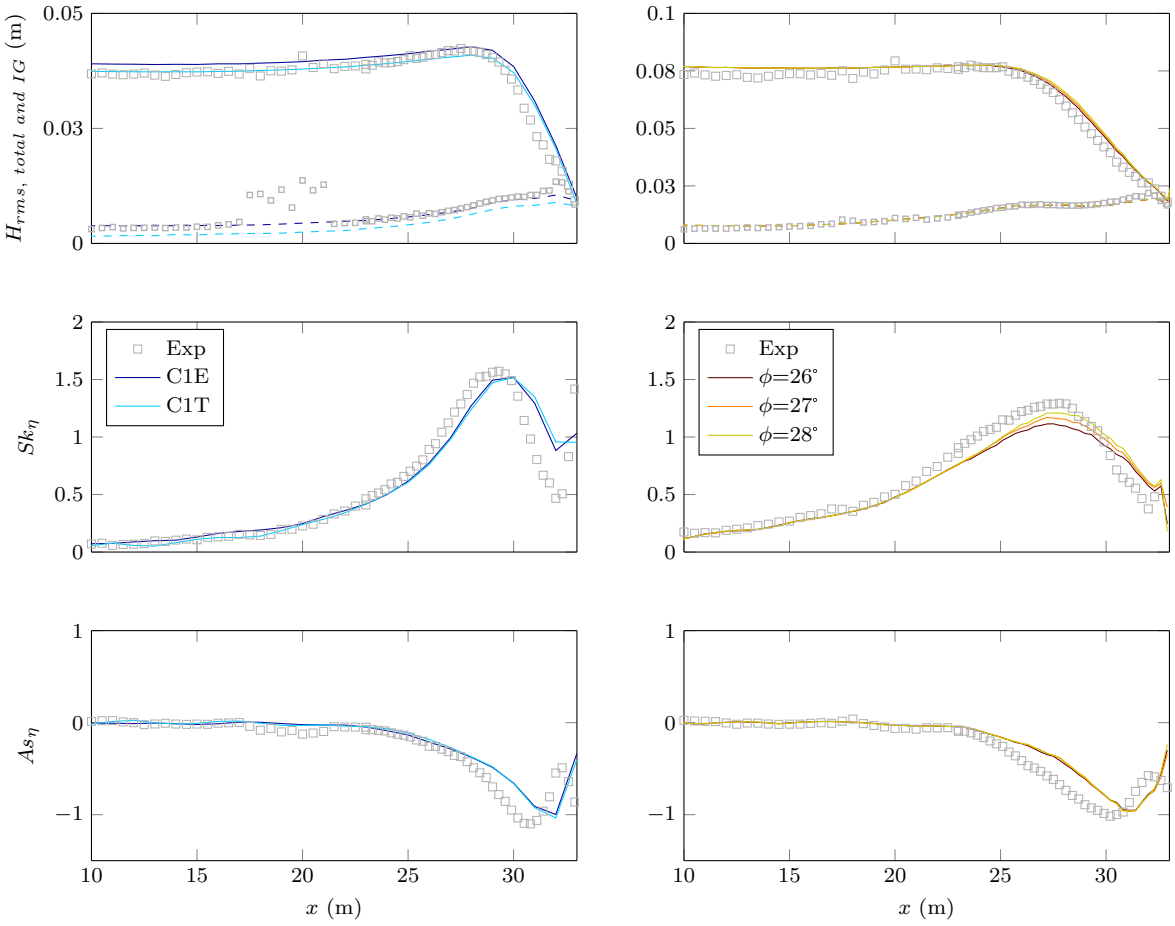

Figure 3.29: Evolution of free-surface elevation statistics along the cross-shore profile, for C-1 and C-3 wave conditions of vN2003. Grey markers - experimental data; dark blue - C-1E; blue - C-1T; dark red - C-3E. Smaller markers in the H_{rms} plot represent the IG waves.

3.3.4 Model results

After validation, the SERR1D model was used to simulate new wave conditions to understand how different wave parameters and beach characteristics may influence the

wave nonlinearities. The default beach chosen was similar to the GLOBEX beach, with the exception of the initial plane section of the bed, which was shortened (in about 7 m) to reduce computation time. The wave conditions simulated were scaled from prototype and represent typical wind- and swell-waves conditions: wave heights from 0.6 to 2.6 m and wave periods from 7 to 17 s, with offshore spectral bandwidths that vary from very-broad to very-narrow banded. This range of wave conditions can be observed along the year, for example, in the west coasts of Europe, where Summer waves have easily half a meter height and periods as short as 7 s and present commonly broad-banded spectra and Winter high-energy swell waves having more narrow-banded spectra and reaching frequently heights of 2.6 m and periods up to 17 s.

In order to better characterize the range of wave conditions that will be analysed, the Ursell (eq. 3.25) and Iribarren (eq. 3.26) numbers can be calculated, as they describe conveniently the characteristics of the waves and the beach slopes over which they propagate. The Ursell number is used herein as in Ruessink *et al.* (2012),

$$Ur = \frac{3}{4}\frac{a_w k}{(kh)^3}, \tag{3.25}$$

with $a_w = 0.5H_s$, k the local wave number computed with the linear theory using $T = m_0/m_1$, where m_n is the spectral moment of order n, and h is the local water depth. The Iribarren number is calculated following Iribarren Cavanilles & Casto Nogales (1949),

$$Ib = \frac{\tan(\beta)}{\sqrt{\frac{H_s}{L}}}, \tag{3.26}$$

where H_s is the local significant wave height calculated for the duration of the time series, L is the local wave length computed with the linear wave theory using $T = m_0/m_1$ and $\tan(\beta)$ the beach slope. For calculating the Iribarren number offshore (or at the wave-maker), the offshore values of H_s and L are considered.

Fig. 3.30 shows the distribution, in the Ur_0 (Ur at the wave-maker) and Ib_0 (Ib at the wave-maker) space, of all the irregular-wave conditions simulated. It also illustrates that the synthetic wave conditions analysed in the following section have Ur and Ib numbers similar to or within the range of the experimental wave conditions of GLOBEX and vN2003 experiments. Therefore, the good results obtained by SERR1D in the simulation of these experimental data support its usage for simulating a wide range of wave conditions in which the subsequently-analysed wave conditions are included.

For the wave conditions considered, the spectra at the first wave gauge and the results in terms of H_{rms}, Sk_η and As_η evolutions and B_{max} values are presented subsequently.

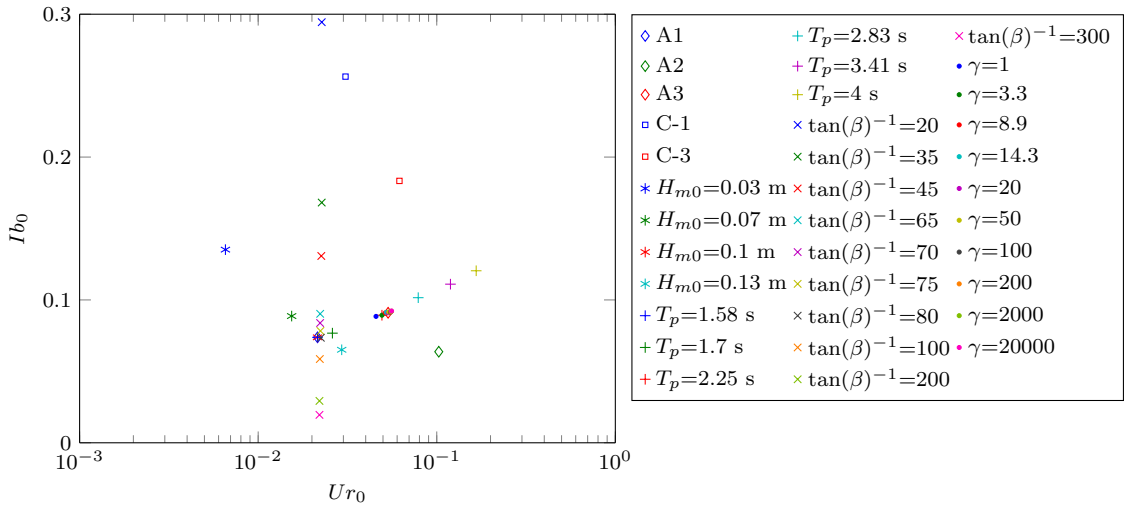

Figure 3.30: Distribution of the irregular-wave conditions in the Ib_0-Ur_0 space. Diamonds: GLOBEX wave conditions; squares: vN2003 wave conditions; asterisks: varying H_{m0} runs; pluses: varying T_p runs; dots: varying γ runs; crosses: varying $\tan(\beta)$ runs.

Influence of offshore wave height, H_{m0}

Varying the offshore wave height influences both short-wave and IG-wave energy. Further, if the offshore wave period is kept constant, changing wave height also changes wave steepness: for the same period (and thus wave length), increasing wave height will increase wave steepness. Fig. 3.31 shows how the increase in offshore short-wave energy affects the non-linearity of the propagating waves. Smaller waves become very skewed,

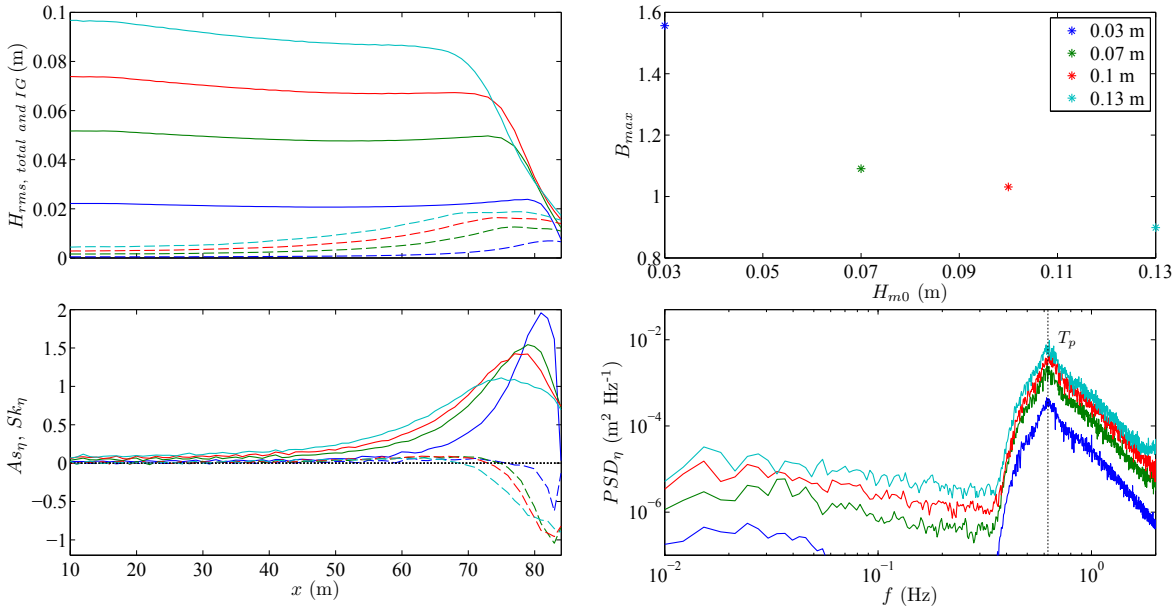

Figure 3.31: Influence of offshore H_{m0} on H_{rms} (solid line - total; dashed line - IG waves only), Sk_η (solid line) and As_η (dashed line) and B_{max}. The last plot shows the spectra of free-surface elevation at the first wave gauge. Note: the red curves correspond to A1T run.

with the skewness increasing fast over a short cross-shore distance, while bigger waves reach a lower maximum skewness (around 74% lower), but stay skewed along a greater cross-shore distance and reach larger asymmetry than very short waves. The overall nonlinearity diminishes by 42% when the wave height is increased fourfold.

The input H_{m0} was limited to 0.13 m, because the model runs became unstable when greater offshore wave heights were chosen (without changing the values of the other wave and beach parameters nor those of the breaking model). Slightly changing the wave-breaking parameters or the model resolution allowed the extension of the model application to greater wave heights but, for a question of consistency, runs with different model parameters are not considered for comparison.

Influence of offshore peak period, T_p

Like varying the offshore wave height, keeping the offshore wave peak period constant changes wave steepness, the inverse is also valid: for the same wave height, if the period is increased, wave steepness decreases. Fig. 3.32 shows that ss the offshore peak period increases, both the wave skewness and asymmetry start developing earlier in the shoaling zone, increasing until their maxima are reached. B_{max} can increase up to about 22% when the peak period is doubled. For the greater-T_p runs, H_{rms} increases before wave breaking, reflecting the need for a greater wave height to develop (and greater wave steepness) to allow wave-breaking initiation. Furthermore, the wave

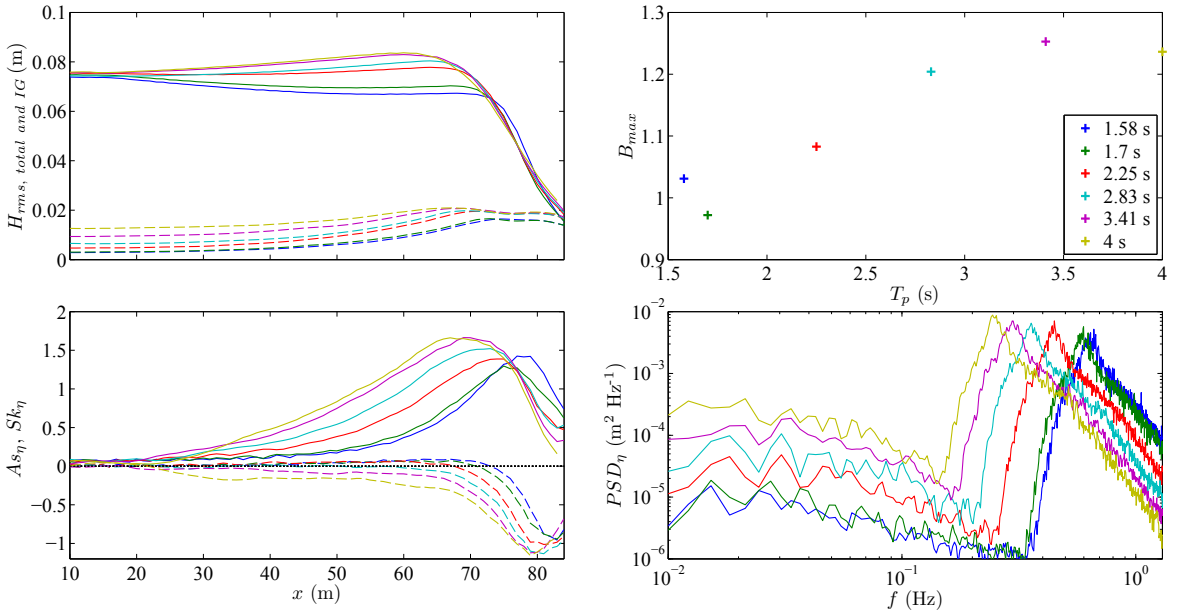

Figure 3.32: Influence of offshore T_p on H_{rms} (solid line - total; dashed line - IG waves only), Sk_η (solid line) and As_η (dashed line) and B_{max}. The last plot shows the spectra of free-surface elevation at the first wave gauge. Note: the blue curves correspond to A1T run.

conditions with longer offshore peak period are shown to have higher IG-wave energy at the wave-maker and in the shoaling zone. However, this is simply a direct result of the fact that the wave conditions with longer peak periods were designed with greater energy at the peak frequency (because the spectral range of frequencies considered was smaller than for shorter peak periods), which implies higher IG-wave energy as well.

Influence of bandwidth, γ

A JONSWAP spectrum of irregular-wave conditions can have different bandwidths, from broad- to narrow-banded, which essentially determines the main range of frequencies that will interact along the beach profile, increasing wave nonlinearity and feeding higher and lower frequencies than the peak frequency. Fig. 3.33 shows how changing the bandwidth of the JONSWAP spectrum may influence the presence of IG waves and nonlinearity. B_{max} increases by about 20% if γ is varied between 1 and 20,000 while IG-wave height in the surf zone can decrease more than 80%.

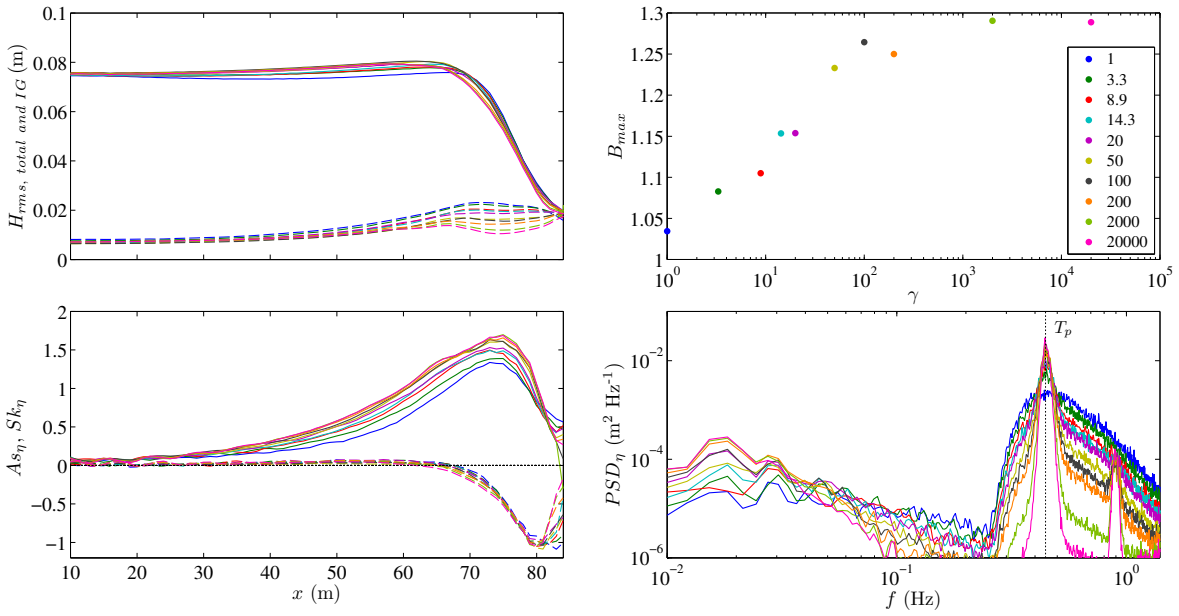

Figure 3.33: Influence of offshore γ on H_{rms} (solid line - total; dashed line - IG waves only), Sk_η (solid line) and As_η (dashed line) and B_{max}. The last plot shows the spectra of free-surface elevation at the first wave gauge. Note: the purple curves correspond to A3T run.

Influence of beach slope, $\tan(\beta)$

The beach slope has long been recognized to influence wave propagation. It conditions the evolution of wave nonlinearity, the type of breaking and the reflection of IG waves. Here, the bed slope was changed from 1/20 to 1/300 to analyse its influence on the control variables. Fig. 3.34 shows how changing the bed slope, from very steep to very

gentle, influences wave propagation. Unlike for the previous cases, here the cross-shore direction is considered in terms of water depth (h), instead of cross-shore distance (x), which allows an easier comparison of the wave propagation over the different beach slopes considered. In the case of steeper beaches, a sudden increase of wave height close to the coast can be observed, which allows wave breaking to occur. The IG waves increase their height towards the shore and only in the case of very gentle slopes ($\tan(\beta) > 80$) does their height decrease before reaching the shoreline. There is an increase of 58% of the B_{max} when the beach slope is diminished from 1/20 to 1/300. This increase is more significant for very-gentle slopes (gentler than 1/80), for which the nonlinearities have more time to develop before reaching the coast. The fundamental difference can be seen in the maximum value of Sk_η, which can increase by 122% when the beach slope changes from very steep to very gentle, or by 43% when the beach slope is diminished only until 1/80. For steeper slopes, asymmetry starts increasing at a greater water depth than for gentler slopes.

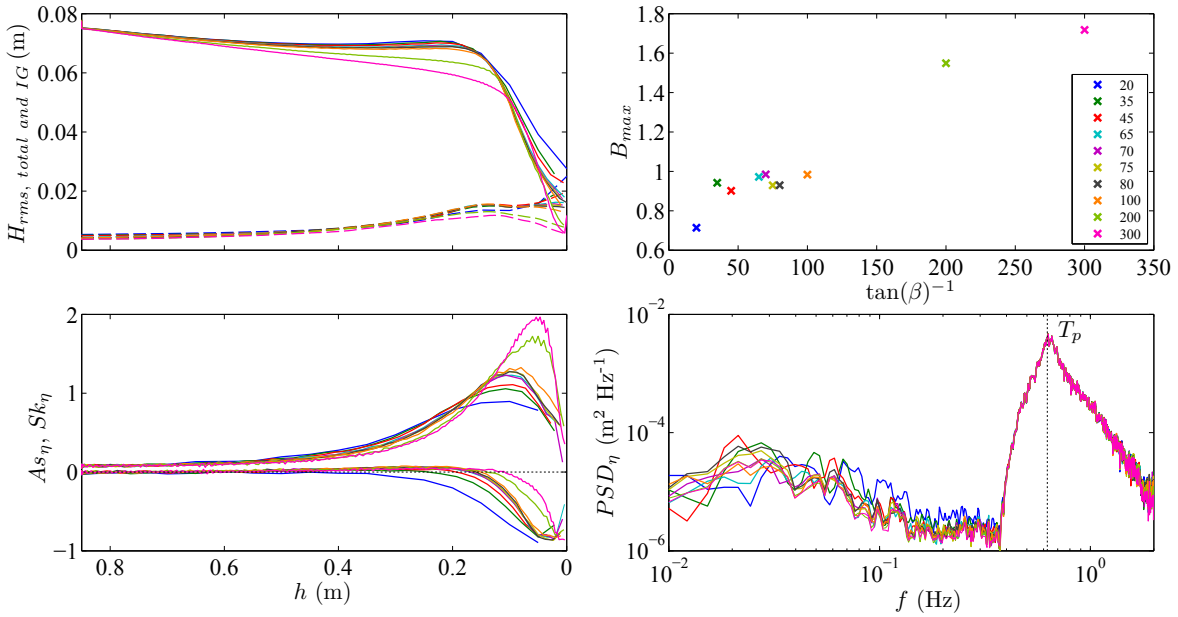

Figure 3.34: Influence of $\tan(\beta)$ on H_{rms} (solid line - total; dashed line - IG waves only), Sk_η (solid line) and As_η (dashed line) and B_{max}. The last plot shows the spectra of free-surface elevation the first wave gauge.

Influence of modulation

Changing the modulation of bichromatic wave groups is a direct way of analyzing the effect of varying IG-wave height. Therefore, various bichromatic wave conditions with different modulation were simulated, in order to investigate the effect on wave propagation and nonlinearities. This was done by varying the amplitude of the main

frequency components (a_1 and a_2) of the bichromatic wave groups. The closer the values of a_1 and a_2, the greatest the modulation and thus the IG-wave height. The influence of the modulation on wave propagation is not analysed in terms of B_{max} values and hence Fig. 3.35 is slightly different from the figures presented for the previous parameters evaluated. Since the focus is not on the maximum nonlinearity value, but on the multiple existent maxima, instead of representing B_{max}, the evolution of B along the beach profile is shown. The spectra are zoomed on the main frequency peaks, highlighting the amplitude differences of the main components between wave conditions.

Initially, the first six conditions (from blue to purple) are analysed. Among these, the wave conditions with less modulation have significantly-smaller IG-wave height (blue and green), even though total wave height is greater in the shoaling zone, due to the greater short-wave energy resulting from the values of a_1 and a_2. They reach, locally, greater values of nonlinearity, but the maxima are not located at the same cross-shore positions as they are for the wave conditions with greater modulation.

From the analysis of GLOBEX B conditions, it was pointed out that the multiple peaks of skewness could be attributed to both the existence of two breaker zones and the influence of IG waves on short-wave nonlinearities. Among these, the first and the second peaks can be accurately represented by the model, in terms of cross-shore position (and, for the first, also in terms of amplitude). Fig. 3.35 shows that, when wave breaking happens over a narrow surf zone, it has a local skewness and nonlinearity peak associated (just before $x = 60$ m). This peak is greater for greater short-wave

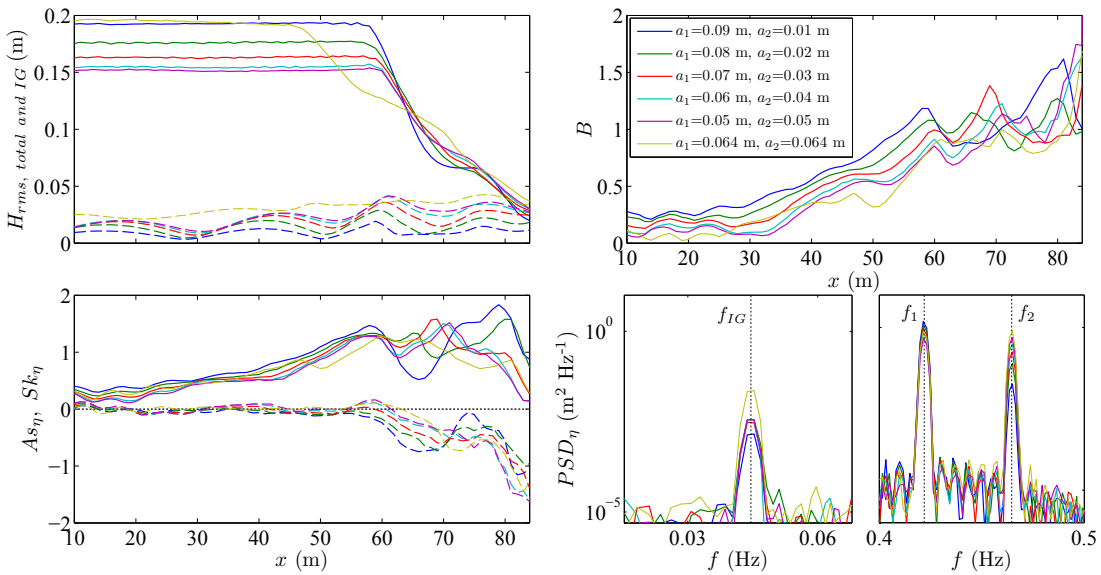

Figure 3.35: Influence of modulation on H_{rms} (solid line - total; dashed line - IG waves only), Sk_η (solid line) and As_η (dashed line) and B. The last two plots show, respectively, the bound-wave energy peak (f_{IG}) and the main frequency peaks (f_1 and f_2) of the free-surface elevation spectra at the first wave gauge.

height and weaker modulation. The position and value of the other peaks, however, vary significantly as a function of the modulation. The blue lines of Fig. 3.35 plots represent the wave condition with less modulation and greater short-wave energy. Contrary to the other conditions, it has no skewness peak corresponding to the IG-wave trough located between $x = 65$ m and $x = 75$ m and the greatest B and Sk values are reached in the beginning of the swash zone. The green curves, corresponding to a wave condition with slightly more modulation than the blue ones, show a decrease of the swash-zone peak and the appearance of a peak at the IG-wave trough just after x=65 m. For the other wave conditions with increasing modulation (red, cyan, violet) this skewness peak at the IG-wave trough position is greater and more marked. The maximum B values occur in the beginning of the swash zone, for conditions with less modulation, and closer to the shoreline, when the modulation is greater. The first asymmetry maximum is greater when modulation is weaker, and the second one when the modulation is stronger.

The influence of the modulation, when the short-wave height is kept the same, can be seen in the difference between the condition with $a_1 = 0.09$ m and $a_2 = 0.01$ m (blue), which has the smallest modulation of all the bichromatic conditions presented, and the condition with $a_1 = 0.064$ m and $a_2 = 0.064$ m (yellow), which has the same energy, but the greatest modulation possible. The higher modulation implies a larger variability of the short-wave height, and thus a greater similitude with the irregular-wave conditions. Hence, the breaking happens more gradually over a wider region of the domain, with the higher waves breaking sooner than the smaller ones. The IG-waves height does not follow an oscillating trend and the trends of Sk, As and B are smoother and with smaller and less marked peaks, like it was observed for irregular-wave conditions. The tendency for wave conditions with weaker modulation to have greater absolute values of skewness and asymmetry maxima and greater B values is again confirmed when conditions with the same short-wave energy but distinct modulations are considered (the blue and yellow curves).

Overall, it is shown that the IG waves do influence the nonlinearities depending on the modulation, but also depending on the ratio between the short-wave and the IG-wave energy.

3.3.5 Discussion

The bichromatic-wave runs with different modulation have highlighted the influence of IG waves on the short-wave nonlinearities. For the same short-wave height, larger modulation (and thus higher IG waves) results in smaller nonlinearity maxima. This is in agreement with Elgar & Guza (1985), who found interactions involving low frequencies to tend to reduce free-surface elevation skewness and asymmetry. It is also shown that

increasing modulation of bichromatic-wave conditions results in a greater similitude with the irregular-wave conditions, due to the greater variability of the short-wave height: broader surf zone and less-marked local maxima of nonlinearity in the surf zone.

The irregular-wave runs have proven that the evolution and maxima of wave nonlinearity depend on several non-local parameters, such as the offshore wave height, period and spectral bandwidth and the beach slope.

Dibajnia *et al.* (2001) have argued that waves with small offshore wave steepness become more nonlinear during the shoaling process than those with great offshore wave steepness, which eventually break in deeper waters before undergoing significant shoaling. Hence, they have used in their parameterization of nonlinearities the offshore wave steepness to define the value of the nonlinearity maximum that can be reached along the beach profile for a give wave condition. This is in conformity with the results presented, in which smaller offshore H_{m0} (for the same offshore T_p) and greater offshore T_p (for the same offshore H_{m0}), and thus smaller offshore wave steepness (H_0/L_0) resulted in a greater maximum value of the nonlinearity parameter (B_{max}).

Elgar & Guza (1985) have compared broad- and narrow-banded data sets and found that the interactions between frequency pairs are spread over a wide range of frequencies for a broad-band data set, and happen between relatively few triads (the spectral peak and its harmonics) for a narrow-band case. These authors argued that skewness and asymmetry for both cases are quite similar, but their results show a maximum skewness value for the narrow-band case about at least 30 % larger than that found for the broad-band case. Norheim *et al.* (1998) have found the spectral evolution to be much weaker for wave conditions with broad-banded spectra, because the principal effect of the triad interactions (interactions that involve two different frequencies and their sum frequency) in this case is to spread energy to frequencies where spectral levels are relatively low. For the narrow-banded spectra, thee authors observed harmonic peaks to develop more significantly. The increasing value of the nonlinearity parameter (B_{max}) in response to the narrowing of the offshore wave spectrum presented in the previous subsection thus corroborates the findings of those authors.

The results of the model simulations have also demonstrated that decreasing beach steepness results in a greater development of the nonlinearities, particularly due to the contribution of skewness. This is in agreement with Norheim *et al.* (1998), who found gentler slopes to promote a stronger growth of the harmonic and infragravity peaks, with a more important contribution from the real part of the bispectrum (skewness). For steeper slopes, they found cumulative energy transfers to be smaller and the imaginary part of the bispectrum (asymmetry) to be greater. For the steepest slopes simulated in this work (1/35 and 1/20), asymmetry has indeed a greater contribution to the total

nonlinearity, but this is due to the relatively smaller contribution of the skewness to the total, since the asymmetry increase (from gentle to steep slopes) is not significant. More recently, Filipot (2015) has also argued the dependence of wave nonlinearity (in particular, of wave skewness) on the beach slope. The author has established that wave skewness at the breakpoint is a decreasing function of the bottom slope and thus bottom slope may partially control breaking initiation.

It is then clear that wave nonlinearities may depend on more than local wave parameters. Rocha *et al.* (2013b) (presented in next subsection) have analyzed and applied to field data existing parameterizations and concluded that offshore wave parameters and the beach slope, which can be seen as the history of the waves, could bring an improvement to the present estimations of velocity skewness and asymmetry, which is the aim of the following section.

3.4 Parameterization of velocity nonlinearities

3.4.1 Field data - Parameterizations of wave nonlinearity from local wave parameters

The article below was presented in Plymouth, at the International Coastal Symposium, in 2013. It consists of an analysis of the performance of different parameterizations of the velocity nonlinearities, for various sets of field data collected in different beaches of the Portuguese coast. It is introduced here to highlight the fact that current parameterizations that take into account only local wave parameters may include significant errors in the estimations of velocity skewness and asymmetry, as suggested in the previous section.

Parameterizations of wave nonlinearity from local wave parameters: a comparison with field data

Mariana Rocha†‡, Paulo Silva†, Hervé Michallet‡, Tiago Abreu∞, Delminda Moura§, Juana Fortes+

† CESAM & Physics Department, University of Aveiro, Campus de Santiago, 3810-193 Aveiro, Portugal
m.rocha@ua.pt
psilva@ua.pt

‡ CNRS/Grenoble-INP/UJF-Grenoble 1, LEGI UMR 5519, BP 53, 38041 Grenoble, France
herve.michallet@legi.grenoble-inp.fr

∞ CESAM & Polytechnic Institute of Viseu, Campus de Repeses, 3504-510 Viseu, Portugal
tabreu@estv.ipv.pt

§ CIMA, University of Algarve, Campus de Gambelas, 8005-139 Faro, Portugal
dmoura@ualg.pt

+ LNEC-DHA, National Civil Engineering Laboratory, 1700-066 Lisboa, Portugal
jfortes@lnec.pt

www.cerf-jcr.org

www.JCRonline.org

ABSTRACT

Rocha, M.V.L., Silva, P.A., Michallet, H., Abreu, T., Moura, D., Fortes, C.J., 2013. Parameterizations of wave nonlinearity from local wave parameters: a comparison with field data *In:* Conley, D.C., Masselink, G., Russell, P.E. and O'Hare, T.J. (eds.), *Proceedings 12th International Coastal Symposium* (Plymouth, England), *Journal of Coastal Research*, Special Issue No. 65, pp. xxx-xxx, ISSN 0749-0208.

Three different parameterizations of wave nonlinearity from local wave parameters are applied to field data (free-surface elevation and flow velocities) gathered in different beaches along the Portuguese coast, under diverse wave conditions. The hydrodynamics of the various sites are analyzed, together with the performance of each formulation. The data considered extend the range of the data previously used by the authors of the parameterizations, including longer wave lengths and higher Ursell numbers. A comparison is done, based on skill and agreement index values, to understand the performance and applicability of each parameterization and what could be changed to improve such formulations.

ADDITIONAL INDEX WORDS: *Velocity skewness, velocity asymmetry, Ursell number, Iribarren number.*

INTRODUCTION

The skewness and asymmetry of the free-stream velocity, at the edge of the bottom boundary layer, play an important role on sediment transport, particularly in shallow, wave-dominated conditions, as the bed load transport is determined by the time-varying bottom stress and the suspended-load transport depends on the time-varying residual velocities (Marlarkey and Davies, 2012; Abreu *et al*. 2013). It is thus of paramount importance to accurately describe these nonlinear effects in order to better understand the cross-shore sediment transport and improve current beach profile morphodynamic models.

Highly-advanced phase-resolving wave models, such as those based on the Boussinesq or the RANS equations, are able of accurately describing the transformation of each individual wave as it approaches the shore. However, these models are still too computationally demanding for application to morphodynamics settings and thus, for practical engineering purposes, simple analytical theories (linear and nonlinear) are often employed.

The free-stream velocity, driven by the time-varying free-surface, represents the velocity immediately outside the wave bottom boundary layer and its skewness and asymmetry changes reflect the changing wave shape at the surface. Both skewness and asymmetry can be evaluated using different parameters suggested by several authors (e.g. Drake and Cantaloni, 2001; Elfrink *et al*., 2006; Ruessink *et al.*, 2009; Abreu *et al.*, 2010).

Although a wide set of different formulations has been developed for deriving free-stream wave orbital velocity from nonlinearity parameters (e.g. Isobe and Horikawa, 1982; Drake and Calantoni, 2001, Abreu *et al.*, 2010), it can also be of great use, both for field-work purposes and numerical modeling, defining velocity skewness and asymmetry (and thus, the description of the wave shape) at a certain depth directly from local wave parameters, such as wave height and period and water depth (Ursell number).

Therefore, this work aims to compare three different recent parameterizations (Dibajnia *et al.*, 2001 (DMW01, for simplicity); Elfrink *et al.*, 2006 (EHR06); Ruessink *et al.*, 2012 (RRR12)) with field data acquired in several sites under various wave energy conditions, in order to evaluate the applicability of each parameterization to other data than those considered in its formulation, to better insure the possibility of a wider use of these wave skewness and asymmetry parameterizations from local wave parameters.

PARAMETERIZATIONS

The three formulations considered in this work have in common the fact that some measure of wave nonlinearity is described by means of local wave parameters, for breaking and non-breaking waves, and constant sloping beds. In all cases, the free-stream velocity time series are calculated near the bottom, but outside the bottom boundary layer, and from those, the nonlinearity parameters considered for each formulation are computed.

Dibajnia *et al.* (2001) parameterization

This parameterization was developed for irregular waves, based on a set of wave flume experiments. Nevertheless, its adjustment to field data will be studied in this work and compared with other field-based formulations.

Dibajnia *et al.* (2001) define two parameters: the nonlinearity parameter,

$$Nlp = \left(\frac{u_{max}}{\hat{u}}\right)_{1/3} \quad (1)$$

where u_{max} is the velocity at the wave crest and $\hat{u}$ is the velocity amplitude (from crest to trough), and the asymmetry parameter,

$$Asp = \left(\frac{2T_{pc}}{T}\right)_{1/3} \quad (2)$$

with T_{pc} defined as the time interval between the velocity zero up-crossing before the crest and the wave-crest maximum, and T the wave period. For a purely-sinusoidal wave shape, these parameters have a value of 0.5, increasing or decreasing for greater nonlinearity or asymmetry, respectively. These can be defined for each Ursell number, here described as

$$Ur = \frac{gH_{1/3}T_{1/3}^2}{h^2} = \frac{H_{1/3}{L_{1/3}}^2}{h^3} \quad (3)$$

assuming shallow water approximation ($c = \sqrt{gh}$), where $H_{1/3}$, $T_{1/3}$ and $L_{1/3}$ are the significant wave height, period and length, h the local water depth and g the acceleration of gravity.

The shapes of the parameterization curves include a maximum, for nonlinearity, and a minimum, for asymmetry. The estimation of the position of these peaks depends on offshore wave steepness (H_0/L_0). Hence, this formulation is expected to be sensitive to the definition of offshore wave conditions, which are obtained from the available wave buoys (for field data), often located at a significant distance from each field site. The dependence of *Nlp* and *Asp* peaks on deep water wave steepness has already been analyzed by Dibajnia *et al.* (2001)

The sensitivity to offshore wave conditions can be a positive point for this formulation, as wave history is accounted for, and may lead to a better description of local wave conditions.

When applying this formulation, it should be taken into account that it was developed based on experimental data collected in a wave flume with uniform bottom slope and that the local values of the *Nlp* and *Asp* were obtained using the results of wave height transformation calculated by an energy conservation method.

Elfrink *et al.* (2006) parameterization

This formulation also considers a wave-by-wave analysis to define nonlinearity parameters from local wave characteristics. However, instead of directly calculating skewness and asymmetry parameters, these authors derived synthetic orbital-velocity time series, using a set of simple sinusoidal functions for defining the shape of each segment between the maximum and minimum velocities and the zero-crossings. The nonlinearity of each individual wave is determined from local parameters, such as normalized wave height ($H^* = H/h$), where H is the height of an individual wave and h is the local water depth) and length ($L^* = L/h$, with L the wave length calculated according to Airy wave theory, from the period T of each individual wave) and the Iribarren number, defined as

$$Ib = \frac{\tan\beta}{\sqrt{\left(\frac{H}{L_0}\right)}} \quad (4)$$

where β is the local bed slope and L_0 the offshore wave length. Skewness and asymmetry can then be calculated from the synthetic orbital-velocity time series and analyzed in function of the Ursell number, here defined as:

$$Ur = HL^2/h^3 \quad (5)$$

Skewness (S_u) and asymmetry (A_u) calculated for this parameterization and also for the next one, proposed by Ruessink *et al.* (2012), are calculated from the third-order moments defined in (6) and (7).

$$S_u = \frac{\overline{u_w^3(t)}}{\sigma_{u_w}^3} \quad (6)$$

$$A_u = \frac{\overline{\mathcal{H}(u_w(t))^3}}{\sigma_{u_w}^3} \quad (7)$$

where the over bar represents a time average, $u_w(t)$ is the total sea-swell orbital velocity in the direction of wave advance, σ_{u_w} is the standard deviation of $u_w(t)$ and $\mathcal{H}(u_w(t))$ the imaginary part of the Hilbert transform of $u_w(t)$.

For a purely-sinusoidal shape, both parameters have a 0 value, which becomes progressively more positive or negative, for larger skewness or asymmetry, respectively.

Ruessink *et al.* (2012) parameterization

Most recently, a new methodology to compute nonlinearity parameters representative of a series of random, natural waves from local wave parameters was suggested by Ruessink *et al.* (2012). These authors argue that even though individual waves may be rather accurately described by parameterizations based on a wave-by-wave analysis, error accumulation makes the use of a series of individual waves to estimate time-averaged measures of wave nonlinearity questionable. Thus, based on statistical and spectral parameters, the authors compute the dependence of S_u and A_u on the Ursell number, defined here as

$$Ur = \frac{3}{4}\frac{a_w k}{(kh)^3} = \frac{3}{32\pi^2}\frac{H_s L^2}{h^3} \approx 0.01\frac{H_s L^2}{h^3} \quad (8)$$

where $a_w = 0.5 \cdot H_s$ (H_s being the significant wave height), k and L are, respectively, the local wave number and corresponding wave length computed with linear wave theory using T ($T = \frac{m_1}{m_0}$, where m_n is the spectral moment of order n). If the significant wave length is considered, then the *Ur* defined in equation (8) is about 0.01 times the *Ur* described in equation (3).

The authors of this parameterization also stress the fact that it is based predominantly on directionally-spread sea conditions and will tend to underestimate the skewness of orbital velocity in narrow-banded swell and unidirectional laboratory waves and that the data used in the development of these formulations were collected in low sloping (< 1/30) wide sandy beaches.

It should be further noted that, although in this paper the wave nonlinearities are always referred to as skewness and asymmetry, this is only literally true for EHR06 and RRR12 parameterizations, in which these parameters are calculated from the third-order moments of orbital velocity. For DMW01 case, the parameters considered are instead a nonlinearity parameter, as an equivalent for skewness and an asymmetry parameter, for asymmetry. These depend on the values and time instants (along the wave period) of velocity maxima, minima and zero-crossing values.

Also, a good agreement is not expected when the results are extrapolated beyond the range of the empirical data in which the formulations are based.

FIELD DATA

The data used in this work were collected at four different field sites in Portugal: Mira and Ofir beaches, on the northwest coast, Costa da Caparica (CC) beach, on the west coast, near Lisbon, and Galé beach, on the southern coast (Figure 1). During each tidal cycle, in every field site, one or more pairs of a pressure transducer (PT) and a collocated electromagnetic current meter (ECM) were placed at different points along the beach profile, to measure free-surface elevation and horizontal velocity, respectively, outside the bottom boundary layer. Table 1 offers a brief description of the offshore wave conditions and beach

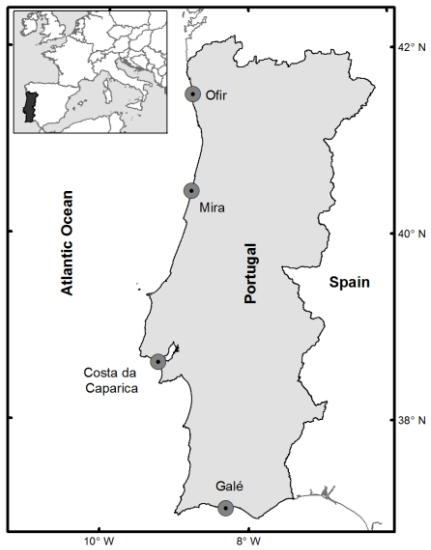

Figure 1. Location of the sites of the field campaigns along the Portuguese coast.

characteristics of each field site. The rocky bottom of Galé beach corresponds to a 50 m-wide shore platform with constant steepness, extending from the cliff foot and adjacent to the sandy beach profile. Galé 1 and 2 data sets were collected in the beginning of the seaward-end of the platform and Galé 3 and 4 near the cliff.

Figure 2 depicts the field data coverage in terms of wave height over water depth (H/h) and wavelength over water depth (L/h) and Figure 3 also shows the data coverage, but considering Iribarren (Ib) and Ursell (Ur) numbers.

Most data were collected in the inner surf zone, encompassing all types of breakers, with a greatest occurrence of spilling ($Ib \leq 0.4$) and plunging ($0.4 < Ib \leq 2.5$) breakers, for all data sets, and some collapsing ($2.5 < Ib \leq 3$) and surging breakers ($Ib > 3$), for Mira field site. The data span a wide range of wave heights and lengths and different beach slopes and types of bed are considered. Relatively to the data used by the authors of DMW01, EHR06 and RRR12 parameterizations, the data sets considered herein present greater wavelengths and larger Ursell numbers.

Table 1. Description of field data. Hs_0 = significant wave height offshore; Ts_0 = significant wave period offshore; h_{max} = maximum water depth (at high tide). The "Symbol" column presents, on the left, the symbols used to identify each data set in every plot and, on the right, the line-type used in DMW01 parameterization for each set of offshore wave conditions.

Data set	Tidal cycle	Hs_0 (m)	Ts_0 (s)	h_{max} (m)	Bed type and beach slope	Symbol
Ofir	1st	2.5	11	1.7	Sandy, 0.026	+ / -
Mira	1st	3.0	25	1.2	Sandy, 0.070	× / -.
Galé 1	1st	0.5	9	2.4	Rocky, 0.021	* / --
Galé 2	2nd	0.7	8	2.5	Rocky, 0.021	* / --
Galé 3	1st	0.5	9	1.7	Rocky, 0.021	* / --
Galé 4	2nd	0.7	8	1.9	Rocky, 0.021	* / --
Galé 5	1st	0.5	9	2.5	Sandy, 0.036	* / --
Galé 6	2nd	0.7	8	2.8	Sandy, 0.036	* / --
CC	1st-5th	1.0	7	1.5	Sandy, 0.025	∘ / ..

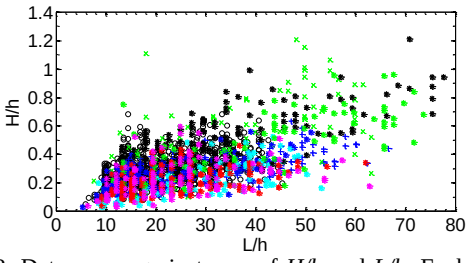

Figure 2. Data coverage in terms of H/h and L/h. Each symbol represents a wave.

METHODS

In order to evaluate which of the three chosen parameterizations performs better for the field data collected, local wave parameters were obtained from free-surface elevation time series and applied to calculate free-stream wave orbital velocity skewness and asymmetry, according to each chosen parameterization. These nonlinearity values were then compared with the values calculated directly from the free-stream wave orbital velocity measured with the collocated current meters.

The PT and ECM data corresponding to periods of emersion of the instruments were removed, implying that the analysis performed did not include any data from the swash zone. All free-surface elevation time series were then divided into 15-min intervals and filtered, so that only sea-swell waves were considered (frequency range 0.05-0.33 Hz), following the work of Ruessink *et al.* (2012). Also for the velocity time-series 15-min intervals were considered, and low- and high-frequency components ($f < 0.05$ Hz and $f > 1$ Hz) were filtered out. All gathered records of cross-shore and longshore orbital velocities were combined into time series of total sea-swell orbital velocity in the direction of wave advance, using eigenfunction analysis, for which the required nonlinearity parameters were then computed. Further, it is important to stress that for the various field sites, a different number of 15-min intervals was considered depending on the length of the time series available.

For both DMW01 and EHR06 methods a wave-by-wave analysis was necessary for calculating the Ursell number, and in the case of DMW01, also for calculating nonlinearity and asymmetry parameters. Hence, it was necessary to identify each individual wave present in the complete free-surface elevation/velocity time series. For that, a zero-crossing method was used, implying a need for defining a threshold value for the smallest height that an individual wave must possess to be considered a single wave (this threshold is defined as a certain percentage of the maximum wave height of the time series). After

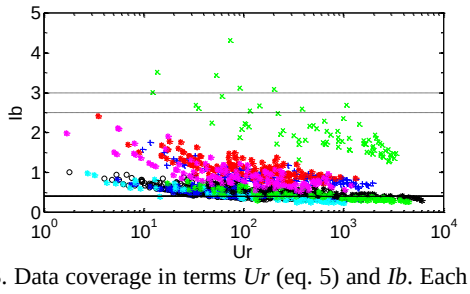

Figure 3. Data coverage in terms Ur (eq. 5) and Ib. Each symbol represents a wave. Dashed lines separate the different breaker types.

some testing, both EHR06 and DMW01 parameterizations have shown some sensitivity to the choice of such threshold and a value of 0.01 (corresponding to 1% of the maximum wave height of the time series) was chosen for both the free-surface elevation time series and the velocity time series.

Per contra, RRR12 parameterization involves instead a statistical analysis, avoiding possible problems derived from the wave-by-wave analysis, such as the mentioned sensitivity to the zero-crossing method threshold and error accumulation.

Furthermore, DMW01 parameterization depends as well on deep-water wave conditions (wave steepness) for defining the maximum and minimum peaks in the curves of nonlinearity and asymmetry. Also EHR06 parameterization depends on offshore conditions, although indirectly, through the Iribarren number. In the laboratory, these conditions are easy to define, since the input conditions for the wave maker are known. However, in the field, it becomes substantially more difficult to have good-quality wave data offshore. In the case of the considered field campaigns, these data were gathered from low-resolution wave buoy measurements, from the closest-available wave buoy for each field site. Hence, the inaccuracy of deep-water conditions used in the parameterizations must also be taken into account.

For evaluating the capability of each formulation to fit field data, two different parameters were considered. The skill coefficient, which represents, for each field data point, a scaled measure of its deviation from the parameterization, can be formulated as:

$$Skill = 1 - \sqrt{\frac{\sum_{i=1}^{n}(y_i - x_i)^2}{\sum_{i=1}^{n}(x_i)^2}} \qquad (9)$$

where x_i are the field data values, y_i the values calculated with the parameterizations and n is the number of values considered. Negative skill values can occur if $(y_i - x_i) > x_i$, corresponding to a very poor performance of the parameterization. A perfect performance will reach a skill score of 1.

The other parameter considered, the agreement index, has the advantage of depicting if the general trend of the field data follows each parameterization, instead of just evaluating the proximity between numerical and field values at each point, and will thus be of great importance for choosing the best formulation. It can be calculated as:

$$AI = 1 - \frac{\sum_{i=1}^{n}(y_i - x_i)^2}{\sum_{i=1}^{n}(|y_i - \bar{x}| + |x_i - \bar{x}|)^2} \qquad (10)$$

where $\bar{x}$ represents the mean value of the n field data values considered. This index can only have values from 0 (poor performance) to 1 (perfect performance).

PARAMETERIZATIONS AND FIELD DATA

In this section, the results obtained with the three different parameterizations are compared with the field data obtained in the various field sites.

Dibajnia *et al.* (2001) parameterization

Figure 4 shows the different curves obtained with DMW01 parameterization for each field site (characterized by different offshore wave steepness) and the distribution of field-data values.

In general, the magnitude of the values is fairly well described, which is corroborated by skill values over 0.95, for *Nlp* and 0.7, for *Asp* (see Figure 8). The cloud of points approximately follows the parameterization curve, although a shift towards higher Ursell numbers is notorious. This results in fairly good agreement indexes for some particular cases, but an average *AI* around 0.4, for *Nlp*, and lower, for *Asp*. CC and Ofir field sites present the best fits, with fairly high *AI* for *Nlp*.

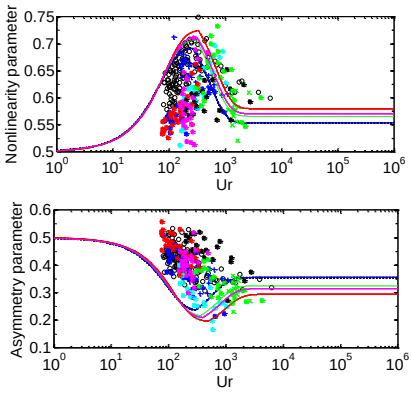

Figure 4. Dibajnia *et al*. (2001) parameterization for nonlinearity and asymmetry parameters (lines) and field data (symbols). *Ur* is defined according to (3).

This parameterization was developed based on wave flume experimental data. For this type of data, the mean period, T_z, calculated from the spectral moments m_1 and m_0, can be considered equivalent to the significant wave period, $T_{1/3}$ or T_s, as the wave spectrum is narrow banded. However, when field data are considered, the wave spectrum cannot always be considered narrow banded. Therefore, the equivalence $T_z = T_{1/3}$ does not necessarily hold, and T_z tends to be smaller than $T_{1/3}$. Hence, the Ursell numbers calculated for this parameterization for the data sets considered herein are overestimated (as a higher *T* implies a higher *Ur*), which explains the shift of field-data values to the right side of the theoretical curves of the parameterization. Figure 5 shows the results obtained with this parameterization when T_z is considered instead of T_s (calculated with the zero-crossing method), and it can be clearly seen that the shift to higher *Ur* present in Figure 4 is corrected. This is corroborated by an increase of skill, particularly for asymmetry, for which the scores rise for values above 0.9 for most data sets (not shown). The *AI* values also increase, both for the nonlinearity and the asymmetry parameters, which reach values of almost 0.9.

Elfrink *et al.* (2006) parameterization

The results for this parameterization are shown from a different perspective (Figure 6). The main aim for which it was

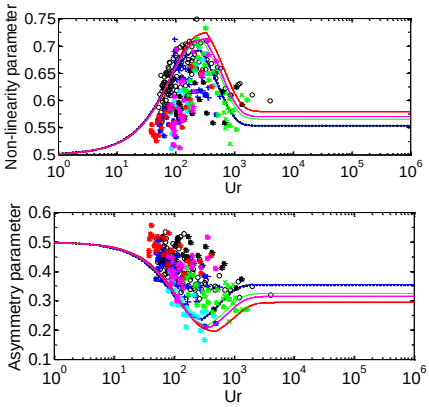

Figure 5. Dibajnia *et al*. (2001) parameterization for nonlinearity and asymmetry parameters (lines) and field data (symbols), considering T_z instead of T_s, for calculation of the Ursell number (defined according to equation 3).

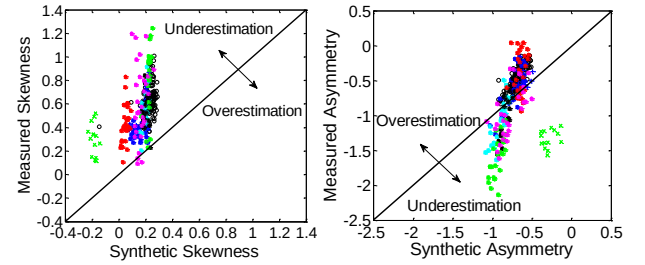

Figure 6. Measured skewness and asymmetry versus synthetic skewness and asymmetry computed following the method of Elfrink *et al*. (2006).

developed was the construction of a synthetic velocity time series from local wave parameters that was able of including different individual wave shapes. Thus, skewness (eq. 6) and asymmetry (eq. 7) were calculated both for the measured and the synthetic time series and directly compared, independently of the Ursell number, although the parameters employed for the evaluation of its performance are, for a question of consistency, the same as for the other parameterizations.

There is clearly a great scatter both for skewness and asymmetry: the field values are mostly under- and overestimated, respectively, except for the values corresponding to the second tidal cycle in Galé beach and to Mira beach, where asymmetry is mostly underestimated. Particularly for skewness, most skill scores are rather low, between less than 0.2 to less than 0.5, and the *AI* is never higher than 0.5 (see Figure 8). Also, synthetic skewness calculated for Mira data set has negative values, while measured skewness presents only positive values, and hence the performance of EHR06 parameterization is particularly poor for this field site, which results in a negative value of the skill score, significantly lower than the other values. For asymmetry, the performance of this formulation is better, although skill values can vary substantially depending on the data set.

Ruessink *et al.* (2001) parameterization

Observing Figure 7 it is clear that data still present a considerable scatter relatively to this parameterization, particularly for Mira and Galé sites. However, for the other field sites, the general trends of skewness and asymmetry dependency on the Ursell number are significantly well described, as it is depicted by the high agreement indexes, particularly for asymmetry (almost reaching 0.9), that are above the ones calculated for the other parameterizations (see Figure 8). Especially if only data from Costa da Caparica and Ofir beach sites are looked at, asymmetry skill scores calculated are high, above 0.75. Nevertheless, there is still a considerable spread for both skewness and asymmetry agreement-index values from very low values to high values, depending on the data set considered.

Still, it should be noted that, except for the data corresponding to the second tidal cycle in Galé beach, the scatter observed both for skewness and asymmetry is very similar to the scatter obtained by Ruessink *et al.* (2012) for their own data. This parameterization performs notoriously worst for Mira and Galé field sites.

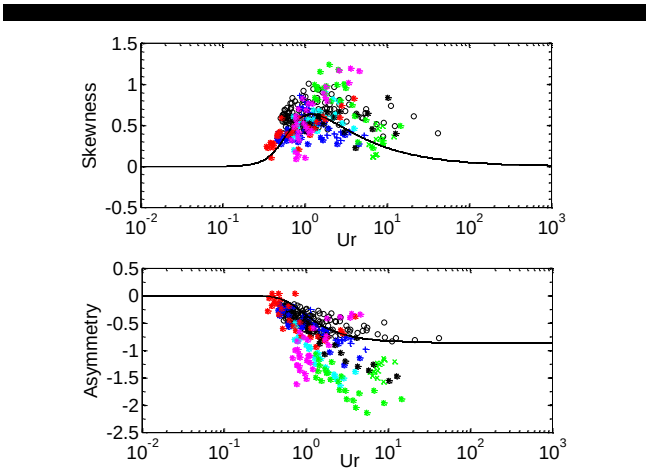

Figure 7. Ruessink *et al.* (2012) parameterization for skewness and asymmetry (dark lines) and field data (symbols). *Ur* is defined according to (8).

DISCUSSION AND CONCLUSIONS

EHR06 parameterization generally presents the worst performance for the field data considered in this work. Not having been directly developed for parameterizing skewness and asymmetry, but instead for creating synthetic velocity time series, it is clear that wave velocity nonlinearities are not easily well reproduced with this formula. Also, the offshore wave period was found to have a significant influence on synthetic skewness and asymmetry and this is a variable for which it is hard to get high-quality data. Further, this parameterization fails completely to predict skewness for Mira field site, when local *H/h* and *L/h* are substantially outside the range of values used to develop the formulation (higher and longer waves) and the Iribarren number is higher (steeper beach slope), corresponding to plunging, collapsing and surging breaker types. Also, a long set of equations is needed to define the shape of each individual wave, which makes the application of this formulation rather cumbersome. It shall be of greater interest in the case of the specific shape of each wave being important, rather than when statistical parameters (such as skewness and asymmetry) are calculated for a set of waves, as it is done herein.

DMW01 parameterization describes quite well *Nlp* and *Asp* magnitudes. Skill scores for this parameterization are very similar for all field campaigns, unlike what is found for the other formulations, particularly RRR12, for which the measurements of

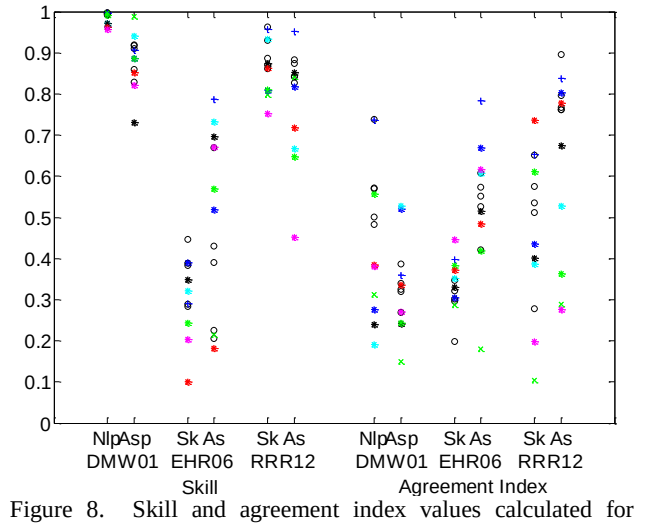

Figure 8. Skill and agreement index values calculated for skewness and asymmetry for each of the three parameterizations considered. Skewness skill value for EHR06, for Mira data set, is not presented in the plot for convenience (≈ -0.5).

Galé and Mira beaches deviate more significantly from the theoretical curves than the rest. The shift of data points to higher Ursell numbers than predicted by the theoretical curves can be attenuated by calculating *Ur* from T_z (like it is done for RRR12 formulation) instead of from T_s. The fact that this parameterization, even having been developed based on wave flume experimental data, is able of reproducing well all the field data sets (particularly if T_z is considered), may point out the importance of considering offshore wave conditions for encompassing a greater range of wave conditions and beaches.

Regarding RRR12 parameterization, Ofir and Costa da Caparica data sets seem to fit really well to the theoretical curves and even the variation of skewness and asymmetry in function of the Ur number is well represented, not only their magnitudes. This is corroborated by the higher agreement index values calculated for almost all data sets and constitutes the greatest achievement of this formulation when compared to the others (if DMW01 is not applied considering T_z).

However, for Galé and Mira beaches, a greater scatter can be observed for skewness and a strong underestimation of asymmetry is also clear. This possibly denounces an important handicap of parameterizations based on few and local-only wave parameters: these can perform very well when applied to beaches very similar to the ones used for developing the formulations, but fail to predict skewness and asymmetry for field sites with different characteristics. This explains why Ofir and Costa da Caparica field sites, being the only sandy beaches considered with slopes inferior to 1/30, fit nicely to that parameterization, which was developed based on data collected in such type of beaches. Nevertheless, this formulation seems to be more robust for inner surf zone and/or strong plunging breakers.

The data sets deviating the most from RRR12 parameterization seem to show one of two or both characteristics: either these measurements present higher values of *L/h* and *H/h* than the rest, or higher *Ib* values. The Mira data set, which never really fits any parameterization, possesses both characteristics, with a particularly high ratio of *H* and *h* and the highest *Ib* measured. The first may be due to bed erosion/accretion along the tidal cycle that could result in a higher water depth during high tide than the measured during the previous and the following low tides, which would have reduced *H/h* during that period to more common values. However, this cannot be confirmed with the data available. The second is associated with both a steeper beach slope and longer wave periods ($Ib \propto \sqrt{T^2}$). Also, the combined effect of both larger wave heights and shorter wave periods leads to large *Ib* values, associated with very asymmetric waves, as it can be seen for the second-tidal-cycle data of Galé beach, which deviate further from the parameterization than the rest.

Galé data sets do not have a very high *Ib*, but have instead significantly-large wave lengths for the small wave heights and water depths measured. Since this particular beach has a complex morphology with shore platforms, the cliff, a mixture of sandy and rocky beds, inducing wave refraction and reflection along the shoaling and breaking zones, it is not possible with the data available to explain the exact origin of the measured wave conditions, but only to analyze their characteristics.

Overall, it is clear that, although RRR12 parameterization can simulate very accurately the dependence of skewness and asymmetry on the Ursell number for a specific set of wave conditions and low-sloping sandy beaches, it cannot be used to parameterize nonlinearities from local wave parameters for other types of beaches.

The characteristics of the data sets that deviate the most from the theoretical curves and the fact that DMW01 parameterization is fairly capable of reproducing the magnitude of nonlinearity and asymmetry parameters (even though it was developed from laboratory data sets and is unable of reproducing so well the general trend of the data), lead to the conclusion that both beach slope and offshore wave conditions should be incorporated in any parameterization aiming to define skewness and asymmetry in the nearshore for a wide range of beach types and wave conditions.

Further developments of this work should include the search of such parameterization, starting by the quantification of the relative importance of the different offshore wave parameters and the beach slope on the variation of skewness and asymmetry in the nearshore.

ACKNOWLEDGEMENTS

This work was supported by the FCT (Portuguese Science and Technology Foundation), through the PhD grant SFRH/BD/80644/2011, by the FCT and European Union (COMPETE, QREN, FEDER) in the scope of the research projects BRISA (PTDC/ECM/67411/2006) and EROS (PTDC/CTE-GIX/111230/2009) and by INSU/LEFE in the framework of BARCAN project.

The authors would also like to acknowledge the collaboration of the numerous people involved in the field campaigns, in particular Francisco Sancho, Joaquim Barbosa, Paulo Batista, Selma Gabriel and Daniela Santos.

LITERATURE CITED

Abreu, T., Silva, P.A., Sancho, F. and Temperville, A., 2010. Analytical approximate wave form for asymmetric waves. Coastal Engineering, 57, 656-667.

Abreu, T., Michallet, H., Silva, P.A., Sancho, F., van der A, D.A. and Ruessink, B.G., 2013. Bed shear stress under skewed and asymmetric oscillatory flows. Coastal Engineering, 73, 1-10.

Dibajnia, M., Moriya, T. and Watanabe, A., 2001. A representative wave model for estimation of nearhore local transport rate. Coastal Engineering Journal, 43(1), 1-38.

Drake, T.G. and Calantoni, J., 2001. Discrete particle model for sheet low sediment transport in the nearshore. Journal of Geophysical Research, 106, 19,859 - 819,868.

Elfrink, B., Hanes, D.M. and Ruessink, B.G., 2006. Parameterization and simulation of near bed orbital velocities under irregular waves in shallow water. Coastal Engineering, 53(11), 915-927.

Isobe, M. and Horikawa, K., 1982. Study on water particle velocities of shoaling and breaking waves. Coastal Engineering Japan, 25, 109-123.

Malarkey, J. and Davies, A.G., 2012. Free-stream velocity descriptions under waves with skewness and asymmetry. Coastal Engineering, 68, 78-95.

Ruessink, B. G., van der Berg, T.J.J. and van Rijn, L.C., 2009. Modeling sediment transport beneath skewed asymmetric waves above a plane bed. Journal of Geophysical Research, 114, C11021.

Ruessink, B.G., Ramaekers, G. and van Rijn, L.C., 2012. On the parameterization of the free-stream non-linear wave orbital motion in nearshore morphodynamic models. Coastal Engineering, 65, 56-63.

3.4.2 The RRR12 parameterization

Ruessink *et al.* (2012) recently proposed a parameterization (RRR12) that constitutes an extension of previous work done by Doering & Bowen (1995) and Kuriyama (2009) and defines, for irregular waves, the dependency of velocity nonlinearity on local wave height and period and water depth (the Ursell number, eq. 3.25). This parameterization has been shown to perform better than other existing parameterizations within a certain range of wave conditions and beach slopes (discussed in the previous subsection, Rocha *et al.*, 2013b). However, since it is based only on the Ur number, it still presents some limitations when the wave conditions or beach slopes are beyond range of those in which it was based. This section is hence dedicated to the improving of this parameterization by the inclusion of non-local wave parameters.

In RRR12 parameteriztion, B (eq. 3.24) and ψ ($\psi = \tan^{-1}\left(\frac{As_u}{Sk_u}\right)$) nonlinearity parameters are parameterized as

$$B = p_1 + \frac{p_2 - p_1}{1 + \exp(\frac{p_3 - \log(Ur)}{p_4})} \tag{3.27}$$

and

$$\psi = -90^\circ + 90^\circ \tanh(p_5/Ur^{p_6}), \tag{3.28}$$

with $p_1 = 0$, $p_2 = 0.857 \pm 0.016$, $p_3 = -0.417 \pm 0.025$, $p_4 = 0.297 \pm 0.021$, $p_5 = 0.815 \pm 0.055$ and $p_6 = 0.672 \pm 0.073$, where the range represented by the $\pm$ values is the 95% confidence interval. The parameterizations of Sk_u and As_u can thus be deduced,

$$Sk_u = B\cos(\psi) \tag{3.29}$$

and

$$As_u = B\sin(\psi)\,. \tag{3.30}$$

Fig. 3.36 shows the parameterization curves of Sk_u and As_u, as a function of Ur and the data points in which the RRR12 parameterization is based.

In order to compare the numerical results with the parameterization, the velocity nonlinearities must be calculated. As it was shown before, SERR1D model represents well the free-surface elevation evolution and the wave nonlinearities. However, since it calculates the velocity integrated over the entire water column, it overestimates the experimental velocity. Although for the velocity asymmetry the model still provides a correct estimation, it overestimates velocity skewness along the beach profile (in up to 22%, for A3, see Fig. A.1). Therefore, a direct comparison of the SERR1D results with RRR12 parameterization would include a bias due to this limitation of the

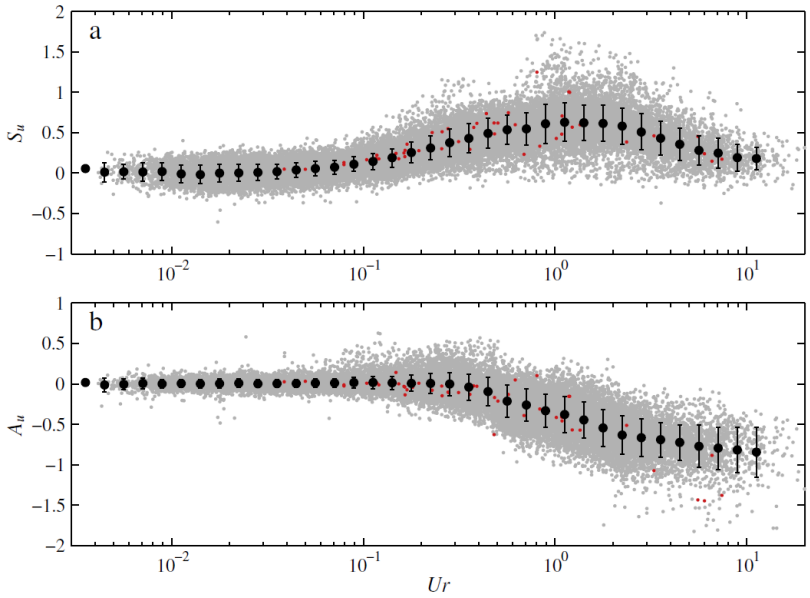

Figure 3.36: (a) Near-bed velocity skewness (here Su), and (b) asymmetry (here Au), as a function of the Ursell number Ur. The gray dots are the 33.962 individual estimates, the filled circles are class-mean values based on binning the individual estimates according to $\log(Ur) \pm 0.05$. The vertical lines represent $\pm$ one standard deviation in each bin. The 48 red dots are the data of Doering & Bowen (1995) (taken from Ruessink *et al.* (2012)).

numerical model. To overcome this limitation, u_η is used instead of the velocity time series provided by the model. u_η is calculated as previously described in subsection 3.2.5, from the computed free-surface elevation time series, for a depth of 0.02 cm above the bottom and it is shown (see the dots in Figs. 3.23 and A.1) to provide an accurate estimation of the velocity nonlinearities until their maxima (near the beginning of the inner-surf zone).

3.4.3 Comparison with GLOBEX and vN2003 experimental and numerical data

Initially, the RRR12 parameterization is applied to GLOBEX A1, A2 and A3 (for which experimental velocity measurements are also available) and vN2003 C-1 and C-3 wave conditions and then to the results of SERR1D simulations, in order to evaluate the possibility of velocity skewness and asymmetry being simply described as a function of Ur. The results are presented in terms of Sk_u, As_u, B and ψ, in function of Ur.

Fig. 3.37 shows the comparison between the numerical and experimental results obtained for the three irregular-wave conditions of the GLOBEX experiments and the RRR12 parameterization. It is for A1 and A2 experimental results that the RRR12 parameterization provides the best estimation of nonlinearity. For A3 (more narrow-banded and smaller wave steepness than A1 and A2), the deflection point of the

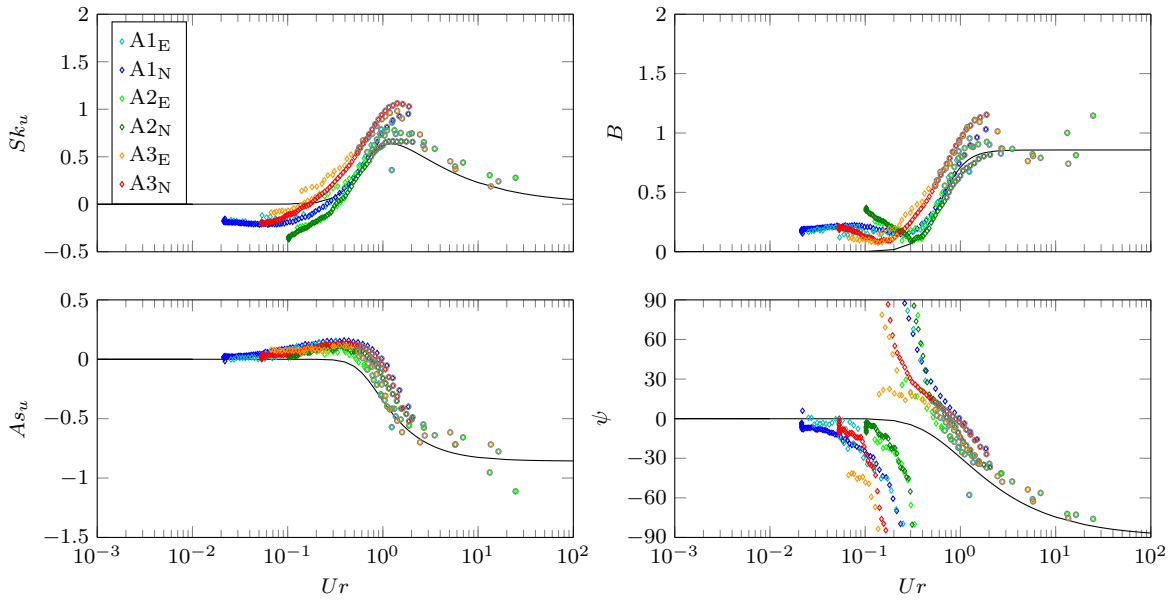

Figure 3.37: Velocity skewness, velocity asymmetry, B and ψ in function of Ur, for experimental/ numerical (u_η from η_N) velocity time series A1 (cyan/blue), A2 (green/dark green) and A3 (orange/red). The black curves correspond to the RRR12 parameterization. Grey circles mark the data points corresponding to positions after the breakpoint.

values of parameter B is observed for lower Ur values than those proposed by the parameterization, and skewness is underestimated, particularly after the breakpoint (grey circles of Fig. 3.37). Very small values of Sk_u imply unrealistic values of ψ and thus the data points deviate from the parameterization of ψ in the shoaling zone (presenting an asymptotic behaviour before the nonlinearity starts increasing).

Fig. 3.38 is similar to the previous figure, but since for vN2003 experiments very few measurements of velocity are available, the experimental velocity is actually the u_η velocity computed from the experimental free-surface elevation measurements, in contrast to the numerical velocity, which is the velocity u_η obtained from the numerical free-surface elevation data. As for the GLOBEX case, the parameterization better estimates the nonlinearities for the wave conditions with characteristics within the main range of Ruessink *et al.* (2012) data, C-3. For C-1, which has a much lower wave steepness than the main range of simulations presented herein (recall Fig. 3.30), RRR12 parameterization clearly underestimates the maximum Sk_u by about 40% and the maximum B by around 30%.

3.4.4 Comparison with a varied set of wave conditions

In the previous section, the SERR1D model was used to simulate wave conditions with varying offshore wave height, period and spectral bandwidth and different beach slopes. The results obtained are subsequently compared to the nonlinearity values predicted

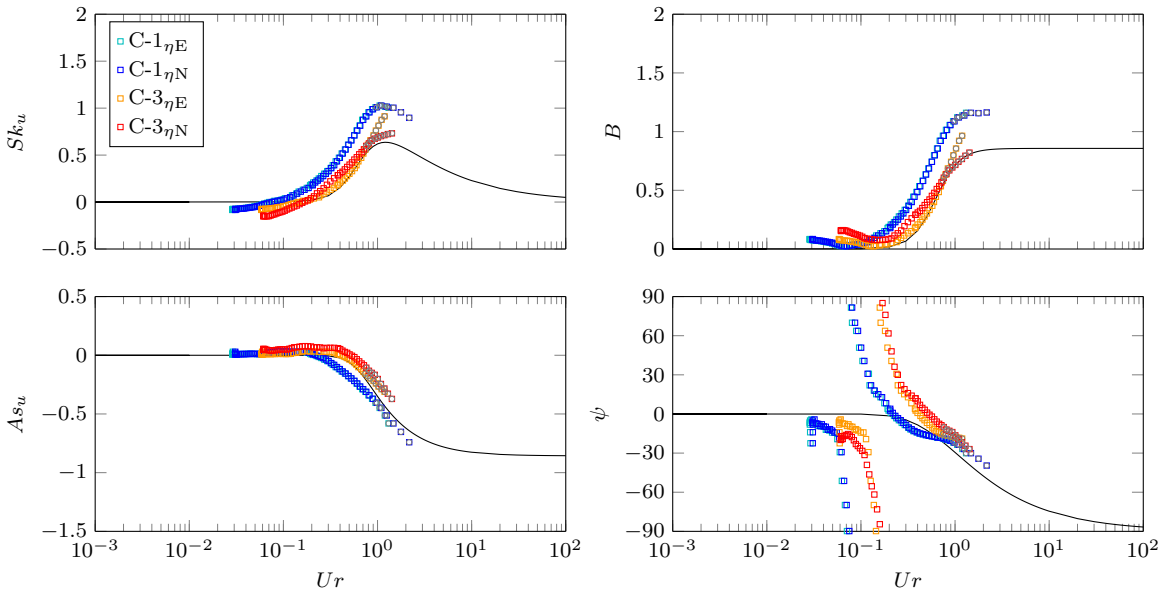

Figure 3.38: Velocity skewness, velocity asymmetry, B and ψ in function of Ur, for experimental (u_η from η_E)/numerical (u_η from η_N) velocity time series C-1 (cyan/blue) and C-3 (orange/red). The black curves correspond to the RRR12 parameterization. Grey circles mark the data points corresponding to positions after the breakpoint.

by the RRR12 parameterization to investigate the capacity of the parameterization for predicting the nonlinearity of wave conditions with different characteristics. This comparison is depicted in Figs. 3.39, 3.40, 3.41 and 3.42, for varying offshore H_{m0}, T_p and spectral bandwidth and beach slope, respectively.

The different wave and beach characteristics result in a deviation from the curves of the RRR12 parameterization and an over- or underestimation of the nonlinearities, which can be summed up in the following points:

- the underestimation of Sk_u and B increases with decreasing offshore wave height (Fig. 3.39), increasing offshore wave period (Fig. 3.40) and decreasing beach slope (Fig. 3.42), especially after breaking;
- for very-long-period waves As_u is underestimated in the shoaling zone (Fig. 3.40);
- for very steep slopes ($\tan(\beta)^{-1} = 1/20$, Fig. 3.42), phasing is underestimated after breaking (which is in accordance with the limit of application of the parameterization prescribed by Ruessink *et al.* (2012): it should not be applied when $\tan(\beta)^{-1} = 1/20$);
- narrowing the bandwidth increases the underestimation of Sk_u and B along the entire profile (even in the end of the shoaling);
- Sk_u values at the beginning of the shoaling ($Ur < 0.1$) are overestimated for all

wave conditions and beach slopes, while corresponding B values are underestimated;

- Sk_u is more influenced by the characteristics of the wave conditions and the beach slope than As_u.

The small overestimation of As_u and of ψ present for all conditions is inherent to the computation of u_η from the numerical η, which has a small cross-shore shift of 3-4 m between numerical results and experimental data. However, since the major changes of the nonlinearity are driven by Sk_u changes, this shift is of minor importance for the following analysis.

Most wave conditions simulated have Sk_u and As_u values that fall within the cloud of points presented by Ruessink *et al.* (2012) (Fig. 3.36). However, that cloud of points has a considerable scatter around the parameterization trend and thus, for one same Ur value, the Sk_u and As_u can vary between 0 and 1.5. Hence, for some of the wave conditions simulated, the Sk_u overestimation may reach more than 100%. Therefore, the hypothesis that Ur is not the unique parameter that defines the nonlinearity of the waves along the entire profile, already proposed by other researchers (see subsection 3.3.5), seems very likely. This is particularly evident for the greatest values of nonlinearity, corresponding to cross-shore positions near the end of shoaling and throughout the surf zone, meaning that the greater misestimation of the velocity nonlinearities is precisely focused on the zones of the profile where they contribute the most for sediment

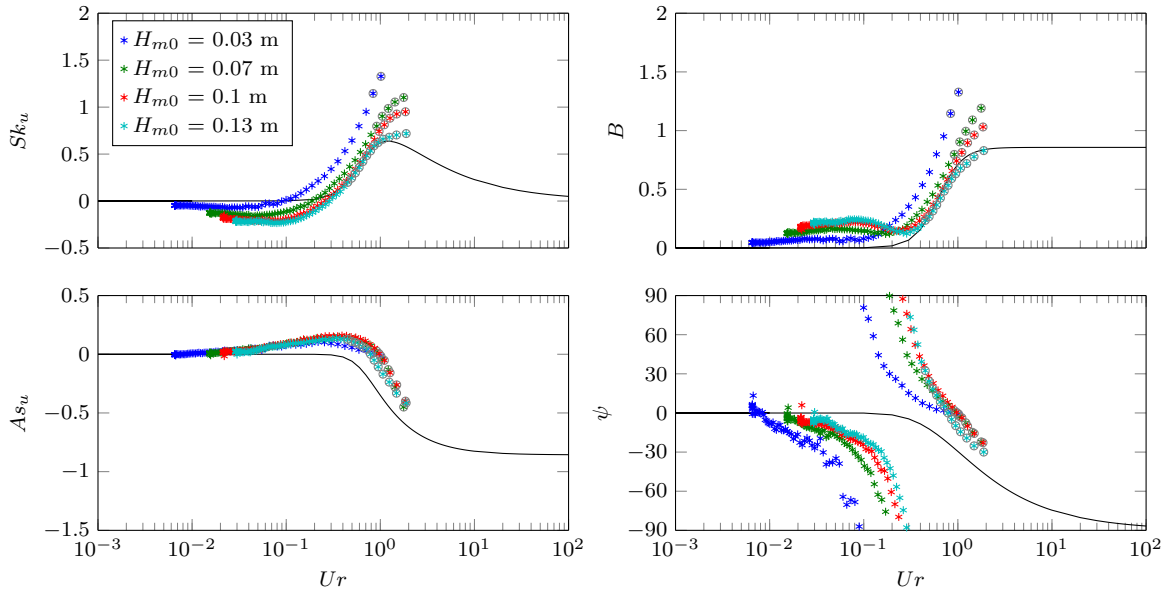

Figure 3.39: Velocity skewness, velocity asymmetry, B and ψ in function of Ur, for different-H_{m0} runs. The black curves correspond to the RRR12 parameterization. Grey circles mark the data points corresponding to cross-shore positions after the breakpoint.

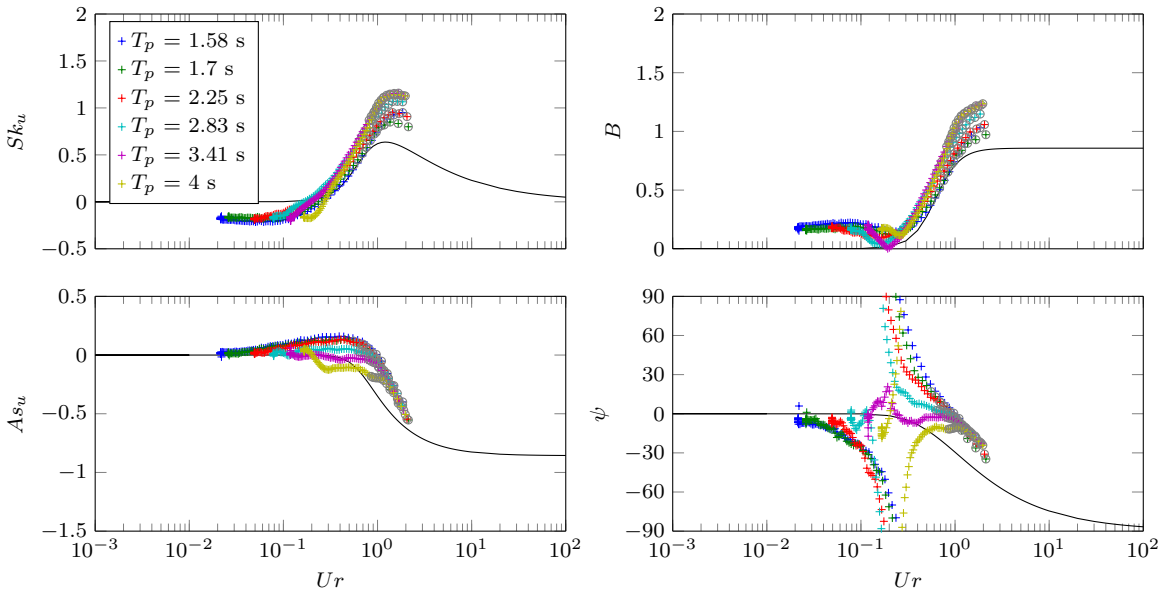

Figure 3.40: Velocity skewness, velocity asymmetry, B and ψ in function of Ur, for different-T_p runs. The black curves correspond to the RRR12 parameterization. Grey circles mark the data points corresponding to cross-shore positions after the breakpoint.

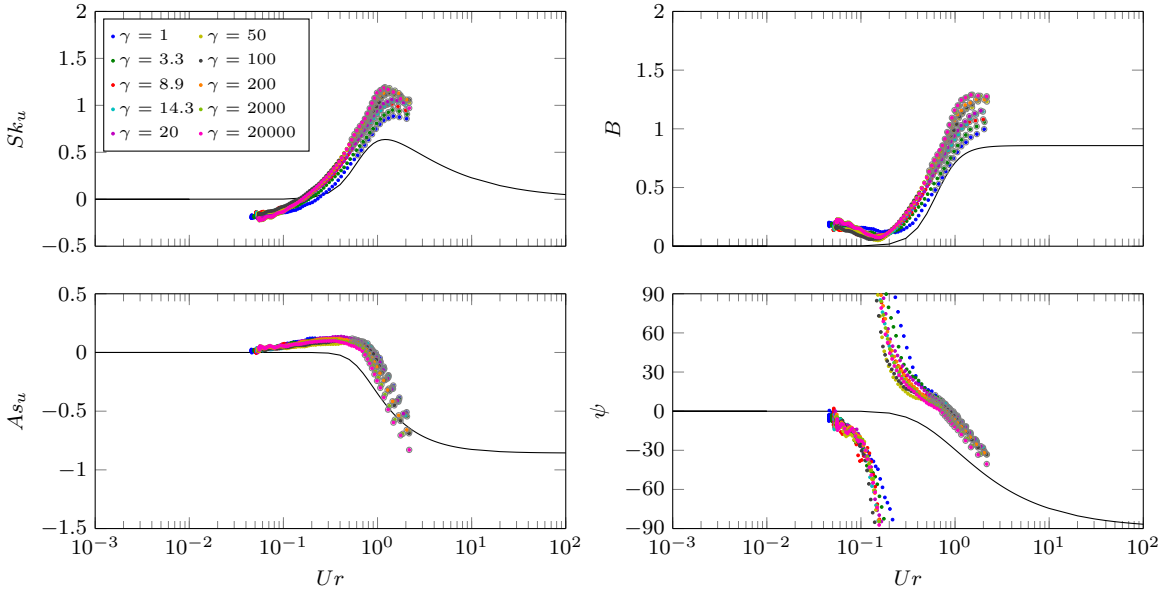

Figure 3.41: Velocity skewness, velocity asymmetry, B and ψ in function of the Ur, for different-γ runs. The black curves correspond to the RRR12 parameterization. Grey circles mark the data points corresponding to cross-shore positions after the breakpoint.

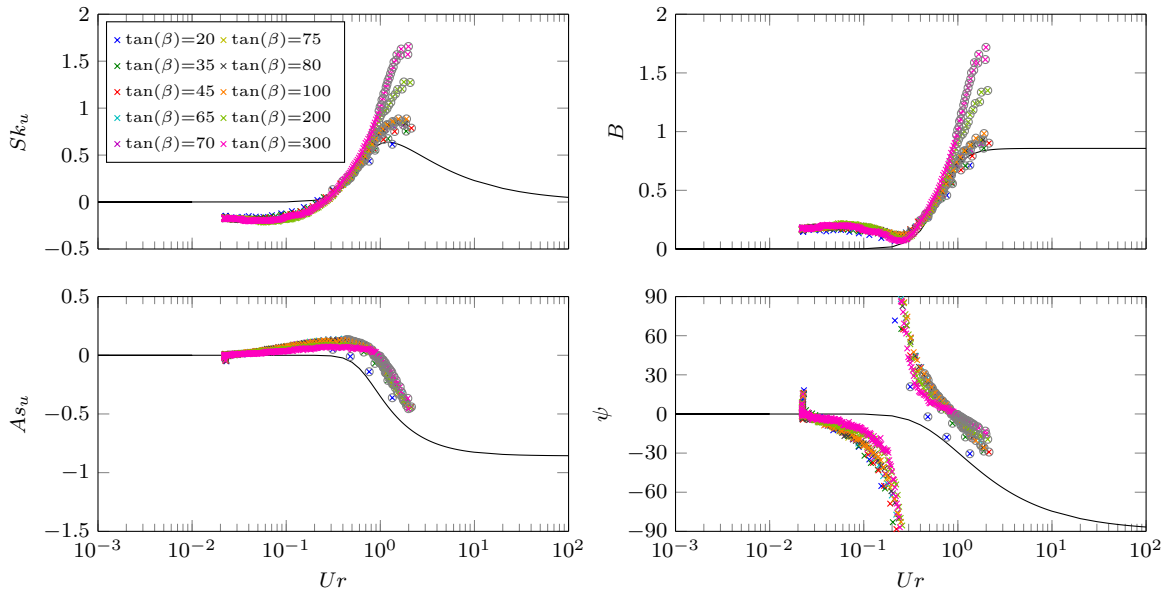

Figure 3.42: Velocity skewness, velocity asymmetry, B and ψ in function of the Ur, for different-tan(β) runs. The black curves correspond to the RRR12 parameterization. Grey circles mark the data points corresponding to cross-shore positions after the breakpoint.

transport.

Since the RRR12 parameterization has been recently used by several researchers to calculate the sediment transport related to velocity skewness and asymmetry (*e.g.* Aagaard & Jensen 2013; Dubarbier *et al.* 2015), it is of interest to seek its improvement to ameliorate the estimations of sediment transport. Abreu *et al.* (2014) has shown that varying the values of the p parameters in the RRR12 formulation within the error intervals defined by Ruessink *et al.* (2012) (which somehow take into account the dispersion of the experimental values) did not change significantly the predicted morphodynamics of the littoral bar in the LIP experiments (Arcilla *et al.*, 1994). Hence, the inclusion of other non-local parameters may be a good contribution to improve the RRR12 parameterization, so that it can adjust to more varied wave conditions and beach slopes. The common characteristics of the wave conditions with nonlinearity values that tend to deviate more from the predicted curves can help in underpinning the parameters necessary for this adjustment.

3.4.5 Dependence of nonlinearities on the new parameter NP_0 and on γ

Two characteristics of the wave conditions for which Sk_u and B values were shown to deviate from the main cloud of data points were smaller wave heights and longer periods. For the same wave period, if the offshore wave height is decreased (Fig. 3.39),

offshore wave steepness (H_0/L_0) is also decreased. If instead it is the wave height that is kept constant and the wave period increased (Fig. 3.40), wave steepness also decreases. This suggests that small wave steepness is the characteristic promoting the deviation of Sk_u and B values of wave conditions with small wave heights and long wave periods from the RRR12 parameterization. Besides small offshore wave steepness, also very steep or very gentle beach slopes tend to deviate Sk_u and B values from the RRR12 parameterization curves.

The Iribarren number (eq. 3.26) includes both the contribution of the beach slope and the square-root of wave steepness. However, since the wave steepness is included through its square-root, its effect on the variation of the nonlinearity is minored. Consequently, it is also considered separately from the Ib parameter. The dependence of the $Sk_{\eta,max}$ on both parameters (offshore wave steepness and Iribarren) is depicted in the first and second plots of Fig. 3.43, for GLOBEX (A1, A2 and A3) and vN2003 (C-1, C-2, C-3, D-1, D-2, D-3) experimental data.

Neither the offshore wave steepness nor the Iribarren number are shown to be able of fully describing the variation of nonlinearity as a function of the wave condition considered. Therefore, a new combined parameter, $NP_0 = Ib_0(H_0/L_0)^2$ is defined (third plot of Fig. 3.43). This parameter includes the influence of the beach slope, through the Ib_0 parameter, and the influence of offshore wave steepness, but magnified, through $(H_0/L_0)^2$. The third plot of Fig. 3.43 depicts the dependence of $Sk_{\eta,max}$ on NP_0, which indicates a marked decrease from higher values of nonlinearity, for lower values of NP_0, to lower values of nonlinearity, for higher values of NP_0. The same dependence of $Sk_{\eta,max}$ on NP_0 is observed for the numerical data, presented in Fig. 3.44.

Departing from the power dependence of $Sk_{\eta,max}$ on NP_0, the dependence on this parameter on other measures of nonlinearity ($Sk_{u,max}$, B_{max} and the value of ψ at

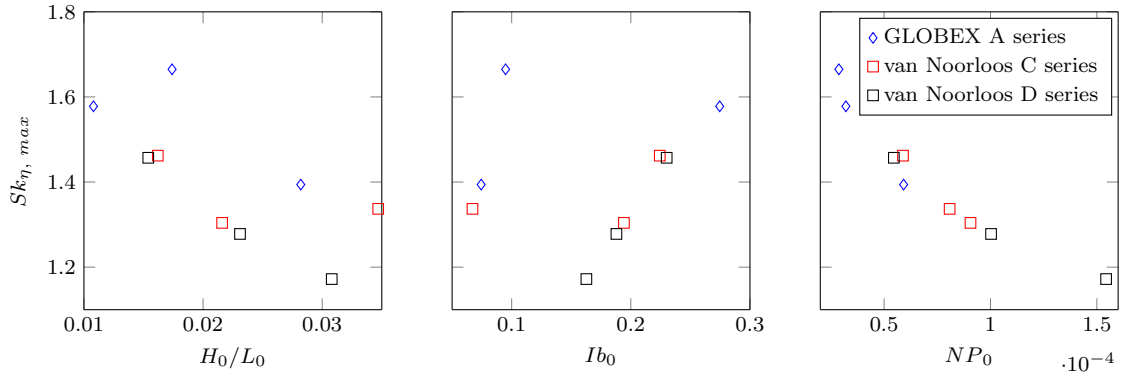

Figure 3.43: Dependency of $Sk_{\eta,max}$ on H_0/L_0, Ib_0 and NP_0, for experimental data. Note: for this plot, H_0 is the theoretical H_s of the experimental wave condition considered and L_0 is obtained with the dispersion relation from the theoretical T_p.

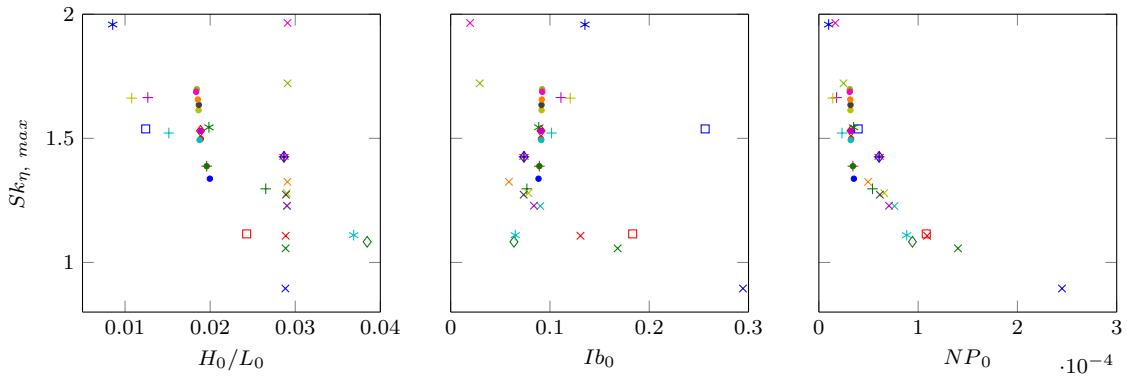

Figure 3.44: Dependency of $Sk_{\eta,max}$ on H_0/L_0, Ib_0 and NP_0. Same colour and symbol code as Fig.3.30 (diamonds: GLOBEX wave conditions; square: vN2003 wave conditions; asterisks: varying H_{m0} runs; pluses: varying T_p runs; dots: varying γ runs; crosses: varying tan(β) runs).

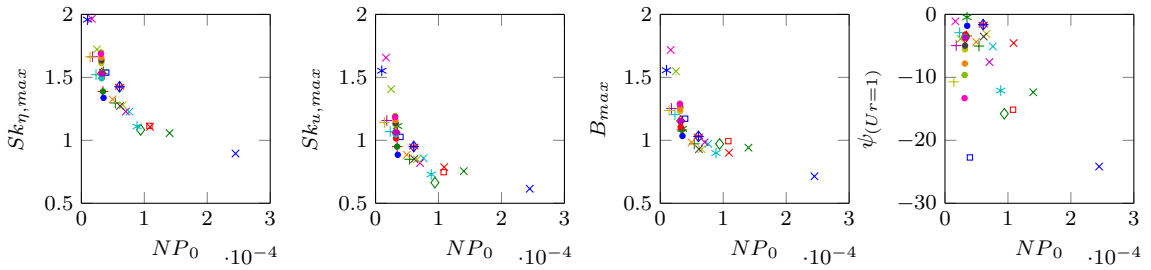

Figure 3.45: Dependence of $Sk_{\eta,max}$, $Sk_{u,max}$, B_{max} and $\psi_{(Ur=1)}$ on NP_0. Same colour and symbol code as Fig. 3.30 (diamonds: GLOBEX wave conditions; squares: vN2003 wave conditions; asterisks: varying H_{m0} runs; pluses: varying T_p runs; dots: varying γ runs; crosses: varying tan(β) runs).

$Ur = 1$) is also evaluated and is shown in Fig. 3.45.

Less important, but also evident in Figs. 3.44 and 3.45, is the dependence on the offshore spectral bandwidth (γ), which is illustrated in those figures by the almost-vertical trend of the data points represented by dots. The influence of γ induces a variation of nonlinearity that is smaller than that associated with NP_0, but independent of wave steepness and beach slope (and thus of NP_0 as well).

3.4.6 Improved parameterization (mRRR12)

The main aim of finding a dependence of nonlinearity on parameters other than the Ursell number, is to reduce the dispersion of RRR12 parameterization and thus allow a better representation of velocity nonlinearities for distinct wave conditions, in different beaches. Therefore, the relationship between the nonlinear parameters and NP_0 must be included in the parameterization.

The non-dimensional parameters p_1-p_6 (see eqs. 3.27 and 3.28) can be used to change the shape of the RRR12 parameterization curves. In particular, p_2 is responsible for the definition of the B_{max} value and p_5 determines the value of ψ at Ur=1. Fig. 3.45 shows

that a relationship between B_{max} and NP_0 can be retrieved. Besides this relationship, if only the changing-γ runs are considered, a different power relationship can be found between B_{max} and γ. B_{max} (and p_2) can, thus, be defined in function of NP_0 and γ according to

$$p_2 = B_{max}(NP_0, \gamma) = q_1 \cdot {NP_0}^{q_2} + q_3 \cdot \gamma^{q_4} + q_5, \tag{3.31}$$

with $q_1 = 0.160 \pm 0.062$, $q_2 = -0.190 \pm 0.038$, $q_3 = -0.333 \pm 0.118$, $q_4 = -0.218 \pm 0.183$ and $q_5 = 0.186 \pm 0.127$, where the range represented by the $\pm$ values is the 95% confidence interval. The first part of eq. 3.31, $q_1 NP_0^{q_2}$, represents the dependence of p_2 on NP_0. The second part, $q_3\gamma^{q_4} + q_5$, represents the dependence on γ. The value of q_5 is defined to include the best adjustment to the trend of the first part of eq. 3.31. The p_5 term, linked to $\psi_{(Ur=1)}$ can analogously be defined in function of NP_0 and γ, as

$$p_5 = \text{arctanh}\left[\frac{\psi(NP_0) + 90}{90}\right] = \text{arctanh}\left[\frac{(q_6 \cdot {NP_0}^{q_7} + q_8 \cdot \gamma^{q_9}) + 90}{90}\right], \tag{3.32}$$

with $q_6 = -2.701 \times 10^5 \pm 8.991^5$, $q_7 = 1.121 \pm 0.062$, $q_8 = -7.001 \pm 13.389$ and $q_9 = 0.098 \pm 0.119$. The coefficients q_1-q_9 were obtained fitting the data with a robust least squares power fit. The fits were obtained with an R^2 of (i) 0.898, for $B_{max}(NP_0)$, (ii) 0.924, for $B_{max}(\gamma)$, (ii) 0.666, for $\psi_{(Ur=1)}(NP_0)$ and (iv) 0.964, for $\psi_{(Ur=1)}(\gamma)$.

Fig. 3.46 shows an example of the application of the modified parameterization to the GLOBEX wave conditions. When the dependence of p_2 and p_5 terms on NP_0 and γ is included in the parameterization, it can adapt to the nonlinearity evolution of each wave condition. Figs. 3.47 and 3.48 summarize the results of the application of the mRRR12 parameterization.

In Fig. 3.47, the results obtained with the mRRR12 (coloured markers in Fig. 3.47) for the nonlinearities are compared with the results obtained using RRR12 parameterization (grey markers in Fig. 3.47) and the root-mean-square errors ($RMSE$, calculated between the data and the parameterization curves) are shown (the values inside the parentheses correspond to the calculations made considering only data points for which $Sk_u > 0.3$). Fig. 3.48 shows the improvement of the $RMSE$ from the RRR12 to the mRRR12 parameterization, for each of the wave conditions, considering, once again, either all data points (darker markers) or only data points for which $Sk_u > 0.3$ (lighter markers). This helps in evaluating for which wave conditions and nonlinearity parameters the improvement is more significant.

The results of the application of the mRRR12 parameterization can be summed up:

- The underestimation of Sk_u is reduced (in terms of $RMSE$) by 26% (or 64% for data with $Sk_u > 0.3$);

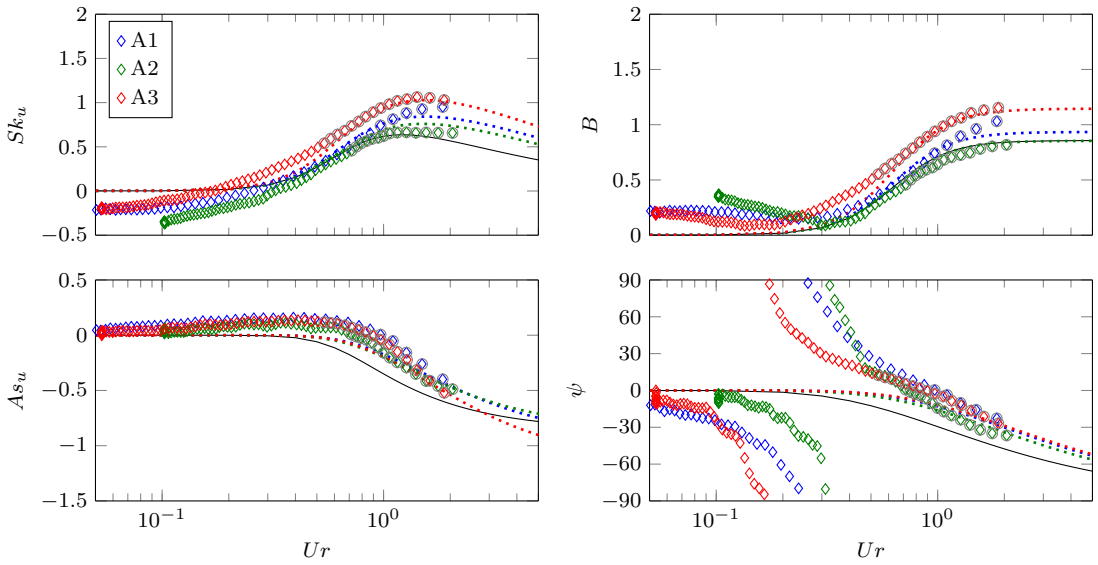

Figure 3.46: Velocity skewness, velocity asymmetry, B and ψ in function of Ur, for GLOBEX runs A1, A2 and A3. The black curves correspond to the RRR12 parameterization. The dotted coloured curves correspond to the mRRR12 parameterization. Grey circles mark the data points corresponding to positions after the breakpoint.

- The underestimation of B is reduced (in terms of $RMSE$) by 29% (or 48% for data with $Sk_u > 0.3$);
- The overestimation of As_u is reduced (in terms of $RMSE$) by 27% (or 53% for data with $Sk_u > 0.3$);
- The overestimation of ψ is reduced (in terms of $RMSE$) by 7% (or 51% for data with $Sk_u > 0.3$);
- The improvement of Sk and As is generally greater for wave conditions with longer offshore peak period or smaller offshore wave height (smaller wave steepness), more narrow-banded spectra and very gentle slopes;
- For the four nonlinearity parameters, the improvement is greater for greater values of nonlinearity.

The ψ values of the data have a greater scatter, and thus the fit is poorer, which results in a smaller improvement than for the other parameters. However, it was shown that Sk and B are the most affected by the different characteristics of the wave conditions and for these parameters the improvement is of almost 30% (and of 64%, for Sk_u and 48%, for B, when Sk_u¿0.3). This $RMSE$ improvement is calculated taking into account the data points along the entire beach profile and therefore results from an averaging of the improvement achieved for each cross-shore position. As it can be observed in Fig. 3.47, in the beginning of the shoaling zone (lower nonlinearity

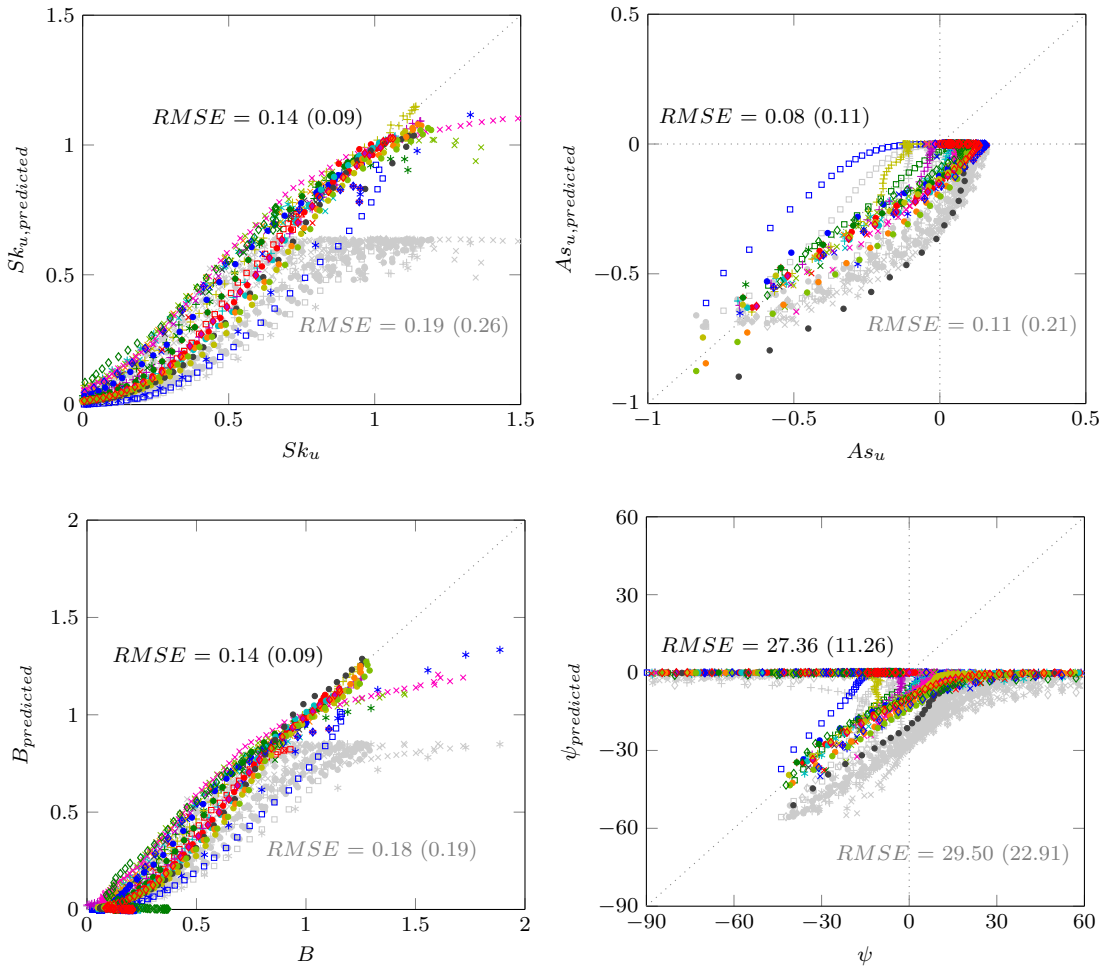

Figure 3.47: Comparison between predicted and numerical values of nonlinearity. Prediction with RRR12 original parameterization: grey markers; prediction with mRRR12 parameterization: coloured markers. Same colour and symbol code as Fig. 3.30 (diamonds: GLOBEX wave conditions; squares: vN2003 wave conditions; asterisks: varying H_{m0} runs; pluses: varying T_p runs; dots: varying γ runs; crosses: varying $\tan(\beta)$ runs). The $RMSE$ values inside the parentheses correspond to the calculations made considering only data points for which $Sk_u > 0.3$.

values) the modified parameterization already performs better than the original RRR12 parameterization, but it is near the breakpoint (greatest values of nonlinearity) that it results in the best improvement of the nonlinearity estimation. This is confirmed by the greater reduction of the $RMSE$ achieved when only data points with Sk_u values higher than 0.3 are considered. The 0.3 threshold was roughly chosen, as an example, to disconsider values which are clearly in the beginning of the shoaling zone. The greater the value chosen for this threshold, the greater the improvement obtained with the mRRR12 parameterization is expected to be. This is particularly important, since the highest values of velocity nonlinearities, corresponding to velocity nonlinearities near the breakpoint and in the surf zone, are expected to have a larger influence on sediment transport than smaller values of velocity nonlinearities, *i.e.*, velocity nonlinearities in

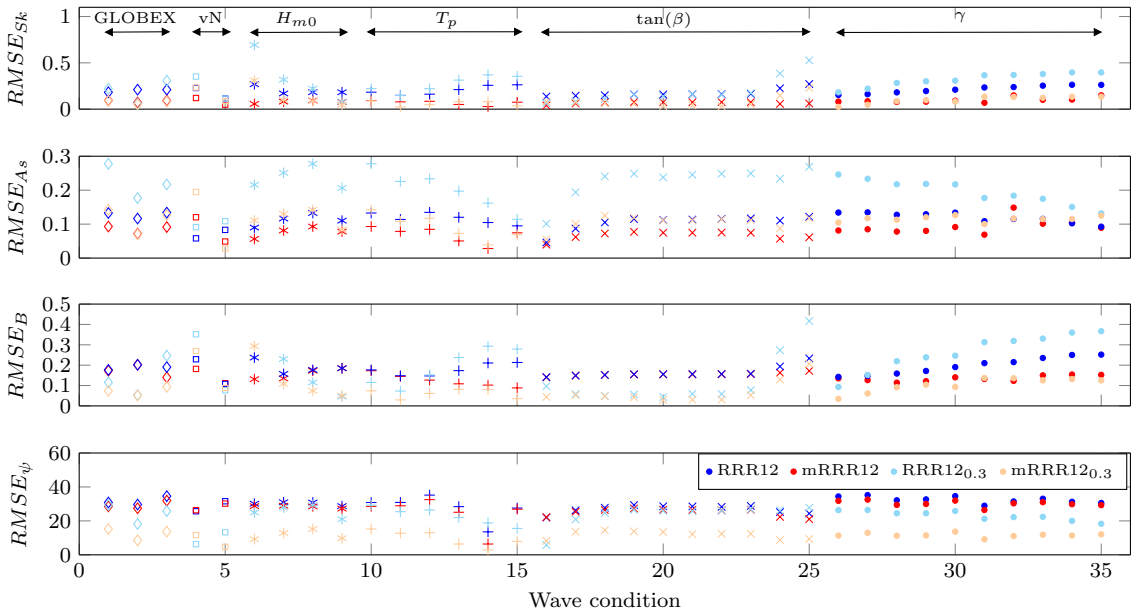

Figure 3.48: Comparison of the $RMSE$ of each wave condition simulated when the RRR12 (blue/cyan) or the mRRR12 parameterizations (red/orange) are applied to Sk, As, B and ψ. The darker markers (blue or red) correspond to the $RMSE$ values calculated considering all data points; the lighter markers (cyan or orange) correspond to the $RMSE$ values calculated considering only data points for which $Sk_u > 0.3$.

the outer/mid shoaling zone.

3.5 Conclusion

The analysis of GLOBEX data presented in this chapter was aimed at improving current understanding of wave nonlinearities. The very gently-sloping beach of the experiments allows a great development of the nonlinearity of the waves and the high-resolution data collection, in time and in space, provides a high quality data set for investigating it. A detailed data analysis, presented in the first section of this chapter, suggested variations of free-surface elevation and velocity nonlinearities depending on some characteristics of the wave conditions considered. Field data previously collected reinforced the idea that particular characteristics of each wave condition (wave history) may determine how the nonlinearity develops and the maximal values it reaches.

The SERR1D numerical model was used for simulating a wide range of wave conditions, aimed at exploring the importance of different parameters in the development of the nonlinearities. The model was validated with GLOBEX data, both for free-surface elevation and velocity measurements. An overestimation of u_{rms} and Sk_u is inherent to the model, and thus an alternative was proposed to obtain velocity time series from the free-surface-elevation time series. Since only three different irregular wave

conditions were available from GLOBEX data, the vN2003 data set, with different wave conditions and beach slope, was also used to validate the model. This helped assessing the capacity of the model to simulate a range of wave conditions beyond that of the three irregular-wave cases of GLOBEX.

Wave conditions with different offshore wave height, peak period and spectral bandwidth and beach slope were simulated for irregular-wave conditions and, for bichromatic-wave conditions, IG-wave height was varied through the changing of the modulation of short-wave groups. All the parameters varied were shown to contribute to more or less significant changes of the evolution of wave nonlinearity, in particular regarding the maximum values attained.

The analysis of the bichromatic wave conditions is brief, since the model was calibrated for the irregular-wave conditions, and thus it is for these last conditions that it works the best. Some issues remain to be investigated further in order to allow a better simulation of the bichromatic-wave conditions by SERR1D, such as the existence of a short-wave reformation zone in the mid-surf zone and the presence of multiple peaks of Sk and As. Nevertheless, it was still possible to highlight the importance of IG waves on the nonlinearities, especially on skewness. Contrary to the irregular-wave conditions, which have a single skewness maximum until the end of the surf zone, the bichromatic-wave conditions reach multiple local maxima along the beach profile. Two of these maxima (the first and the third) are associated to the first breaking and to the short-wave reformation in the mid-surf zone. One of the other Sk_η maxima (the second) was shown to be associated with the presence of IG waves, since (i) for it to exist, a certain degree of IG-wave modulation is necessary and (ii) this maximum corresponds to a maximum of the correlation between short-wave variance and IG-wave velocity. It is potentially associated with a local IG-wave height minimum, but further research is necessary for drawing stronger conclusions.

In order to understand how important is the influence of different parameters in the nonlinearities, the results obtained from the simulation of the irregular-wave conditions were compared to the results of RRR12 (Ruessink *et al.*, 2012) parameterization. This parameterization provides an estimation of velocity nonlinearities based on local wave-parameters only (the Ursell number). It is based on a great amount of field data, to which it provides the best-fit, but not without a significant dispersion. When it is applied to the results obtained for the different wave conditions simulated, it is shown that significant errors can occur, particularly for wave conditions with certain characteristics. From the analysis of the different wave conditions for which the parameterization gives the largest estimation errors, it can be concluded that the offshore wave steepness, in particular, and also the beach slope and spectral bandwidth are the three main factors

that are linked to the nonlinearity values that have a greater deviation from the RRR12 parameterization. Therefore, a modification to the original the RRR12 parameterization is proposed, which includes the effects of these three factors.

A modified version of the Iribarren parameter, the nonlinearity parameter (NP_0), is suggested, in order to include the dependence of the nonlinearities on offshore wave steepness and beach slope. This parameter includes the contribution of the beach slope, through the classical Ib_0 parameter, and the increased contribution of the offshore wave steepness, $(H_0/L_0)^2$. The maximum value of nonlinearity reached for each condition is shown to depend, through a power law, on NP_0 and γ. Therefore, both parameters are included in the RRR12 parameterization, via p_2 and p_5 terms. The inclusion of both NP_0 and γ on the RRR12 parameterization results in a reduction of the $RMSE$ between predicted and real values estimated at around 30%, for Sk_u, As_u and B and 7% for ψ. When only data points for which $Sk_u > 0.3$ (corresponding to cross-shore positions onshore of the outer-shoaling zone) are considered in the calculation of $RMSE$, the reduction of the $RMSE$ between predicted and real values is estimated instead at 64%, for B, and around 50% for the other three nonlinearity variables. Overall, the greatest improvement is observed for the wave conditions with smaller offshore wave steepness and narrower spectral bandwidth and beaches with very gentle or very steep slopes, and for the greatest nonlinearity values (near the breakpoint).

It was clearly shown that the free-surface elevation and velocity nonlinearities cannot be defined only based on local wave parameters. The history of the waves propagating, including the offshore wave characteristics and the beach over which they propagate, has to be taken into account as well, if an accurate description of the evolution of the wave nonlinearities along the beach profile is intended.

Chapter 4

The role of infragravity waves in the beach morphodynamics

4.1 Introduction

The existence of infragravity waves has been proven since the fifties (Munk, 1949; Biésel, 1952; Longuet-Higgins & Stewart, 1962), mostly from field data, and since then a panoply of field, laboratory and numerical studies have been trying to shed some more light on the issue. Most of the research done so far on the hydrodynamics of IG waves has focused on understanding their mechanisms of generation and reflection/dissipation at the shoreline (*e.g.* Symonds *et al.*, 1982; Schaffer, 1993; Herbers *et al.*, 1995; Masselink, 1995; Sheremet *et al.*, 2002; Battjes *et al.*, 2004). More recently, research has also been focusing on unraveling the mechanisms of energy transfer between the short waves and the IG waves and the possibility of IG-wave breaking (*e.g.* Henderson *et al.*, 2006; van Dongeren *et al.*, 2007; Ruju *et al.*, 2012; Guedes *et al.*, 2013; de Bakker *et al.*, 2015b). Little after the acquaintance of the existence of these low-frequency waves, the research community started trying to understand if they could also have a significant influence on sediment transport, and if so, by which mechanism(s) (*e.g.* Wright & Short, 1984; Beach & Sternberg, 1988; Roelvink & Stive, 1989; Beach & Sternberg, 1991; Aagaard & Greenwood, 1994, 1995; Ruessink *et al.*, 1998b; Aagaard & Greenwood, 2008).

While the mechanisms of IG-wave generation and even dissipation are now starting to be significantly well understood, the influence of these waves on sediment transport is still very unclear. Whether they are capable of suspending sediment alone or only of advecting sediment stirred by short waves or even simply influence sediment transport by modulating short-wave nonlinearities, remains an unsolved issue. Furthermore, the IG-wave contribution can result in both offshore- and onshore-directed fluxes depending on the relative phase between the velocity and sediment concentration (Beach

& Sternberg, 1991). The confirmed link between these low-frequency waves and the swash motion further adds to the complexity of the IG-wave influence on the beach morphology and is also an ongoing topic of research (Ruju *et al.*, 2014).

Most studies about the cross-shore sediment transport in the nearshore zone have shown that, in the shoaling zone, the onshore-directed transport by short-waves dominates the total particle flux and the IG-wave sediment transport is generally an order of magnitude smaller (Baldock *et al.*, 2011). Effectively, Ruessink *et al.* (1998a) found the relative contribution of bound IG waves to the gross sediment transport to be small (on average, less than 10-20%). However, near the end of the shoaling zone, these authors considered that, since the suspended sediment transport is a delicate balance between two components of approximately equal magnitude but opposite directions (short-wave skewness and undertow), the small contribution of infragravity waves may sometimes not be negligible and have a relatively large influence on the magnitude and direction of the net suspended sediment transport. The largest sediment concentrations are present under the bound IG-wave troughs, since it corresponds to the largest short waves, which exert larger bed shear stresses. The transport by the bound IG waves is thus directed offshore (Osborne & Greenwood, 1992b), as it is associated with the offshore stroke of these waves. Free IG waves, on the other hand, are considered by the later authors as unimportant under non-breaking wave conditions.

Shoreward of the breakpoint, the opinions on IG-wave sediment transport direction diverge, and no clear model exists so far (Baldock *et al.*, 2010). The most important sediment transport mechanism is generally considered to be the wave-driven undertow, although free IG-wave motion may as well be of importance, especially on dissipative beaches (*e.g.* Beach & Sternberg, 1991; Osborne & Greenwood, 1992a; Aagaard & Greenwood, 1994). Different authors have observed contradictory directions of sediment transport by IG waves in this zone of the beach profile (Beach & Sternberg, 1988, 1991; Osborne & Greenwood, 1992b; Russell, 1993; Aagaard & Greenwood, 1995, 2008). Short (1975) has proposed that sediment deposition will tend to occur under nodes or anti-nodes of the IG waves and Michallet *et al.* (2007) have later shown partial evidence of a nodal structure consistent with the cross-shore bar position. On the other hand, Prel *et al.* (2011) have seen IG-wave motion to influence sediment transport by modulation of the short-wave skewness and asymmetry, but they did not find bar formation to be consistently located under nodes or anti-nodes of standing waves.

Following a different approach, Aagaard & Greenwood (1995) have argued that IG waves may be important to morphological change in the surf zone by imposing spatial gradients on sediment transport associated with mean currents: the asymmetries of the oscillatory velocities in the bottom boundary layer associated with these waves

imply greater velocities and thus a net transport towards the antinodes. An alternative scenario is an interaction between IG-wave free-surface elevation and incident wave velocities, in which IG-wave velocity asymmetries are still required to cause a net sediment transport towards free-surface elevation antinodes. Following these hypothesis, Aagaard & Greenwood (2008) showed that, particularly in the inner-surf zone, sand is mostly re-suspended by orbital velocities associated with incident wind waves, but it is the IG waves that then act as a sediment transport agent through advection, in a manner similar to quasi-steady mean currents. Hence, they can potentially dominate the total transport of suspended sediment in this zone of the beach.

The LEGI (Laboratoire des Écoulements Géophysiques et Industriels, Grenoble, France) wave flume, a light-weight-sediment flume, has already been used for studying the wave propagation, the effects of wave nonlinearities on sediment transport (Michallet *et al.*, 2011; Grasso *et al.*, 2011) and the boundary-layer dynamics (Berni *et al.*, 2013), but also the influence of IG waves on sediment transport (Michallet *et al.*, 2007; Prel *et al.*, 2011). Since few laboratory experiments have been done so far on the role of infragravity waves on the sediment transport and many questions remain unanswered regarding this topic, the aim of this chapter is to improve this knowledge, through an important set of laboratory experiments held in the LEGI wave flume.

Long runs, with a timescale of a few hours, and short runs, with a timescale of only two wave groups (27.2 s), were ran, for three distinct bichromatic wave conditions. Bichromatic wave conditions have the great advantage that the height and period of the IG-waves associated to the short-wave groups can easily be selected and controlled. Hence, in the experiments presented in this chapter, the IG-wave height was varied, keeping the same short-wave height and energy. Therefore, the changes in the effect of each wave condition to the beach profile are necessarily linked, directly or indirectly, to the differences in the IG waves considered. The analysis is done considering free-surface elevation and velocity measurements and bed-profile changes.

The research questions motivating this chapter aim at responding to the fundamental question of what is the influence of IG waves on sediment transport. This question can then be detailed into more specific questions:

- Can IG waves influence the sediment transport by short-waves? By which mechanism(s)?
- Can IG waves work together with short-waves in the sediment transport, combining different transport mechanisms?
- Can free IG waves alone (without the presence of short waves) promote sediment transport?

- What is the importance of the IG waves for the sediment transport in the different zones of the beach profile?
- Can IG waves influence the shape of equilibrium profiles?

This chapter starts by an instruments and methods section, where the experimental facility and wave conditions are described and the different types of measurements performed during the experiments are presented and their applications and limitations are discussed. In the subsequent section, the concept of equilibrium beach profile and evolution towards equilibrium are discussed for the different wave conditions. Since a distinct equilibrium profile is observed for each wave condition, a more thorough analysis of the morphodynamics associated to each wave condition is performed in the ensuing section, where runs of only two wave groups are considered to simplify the research of the various processes influencing sediment transport. An analysis of the hydrodynamics, taking into account both free-surface elevation and cross-shore velocity, is then carried out to explain the disparity in the morphological evolution between wave conditions. The SERR1D model, previously presented in chapter 3, is used to obtain velocity measurements around the breakpoint and in the surf zone, where accurate velocity measurements are difficult to get with the acoustic instruments. The influence of monochromatic IG waves in the sediment transport is briefly debated and subsequently the different mechanisms shown to be involved in the sediment transport by the IG waves are examined in the discussion section. The chapter ends with a conclusion.

4.2 Instruments and methods

4.2.1 The LEGI wave flume

The LEGI flume, presented in Fig. 4.1a, is a 36 m-long and 0.55 m-wide wave flume, with vertical glass walls and equipped with a piston-type wave-maker. This wave-maker, as shown in Fig. 4.1b, consists in a vertical board driven by a servo-valve, which can reach a maximum displacement of ±30 cm along the horizontal direction and allows the reproduction of regular or irregular waves. Although it can generate short and IG waves, the wave-maker is not capable of active reflection compensation, meaning that any IG waves generated in the flume that reach the wave-maker will be reflected back, enhancing standing or partially-standing IG waves that oscillate in the flume until they dissipate.

The laboratory beach, represented in Fig. 4.2 scheme, is formed by Polymethyl Methacrylate (also known as Plexiglas) low-density ($\rho_s = 1.19$ g cm^{-3}) sediments, with a

(a) The LEGI wave flume.

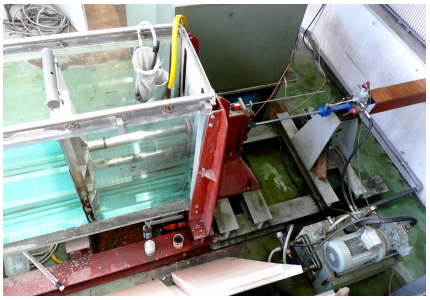

(b) Piston-type wave-maker.

Figure 4.1: Experimental facility.

median diameter d_{50} of 0.64 mm (and a settling velocity, w_s, of 21 mm s^{-1}). A detailed description of the experimental facility can be found in Grasso (2009); Berni (2011).

Measurements of free-surface/bed elevation (using 12 wave gauges, some of which were located in the swash zone, Fig. 4.3a), current velocity (using a side-looking Accoustic Doppler Velocimeter - ADV Nortek Vectrino +, Fig. 4.3b, and an Accoustic Doppler Velocity Profiler - ADVP) and the bed profile (in the beginning and end of each run, with an optical profiler) were made. The wave gauges were moved to convenient locations depending on the run. The ADV was also moved both cross-shore (from run to run) and in the vertical (for 5-20 min intervals during some of the runs) to have a

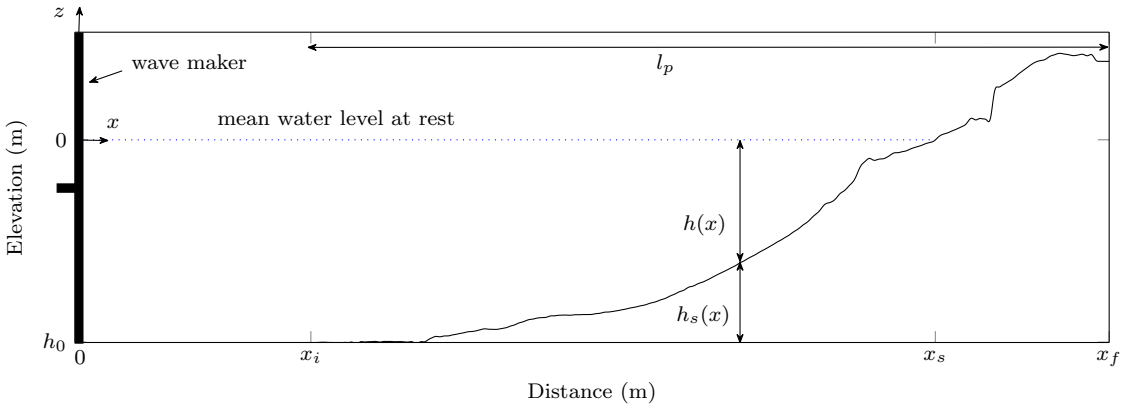

Figure 4.2: Schematic diagram of the LEGI wave flume: h_0 is the mean water level at rest at the wave maker (around 56.60 cm for the experiments that will be presented); l_p is the length of the measured profiles, from $x_i = 6.5$ m to $x_f = 29$ m; x_s is the cross-shore position of the shoreline; $h(x)$ is the water depth and $h_s(x)$ the sediment height, both in function of x cross-shore position.

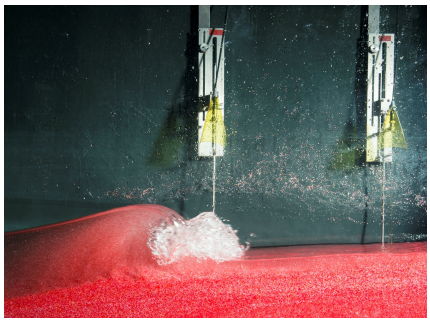

(a) Capacitive wave gauges.

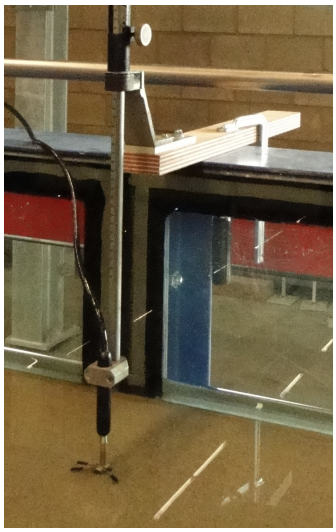

(b) ADV

Figure 4.3: Measurement instruments for free-surface elevation and velocity ((a) photo by Cyril Fresillon - CNRS photothèque).

better description of the cross-shore velocity at several positions relative to different morphological features.

The LEGI flume is designed to reproduce natural beach profiles and their morphological changes. The physics and hydraulics of movable bed models depend on the wave parameters (significant wave height H_s and peak period T_p), sediment parameters (sediment diameter d and density of the sediment ρ_s) the water depth h, the fluid density ρ, the fluid kinematic viscosity ν and the gravity g (Grasso *et al.*, 2009a). These variables must be correctly scaled to their nature equivalents to allow the truthful representation of the fundamental processes aimed to be characterized. Since it is very difficult to scale the eight independent parameters mentioned, the choice of the parameters to scale is done based on the principal processes that are aimed at being simulated by the physical model.

The Froude scaling is essential in physical models that involve waves (Dean & Dalrymple, 2002) and can be written as

$$F = \frac{H_s \omega_p}{2\sqrt{gh}}, \tag{4.1}$$

where $\omega_p = 2\pi/T_p$ is the angular frequency. Since wave dynamics, shoaling, breaking and turbulence generation by the waves must be modelled correctly, an undistorted model is chosen. Therefore, a single length scale λ_l is chosen (λ_i is the ratio of the model value to the prototype value of parameter i). Respecting the Froude similitude between nature and the model implies that the time scale, $\lambda_t = \sqrt{\lambda_l}$. Grasso (2009)

has shown that choosing a length scale of 1/10 relative to nature (which implies a time scale of 1/3 and thus a velocity scale of 1/3) allows the reproduction of beach profiles that can be found on real beaches with sediments with a median diameter of 0.3 mm.

The wave Reynolds number can be calculated according to

$$Re = \frac{A\omega_p h}{\nu}, \tag{4.2}$$

with ν the fluid viscosity and A the particle excursion at the bottom,

$$A = \frac{H_{rms}}{2\sinh(kh)}, \tag{4.3}$$

where k is the wave number. Even though this number is not scaled in the experiments and is smaller than in nature, it is large enough for the flow to be turbulent.

For ensuring sediment transport similitude, Shields and Rouse scalings are adopted. The Shields number is calculated as

$$\Theta = \frac{1}{2} f_w \frac{(A\omega_p)^2}{g(\rho_s/\rho - 1)d_{50}}, \tag{4.4}$$

where f_w is a wave friction factor (Swart, 1974), which can be approximated as

$$f_w = \exp\left[5.213\left(\frac{2.5 \times d_{50}}{A}\right)^{0.194} - 5.977\right]. \tag{4.5}$$

The Rouse number can be expressed as

$$Rou = \frac{w_s}{u'}, \tag{4.6}$$

with u' the turbulent intensity of the flow field, approximated by $\kappa\sqrt{f_w/2}A\omega_p$ (with κ the von Karman constant = 0.4 (Soulsby, 1997)). The Shields number defines the threshold for setting the sediment in motion and the transport regime (bed load, suspension, sheet flow, etc.) and the Rouse number can be seen as the ratio between a turbulent timescale and a settling timescale (for a given characteristic length).

The Dean number (Dean, 1973) (recall, $\Omega = \frac{H_s}{T_p w_s}$) was constant and of about 3.4 (H_s = 0.12 m, T_p = 1.7 s, w_s = 0.021 m s^{-1}) for the experiments performed, which places all the beach profiles obtained in the intermediate range of Wright & Short (1984) classification (presented in chapter 2). These profiles are characterized by beaches with a moderate mean slope and spilling or plunging breakers and can have bar-trough systems, rhythmic bars and terraces.

Previous authors (Grasso *et al.*, 2009a,b) have studied in depth the scaling of the

LEGI wave flume and compared it to natural beaches that also have intermediate profile types. They have found the overall beach hydrodynamics and morphodynamics to be correctly reproduced by fulfilling the three scalings mentioned.

4.2.2 Wave conditions

The main aim of the experiments held in the flume was to understand the importance of infragravity waves on sediment transport. Bichromatic waves were chosen instead of irregular waves (which would be more similar to nature) so that only two different sinusoidal wave components are generated by the wave-maker, together with the lower frequency of the bound wave resulting from the difference interaction between the two main components. As the waves propagate and evolve along the flume, it is thus easier to track the developing of higher and lower harmonics, as they tend to be multiples of the main frequencies f_1 and f_2, or of the bound IG wave frequency, $f_2 - f_1$. Baldock *et al.* (2011) have previously shown that a given bichromatic-wave condition with the same short-wave energy of a given irregular-wave condition is capable of generating a similar sediment transport. Therefore, in this work, bichromatic-wave conditions are used instead of irregular-wave conditions in the study of the effect of IG waves in the sediment transport. This greatly simplifies the processes to be studied, due to the regularity and repeatability of the waves propagating and makes it easier to control the IG frequencies present in the flume.

At the first order, the free-surface elevation for bichromatic waves can be analytically calculated as it follows,

$$\eta\left(x,t\right) = A_1 \cos\left(w_1 t - k_1 x\right) + A_2 \cos\left(w_2 t - k_2 x\right), \tag{4.7}$$

where A is the wave amplitude ($= H/2$), k the wave number, ω the angular frequency and x and t the time and space coordinates, respectively. The indexes 1 and 2 represent each main frequency.

The theoretical solution for the wave-maker displacement was computed according to Hughes (1993) and included second-order compensating generation to correctly reproduce the bound IG wave.

Three different bichromatic wave conditions with the same short-wave energy were designed: C1 (first-order solution with addition of free IG waves of opposite sign to that of the bound IG waves), C2 (standard condition) and C3 (smaller IG-wave amplitude than C2). For the three, short-wave $H_s = 14.8$ cm and $T_p = 1.7$ s and the two main frequencies were $f_1 = 0.5515$ Hz and $f_2 = 0.6250$ Hz (T_{IG} or $T_g = 13.6$ s). The frequencies were chosen so that $f_p = \frac{f_1+f_2}{2}$. The time series of the wave conditions

were composed by successive pairs of two wave groups (which had slightly different short-waves between them). C1 and C2 had a maximum modulation, with a_1 and a_2 of 0.03 m, while C3 had smaller modulation, with $a_1 = 0.0413$ and $a_2 = 0.01$ m. The difference between C1 and C2 was subtler and linked to the generation process. In the case of C2, the IG wave reproduced by the wave-maker corresponded to the second-order bound wave computed and expected to develop as the waves start propagating. Forcing this IG wave in the theoretical solution ensures that it establishes correctly in the flume as the waves propagate. For C1, this IG wave was generated by the wave-maker in the direction opposite to that of wave propagation. Since an IG bound wave still develops anyway as the wave groups propagate, the IG wave that was artificially generated with an opposite direction of propagation behaves as an additional free-wave propagating in the flume, with a phase relative to the wave group that is distinct from that of the bound wave. This results in both additional IG-wave energy and a different IG phasing from that of C2.

Fig. 4.4 helps understand the differences between the wave conditions. At $x = 9$ m, the main differences between C1 and C2 are in terms of IG-wave phasing. The spectral peak corresponding to the bound IG waves ($f_2 - f_1$) has roughly the same energy for both conditions (for C2, it has 1.5 times more energy than for C1). However, at the end of shoaling, IG waves have an energy about 4 times greater for C1 than C2. For the first harmonic of the bound IG wave ($2\,(f_2 - f_1)$), C1 also has higher energy than C2 and C3. C3 bound IG waves have, for both cross-shore positions, energy one order

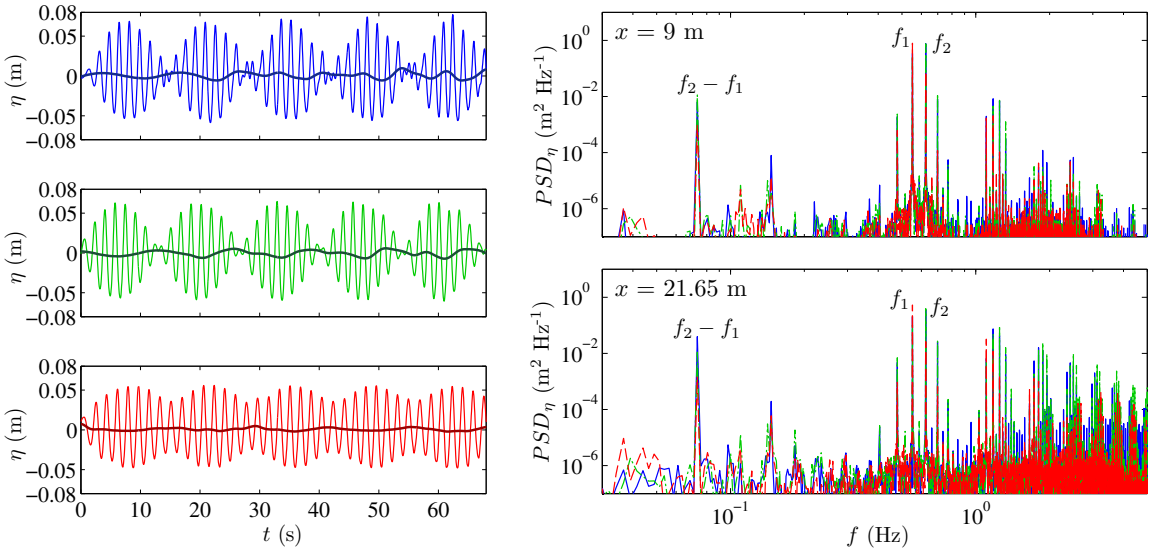

Figure 4.4: Left column: free-surface elevation (total and IG, with a lighter colour) at $x = 9$ m for the three wave conditions: C1 in blue, C2 in green and C3 in red; right column: free-surface spectra for the three wave conditions, at $x = 9$ m (beginning of shoaling) and $x = 21.65$ m (end of shoaling). The spectra were computed from 132 wave groups near the end of the long runs.

of magnitude smaller than C1 and C2, which can also be seen in the time series as a much smaller bound IG wave. C3 has also less energy on harmonics of f_2 frequency than the other two conditions.

The duration of the wave-maker action was variable, ranging from only two short-wave groups (about 27.2 s) to longer runs of over 5 h. Apart from C1, C2 and C3, some runs were also made with free IG-waves only, with the same height and period of the bound IG waves of C2, or multiples of that height.

4.2.3 Free-surface elevation measurements

Free-surface elevation measurements were made using 12 capacitive wave gauges positioned along the cross-shore profile. The wave gauges have a precision of 1 mm and a sampling rate of 128 Hz and were calibrated regularly (for details on the calibration, see Grasso (2009)). Depending on the runs, the wave gauges were moved to different positions, in order to get a better coverage of the region of interest. The cut-off between high and low frequencies is considered at half the peak frequency, which corresponds to the minimum of the variance density spectrum of η measured at the wave gauge closest to the wave-maker ($x = 2.01$ m). It separates the range of frequencies that initially have more energy and will tend to loose energy as the waves propagate towards the coast, from the range of frequencies that initially have less energy and will gain energy closer to the coast.

The wave gauge measurements allow the characterization of the hydrodynamics associated with each beach profile. Different wave statistics can be computed, such as the root-mean-square wave height (3.1), for short and infragravity waves, skewness (3.8), asymmetry (3.9), energy dissipation (3.3) or mean water level ($\bar{\eta}$) to evaluate the set-up and the set-down. The wave statistics corresponding to each beach profile are computed on a pair number of wave groups, which, for the short runs, corresponds to two wave groups only, and for the long runs depends on the aim for which the statistics are being calculated.

Resonant modes

Since the wave-maker of the LEGI-flume is not equipped with active reflection compensation, the free IG waves that reflect at the beach are "trapped" in the flume, creating stationary IG waves and increasing the low-frequency energy present in the flume. This implies that the IG-wave height may be near zero for the cross-shore locations coincident with standing-wave nodes, or maximal, at locations coincident with the antinodes.

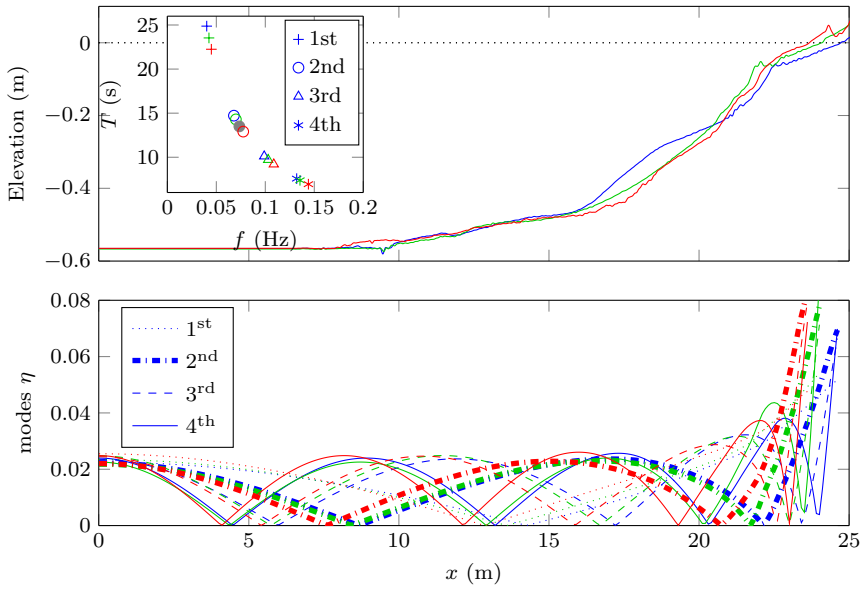

Figure 4.5: C1 (blue), C2 (green) and C3 (red) equilibrium profiles. On the top: the beach profile and the frequencies (*vs* periods) of the first-four resonant modes of the flume and the bound IG-wave frequency/period (filled green circle). On the bottom: the cross-shore structure of the first-four resonant modes.

For each beach profile, the theoretic resonant modes of the IG waves can be calculated to help explaining the minima and maxima of IG-wave height measured by the wave gauges. Small differences in the shoreline position can influence the distribution of the nodes and antinodes along the beach profile. Fig. 4.5 shows the first four normal modes that may be forced for C1, C2 and C3 equilibrium profiles, and their frequencies (and periods). The second normal mode has a period very close to the period of the short-wave groups (T_g) and thus of the bound IG wave. Therefore, since the IG-wave motion in the flume is preferentially forced at this period, the second normal mode (f = 0.05-0.085 Hz) is the most enhanced. This is depicted in Fig. 4.6, where the H_{rms} of the IG waves is represented for the frequency bands that include the first six normal modes. The wave height of the frequency band corresponding to the second

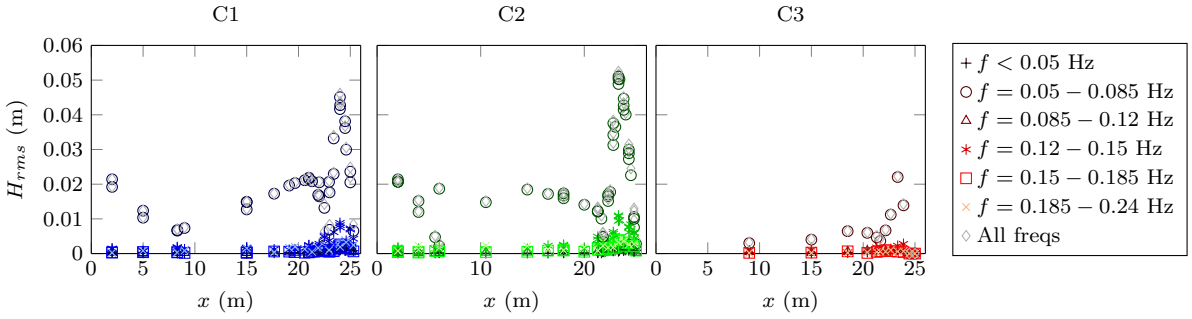

Figure 4.6: H_{rms} of the IG-wave frequency bands corresponding to the first-six normal modes of the equilibrium beach profiles, for C1, C2 and C3.

normal mode is almost equivalent to the total IG-wave height. The fourth mode has some relevance in the surf and swash zones, but all the other modes have negligible contributions to the total IG-wave height. This is the case for all the three equilibria. The greatest difference between conditions consists in the IG-wave height evolution in the shoaling zone: for C1, the maximum IG-wave height is reached just before the slope break of the beach profile (around $x = 21$ m), and for C2, this maximum is located at the beginning of the steepening of the beach slope in the shoaling zone (around $x = 15$ m). For C3, the total IG-wave height is significantly smaller than for C1 and C2 and the maximum of the shoaling zone is reached around $x = 18$ m, where a small "bump" can be seen in the equilibrium profile of C1.

Swash-zone wave gauges

The swash zone is the highest zone of the profile where wave gauges were positioned. Since this zone is intermittently covered by water, free-surface elevation can only be retrieved when the wave gauges are immersed. However, even when the water retreats, the bed is fully saturated and thus these gauges detect the bed position, which can be used to track the evolution of the beachface position along the runs. This is depicted in Fig. 4.7, where the black lines represent moments of emersion and thus the position of the bed. This allows the quantification of bed-level variation (red crosses in Fig. 4.7) between swash events and the duration of the events (the central point of each black line is considered to calculate the bed-level variation). These are the only measurements of the bed position available during wave action, since the bed profiling of the entire beach can only be done before or after each wave condition is ran, as the water surface

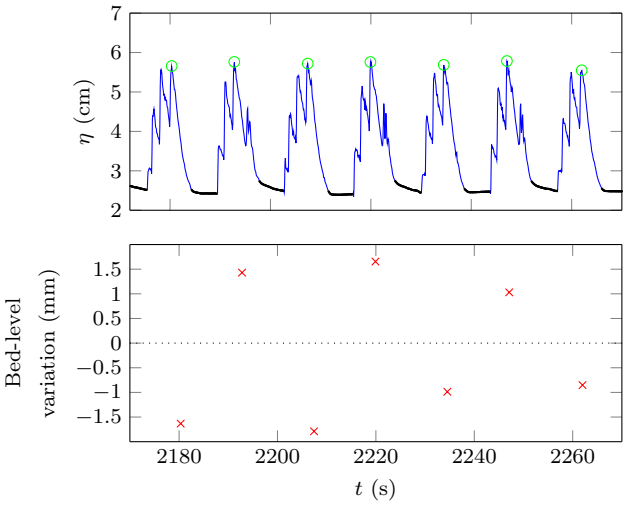

Figure 4.7: Example of bed-level detection during an interval of a C2 run. The swash events are in blue, maximum swash height in green (circles), the bed level in black and the bed-level variation between two swash events in red (crosses).

needs to be completely still. The detection of the bed-position in the time series of the swash wave gauges was done following the method of Turner *et al.* (2008).

The detection of the bed position in the swash zone can also be used to track the effect of the residual IG waves (at the end of the runs) on the beach. Even though the short-runs consisted in only two wave groups to avoid the effects of IG-waves reflected at the wave-maker, after the arrival of the wave groups to the beach, residual IG waves keep oscillating in the flume until their energy if fully dissipated. It is thus important to be sure that these residual waves are not significantly morphogenic, as this could bias the interpretation of the results.

Fig. 4.8 shows a zoom of the minimum level of the free-surface elevation at two swash-zone wave gauges (positioned at $x = 24.45$ m and $x = 23.89$ m) for a C2 run with a duration of two wave groups. Since the bed is fully saturated in the highest zones of the beach and the lower and flatter sections of the curves correspond to moments when there is no water, they represent the bed position, similarly to the black flatter sections in Fig. 4.7 (which shows an experiment with a duration of more than two wave groups).

For the wave gauge located higher on the beach ($x = 24.45$ m), bed changes are very small (of the order of 1 mm), whether they are provoked by the passage of the two wave groups or the residual IG waves. Therefore, in both cases, the waves are hardly morphogenic. However, for the other gauge lower in the beach ($x = 23.89$ m), just at the limit of the swash zone, changes are more significant. The first and the second wave groups promote the greatest erosion observed during the runs. This erosion is of about 8 mm, for the first wave group, and 2.5 mm, for the second one. The following cycles of residual IG waves (together with some small residual short waves) account for changes an order of magnitude smaller, of around 1 mm. Even though the absolute values of bed change may vary a lot depending on the bed profile for each wave condition, the orders of magnitude are comparable between experiments. Independently of the experiment considered, even though residual IG waves may be weakly morphogenic, the bed change they promote is much smaller than that promoted by the two wave groups and can thus be disregarded.

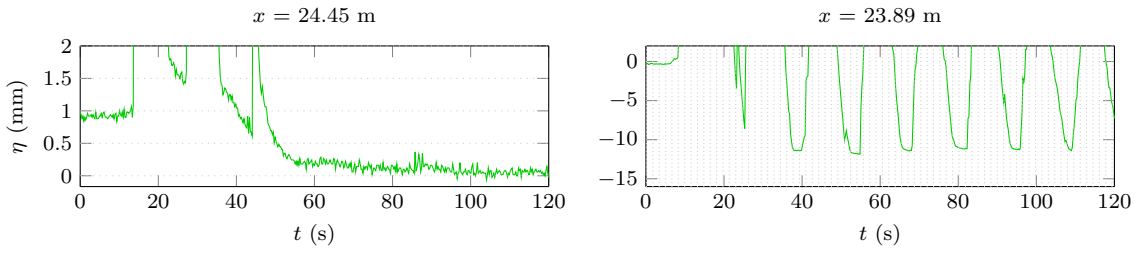

Figure 4.8: Zoom of the minimum level of the free-surface elevation at two swash-zone wave gauges during one C2 run of two wave groups. The grid lines have a spacing of 0.5 mm.

4.2.4 Bed profiles

Before or after each run, the beach-profile position was measured with an optical laser beam (with a sampling frequency of 50 Hz) installed on a motorized trolley that moved at an almost constant velocity (100 mm s^{-1}) on the metallic rails that run over each side of the flume. As the trolley moves, the laser beam is emitted towards the bed and its reflection is retrieved by a receptor located next to the laser source. If there are suspended particles in the water column, the laser beam is reflected in those particles and does not reach the bed, which results in erroneous measurements of the bed position. In order to overcome this limitation, a correction procedure is applied.

The raw measurements of the beach profile are obtained in terms of voltage (Fig. 4.9 A). Then, they are converted to meters, multiplying by a calibration value (Fig. 4.9 B). The initial (x_i = 6.5 m) and final (x_f = 29 m) positions for the profile measurement are defined before the trolley is set in motion, but, since it does not move at exactly the same velocity along the entire flume, the trolley usually stops some centimeters before its defined final position. Therefore, after converting the measurements from volts to meters, a correction to the final position is done for having all profiles with matching x_i and x_f. Afterwards, the profile is de-spiked (red profile, Fig. 4.9 C) to reduce the number of erroneous points obtained by reflection of the laser beam at the surface or along the water column. Then, since the bars over which the trolley moves are not completely horizontal, the bed position is corrected (red to green profile in Fig. 4.9 D) to eliminate this error. Moreover, the laser beam is refracted as it traverses the air-water interface and hence, a re-scaling of the profile is done (green to magenta profile in Fig. 4.9 D). Finally, since the de-spiking process is not 100 % efficient for all the profiles measured, for each profile done from x_i to x_f, pA (magenta profile in Fig. 4.9 E), another profile is done just after it, from x_f to x_i, pB (purple profile in Fig. 4.9 E). When a spike is present at a given cross-shore position for one of the profiles, the value of the other profile at that cross-shore position is considered instead. When this correction if done for both pA and pB profiles, the average of both profiles is done and considered as the final profile, p (Fig. 4.9 F).

Profiles were measured between x_i = 6.5 m and x_f = 29 m (total profile length, $l_p = (x_f - x_i)$ = 22.5 m), along the centre of the flume. However, since the part of the profile that is permanently emerged does not change along the runs, x_f is often considered in the analysis at 26 m, for convenience. Depending on the analysis wanted and when no significant change is measured for the greatest depths, x_i is considered further onshore than 6.5 m. The profile measurements made were re-sampled so that the vertical position of the bed is retrieved each millimeter, on the cross-shore direction.

Even though the correction procedure aims at minimizing the errors inherent to the

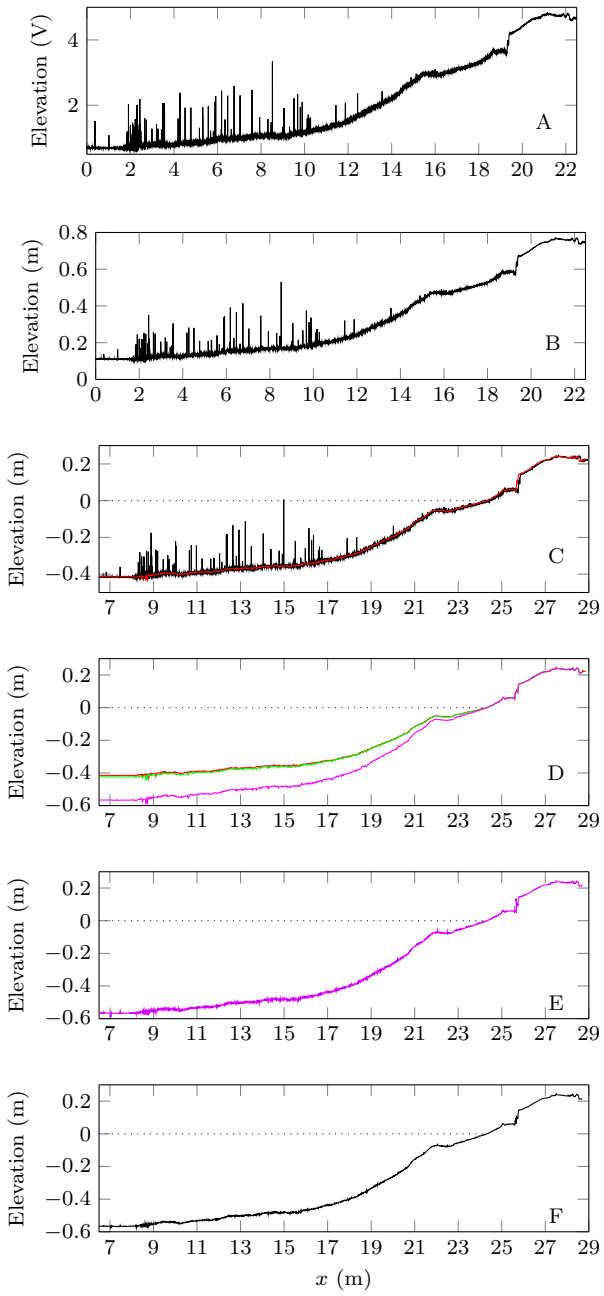

Figure 4.9: Correction procedure of the bed-profile measurements. A - raw measurements in volts; B - raw measurements in meters; C - de-spiked profile (red) and position corrected relatively to the water level at rest (dotted blue line); D - correction of bar horizontality (green) and re-scaling to compensate the laser beam refraction when it crosses the water surface (magenta); E - pA and pB bed profiles; F - p bed profile.

measurement of the bed position, it is not perfect. Not all the profile measurement spikes are completely corrected, especially when at the same location a spike is present for both pA and pB. Also, when the water is less clean, light transmission may change across the water column. The water was clean regularly but the growth of organic matter was dependent on environmental conditions (light, temperature, particles in the water, etc) and thus it was hard to have always the same water quality along the experiments that were performed during more than two years. As it can be seen in Fig. 4.9 C, for cross-shore positions closer to the wave-maker than $x \approx 15$ m, larger errors associated to the profile measurements. This happens in part due to the higher water column (that can have more suspended particles) and to changes in the transmissivity of the water due to the presence of impurities. Also, from the wave-maker until $x \approx 8.5$ m, the bed of the flume (made of glass) is not covered by sediments, which also contributes to measurement errors. The beach morphodynamics below $x = 15$ m is not analysed in this work and is hence excluded from the profile measurement-error quantification.

In order to quantify the uncertainty of the bed profile measurements resulting from the mentioned factors, the bed profile measurement uncertainty (MU) averaged along the length of the beach profile (starting at $x = 15$ m), MUh_m, and the mean relative error, MUh_{rel}, are calculated for each beach profile and shown in Fig. 4.10.

$$MUh_m = \frac{\sum_{n=1}^{N} |h_{sB,\,n} - h_{sA,\,n}|}{N} \tag{4.8}$$

and

$$MUh_{rel} = \frac{\sum_{n=1}^{N} |h_{sB,\,n} - h_{sA,n}| \,/h_{s,\,n}}{N} \times 100, \tag{4.9}$$

where the indexes A and B correspond to profiles pA and pB, respectively, n is the index of the cross-shore point considered, varying from 1 (corresponding to $x_i = 15$ m) to N (corresponding to $x_i = 26$ m) and $|.|$ denotes the absolute value.

Averaging MUh_m and MUh_{rel} over the entire set of experiments, results in a value that can be considered as the measurement uncertainty associated to the bed position measurement for any measured profile. Thus, each bed position measurement has an uncertainty of ± 2.1 mm, corresponding to a relative error of $\pm 1.0\%$. The measurement uncertainty is, however, dependent on the cross-shore position considered. As it was mentioned, in deeper water larger errors are associated to the bed position retrieved by the laser beam, due to the highest probability of the laser being reflected at particles in suspension or due to the water quality. Therefore, the further inshore x_i is considered for a given analysis, the smaller the measurement uncertainty. This is illustrated by the difference between the blue circles and the red asterisks in Fig. 4.10: only by

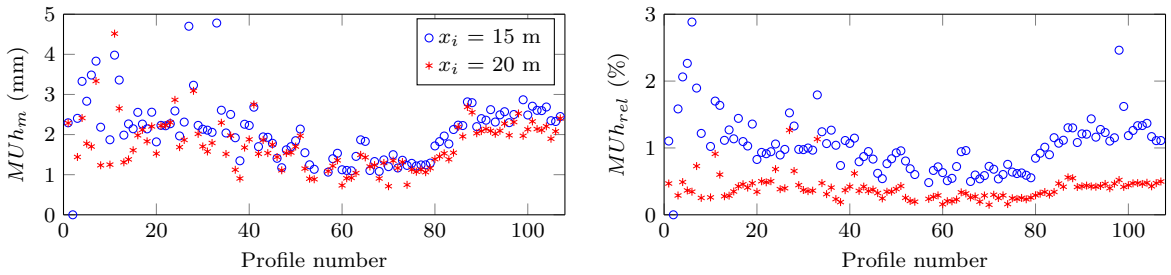

Figure 4.10: MUh_m and MUh_{rel} calculated for each beach profile measured during the entire set of experiments, considering the start of the profile at $x_i = 15$ m (blue circles) and $x_i = 20$ m (red asteriks).

considering $x_i = 20$ m instead of 15 m, the measurement uncertainty if reduced to ± 1.8 mm and the relative error to $\pm 0.4\%$ and the number of MUh_m and MUh_{rel} outliers is significantly smaller. A very similar laser-profiling system was recently proposed by Atkinson & Baldock (2016), which also measures with high resolution the subaerial and subaqueous areas of the beach profile.

Different useful quantities can be deduced from the measurements of the bed position that contribute to the understanding of the change of the beach profile after each experiment. Knowing the flume width ($L = 0.55$ m), the sediment height (h_s) and the length (l_p) of a given profile, and assuming no cross-flume variation, the sediment volume (V) can be calculated,

$$V = L \int_0^{l_p} h_s(x) dx. \tag{4.10}$$

Then, the sediment-volume change resulting from one experimental run can simply be calculated from the difference between the sediment volumes of the initial (V_i) and final (V_f) profiles.

The sediment transport rate (Q_s) can be deduced from the variation of the profile elevation between two consecutive profiles measured before and after a given run, taking into account the equation of sediment mass conservation ($\frac{\partial Q_s}{\partial x} = (1-p)\frac{\partial h}{\partial t}$, where p represents the porosity of the sediment, estimated in about 0.5 in the flume and Δt the duration of the wave condition). At each cross-shore position x during the Δt interval:

$$Q_s(x_f) = Q_s(x_i) - \int_{x_i}^{x_f} (1-p)\frac{\Delta h_s(x)}{\Delta t} dx. \tag{4.11}$$

A correction of the profile volume due to potential variations of porosity or compaction is considered, following the procedure of Grasso (2009). This correction insures that Q_s is zero at both ends of the beach profile. Q_s thus represents a volume of sediment displaced per width unit and time unit and a bulk sediment transport (q_s) can be

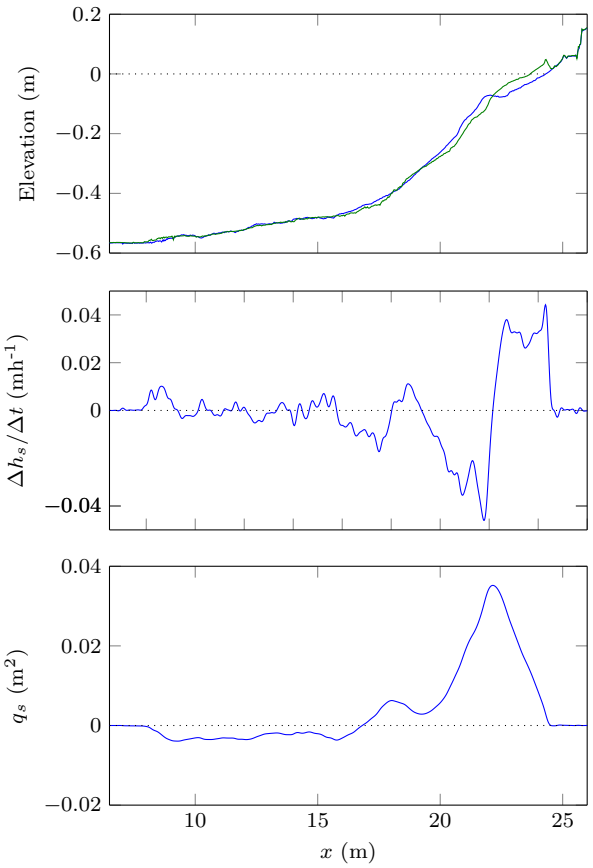

Figure 4.11: Initial (blue) and final (green) bed profiles, variation of sediment height and bulk sediment transport during an example run of C3 (1h duration).

obtained, for each experimental run, by multiplying Q_s by the duration of the wave condition (Δt). The positive (negative) values of Q_s (and of q_s) indicate net onshore (offshore) sediment transport. Fig. 4.11 shows an example of the results obtained for the variation of bed position and bulk sediment transport during one run, between two beach profiles.

A limitation of the bed-profiling technique is that the bed position can only be measured before and after each experiment. However, it was visually observed that the bed position measured during the experiment is not exactly the same. The real bed position during wave motion is found to be deeper than the position measured by the bed profiler since a certain layer of the bed is put in suspension during the runs.

Figure 4.12: Bed mobilization at the breakpoint (photos by Cyril Fresillon - CNRS photothèque).

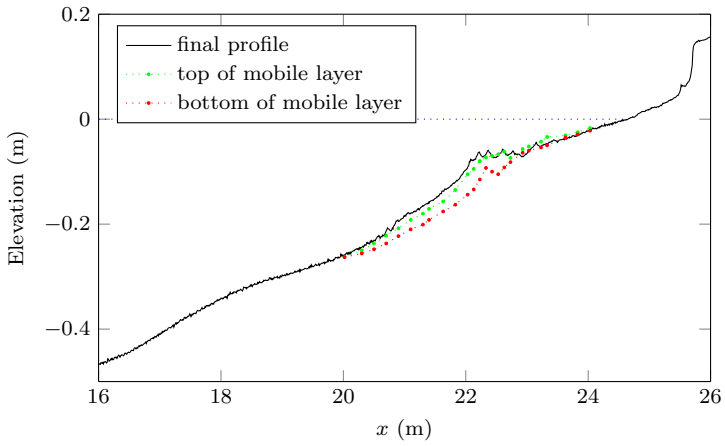

Figure 4.13: Example of the difference between the position of the bed measured before a C1 run and the position visually estimated during one run for the top and the bottom limits of the mobile layer around the breakpoint.

This is particularly important near the breakpoint where a thicker layer of sediment is stirred into motion (both as suspended-load or bed-load) by action of wave breaking. In this zone, the no-motion limit of the bed during the experiments can be around 6

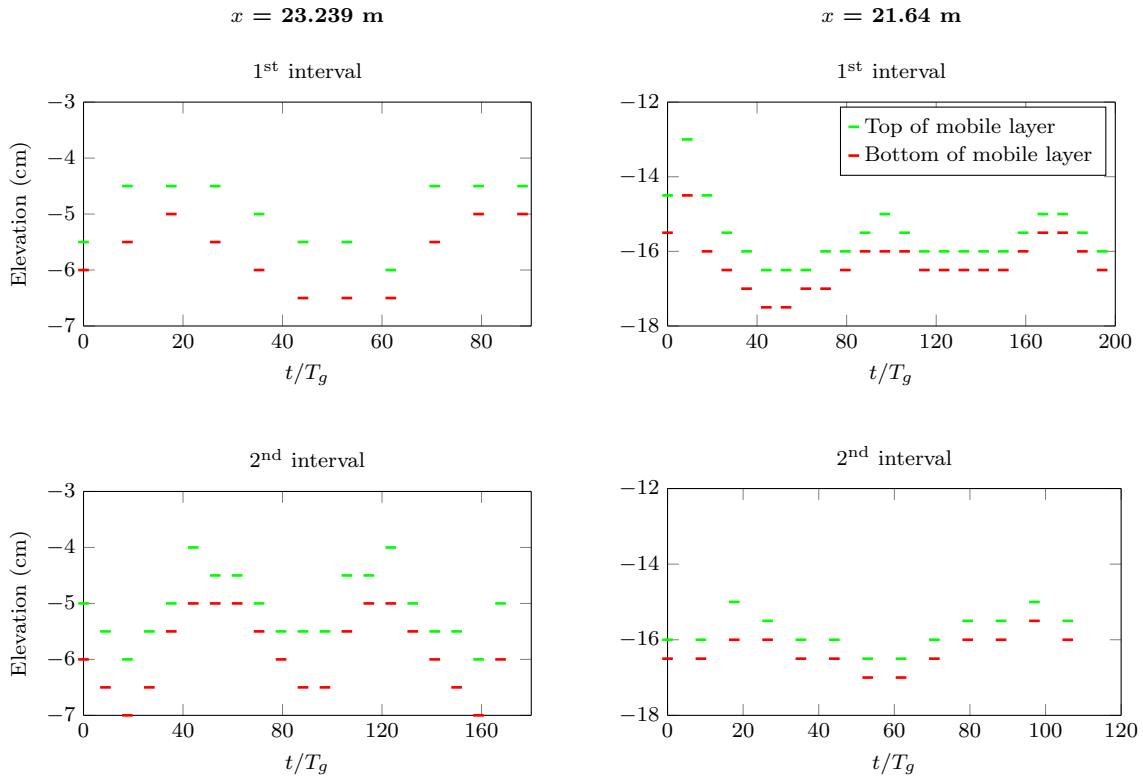

Figure 4.14: Position estimated for the top and the bottom limits of the mobile layer, at two different cross-shore positions (left and right columns) and during two different intervals (top and bottom plots of each column). Note: the measurement intervals have different durations and were obtained at different moments along the runs.

cm lower than the bed position measured after the runs. This bed mobilization near the breakpoint is illustrated in Fig. 4.12.

Fig. 4.13 shows an estimation of the top and bottom limits of the mobile layer around the breakpoint during a C1 run, from where it can be seen that the lower limit of the mobile layer is significantly below the bed position measured by the laser profiler before the start/end of the run. However, these are visual observations which are difficult to precise, in particular because the position of the top and bottom limits of the mobile layer also change during the run. Fig. 4.14 illustrates this change, at two different cross-shore positions, during two different time intervals of C1 runs. Periodic oscillations are obvious for both time intervals and cross-shore positions considered. Along these oscillations, the thickness of the mobile layer is variable.

4.2.5 Velocity measurements

Velocity measurements considered herein for analysis were done at different cross-shore and vertical positions, using a side-looking ADV with a sampling rate of 128 Hz. Measurements along the cross-shore, alongshore and vertical directions were obtained, but the velocity analysis presented herein focuses on the cross-shore velocity. Several parameters can be retrieved from these measurements, such as the mean (u_m) or root-mean-square (u_{rms}) velocities and velocity skewness (Sk_u) and asymmetry (As_u).

Obtaining reliable measurements with an ADV requires some care. Measurements can become noisy both due to emersion of the four beams of the ADV or due to strong sediment-suspension events. In order to distinguish both sources of noise, a joint analysis with a collocated wave gauge must be done. When the wave gauges measure a zero water level, the noise in the velocity measurements is easily linked to the emersion of the ADV. The greatest problem is posed by the episodes of high concentration of suspended sediment in the water, which are more difficult to track. Since this issue is a necessary drawback of acoustic instruments, it is essential to know where exactly clean velocity measurements can be obtained.

The cross-shore positions at which it is possible to obtain measurements of velocity with no noise during the full time series depend on the beach-profile shape and range from about $x = 21.5$ m to $x = 24$ m. For the vertical position of the ADV, a limit of about 3 cm height above the bottom is mandatory to avoid measurement noise and the ADV has to be placed at a minimum distance of 3 cm from the free-surface at rest, to insure that at least the two lower beams of the probe are immersed during the entire duration of the runs. These limits must however be considered together with visual observation during the experiments, since for some particular positions (such as near the breakpoint) sediment suspension may be high, not allowing good measurements

even within the mentioned limits. When isolated spikes were present along the time series, they were corrected using both a de-spiking method by Mori *et al.* (2007) and a low-frequency pass filter at 2 Hz. Fig. 4.15 shows the example of some raw (light green) and de-spiked (green) measurements at distinct cross-positions which shows the noise-level differences between cross-shore positions.

The noise in the velocity measurements due to reflection of the acoustic signal in the sediment particles can be a problem when the aim is to obtain good-quality accurate velocity measurements. However, it can also be an advantage.

During the experiments, no instruments capable of directly measuring sediment concentration were available. While the total sediment transport per wave condition is calculated from the changes of the bed position measured and the beachface bed position can be inferred from the swash-zone wave gauges, the sediment suspended during wave action cannot be measured. As it will be referred later in this chapter, it is important to track the episodes of larger sediment suspension and, especially, their phasing relatively to the wave groups. For this purpose, the noise in the velocity

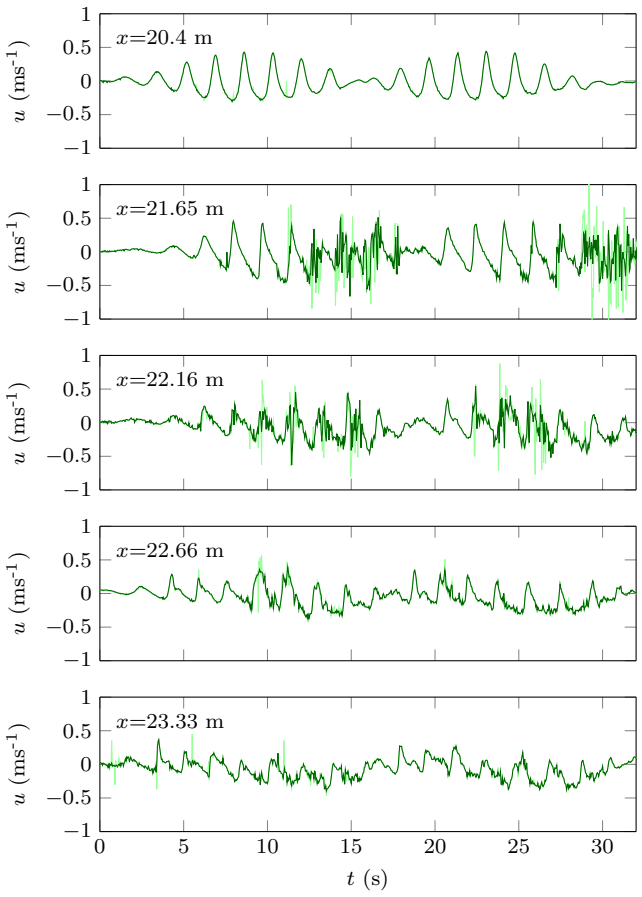

Figure 4.15: Cross-shore velocity measurements, for C2, at different cross-shore positions. Light green: raw measurements; dark green: measurements de-spiked following the method of Mori *et al.* (2007).

measurements becomes an advantage. When the water is sufficiently high to prevent the emersion of the ADV sensor, which was always the case when it was positioned offshore of the swash zone, all the noise in the velocity measurements is directly linked to the presence of sediment in the water column at the sensor height. Hence, the ADV measurements can give an indication of at which cross-shore positions there is more sediment suspension, at which height from the bottom and during which interval of the wave groups. For example, Fig. 4.15 illustrates high sediment suspension at the end of each short-wave group, at $x = 21.65$ m (second plot), which is the approximate cross-shore position of the bar/breakpoint at the time of the measurements. Significant sediment suspension also occurs just after breaking, at $x = 22.16$ m (third plot), but it is weaker.

The episodes of larger sediment suspension inferred from the velocity measurements were also confirmed by visual observation during the experiments. The side-walls of the LEGI wave flume are made of glass, which allows the direct observation (or filming) of the sediment suspension events during wave action, as it is shown in Fig. 4.16.

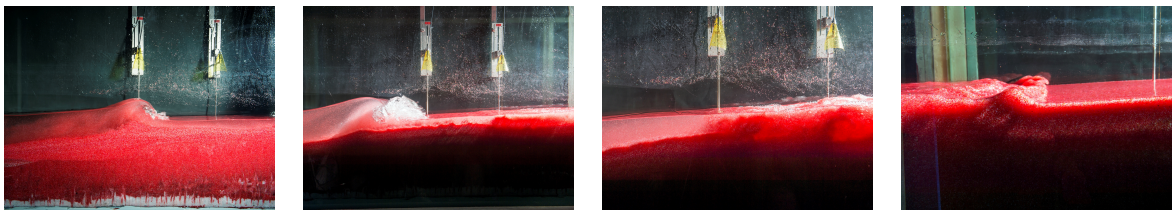

Figure 4.16: Examples of sediment suspension observed in different zones of the beach profile (photos by Cyril Fresillon - CNRS photothèque).

SERR1D contribution

The cross-shore positions where the flow-velocity measurements are more important are those near the breakpoint and in the surf zone. This is where high sediment-transport rates are expected to occur. However, as it was discussed before, these are also the positions where velocity measurements are more difficult to obtain and more noisy. In order to overcome this limitation, the SERR1D model (described in chapter 3) can be used to obtain an estimation of the cross-shore velocity for the different wave conditions simulated.

For all the three wave conditions, clean velocity measurements were available at $x = 20.4$ m, the end of the shoaling zone. Since at this position there were collocated measurements of free-surface elevation and velocity, the measured free-surface elevation time series can be retrieved from the wave gauges and the reflected IG waves can be extracted from the total signal (following the method of Guza *et al.* (1984) described in

chapter 3). This time series is a more precise representation of the waves present in the flume at the end of the shoaling zone (already including reflected IG waves) than the theoretical solution that is provided at the wave-maker (which does not include reflected IG waves) and thus it is used as the input wave condition for SERR1D.

The SERR1D numerical model, as it is applied in this work, does not have a morphodynamics module. Therefore, the bottom position is defined as constant along each run, which is not true in reality (especially near the breakpoint) and further implies that a real bottom-friction coefficient is not constant (both in space or in time). However, the model does not consider a mobile bed and the friction coefficient is set, for the simulations presented in this section, to 0.002. The values of the breaking-model parameters are the same as ones discussed in chapter 3.

C2 was initially used for model validation. Fig. 4.17 shows the comparison of free-surface elevation and velocity experimental and numerical data obtained for a model simulation of two wave groups of C2 wave condition and also illustrates the uncertainty related to the bed position.

In a general way, taking into account the limitations mentioned, the model is capable of representing both the free-surface elevation and the cross-shore velocity of short-waves. However, it underestimates IG waves, particularly in the inner-surf and swash zones.

IG-waves reflected at the wave-maker are already present at the end of the second wave group for cross-shore positions close to the coast. This results in an increase of IG-wave height near the coast that the model partially reproduces.

The bed position measured at the end of each experiment is not exactly the bed position over which the waves act, since a certain layer of the bed is put in suspension during the runs: the real bed position during motion is found to be deeper than the position measured by the bed profiler. This contributes to small differences between measured and simulated data, particularly near the breakpoint, which is a zone of great bed mobilization during the runs. These differences are illustrated in Fig. 4.17, between the darker and lighter markers.

Fig. 4.18 shows the times series of model and experimental data for several cross-shore positions. As it was already stated, the model does very well in the shoaling and outer-surf zone, representing even the correct phasing of the waves along the groups. However, in the inner-surf and swash zones, there is an IG-wave height difference between numerical and experimental data (particularly at the end of the second wave group), which promotes shallower short-wave troughs (and thus less negative velocities) at the trough of the IG wave, for the numerical data. Nevertheless, the phasing of each wave remains very good along the beach profile, even for velocity.

Besides the limitations already mentioned, there is also the difficulty in validating

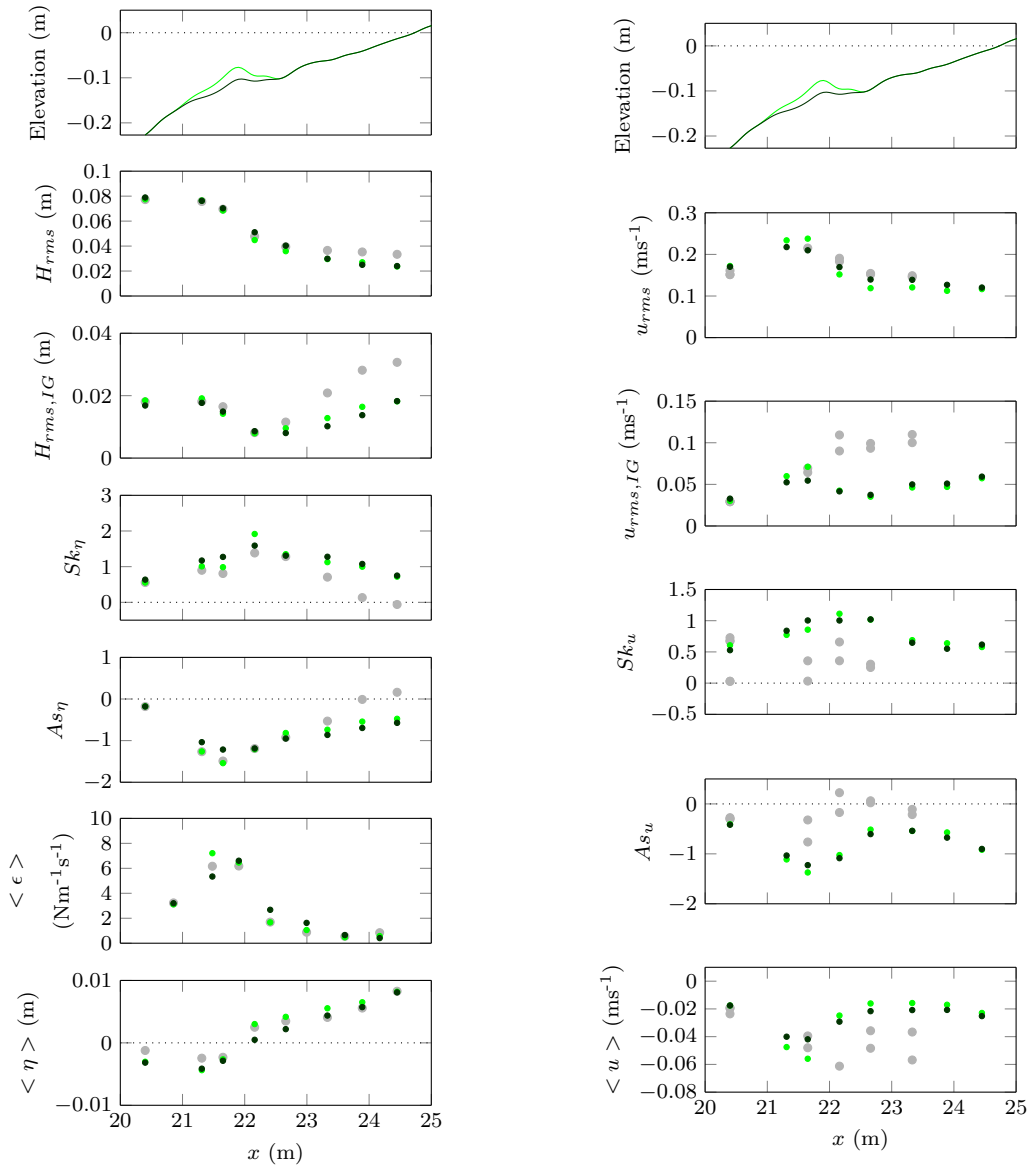

Figure 4.17: Free-surface elevation (left column) and velocity (right column) statistics for C2, for experimental and numerical data. In light green, considering the original beach profile measured at the end of the run; in dark green, a profile slightly lower around the breakpoint, visually estimated as the inferior limit of the mobile layer during wave action. The experimental data are shown in grey.

the numerical results for velocity, since the velocity measurements are usually very noisy around the breakpoint and, depending of the bed profile, until the shoreline. Several velocity measurements are plotted in Fig. 4.17, although between $x = 22$ m and the shoreline they are only indicative of the order of magnitude of the velocity (and of the total u_{rms}), and cannot be used to validate Sk_u, As_u and $\langle u \rangle$, which are very sensitive quantities to noise in the measurements. For some cross-shore positions, two velocity measurements made during runs of C2 are plotted, which illustrates the dispersion in the statistics that can result from the noise in the measurements. Moreover, velocity

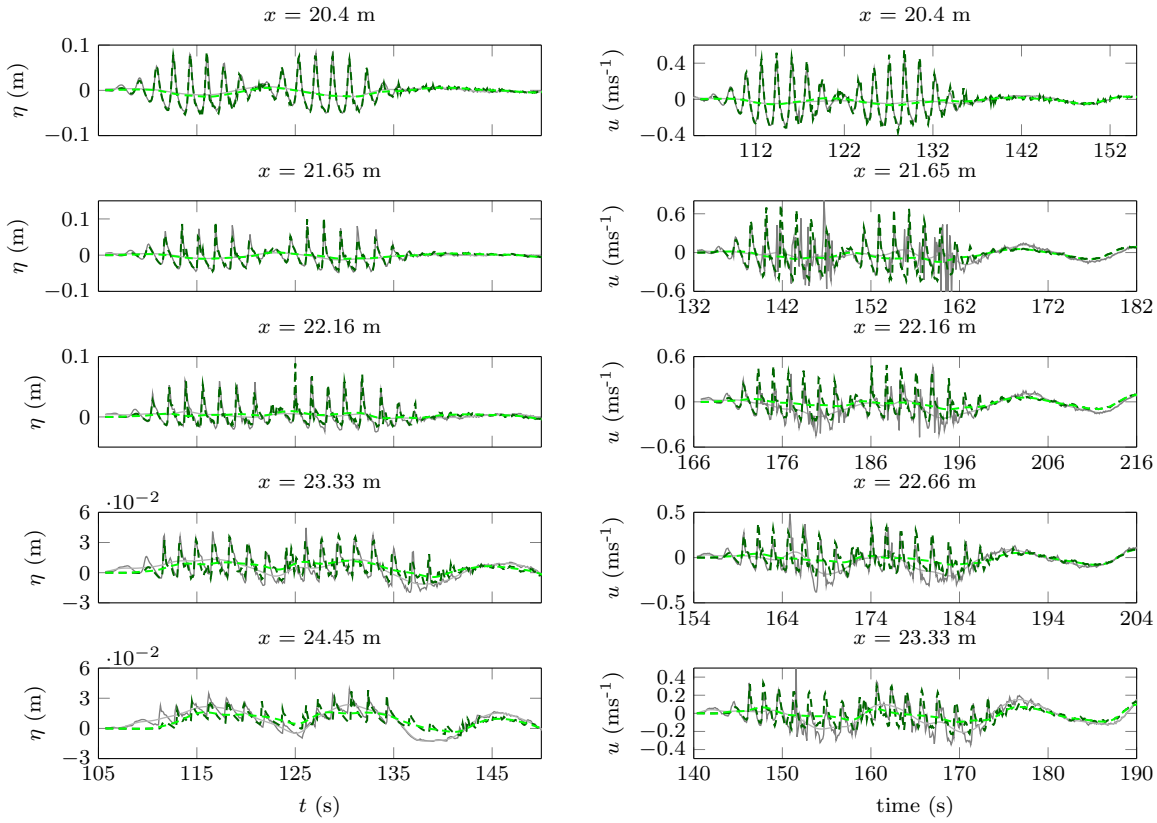

Figure 4.18: Time series of free-surface elevation (left column) and cross-shore velocity (right column), for total (darker) and IG-waves only (lighter), for experimental (grey) and numerical (green) data, for C2, at different cross-shore positions. The velocity measurements were obtained during different experimental runs.

measurements were made at a given vertical position in the water column and SERR1D model provides velocity results integrated over the entire water column, which induces differences between experimental and numerical results, as was already discussed in chapter 3. The limitations of the velocity measurements make it unavoidable to trust completely the free-surface elevation data for validating the model near the breakpoint.

Fig. 4.19 represents the results of the simulation of C1 and C3. For C1, which has even greater IG-wave heights in this zone than C2, the underestimation is more significant; for C3, which has smaller IG-waves heights, the model is capable of estimating almost correctly the measured data, with a small overestimation of skewness and asymmetry.

Overall, SERR1D represents the main free-surface elevation trends sufficiently well (and u_{rms}, for C2) and can thus provide an estimation of the cross-shore velocity for the different wave conditions, even if only in a qualitatively (and comparative between conditions) way.

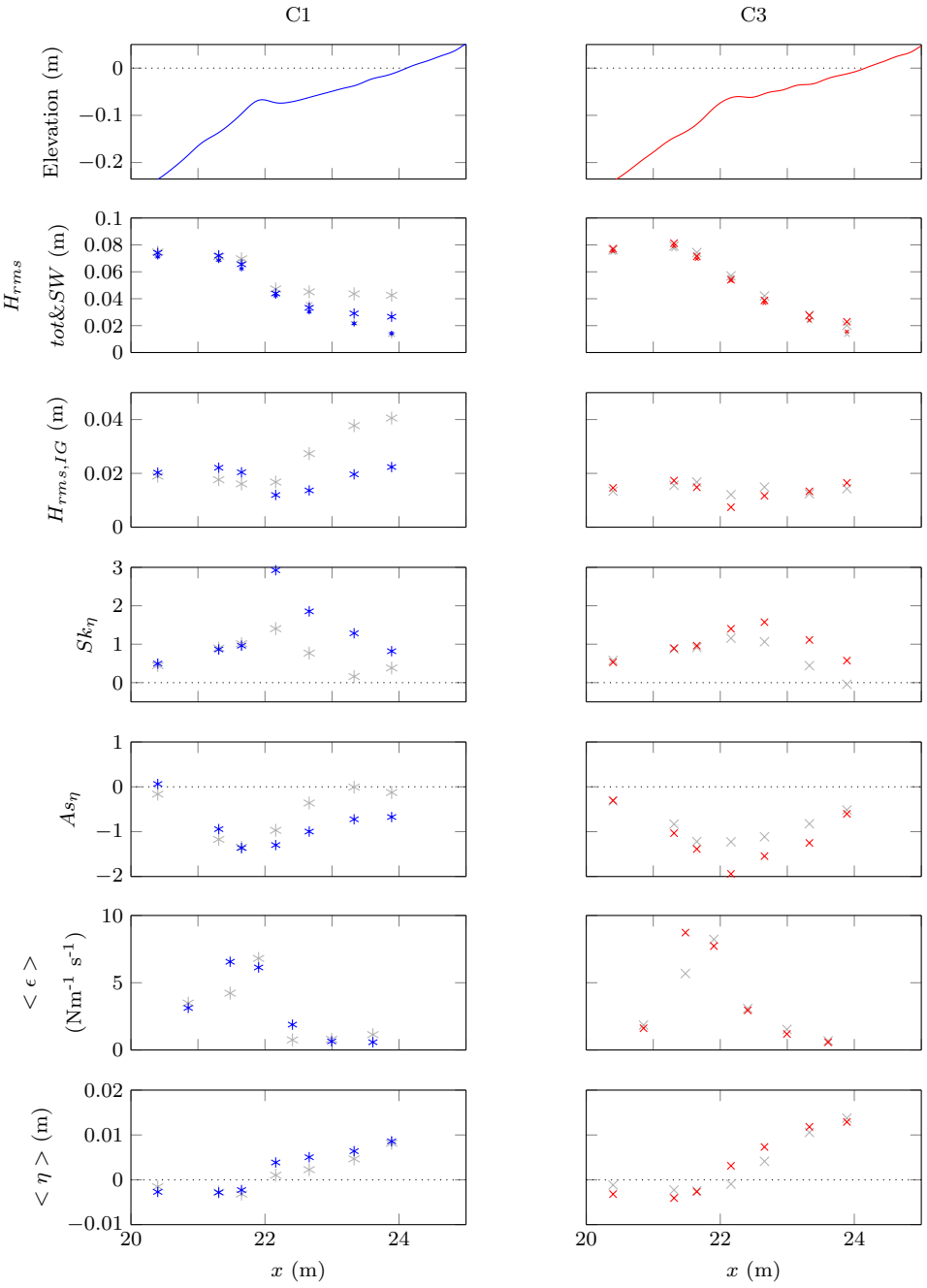

Figure 4.19: Free-surface elevation statistics for C1 and C3, for experimental (grey) and numerical (blue and red) data.

4.3 Beach evolution towards equilibrium

When the same wave condition is run for long enough, an equilibrium profile is attained. This means that the different transport mechanisms at play start balancing each other at some point in time and the profile shape stops evolving. The time needed for this to happen depends on how different is the initial profile from the equilibrium profile.

Fig. 4.20 depicts the equilibrium beach profiles obtained for each wave condition. According to Grasso *et al.* (2009a), the shape of the equilibrium profile depends only on the Dean number and thus on significant wave height and peak period and the sediment settling velocity. However, Fig. 4.20 shows that, even though C1, C2 and C3 have the same H_s, T_p and sediment particles, the equilibrium beach-profile shape is different, particularly in the shallower zones (namely, in the beachface). At first sight, four features mark the main differences between the equilibrium profiles: the beach slope, the depth of the surf zone, the width of the emerged beach and the presence (or absence) of a bar. C3 has shallower surf and swash zones and a larger emerged beach, while for C1 the shallowest zones of the beach profile have greater water depth and the sediment is instead accumulated in deeper waters, around $x = 18.5$ m. The C2 surf and swash zones are deeper than for C3 and shallower than for C1. The C2 equilibrium profile is the only one with a marked bar separating the shoaling and the surf zones. For depths greater than $x = 16$ m, the beach profiles are very similar for the three wave conditions.

Fig. 4.21 presents the wave statistics obtained for each wave condition during the equilibrium runs. The major disparity that can be observed between wave conditions is the IG-wave height, which is especially smaller for C3 wave condition along the entire beach profile, and smaller for C2 than for C1 around $x = 21$ m. Furthermore, the bar (C2) and slope break (C1 and C3) are located at a cross-shore position of minimum IG-wave height. This minimum is located at the central nodal point of the prevailing free-surface elevation standing pattern (mode 2, as seen in Figs. 4.5 and 4.6) and is located slightly further offshore for C2 than C1, and even more for C3 (as predicted for the second theoretic resonant mode of each wave condition in Fig. 4.5). Both factors, that (i) IG-wave height is the largest difference in wave statistics between wave conditions and that (ii) an important feature of the beach profile (the bar or the slope

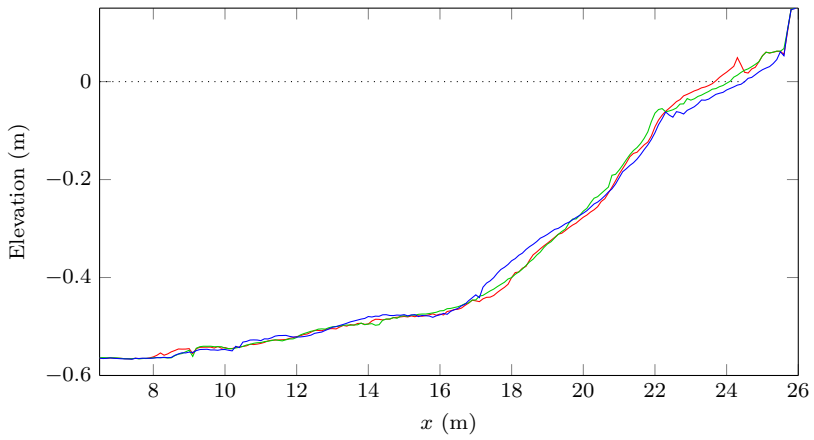

Figure 4.20: Equilibrium profiles for C1 (blue), C2 (green) and C3 (red).

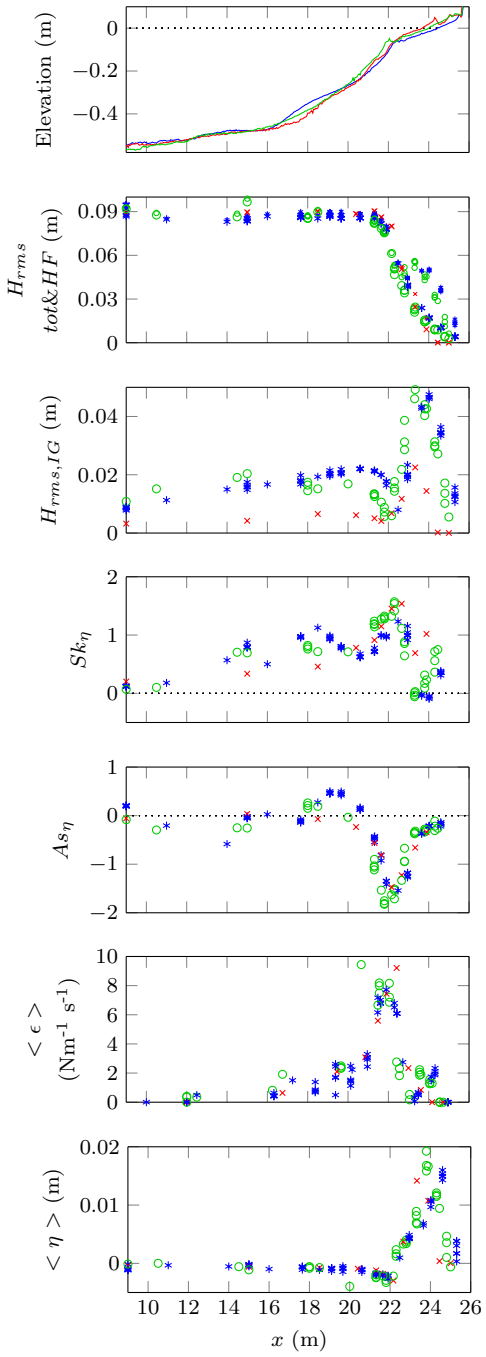

Figure 4.21: Free-surface elevation statistics for C1 (blue asterisks), C2 (green circles) and C3 (red crosses) equilibrium runs. Note: not the same number of experiments were run for each wave condition over the corresponding equilibrium profile, which justifies the different number of measurements presented for each.

break, where H_{rms} starts decreasing, signaling wave breaking) corresponds to a node of the IG-wave height, hint a possible role of the IG waves in the shape of the beach profiles.

Fig. 4.22 shows the evolution of the beachface bed position (in black) at a defined cross-shore location, during part of C1, C2 and C3 equilibrium runs, tracked by a wave

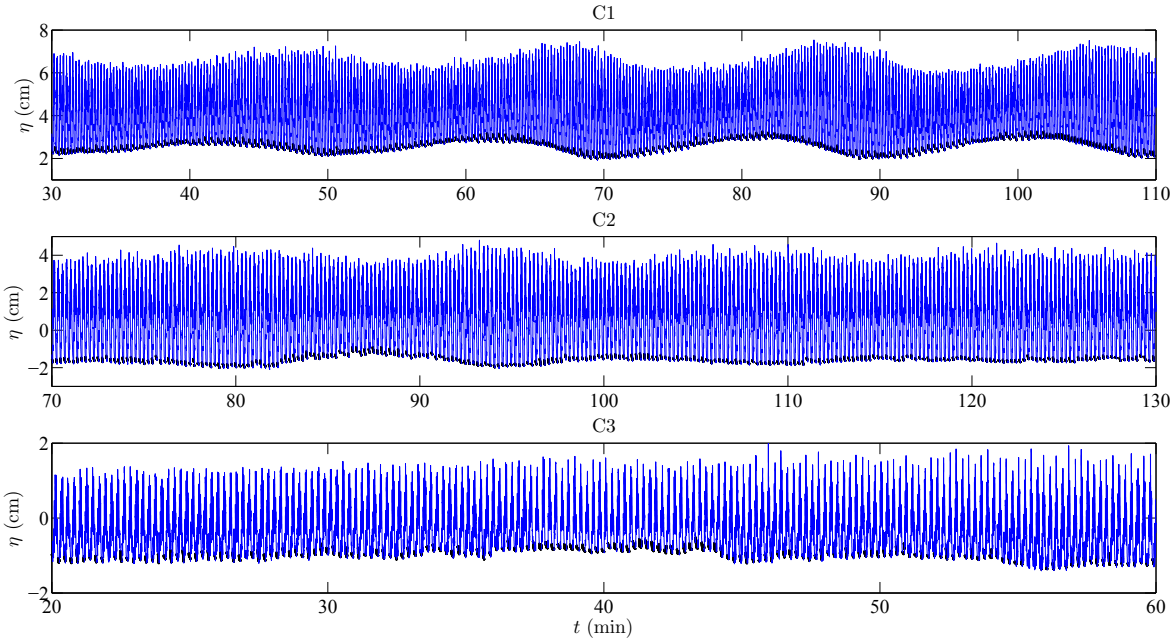

Figure 4.22: Swash (blue) and bed-level (black) evolution during part of C1 ($x = 24.6$ m), C2 ($x = 23.8$ m) and C3 ($x = 23.89$ m) equilibrium runs. Note: The runs do not have the same duration, but they are all equilibrium runs.

gauge located in the swash zone (at less than 20 cm of the still-water shoreline position), following the method previously described in the subsection 4.2.3. Even though for the three wave conditions the measurements represented correspond to equilibrium runs, the beachface bed position is not constant for all. For C3 the bed position measured is effectively the same along the entire run, except for very small variations of a few millimeters. For C2, some variations of about 0.5 cm are present but tend to disappear during the run. However, for C1, even though the mean bed position remains constant (around 2.8 cm above the mean water level, for the example of Fig. 4.22), there are periodic variations (of up to 1 cm height) with a timescale of about 18 min (which will be called "oscillations" in the rest of this manuscript). As C1 is the wave condition with the greatest IG waves, once again a link between IG-waves and the beach profile shape (in this case, the height of the beachface) is suggested.

Fig. 4.23 shows the evolution in time of the IG-wave height along the beach profile, for the C1 equilibrium run whose beachface bed-position variation was presented in de top plot of Fig. 4.22. Like for the beachface bed position, an oscillation of around 18 min can also be seen in the IG-wave height in different regions of the beach profile. Maxima (in time) of the bed-elevation near the shoreline (around $x = 24.6$ m, for C1 equilibrium run) are associated to maxima (in time) of IG-wave height at the same locations, in the surf and swash zones, and in deeper waters. The cross-shore position of the minimum of IG-wave height located around $x = 22$ m (and associated to the

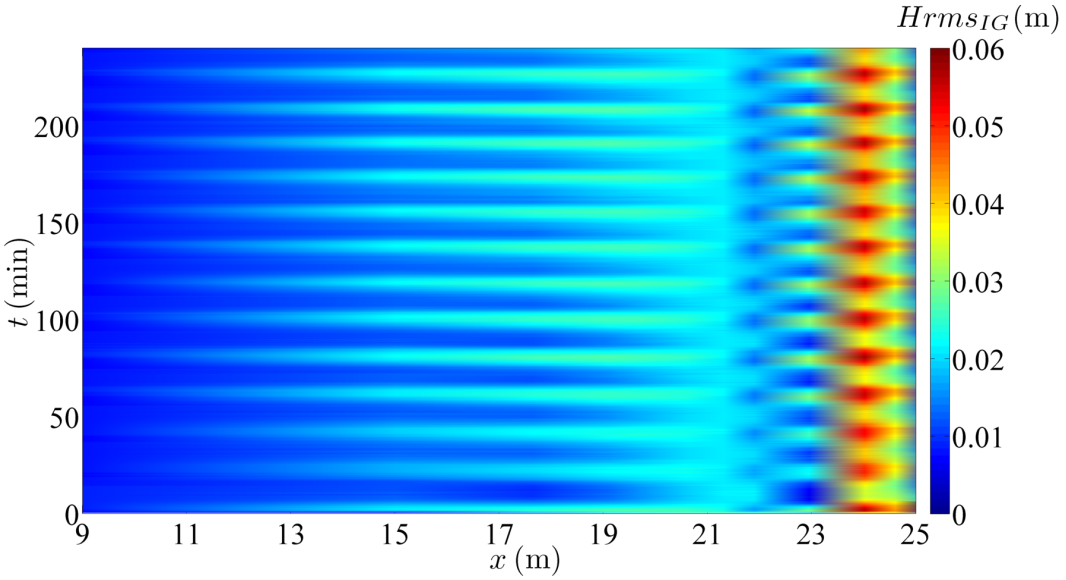

Figure 4.23: H_{rms} of IG waves along the beach profile calculated for each two wave groups during C1 equilibrium run.

bar/slope-break position) varies in the cross-shore direction in around 1 m (between $x \approx 21.9$ m and $x \approx 22.9$ m), also responding to the 18-min oscillations.

Since (i) for C1 (greater IG waves near the shore) there are marked oscillations of the beachface bed position, while for C3 (much smaller IG waves than C1 and C2) only minor variations are observed during the equilibrium run and (ii) the oscillation of the beachface bed position is coupled to the oscillation of IG-wave amplitude, there must be an implicit link between the oscillations of the beachface bed position and the action of the IG waves (or wave groups). However, the beachface bed-position oscillations have a long period of 18 min, too long for being only of the timescale of hydrodynamic forcings (which are expected to be of the order of a few minutes). Therefore, even though an implicit link between the oscillations of the beachface bed position and the IG waves seems to exist, the IG-waves cannot be the sole responsible agent: there must exist a morphodynamic feedback, linked to the IG-wave motion, that also plays a role in the dynamics of the oscillations.

Fig. 4.24 shows the sediment transport patterns of five C1 20-min runs for which the oscillation of the beachface is particularly noteworthy. These are runs with a shorter duration than the equilibrium runs and with a beach profile still far from the equilibrium profile, but which mimic the behaviour of the beachface during C1 equilibrium. The sediment transport patterns observed highlight once more the link between the oscillations of the beachface and the oscillations of the surf and inner-shoaling zones, already observed in Fig. 4.23 for the IG-wave height. When the upper beach is eroded (accreted), accretion (erosion) dominates the surf and lower swash

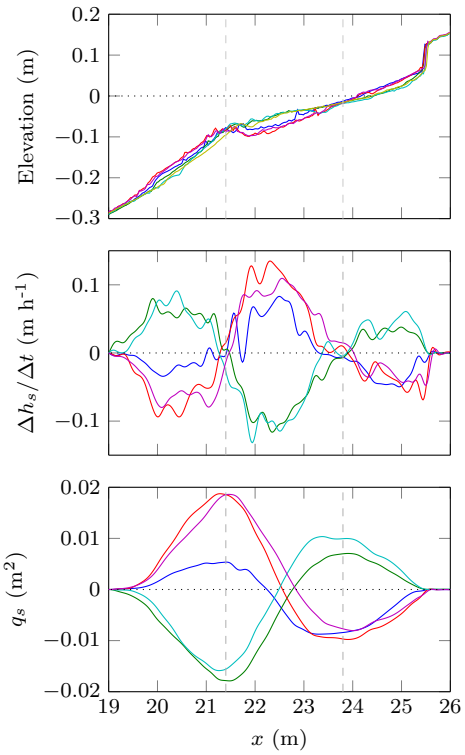

Figure 4.24: Beach profiles, variation of sediment height and bulk sediment transport for five C1 20-min runs. Color code, from the initial profile to the last one: blue, green, red, cyan, violet, yellow (yellow for the top plot only). Grey dashed lines mark the approximate cross-shore positions for which the bed remains at the same position during the five runs (nodal points of the bed-profile oscillation).

zones, smoothing (sharpening) the bar and erosion (accretion) also occurs at the end of the shoaling zone. This dynamics is associated with an onshore (offshore) sediment transport until the mid-surf zone, and an offshore (onshore) sediment transport further up the beach. In the outer-shoaling zone and in deeper waters, sediment transport is less linked with the dynamics of the upper profile, responding to sediment transport processes of longer time scale.

Fig. 4.25 shows the IG free-surface elevation and velocity evolution along a C1 equilibrium run, for a single cross-shore position located at the end of the shoaling zone ($x = 21.9$ m). During this long run, input wave conditions at the wave-maker remained constant. Nonetheless, since the IG waves that are generated by the wave-maker at every instant are added to the ones that remained in the flume since the beginning of the run, the phase of the IG waves changes along the run. At this cross-shore position (which is close to an IG free-surface-elevation minimum), the oscillation (the periodic oscillation of 18 min mentioned before) of the phase of the incident IG waves ($\Delta\phi_{inc}$) is approximately in anti-phase to the oscillation of the reflected IG-wave phase ($\Delta\phi_{ref}$): as $\Delta\phi_{inc}$ increases, $\Delta\phi_{ref}$ decreases, which results in weak oscillations of the total IG-waves phase along the run. These oscillations of the incident and reflected IG-waves phases

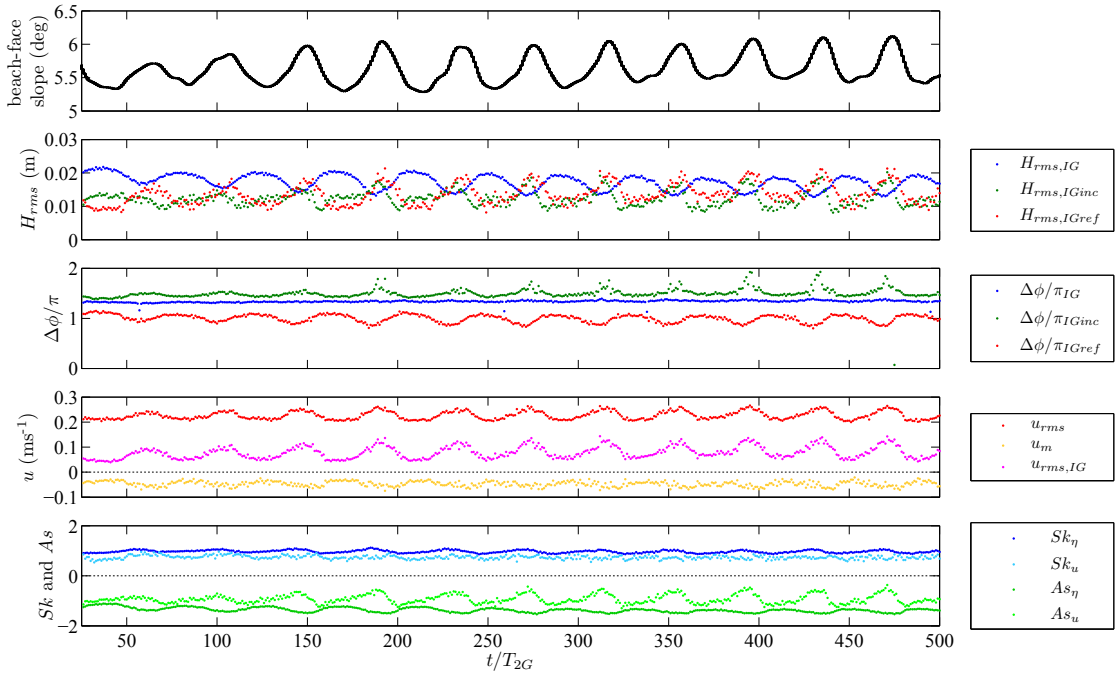

Figure 4.25: Statistics of a C1 equilibrium run computed for each pair of wave groups, at $x = 21.9$ m. 1st plot: slope of the beachface calculated for the beach length comprised between the last two wave gauges ($x = 24.6$ m and $x = 25.3$ m); 2nd plot: $H_{rms,IG}$ of the total IG waves and incident and reflected components only; 3rd plot: phase of IG total, incident and reflected waves relatively to the wave envelope of the two short-wave groups; 4th plot: u_{rms} of total and IG waves only and u_m; 5th plot: Sk and As of η and u.

results in oscillations of the incident ($H_{rms,IGinc}$) and reflected ($H_{rms,IGref}$) IG-waves heights. These can be in phase or not with the oscillations of $\Delta\phi_{inc}$, depending on the cross-shore position considered. Since $H_{rms,IGinc}$ and $H_{rms,IGref}$ vary, the total IG-wave height also varies with the same 18-min period. The signature of these oscillations is present as well in the velocity data, particularly near velocity maxima positions (such as the cross-shore position considered in Fig. 4.25, where high velocities are expected and thus variations are more notorious). Greater IG-wave velocity is observed close to the maximal $\Delta\phi_{inc}$ values and minima $H_{rms,IG}$. Skewness and asymmetry are also affected by the changing of the IG-wave phase.

The variation of the absolute values of all these hydrodynamic variables along the C1 equilibrium run is linked to the oscillations of the beachface previously mentioned, which are in turn linked to the dynamics of the entire profile. The changing of the beachface slope and associated change in the surf-zone morphology can, in turn, be influencing the hydrodynamics. Slow accretion of the beachface, when IG-wave height is minimal, results in a more reflective beachface, which contributes to a more energetic swash dynamics and to greater IG-wave reflection, thus promoting IG-wave growth. The accretion of the beachface is accompanied by an accretion just offshore of the

breakpoint and by the delineation of a better-defined bar (due to the transport of sediment from the surf zone to the beachface), which eventually shifts the location of short-wave energy dissipation from the lower beachface to the surf zone. This results in a less energetic swash zone and a less reflective beachface, which promotes IG-wave height decrease. When an IG-wave minimum height is reached, the slow accretion of the beachface can start again and so on.

Since several mechanisms are constantly at play along the beach profiles, a static equilibrium (for which the beach profile remains always at the same position) is hard to attain, particularly if one or more mechanisms are periodically enhanced. Instead, a dynamic equilibrium is more likely, with multiple slightly-different profiles oscillating around a certain profile shape. In the flume, the oscillations of the beach profile around an equilibrium shape are enhanced by the presence of the "trapped" IG waves that reflect at the beach and re-reflect at the wave-maker, generating standing modes that are only dissipated after the end of each run. This effect is particularly important for C1, since it has greater IG waves.

The equilibrium profiles reached by several long runs of C1, C2 or C3 wave conditions are not the same that would be attained if only a few short-wave groups were run with the same wave conditions, run by run, until equilibrium, since long runs allow steady IG standing-wave patterns to establish and be enhanced, contrary to very-short runs.

4.4 Beach response to wave groups

The multiple feedbacks between the hydrodynamics and the morphology make it difficult to further dissect the dynamics of the oscillations observed during the long equilibrium runs. Therefore, two wave-group runs were conceived to allow the analysis of the effect of each wave condition on the beach profile without the influence of IG waves artificially added and enhanced by re-reflection at the wave-maker. This results in a more realistic approach since, in nature, waves can be reflected at the beach but they will then propagate towards deep waters and will not be re-reflected back.

During each short run only two wave groups were ran (27.2 s). In this case, the IG waves re-reflected at the wave-maker will only arrive at each cross-shore position at the end of the second short-wave group. However, IG waves produced by the first wave group that reflect at the beach will influence the second wave group.

Fig. 4.26 shows the propagation, both in time and in space, of the two wave groups and the IG waves associated, for each of the three wave conditions. The beach profiles during the three runs, represented in Fig. 4.27, were very similar (except for a deeper trough around $x = 22$ m, for C3 run initial profile), therefore the differences observed

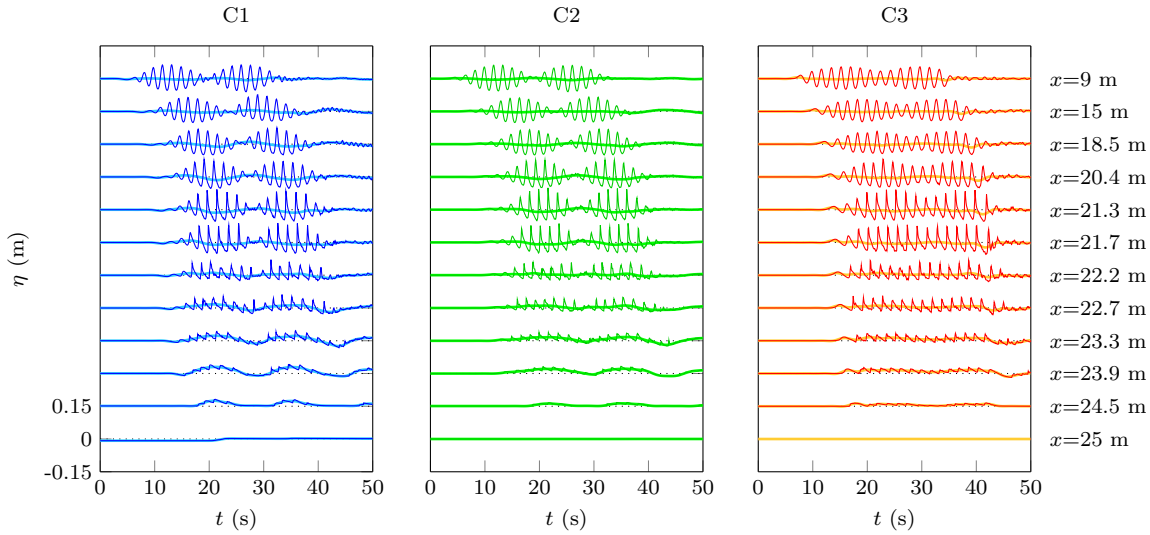

Figure 4.26: Time series of η at different cross-shore positions, for the three wave conditions (the thicker and lighter-coloured lines represent the IG waves).

are directly linked to the wave conditions and not to distinct morphological features.

Since the short waves have the same energy for the three wave conditions, the differences that may be found in the hydrodynamics and morphodynamics are necessarily, directly or indirectly, linked to the IG waves. The IG-wave period is also the same, it is the IG-wave height and phasing that change. The following analysis aims at understanding what is the importance of these two parameters of IG waves on the overall hydrodynamics and morphodynamics along the beach profile and what are the mechanisms behind a distinct morphological behavior for each wave condition. For that purpose, short runs of two wave groups, run over three different types of initial beach profiles, are presented. The differences in the morphodynamics between wave conditions are highlighted and an analysis of the hydrodynamics is subsequently done to try to identify the mechanisms behind these differences. This analysis is extended with velocity experimental and numerical data and the results of monochromatic IG-wave

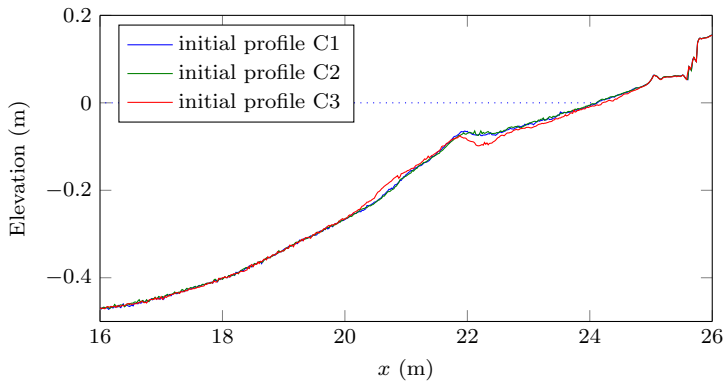

Figure 4.27: Initial beach profiles for the three short runs of C1, C2 and C3 shown in Fig. 4.26.

runs.

The short runs were run after long runs or after other short runs. This implies that C1, C2 and C3 were not always run over the same initial profile. They were run over different profiles, similar until about $x = 20$ m and with greater differences from the end of the shoaling zone until the upper beachface. The initial beach profiles can schematically be divided into three types, depicted in Fig.4.28: one with slightly more dissipative surf and swash zones and a smooth slope break between the surf and the shoaling zones (type A); one with a more defined bar just before $x = 22$ m, deeper surf and swash zones and steeper surf-zone beach slope (type B); and one with no bar and almost no slope break, a significantly more shallow beachface and a wider emersed beach (type C). This last one was only obtained when a C3 long run was run, which was done once in the full set of experiments.

All three types of profiles are very similar until around $x = 20$ m. The breakpoint is located near $x = 22$ m for the three wave conditions. Contrary to profiles of type B, profiles of type A and C have no marked bar near the breakpoint and have shallower surf and swash zones. Type C profiles have the shallowest surf and swash zones (about 4-cm and 2-cm shallower than for profiles of type B and A, respectively), which implies that the shoreline is positioned further offshore, about 1 m from type-B-profiles shoreline and 0.5 m from type-A-profiles shoreline. All profile types produced during the experiments have a mean beach slope typical of intermediate beaches in nature.

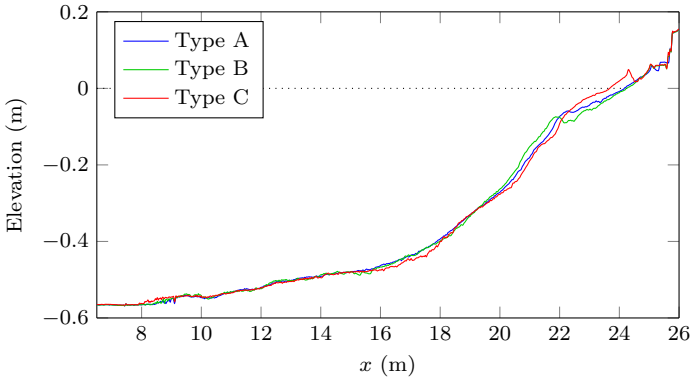

Figure 4.28: Beach profiles representative of types A, B and C.

4.4.1 Morphodynamics

Depending on the initial profile, the sediment transport induced by each wave condition can be different. However, for different runs of each wave condition, a specific tendency (or pattern) of sediment transport can be observed, which is distinct for the three wave conditions. The way each wave condition acts on each type of initial

bed profile (eroding, accreting, ...) allows an understanding of its sediment transport potential.

Since in this section of the work the focus is on the two wave-groups runs, the analysis of sediment transport is done for the upper section of the profile (onshore of $x = 20$ m), as the small duration of these runs was not enough to induce significant change in the deeper parts of the profile. Fig. 4.29 shows the effect of three C2 short runs over initial beach profiles of type C (with the shallowest surf and swash zones), type A (with surf and swash zones deeper than type C) and type B (with the deepest surf and swash zones).

For initial profiles of type C and A, C2 promotes erosion of the surf and swash zones, concomitant with an offshore transport that then results in accumulation in the upper-shoaling zone. Acting over the shallower surf zone and beachface of type C profile, the maximum magnitude of the offshore transport promoted by C2 diminishes by only around 25% from the first to the last run. For the type A profile, C2 capacity for offshore transport decreases significantly to less than half in just two runs. When

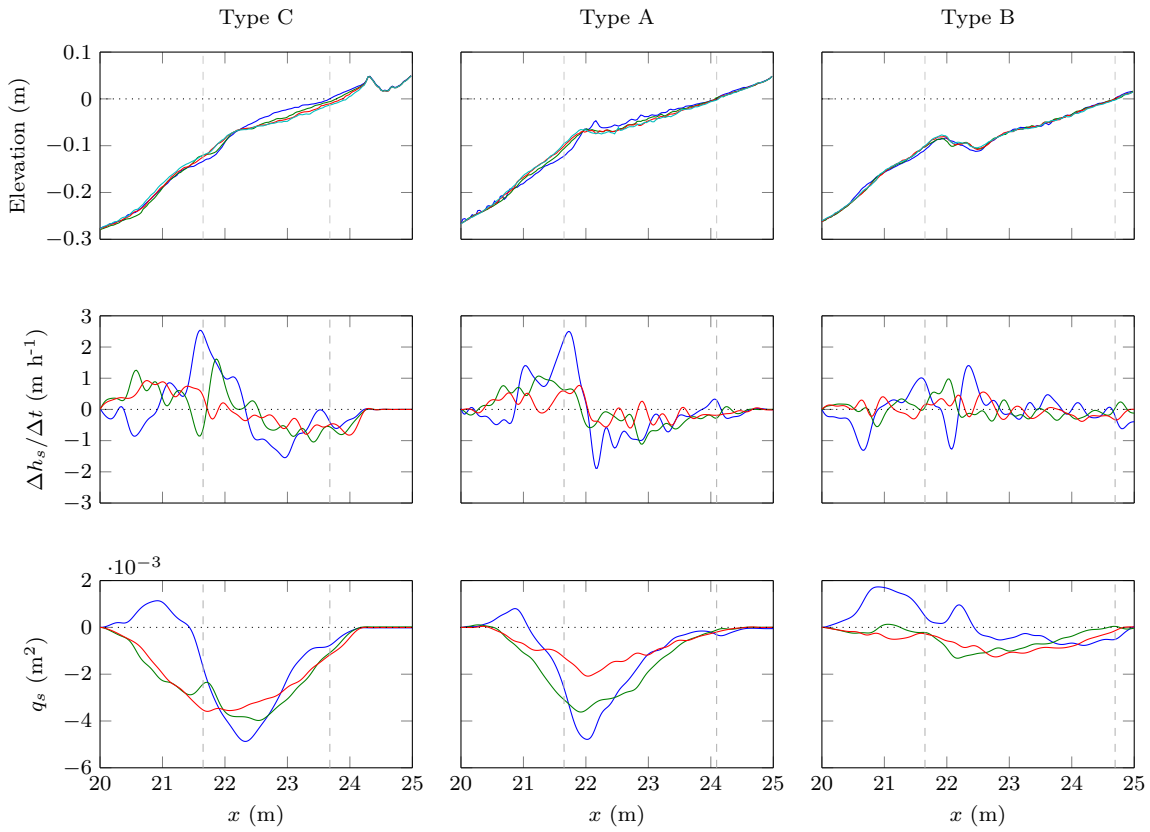

Figure 4.29: Beach profiles, variation of sediment height and bulk sediment transport for groups of three C2 short runs run over initial beach profiles of types C, A and B. Color code, from the initial profile to the last one: blue, green, red and cyan (cyan for top plots only). Grey dashed lines mark the approximate position of the breakpoint and the shoreline.

the initial profile is of type B, C2 is even less capable of offshore transport, showing very low rates of transport, and the first run even has an accreting action near the breakpoint.

C1 is the wave condition with more IG waves at the upper beach, and a different IG-wave phasing relative to the group. Fig. 4.30 illustrates how C1 acts on initial beach profiles of types A and B. As C2, C1 promotes erosion in the surf zone with offshore transport towards the shoaling zone, for initial profiles of type A. However, erosion is more intense just after the breakpoint (instead of being more gentle but over the entire surf and swash zones) and the magnitude of the maximum offshore transport does not weaken significantly along the three runs. Furthermore, for C1 runs, the sediment that is deposited in the shoaling zone, is deposited at a location further offshore than for C2. For the type-B initial profile, while C2 no longer promotes a marked offshore transport, C1 is still capable of doing so, continuing to erode the trough after the breakpoint, accentuating the bar. The sediment eroded keeps being transported offshore as for C1-over-type-A case, and deposited between $x = 20.5$ m and $x = 22$ m. It is thus

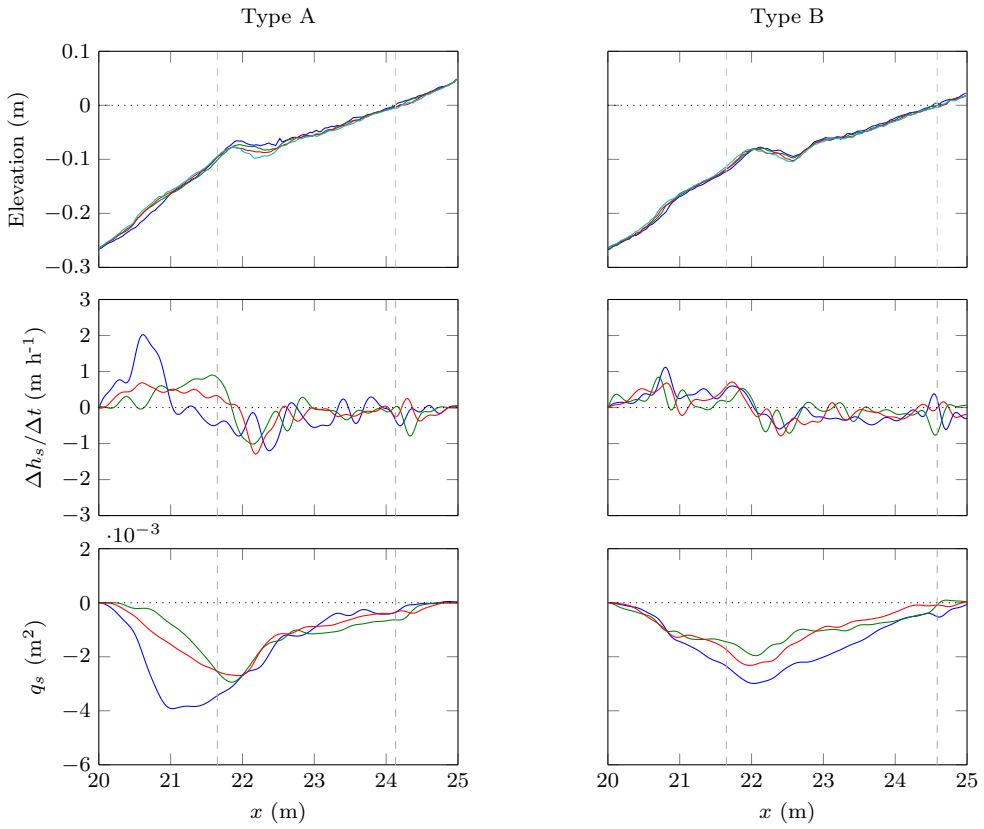

Figure 4.30: Beach profiles, variation of sediment height and bulk sediment transport for groups of three C1 short runs run over initial beach profiles of types A and B). Color code, from the initial profile to the last one: blue, green, red, cyan (cyan for top plots only). The grey dashed lines mark the approximate positions of the breakpoint and the shoreline.

clear that C1 still promotes the pattern of sediment erosion after the breakpoint and deposition in the end of the shoaling zone for profiles for which C2 is no longer capable. No results are presented for the type-C beach profile for C1 wave condition. However, it is logic to assume, from the results depicted in Fig. 4.29, that if C1 was ran over a type-C initial profile, the tendency would be for sediment transport to follow the same transport pattern that it does for C2, but with even greater magnitude.

The C3 wave condition, with less modulation, shows less capacity for transporting sediment, when compared with C2 and C1. Fig. 4.31 shows the effect of two and three short runs, over profiles of type A and B, respectively. Over profiles of type A, only two runs are enough to show that C3 essentially smooths the initial profile, with no major zones of accretion or erosion. For type-B initial profiles, C3 results in a transport tendency with an opposite direction to that of C1. While C1 tends to promote the erosion of the through inshore of the bar, C3 promotes accretion instead. The sediment accumulating just inshore of $x = 22$ m is transported onshore from the region between $x = 20$ m and $x = 22$ m, which is the same region where sediment transported by C1 from inshore of the bar accumulates.

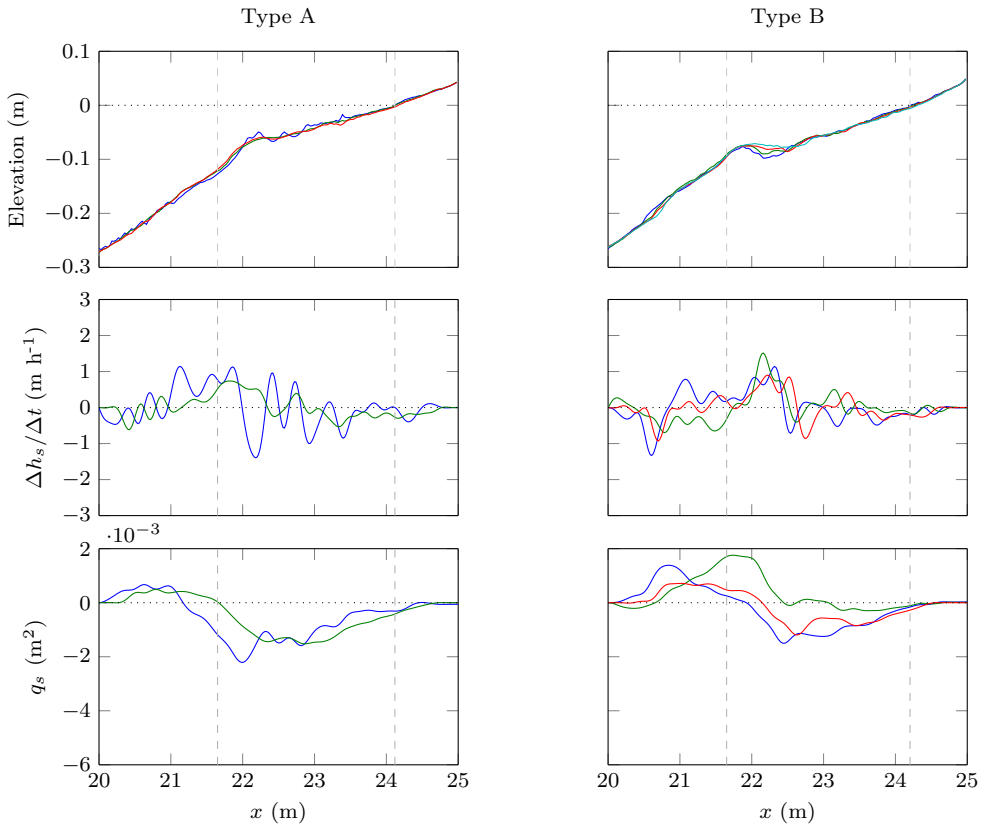

Figure 4.31: Beach profiles, variation of sediment height and bulk sediment transport for groups of two and three C3 short runs, run over initial beach profiles of types A and B, respectively. Color code, from the initial profile to the last one: blue, green, red, cyan (cyan for top plots only). The grey dashed lines mark the approximate positions of the breakpoint and the shoreline.

For all wave conditions and all profile types the same weak tendency for erosion of the swash zone is found. Also for C1, C2 or C3, the absolute magnitude of the transport rate for one single run depends very strongly on the initial profile considered and should thus not be compared between conditions (when the first run was not ran over the exact same initial profile for all conditions). However, the capacity for promoting sediment transport over one same profile type along two or three runs is meaningful and can be compared between wave conditions.

Even though the magnitudes may diverge depending on the initial profile type considered and other morphological characteristics of the profiles (such as ripples), a common pattern of sediment transport was found for each wave condition. Summing up, at the time scale of two to three runs of two wave groups each:

- for all conditions, sediment is transported from (to) the region of the shoaling zone comprised between $x = 20$ m and $x = 22$ m, to (from) the surf zone, in particular the inner-surf zone; this means that these two zones of the beach profile are morphodynamically coupled;
- for C1 and C2, the general tendency of transport between the shoaling and the surf zones is offshore-directed, while for C3 is onshore-directed;
- C1 has a greater capacity for eroding the trough after the bar and transporting sediment offshore than C2;
- C3 is the only condition promoting sediment accretion in the inner-surf zone over the profile type considered;
- C1 and C2 (higher IG waves) tend to develop a bar/trough near the breaking zone, while the onshore sediment transport promoted by C3 promotes the disappearance of the bar/trough system;
- the morphodynamic changes observed are greater for the wave conditions further apart from their equilibrium profiles.

4.4.2 Hydrodynamics

Sediment transport patterns and beach-profile morphology changes were shown to be different for each wave condition. In order to understand the mechanisms behind these differences, the wave hydrodynamics are subsequently analysed through means of H_{rms} of both total and IG-wave only, Sk, As, $\langle\epsilon\rangle$ and $\langle\eta\rangle$. The residual oscillations that remain in the flume after the passage of the two wave groups are not to be included in the statistics as they may bias the results and therefore a method based on the

wave-group envelope width was used to select the part of the free-surface elevation signal to be considered. An example for each of the wave conditions is depicted in Fig. 4.32. The resulting time series do not have the same length for all the wave gauges and, in the case of the most offshore gauges, a limit of 27.2 s was imposed as the maximum duration of the time series to include. Considering the wave-envelope duration allows the inclusion of important short-waves at the end of the IG wave, for gauges in the surf zone. If only the length of the two wave groups, as they were input at the wave-maker (27.2 s), was considered for these gauges, an important part of the wave amplitude signal would be ignored in the statistics. This method, applied to establish the duration of the free-surface-elevation signal to be considered, is thus a compromise for the different cross-shore positions and wave conditions. Small differences in the statistics that may be found for the most offshore wave gauges (for which short-wave height is the same for all wave conditions) are linked to small variations in the selected part of the time series.

Since the hydrodynamics depends not only on the wave condition but also on the beach profile over which it acts, in order to understand the differences between wave conditions, the beach profiles must be the most similar possible. Therefore, the hydrodynamics are analysed in pairs of runs (C2-C1, C2-C3 and C1-C3), between which very little bed-profile changes were observed. This analysis is presented in Fig.4.33.

From the comparison of the free-surface elevation statistics between wave conditions, some observations can be summed up:

- As expected, short-wave height is about the same for all wave conditions until the end of the shoaling zone and very similar beyond;

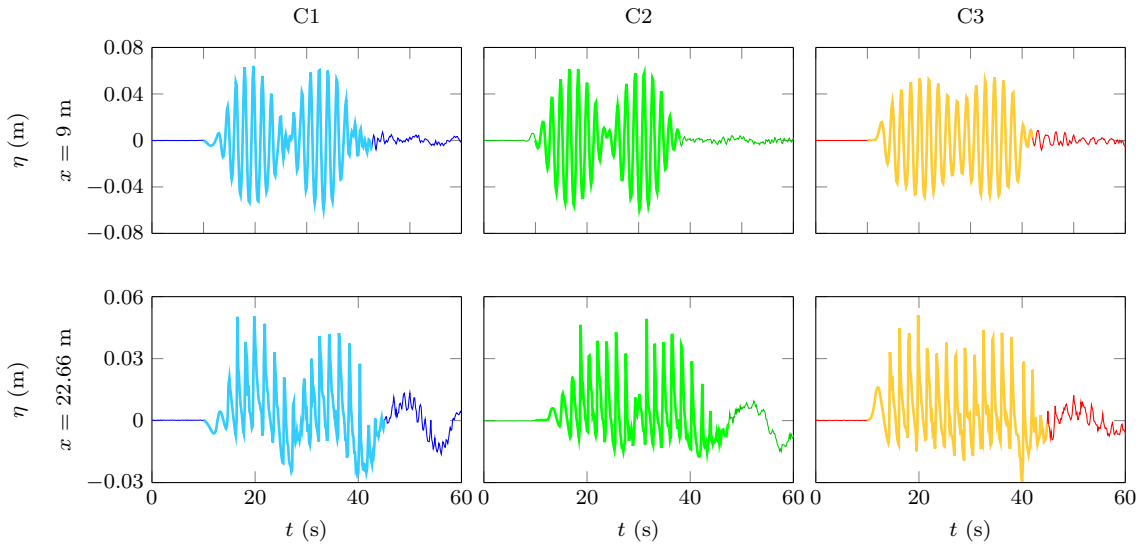

Figure 4.32: Example of selected time series (thicker and lighter-coloured part of the curves) from wave gauge data, for C1, C2 and C3, at two different cross-shore positions (top and bottom).

- IG-wave height is greater for C1 and smaller for C3. This difference is higher in the surf and swash zones;

- While for C1 the greater IG-wave height is present from deep waters to the shore, between C2 and C3 the difference is only significant in the surf and swash zones;

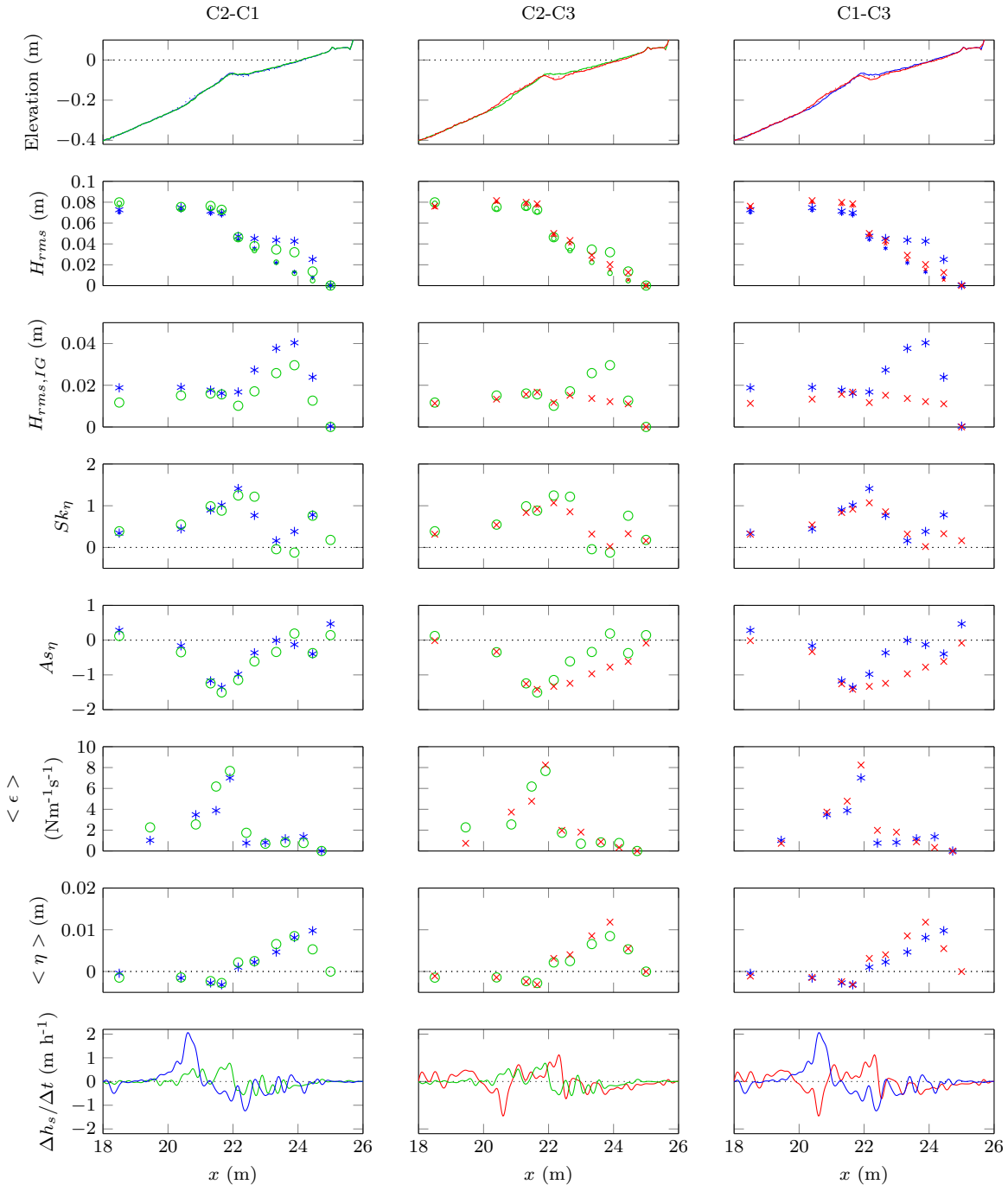

Figure 4.33: Comparison of free-surface elevation statistics for: C2 (green circles) and C1 (blue asterisks), C2 and C3 (red crosses) and C1 and C3. For the plots of H_{rms} (second line), the bigger markers are for the total signal and the smaller markers for the SW only.

- Nonlinearities increase in the shoaling zone until the breaking zone and decrease in the surf zone;
- As_η in the surf and swash zones is greater for the conditions with less IG waves, in particular for C3;
- Sk_η, dissipation and set-up/set-down are very similar between conditions.

The differences in sediment transport between wave conditions have to be justified by a distinct balance between the hydrodynamic processes for each wave condition. In this case, the main parameters that vary significantly between the three wave conditions are the IG-wave height and the asymmetry.

On the one hand, asymmetry is known to contribute to onshore sediment transport. A greater asymmetry is observed for C3 (comparatively to the other conditions) shorewards of $x = 22$ m, which may contribute to an onshore-transport tendency in the surf zone. On the other hand, the IG-wave height is the only parameter shown in Fig. 4.33 that is different for the three wave conditions in the shoaling and surf zones and may thus help justifying the sediment transport between these zones of the beach profile.

Another mechanism that could justify the offshore sediment transport observed for certain experiments and has not been discussed yet is the phase-lag effect. Positive wave skewness is generally associated with net onshore sediment transport. However, waves that are purely skewed may generate a net sediment transport offshore directed due to the phase lag between the mobilization and the transport of the sediment. This mechanism can be characterized by a phase-lag parameter (Dohmen-Janssen *et al.*, 2002), which essentially depends on two variables: the particle settling time and the wave period. Grasso *et al.* (2011) have investigated the occurrence of phase-lag effects in the LEGI wave flume under wave conditions with similar heights and periods to the ones analysed herein and have shown that, effectively, for most of their experiments, unsteady behavior was observed, during which phase-lag effects can occur. However, in their case, these effects were observed when large wave skewness was associated to small wave asymmetry, which is not frequent in the experiments analysed in this work. Furthermore, for all the three conditions, C1, C2 and C3, the particle settling time (settling velocity) and the short-wave period are the same. Therefore, at the timescale of short waves, the phase-lags effects can be expected to be of the same order independently of the wave condition considered. Hence, phase-lag effects linked to short-wave-action only cannot be responsible for the differences observed in the sediment transport between wave conditions.

Analysing the velocity measurements for the different wave conditions may provide further insight into the differences observed in the sediment transport. Velocity measure-

ments were done during the experiments at various cross-shore positions. Nonetheless, as it was depicted in Fig. 4.15, it was not possible to obtain good velocity measurements with the ADV along all the profile. In particular, the region where the greatest undertow is expected (near breaking), is particularly difficult for getting clean measurements, as there are large amounts of sediment in suspension. Since the undertow may promote an important offshore sediment transport, it is crucial to evaluate its contribution for the different wave conditions. To overcome the lack of accurate ADV velocity measurements near the breakpoint and in the surf zone, the SERR1D model was used to simulate the C1, C2 and C3 short runs, providing velocity predictions for all wave-gauge positions. Fig. 4.34 depicts the comparison of the cross-shore variation of velocity for C2 and C1

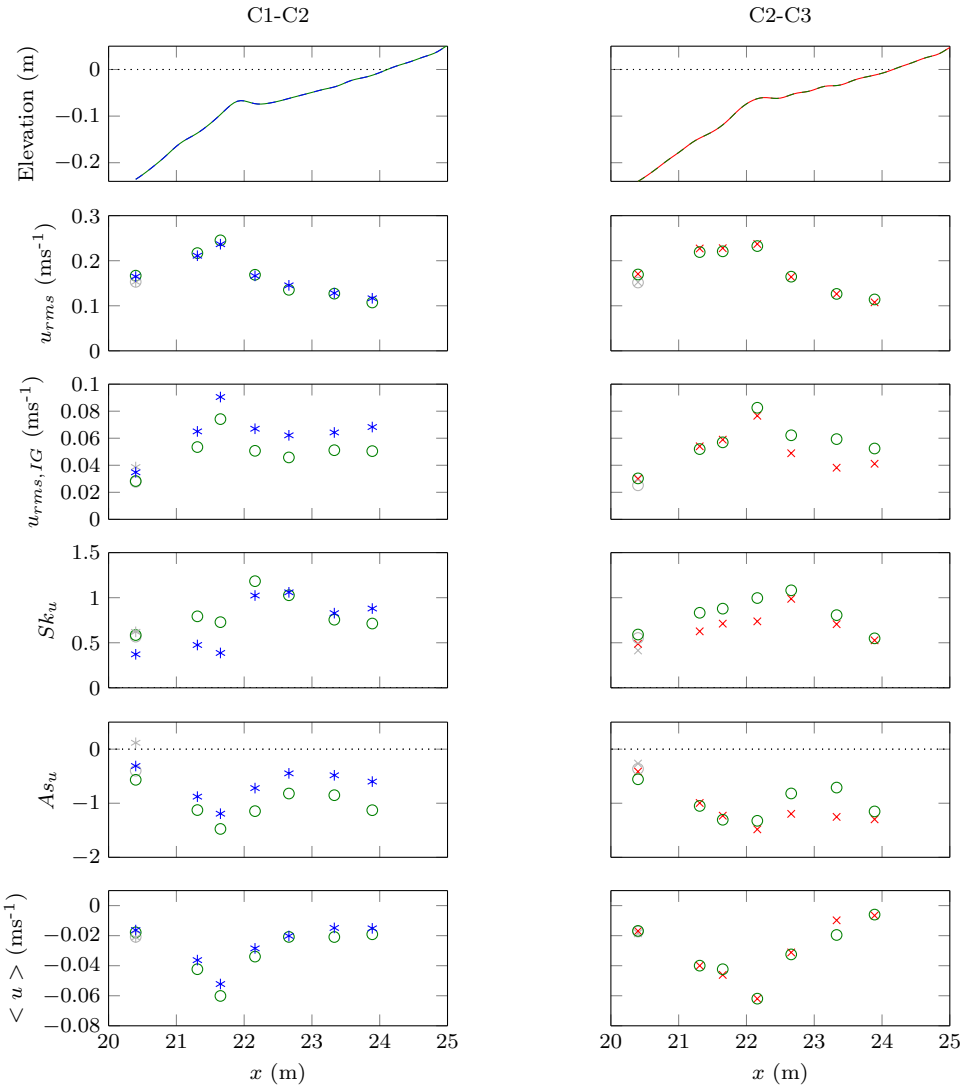

Figure 4.34: Left column: comparison of velocity statistics for C2 (circles), C1 (asterisks). Right column: comparison of velocity statistics for C2 and C3 (crosses). Experimental data are in grey, numerical data are in green (C2), blue (C1) and red (C3). Note: The beach profiles are not the same in both columns (and thus the two C2 runs considered are not the same).

(left column) and for C2 and C3 (right column), obtained with SERR1D. For the first point of the domain, the velocity experimental values are also depicted in Fig. 4.34. For each pair of wave conditions, the experimental runs chosen for providing the input conditions had been run one after the other and thus over beach profiles almost equal.

The estimated u_{rms} is nearly the same for the three wave conditions and is maximal near the breakpoint (and thus near the bar/slope-break). The $u_{rms,IG}$ also reaches its maximum near the breakpoint for all wave conditions, but it is greater for C1 and smaller for C3, responding to the different IG-wave heights. Between C2 and C3 this difference is only significant after the breakpoint. Although the trends are very similar for the three wave conditions, Sk_u tends to be greater for C2, until the surf zone. As it was already observed for As_η, the As_u is larger when IG-waves are smaller. The undertow increases until the breakpoint (near the bar), decreasing afterwards towards the beach, being very similar for all wave conditions. This was further confirmed by velocity profiles done with an ADVP, although these results are not presented nor analysed in the scope of this thesis. Moreover, the wave conditions which tend to promote offshore transport from the surf zone towards deeper waters are not the ones with slightly greater undertow velocities. Therefore, as a first hypothesis, the undertow is not the preponderant driving mechanism for the offshore sediment transport.

Still in pursuance of a better understanding of the differences in the flow velocity between wave conditions that can contribute to the differences observed in the morphodynamics, Fig. 4.35 shows the comparison of five terms resulting from the decomposition of the third-order velocity moment $\langle |u|^2 u \rangle$ for C1-C2 and C2-C3 pairs, from the end of shoaling until the shore (calculated following the procedure detailed in chapter 3). The other terms that are not presented have a negligible contribution (at least one order of magnitude smaller than the terms presented). Positive/negative values of the third-order velocity moment terms are expected to contribute to onshore/offshore transport.

Among the terms considered, it is the short-wave skewness (Sk_1), the correlation between short-wave variance and IG-wave velocity (Sk_2) and the short-wave stirring and transport by the mean flow that dominate for all wave conditions. For C1, C2 and C3, with the exception of Sk_1 terms, all the terms have negative values, thus potentially contributing to an offshore transport. For both C1 and C2, until the breakpoint, Sk_1 and Sk_2 have values of the same order of magnitude, but of opposite sign. For C1, Sk_1 is slightly smaller than for C2 and than Sk_2. For C2, it is Sk_2 which is slightly smaller than Sk_1 and smaller than for C1. If only these terms are considered, a slight tendency for more offshore transport may thus be expected for C1. If the analysis is extended to the other three terms (Sk_4, Sk_5 and Sk_6), except for the stirring by short-waves

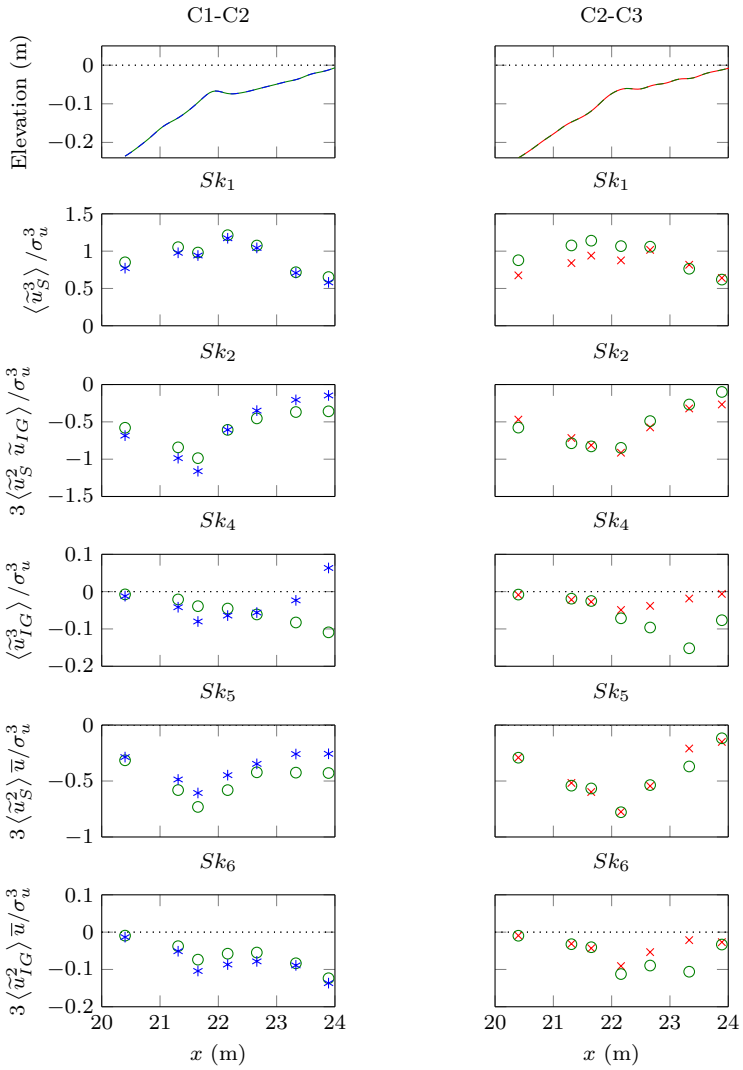

Figure 4.35: Cross-shore variation of the Sk_1, Sk_2, Sk_4, Sk_5 and Sk_6 third-order velocity moments: skewness of short-waves, correlation of short-wave variance and IG-wave velocity, skewness of IG waves, stirring by short waves and transport by mean flow and stirring by IG waves and transport by mean flow, respectively. Each pair of wave conditions was simulation over the same beach profile: in the left column, C1 (blue asterisks) and C2 (green circles); in the right column, C2 and C3 (red crosses).

and transport by mean flow (Sk_5), the tendency is for C1 to have more negative values than C2, reinforcing the contribution to offshore transport. In the inner-surf and swash zones, for C1, the values of Sk_2, Sk_4 and Sk_5 are progressively less negative than for C2, and significantly less negative than near the breakpoint, even changing to a positive contribution (Sk_4) near the shoreline. Therefore, the potential for offshore transport associated with $\langle |u|^2 u \rangle$ terms for C1 seems higher than for C2 until the breakpoint, but decreases in the surf and swash zones, where the potential for offshore transport is greater for C2.

For C3, the distinct terms of $\langle |u|^2 u \rangle$ are very similar to those of C2 until the breakpoint: Sk_1 is greater for C2, but is almost compensated by Sk_2, which is slightly

greater for C2 as well, and the other terms are equal and negative for both C2 and C3. Onshore of the breakpoint, the differences between C2 and C3 for Sk_1, Sk_2 and Sk_5 terms are very small, and it is the terms linked to IG waves (Sk_4 and Sk_6) that are distinct between the two wave conditions: since for C3 the IG waves are very small, the contribution of these terms are small in this zone of the beach profile.

The analysis of the third-order velocity moment terms can be summed up in the following points:

- For the three wave conditions, there are more terms contributing to an offshore than to an onshore transport direction; however, the absolute values of each term vary between conditions;
- C1 and C2 have very similar contributions of the different terms to sediment transport, with C1 having a slightly greater contribution from terms directly dependent on IG-wave motion and C2 from terms more dependent on short-wave motion;
- Short-wave skewness is smaller for C3 than for the other two wave conditions before the breakpoint;
- The terms directly dependent on IG-wave velocity are particularly small for C3 onshore of the breakpoint.

Onshore of the breakpoint it is clear the smaller contribution of the $\left\langle |u|^2 u \right\rangle$ terms responsible for offshore transport (Sk_2-Sk_6) for C3 than for C2. However, near the breakpoint and further offshore, no clear inequality of the former terms is observed between the wave conditions. Furthermore, also before the breakpoint, the values of the various terms for C1 and C2 seem too similar to justify the significantly-greater capacity for accumulating sediment until $x = 20.5$ m previously observed for C1 (Fig. 4.30). Therefore, some other mechanism must be determining the differences in the sediment transport observed around the breakpoint and further offshore.

For all wave conditions, the short-wave velocity reaches its largest values in the breaking zone (around $x = 22$ m), which means that great quantities of sediment are suspended there by short-wave action. In the same zone of the beach profile, IG waves also reach maximal velocities, which means that they may advect the sediment stirred by short-wave action away from its initial location.

For IG waves to be able of transporting sediment suspended by the short waves, not only the magnitude of IG-wave velocity is important, but also the phasing between the IG waves and the short waves. Very small differences in the IG-wave velocity magnitude between conditions are depicted in Fig. 4.34 (especially between C2 and C3), which

supports the idea that the phasing between the IG waves and the short waves may even be fundamental.

Fig. 4.36 shows, for experimental and numerical data, the time series of free-surface elevation and velocity, for the total signal and IG-component only and the separation of the incident and reflected IG-wave components. The time series are presented for three example cases of C1, C2 and C3, run over very similar profiles (those of Fig. 4.33). The incident IG waves are very-accurately represented by the model for all wave conditions, both in terms of amplitude and phasing. The phasing of the reflected IG waves depends strongly on the beach-profile shape (shoreline position, water depth, etc.) and swash zone dynamics, which hinders the model from achieving a totally correct representation of this component of the IG waves. Fig. 4.36 also confirms the ability of the model to approximately simulate the IG waves, particularly in terms of amplitude, for incident, reflected and total IG waves.

For all the conditions, IG velocities are predominantly negative along the cycle, which is also observed for cross-shore positions further inshore. The onshore-directed IG-wave velocities are not only shorter in time and smaller in magnitude, but they are also concurrent with the smallest short waves of the groups. This means that more sediment is expected to be in suspension (and thus available to be advected by the IG waves)

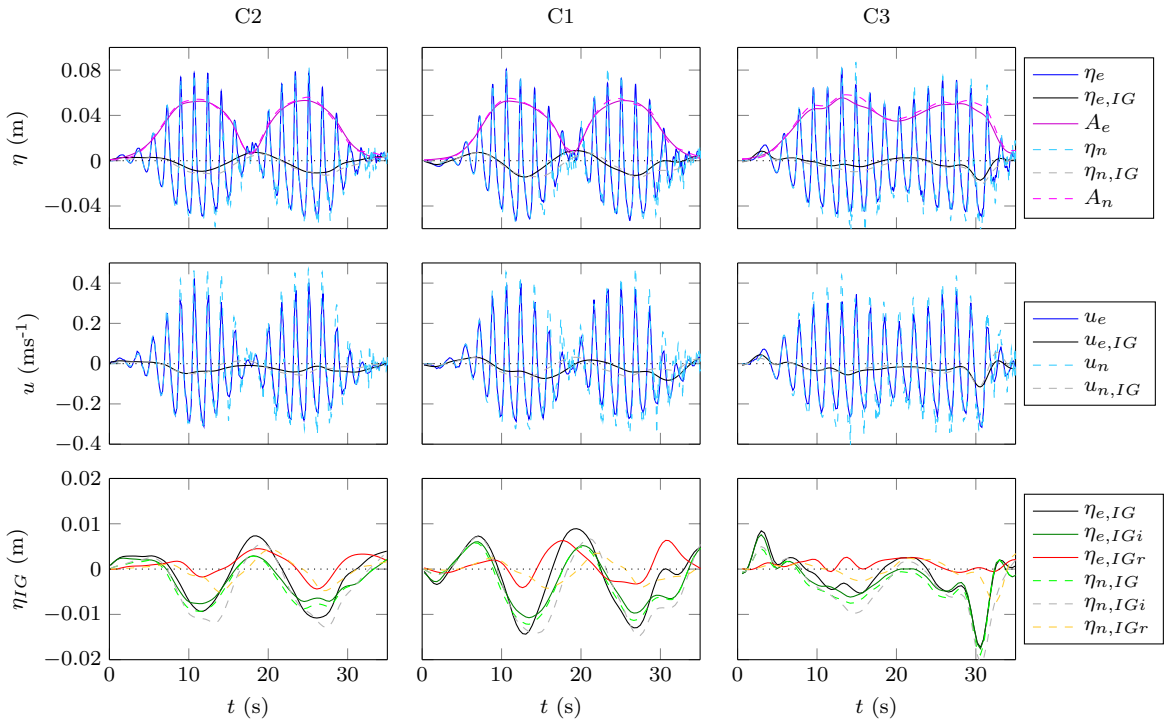

Figure 4.36: Free-surface elevation (total and IG), cross-shore velocity (total and IG) and IG-wave total, incident and reflected components for C2, C1 and C3 example runs (shown in Fig. 4.33), at x = 20.4 m, for experimental and numerical data.

during the offshore stroke of the IG waves. Hence, an offshore sediment transport by the IG-wave oscillatory flow seems more likely than an onshore sediment transport. For the runs represented in Fig. 4.36 (the same runs of Fig. 4.33), C1 has greater IG-wave height and thus greater IG-wave velocity ($u_{rms,IG} = 0.036$ m s^{-1}, instead of $u_{rms,IG} = 0.026$ m s^{-1} for C2, at $x = 20.4$ m). Also, the IG negative velocities reach their maxima near the end of the wave groups when the largest amount of sediment was observed to be in suspension. Both factors justify the greater capacity for sediment transport in the offshore direction of C1 relatively to C2, which was also suggested by the third-order velocity moment terms (in particular, Sk_2).

For the runs considered, C3 has a $u_{rms,IG} = 0.033$ m s^{-1} (at $x = 20.4$ m - Fig. 4.36 run), between the u_{rms} values of C1 and C2. Depending, on the runs considered, the $u_{rms,IG}$ of C3 may be more similar to that of C2 than of C1 (for *e.g.*, in Fig. 4.34, C2 and C3 $u_{rms,IG}$ at $x = 20.4$ m is about the same). However, the duration of the episodes with significant IG-wave velocity is much shorter than for C2 and, especially, than for C1 (and limited to the beginning and end of the wave signal), which results in very weak IG-wave velocities along most of the IG-wave cycle. Furthermore, unlike C1 and C2, C3 short-wave height is important even when IG-wave velocity is the smallest. Thus, for C1 and C2, the very small short waves that correspond to the IG-wave velocity minima can be expected to suspend less sediment than the corresponding short waves of C3, which have comparable heights during the IG-velocity minima and along the rest of the wave group. When there is a significant amount of sediment suspension and the IG-wave velocity is negligible and not strong enough to advect sediment offshore, it is logical to assume that the sediment transport has to be driven by a different mechanism. C3 was seen to have the capacity for onshore transport for the same profile types over which C1 and C2 induced offshore transport. The C3 sediment transport must thus be dominated by the nonlinearities of short-waves, the only mechanism that, in the absence of significant IG-wave velocities, can promote onshore sediment transport.

The ideas explained above are based on the observation of the time series at $x = 20.4$ m, near the outer limit of the deposition zone observed in the beach profiles. Since no clean experimental velocity measurements can be retrieved near the breakpoint, the numerical results equivalent to Fig. 4.36, but obtained instead at $x = 21.65$ m, are presented in Fig. 4.37. The phasing between IG-waves (and IG-wave velocity) and short-waves that was discussed for the results obtained at $x = 20.4$ m can also be observed for the numerical data near the breakpoint ($x = 21.65$ m), which reinforces the idea that this phasing may be a crucial mechanism, determining the distinct sediment transport patterns observed for each wave condition.

Overall, IG-wave amplitude and phasing relatively to the wave group are shown to

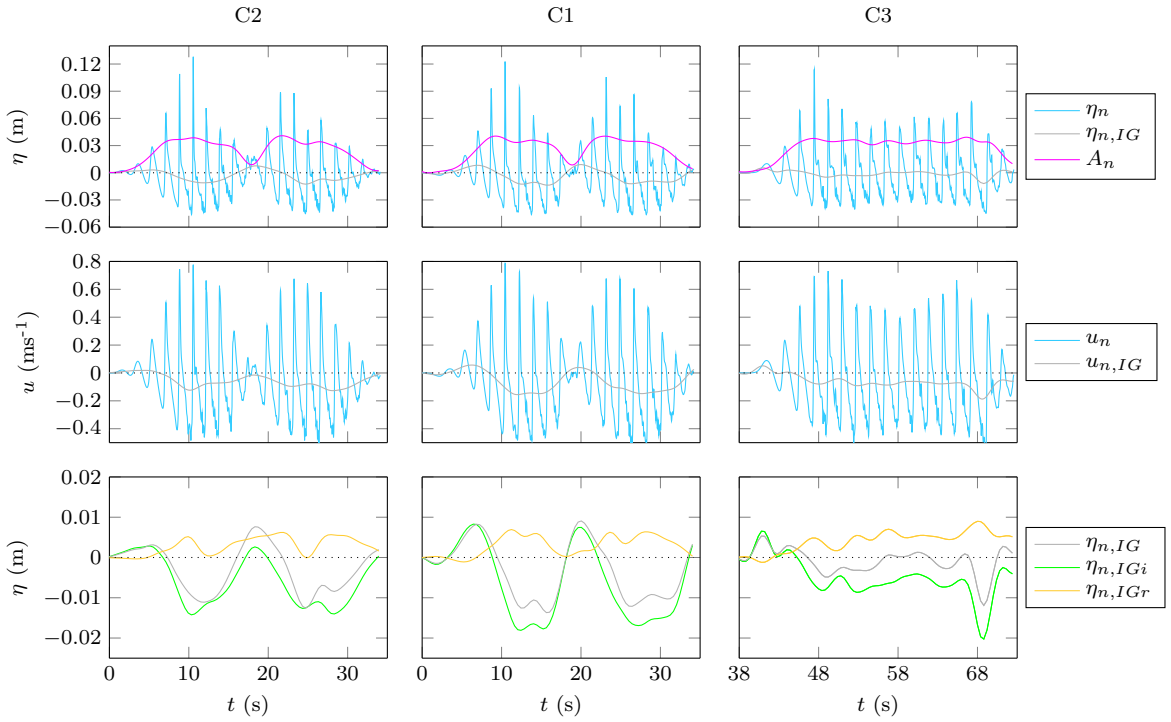

Figure 4.37: Free-surface elevation (total and IG), cross-shore velocity (total and IG) and IG-wave total, incident and reflected components for C2, C1 and C3 example runs (shown in Fig. 4.33), at x = 21.65 m, for numerical data.

be able of conditioning sediment transport magnitude and direction. Furthermore, IG waves are seen to influence short-wave nonlinearities, particularly asymmetry.

The comparison between wave statistics (Fig. 4.33) for the three wave conditions has shown that the more IG-waves are present, the smaller is the asymmetry in the surf and swash zones. This was especially clear for C3 condition (significantly less IG waves, the greatest asymmetry), both in terms of free-surface elevation and velocity, and contributed to onshore sediment transport. Additionally, when SERR1D was used, it partially underestimated the measured IG-wave height in the surf and swash zones (see Figs. 4.17 and 4.19. As a result, the model systematically overestimated asymmetry (and also skewness, in a smaller measure) in these zones of the beach profile. Both these points indicate that surf- and swash-zone asymmetry is being influenced by the IG-wave height.

Elgar & Guza (1985) have stated that contributions from the frequency pairs with low-frequency components is opposite in sign to the contributions from the high-frequency pairs, which can reduce the skewness by 30-60% and asymmetry by about 15-30%. However, taking as an example the cross-shore position in the surf zone of x = 23.33 m and the cases of C1 and C3 shown in Fig. 4.33, a much more accentuated reduction of asymmetry (of more than 30 %) from C3 to C1 is evident and therefore the contribution

of the low-frequency pairs can be one of the causes, but not the main cause of asymmetry reduction. On the other hand, at the same position, the water depth is of about 3.6 cm, at rest. With the set-up, 4 or 7 mm more of water depth can be expected for C1 or C3, respectively, which are small values relatively to the total water depth at rest. While H_{rms} of the short waves is about the same for both C1 and C3 at that cross-shore position, the H_{rms} of IG waves is about three times higher for C3, meaning that instead of a water depth of about 3.6 cm (at rest) $\pm$ 0.7 cm (corresponding to half of $H_{rms,IG}$), for C3, there will be a water depth of around 3.6 cm (at rest) $\pm$ 1.9 cm, for C1. Hence, as wave nonlinearities are dependent on the local water depth, differences in the wave shape, including asymmetry, can be expected as a result of water-depth modulation by the IG waves. This explains the differences in asymmetry found in the surf and swash zones between wave conditions.

4.4.3 Monochromatic infragravity-wave runs

In nature, IG waves that propagate to the shore are most commonly associated with short waves and thus their direct effect cannot be measured. However, in an artificial wave flume, IG waves can be simulated alone, as monochromatic waves with a long period.

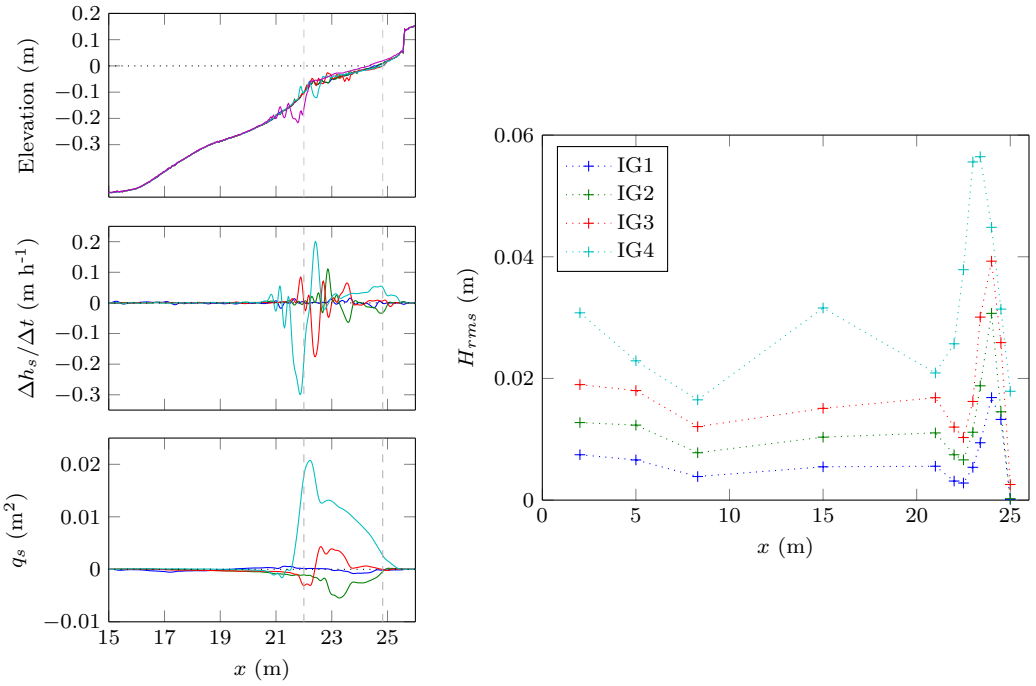

Figure 4.38: Beach profiles, variation of sediment height, bulk sediment transport and H_{rms} for IG1, IG2, IG3 and IG4 experiments. Color code, from the initial profile to the last one: blue, green, red, cyan, violet (violet for top plot only). The grey dashed lines mark the approximate positions of the short-wave breakpoint and the shoreline.

Four 20-min IG-waves experiments were ran in the LEGI wave flume, with increasing input IG-wave heights, presented in Fig. 4.38: IG1, with IG-wave height approximately equal to the maximum IG-wave height of C2 long runs, and IG2, IG3 and IG4, which were designed to have wave heights twice, three times and four times the wave height of IG1 waves. For IG1, IG2 and IG3, sediment transport is very weak and the changes induced on the beach profile consist essentially in some ripples. IG4 has significantly greater capacity for mobilizing the sediments, promoting onshore sediment transport from just before the slope break towards the beachface. The effect of the monochromatic IG waves is only significant in shallower waters, at the velocity anti-node (around $x = 22$ m).

Fig. 4.39 shows the comparison of IG-wave short runs (27.2 s) with C1 and C2 short runs, ran over very similar beach profiles and makes it possible to directly compare the effect on sediment transport of IG waves alone and short-waves and IG waves together.

The net sediment transport of one short run of IG1 plus one short run of IG2

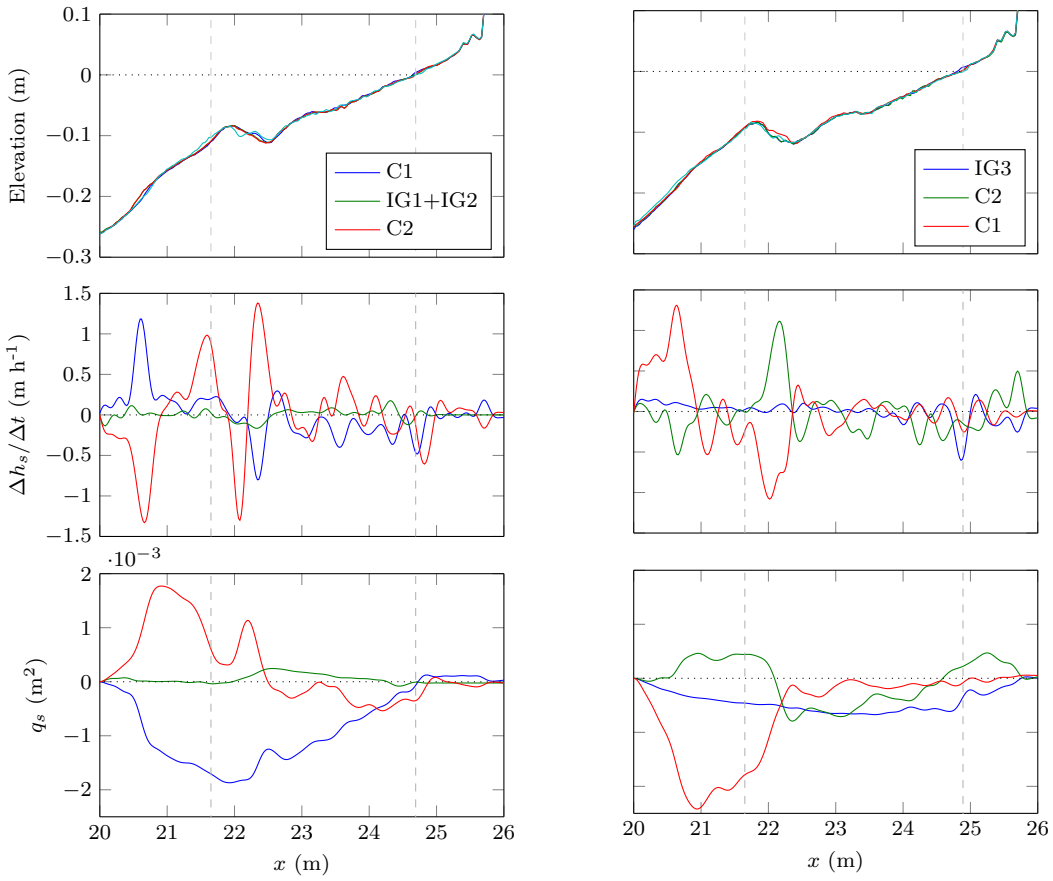

Figure 4.39: Comparison of beach profiles, variation of sediment height and bulk sediment transport for C1, C2, IG1, IG2 and IG3 short runs run over similar profiles. Color code, from the initial profile to the last one: blue, green, red and cyan (cyan for top plot only). The grey dashed lines mark the approximate positions of the breakpoint and the shoreline.

is almost one order of magnitude smaller than that of one C2 or one C1 run. IG3 has a greater capacity for sediment transport than IG1 and IG2, but still very locally (near the shoreline). Therefore, IG waves are capable, depending on their height, of generating sediment transport alone, even if only very locally, but only when their height is significantly greater than the height of the IG waves associated to the short-wave groups in the experiments presented in this work (the case of IG4 wave condition).

4.5 Discussion

In this chapter, infragravity waves were shown to influence sediment transport in many ways. In nature, IG waves that propagate to the shore are associated with short waves and thus their direct effect cannot be measured directly.

Beach & Sternberg (1988) and Russell (1993) have suggested that IG waves are able of suspending sediment themselves, close to the shore, during storm conditions, when they assume the form of swash bores. The research community has been so far inclined to think that, in a general way, IG-waves are not capable of suspending sediment alone and act instead as mean currents, advecting sediment already suspended by short-wave action (Aagaard & Greenwood, 2008).

For the current work, beach profiles are classified as being in the intermediate range, mild to intermediate wave conditions are considered (with IG-wave height corresponding to less than 0.5 m in nature) and C1 and C2 were already designed to have the maximum modulation. Even if for C1 there is the added contribution of free IG waves, Fig. 4.38 shows clearly that no significant sediment transport can occur in the experiments considered in this work by the effect of the IG waves alone. Therefore, for the full set of experiments ran, IG waves were only capable of influencing sediment transport by advecting the sediment suspended by the short-wave action away from its suspension zone.

A turbidity current, represented in Fig. 4.40, was observed transporting from the breaker zone significant quantities of sediment in suspension towards deeper waters. This current started developing near the breakpoint, just after the passing of the greatest

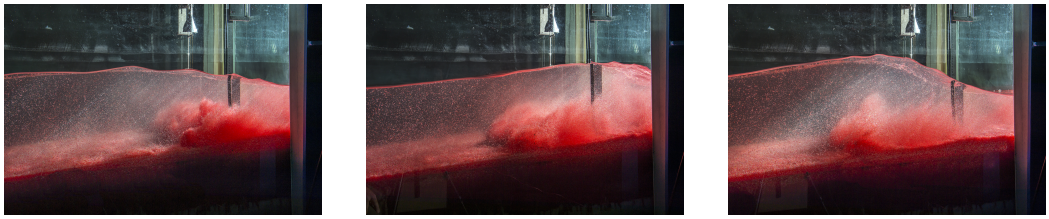

Figure 4.40: Propagation of the turbidity current towards deeper waters (photos by Cyril Fresillon - CNRS photothèque).

wave of the first wave group (of each pair of wave groups), which coincided with the beginning of the offshore stroke of the IG-wave associated with the short-wave groups. The turbidity current then propagated offshore transporting great amounts of sediment, both as bed-load and suspended-load, until the arrival of the next wave group, which contributed to slow it down. However, even with a smaller velocity, it continued moving the sediment particles slowly offshorewards until around $x = 20.6$ m. This current was observed to be more intense during C1 equilibrium runs, than for C2 or C3, which leads to the consideration that IG waves may be, at least partially, influencing/controlling this current.

Aagaard & Greenwood (2008) have stated that if the sand is entrained near a re-suspension maximum (such as the breakpoint, located slightly onshore of $x = 22$ m, for C1 equilibrium profile), its decay distance depends only on the IG-wave orbital diameter, which can be estimated as $d_0 = u_{max}T_{IG}/\pi$ (where d_0 is the IG-wave orbital diameter, u_{max} the maximum IG-wave velocity and T_{IG} the IG-wave period). Hence, for C1, which reaches maximum IG-wave velocities of about 0.15 m s^{-1} (at $x = 21.9$ m) for the moments of the run with higher IG waves, an orbital diameter around 0.5 m can be estimated. The same authors proposed that offshore of a re-suspension maximum the transport by IG waves is directed seawards. Therefore, the offshore stroke of the IG waves (associated with the undertow) is likely contributing to the offshore advection of sediment suspended at the breakpoint (until around $x = 21.9 - 0.5 = 21.4$ m) towards the offshore slope of the bar (instead of the sediment being simply re-deposited closer to the position where it was suspended, still on the onshore side of the bar). From thereon, the turbidity current becomes preponderant on the offshore advection of sediment, carrying the sediment still further offshore and thus strongly influencing the sediment transport. Fig. 4.41 shows five C1 short-runs that were run consecutively and reinforces this idea. For this set of runs, the role of the turbidity current in the transport of sediment from the breakpoint offshorewards is very clear. In the bed profiles it is visible, run after run, a marked accretion until about $x = 20.7$ m (as it was predicted based on the IG-wave orbital diameter). The sediment that is transported offshore is eroded at the breakpoint, creating a trough and defining progressively a bar.

During the equilibrium runs, the IG waves were shown to modulate skewness and asymmetry of short-waves along the beach profile, which vary along the runs responding to the variation of IG-wave phase and height. Prel *et al.* (2011) had previously demonstrated in experiments performed in the LEGI wave flume that IG waves can modulate skewness and asymmetry even in the shoaling zone. The short-runs have shown that the phasing of IG waves relatively to the short-wave envelope can even condition the direction and intensity of the sediment transport. If the other mechanisms

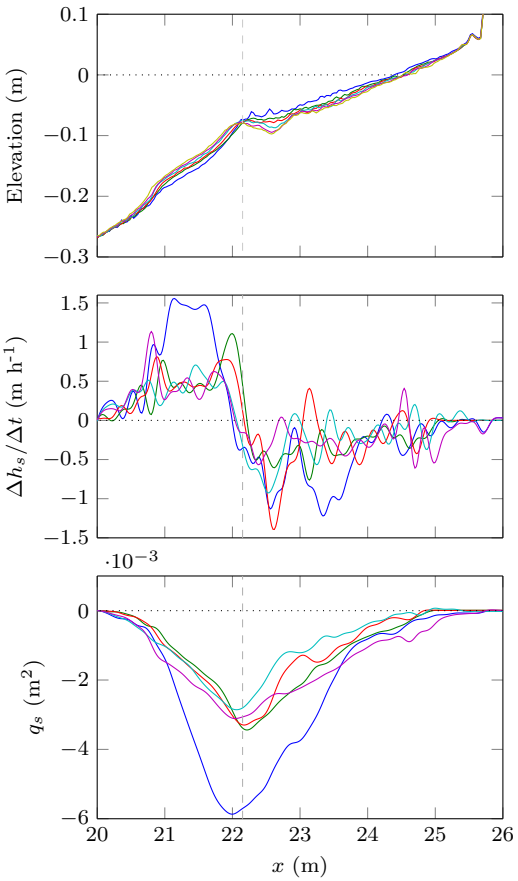

Figure 4.41: Beach profiles, variation of sediment height and bulk sediment transport for five C1 short runs. Color code, from the initial profile to the last one: blue, green, red, cyan, violet, yellow (yellow for the top plot only). The grey dashed lines mark the approximate position of the breakpoint.

driving sediment transport are small enough or balance each other during a certain phase of the IG waves, transport by IG waves becomes significant. If this happens during an IG-wave phase with negative (positive) velocities, sediment advection will be directed offshore (onshore).

By comparison of wave conditions run over the same beach profile, surf and swash zone asymmetry was shown to be influenced by the IG waves, with lower asymmetry for higher IG-wave heights. Wave conditions with higher IG waves allow a greater water depth in the surf and swash zones. Further, IG-wave motion is positively correlated with short-wave motion in this zone of the beach profile, as the crests of IG waves allow the greatest short-wave of the group to propagate. Therefore, greater IG-wave height implies a greater water depth below the greater short-waves of the group, reducing asymmetry (which is larger for shallower depths).

The greater offshore transport observed for C1 is justified by the greater absolute values of IG-wave velocity for this condition, the more negative values of the $\langle |u|^2 u \rangle$ terms directly dependent on IG-wave motion and by the phasing of the moments of

higher sediment suspension (at the end of each short-wave group) with maximal IG-wave offshore-directed velocities. The higher IG-waves further contribute to a smaller asymmetry, promoting even less the onshore sediment transport (in the surf zone). The minor capacity for offshore transport of C3 is justified by the lower IG-wave velocities, the smaller contribution of $\langle |u|^2 u \rangle$ terms directly dependent on IG-wave motion, the larger asymmetry, in the surf and swash zones and the small modulation of the short-wave groups (implying that the short-waves are almost equally important along each wave group). All these factors imply that IG-wave offshore transport never has the possibility of becoming more important than the short-wave-driven onshore transport for this wave condition. The maximal modulation of C2 wave groups allows the existence of moments along the groups when short-waves are less important. It has lower absolute values of IG-wave velocity than C1, a smaller contribution of $\langle |u|^2 u \rangle$ terms directly dependent on IG-wave motion than C1, the maxima of IG-wave velocity are not in phase with the moments when more sediment is in suspension and it has greater asymmetry than C1. Therefore, although it has mostly a tendency for offshore transport, as it is illustrated by the significantly negative values of almost all terms of the $\langle |u|^2 u \rangle$, its capacity for offshore sediment transport is smaller than that of C1.

The differences in the morphodynamics between the three wave conditions are thus explained by two distinct mechanisms linked to the IG waves: (i) advection by IG-waves of sediment suspended by short-wave action (as previously proposed by Aagaard & Greenwood (2008)), which is dependent on IG-wave height and phasing with the short-wave groups and (ii) modulation of short-wave nonlinearities by IG-wave motion, both directly and indirectly, through water-depth modulation (which is also dependent on IG-wave height). Moreover, the IG-wave motion was shown to contribute to the establishment of a turbidity current, further promoting the offshore transport. To the knowledge of the author, this link between IG waves and a turbidity current has not yet been observed in the field.

The results presented in this work extend the previous findings of Grasso *et al.* (2009a) and show that, even when the Dean number is the same, if the IG-wave energy (or short-wave groups) is different, distinct equilibrium profiles are shaped.

The swash-zone dynamics was also demonstrated (particularly through the analysis of the long runs) to be affected by IG-wave height and phasing. Wave run-up and beachface gradient adjusted, reacting to the changes induced to the sediment transport by the varying IG-wave height and phase. As Masselink *et al.* (2006) stated and Alsina *et al.* (2012) also observed, the beachface cannot be considered in isolation from the surf zone: the changes induced by the IG waves in the upper beach were seen to be linked to beach-profile changes in the surf zone and inner-shoaling zone and vice-versa.

In the shoaling zone equilibrium profile of C1 (Fig. 4.20), there is a sediment accumulation region around $x = 18.5$ m. Since in this region of the shoaling the beach profile has already a water depth of about 30 cm, short waves are not able of suspending there significant quantities of sediment and thus sediment transport must rely on other mechanisms. IG waves were shown to be able of transporting suspended sediment only until $x \approx 20.5$ m. Therefore, sediment must have been transported as bed load. Since IG waves are the factor that changes between C1 and C2 or C3, they are probably responsible for this sediment accumulation. However, the sediment accumulated in this region during the evolution of the beach profile towards equilibrium. Therefore, in order to understand the mechanisms responsible for this sediment transport, velocity measurements near the bed during the evolution of the beach profile towards equilibrium are necessary. Unfortunately, the measurements made during the evolution of the beach profiles towards equilibrium were not made simultaneously at different cross-shore positions (since a single ADV was available). Therefore, no further conclusions can be drawn about the accumulation found only for C1 (greater IG waves).

The IG-wave period was not varied during the experiments performed at the LEGI in the scope of this work. Still, the results suggest that the shape of the beach profile may be influenced by it. Earlier researches, such as those of Short (1975) and Bowen (1980) have hypothesized that bar formation may be related to the positions of the standing-wave nodes and antinodes. Michallet *et al.* (2007) have shown, also in the LEGI wave flume, partial evidence of nodal structure consistent with the cross-shore bar position. Aagaard & Bryan (2003) have argued that, for standing IG waves to be capable of imposing spatially segregated sediment transport patterns and thus influence bar position, they have to be sufficiently energetic and have a reasonably well-defined cross-shore structure. In the experiments ran, due to IG-wave reflection at the beach and at the wave-maker, IG-wave height is sufficiently enhanced to generate sufficiently energetic IG waves. Further, as the wave conditions ran were bichromatic, defined and discrete modes and frequencies of IG-wave oscillation were preferentially forced and persisted during the length of the runs (up to 5.3 h, depending on the run), resulting in well-defined (partially) standing IG waves. For the different beach profiles obtained, the slope break or bar (depending on the wave condition) was located just next to a free-surface elevation node of the second mode of oscillation of the flume. This mode has, for the different profiles, a period that is very close to that of the IG wave (13.6 s). Therefore, if wave conditions with a different IG-wave period were run, an adjustment of the position of slope-break/bar would be expected.

4.6 Conclusion

The experiments analysed in this chapter were designed to clarify the role of the infragravity waves in the sediment transport processes. Three different wave conditions were chosen, to have both different IG-wave phasing with the short-wave groups and different modulation (IG-wave height). Short runs of two-wave groups only and long runs of a few hours were made over different initial beach profiles, free-surface elevation and cross-shore velocity were measured and the net sediment transport was quantified.

IG waves alone were shown to be capable of modifying the beach profile, but only when their heights are sufficiently great (highly-energetic waves and storm conditions). For the wave conditions run during the experiments, corresponding to mild to moderate wave conditions in nature, IG waves were only capable of influencing sediment transport in the presence of short waves.

No significant differences in terms of wave nonlinearities until the surf zone were observed between the different conditions when run over very similar beach profiles. Due to the difficulty of having accurate velocity measurements in the surf and swash zones, the SERR1D model was used to simulate cross-shore velocity along the beach profile, and the undertow, calculated for a given bed profile, was found to be very similar for the wave conditions considered. The distinct magnitudes and directions of sediment transport were thus attributed to the influence of the IG waves. Differences in the third-order velocity moment terms linked to IG-wave motion were shown to contribute to differences in the sediment transport. Differences in the phasing of the IG-waves with the short-wave groups were demonstrated to influence the direction of sediment transport, as IG waves advect suspended sediment offshore or onshore, depending on the wave-phase during which the sediment is available to be transported. The modulation of the wave groups was shown to condition the existence of moments of very small short-waves, during which short-wave skewness and asymmetry are less important, and thus sediment advection by the IG waves can be favoured if enough sediment is still in suspension.

When the same wave condition was run for a sufficiently long time, the beach profile reaches an equilibrium. When the IG-wave height is significant, the IG waves form standing (or partially-standing) wave oscillations that condition the profile shape and the morphodynamics. In this case, the equilibrium is dynamic and is characterized by changes of the beach profile around a “static” equilibrium profile, which are more marked for wave conditions with greater IG waves, responding to a changing of incident and reflected IG-wave heights. The changing of IG-wave phasing promotes, then, changes of IG-wave height, wave and velocity nonlinearities and the swash dynamics. The resulting beachface changes are linked and concurrent to changes in the surf and inner-shoaling

beach profiles.

Therefore, both in the long equilibrium runs and in the two-wave-group runs, IG-wave height and phasing were shown to influence sediment transport, both by conditioning the advection by IG-waves of sediment suspended by short-wave action or by modulating the short-wave nonlinearities, both directly and indirectly (through water-depth modulation). Therefore, the direction of sediment transport by IG waves in the surf and swash zones is not the same for all the wave conditions and beaches: it depends on (i) the IG-wave height and phasing with the short-waves, (ii) the modulation of the short waves and of the short-wave nonlinearities promoted by the IG waves and (iii) the beach profile over which the waves propagate.

More velocity measurements and collocated sediment concentration measurements would help better understanding the influence of IG waves on sediment transport, especially in what concerns the sediment accumulation in the shoaling zone and the oscillations of the beachface (and their link to the other parts of the profile) observed during the equilibrium runs of C1. Velocity measurements in the zones of greater sediment suspension (with video imagery, for example) and near the bed (to evaluate the importance of bed-load transport by the IG waves) and during the transitory runs before equilibrium is reached may bring further insight. Varying the input IG-wave period may help improving the understanding on the potential adjustment of the beach-profile shape to the location of the nodes and antinodes of the (partially) standing IG waves.

Chapter 5

Conclusions and perspectives

5.1 General summary

The understanding and prediction of beach evolution necessarily implies the comprehension of the different processes that promote sediment transport and shape the beach morphology. Short-wave nonlinearities (wave and velocity skewness and asymmetry) have long been recognised to be one of the crucial mechanisms. Therefore, it is important to include them in models intended at predicting sediment transport. Currently, this is done by defining the velocity nonlinearities at a given moment from the local height and length of the waves and the water depth. However, it was shown in this work, making use of a physical model data set, a field data set and of results obtained with a Boussinesq-type model, that this represents an incomplete approach and comprises important errors, particularly onshore and near the breakpoint, where sediment transport is very important. Hence, a new parameter which takes into account more than local wave parameters was proposed, resulting in the improvement of existing parameterizations.

Besides the short-wave nonlinearities, also infragravity waves were also demonstrated to have an important role in the dynamics of the beach profile. Contrary to the short-wave nonlinearities, which are consensually considered to play an important role on sediment transport, the role of infragravity waves on sediment transport is still a debated issue. In this work, through a set of experiments held in a light-weight-sediment wave flume, it was confirmed that the IG waves are effectively capable of contributing to sediment transport and this contribution was analysed and characterised.

The developed research is summarised below, together with the main conclusions, which synthesize the partial ones previously presented at the end of the two main chapters.

- A high-resolution (in time and space) data set was collected in a very gently-sloping

beach, for both irregular and bichromatic waves, in the scope of the Hydralab IV GLOBEX project. The analysis of this data set, from the shoaling zone until the swash zone, helped distinguishing the distinct behaviours of irregular waves and bichromatic waves. Irregular waves have a broader surf zone and a linear development of the wave nonlinearities until the mid-surf zone; bichromatic waves dissipate their energy over a narrower surf zone, reform in the mid-surf zone and have multiple local maxima of nonlinearity along the cross-shore profile, which are associated to short-wave breaking, but also to the presence of IG waves, when the modulation is sufficiently important. For the same short-wave energy, larger modulation results in wave statistics more similar to those of irregular waves: broader surf zone, one skewness and asymmetry peak and smaller maximum nonlinearity.

- Similarly to the short waves, also the IG waves were shown to become progressively more nonlinear towards the coast and to end up by breaking (large increase of wave height and velocity followed by a great decrease). Free IG waves and IG waves associated to wave groups do not shoal similarly: while the height of the incident free IG waves increases linearly towards the coast, incident IG waves associated to short-wave groups have a greater height increase near the breakpoint and have a local wave-height minimum in the mid-surf zone, from whereon their height increases again.

- The GLOBEX data set comprised high-resolution measurements of both free-surface elevation and velocity. Hence, it was also used to explore the similarities/differences between free-surface elevation and velocity nonlinearities. Even though the absolute values of skewness and asymmetry are different, the main trends are common to free-surface elevation and velocity. Departing from this notion and following the linear wave theory for intermediate water depths, it was shown that the cross-shore velocity, particularly its skewness and asymmetry, can be deduced from the free-surface elevation time series. This is valid until the inner-surf zone, where the maxima of skewness and asymmetry are reached. Beyond, the linear wave theory fails. This procedure can be particularly useful to retrieve velocity nonlinearities in situations where only free-surface elevation data are available.

- Differences in the offshore characteristics of some of the GLOBEX wave conditions were shown to result in distinct cross-shore trends of the nonlinearities and especially on distinct maximum values. This was initially observed for differences in the spectral bandwidth, for irregular waves, and for differences in the modulation,

for bichromatic waves.

- Using field data collected on several beaches, currently-used parameterizations of velocity nonlinearities were analysed, leading to the conclusion that local parameters, such as the local wave height and length and water depth, are not sufficient to accurately describe skewness and asymmetry. The wave history must be taken into account as well.

- The SERR1D numerical model (Cienfuegos *et al.*, 2006, 2007) was validated for GLOBEX and van Noorloos (2003) data sets. Subsequently, the model was used to extend the GLOBEX data by simulating sets of wave conditions for which (i) offshore wave height, (ii) offshore peak period, (iii) offshore spectral bandwidth and (iv) beach slope were varied. This, together with the field data analysis, led to the conclusion that the cross-shore evolution of the nonlinearity of irregular waves cannot be estimated from local wave parameters only and is effectively dependent on, at least, three non-local parameters: offshore wave steepness (the most important), offshore spectral bandwidth and beach slope (in particular for very steep or very mild slopes). For bichromatic waves, the modulation (infragravity-wave height) was also shown to condition the nonlinearity trends and maxima.

- A new parameter, NP_0, was defined, on which the maximum of nonlinearity reached by each wave condition was shown to depend. This parameter was then incorporated, together with the spectral bandwidth, γ, on Ruessink *et al.* (2012) parameterization. This resulted in a reduction of the root-mean-square error between real and predicted values of nonlinearity in up to about 60%, relatively to the former parameterization.

- The short-wave modulation was shown to influence the nonlinearity of bichromatic waves. Hence, to explore the possibility that it may also influence sediment transport, a set of experiments was performed in the LEGI wave flume with light-weight sediments. Three wave conditions with the same short-wave energy but different IG waves were simulated. When run long enough, each wave condition produced a distinct equilibrium profile. For smaller IG waves, more sediment was accumulated in the surf zone and beachface. For greater IG waves, the bar was more marked and sediment accumulated in the shoaling zone before the breakpoint. It is thus clear that IG waves influence the shape of equilibrium profiles. This extends the previous findings of Grasso *et al.* (2009a), who had argued that when the Dean number is the same, the beach profile at equilibrium is the same.

- Two different types of equilibrium were reached: a static and a dynamic. The static equilibrium was observed when IG waves were smaller and was characterised by a constant bed position. The dynamic equilibrium consisted instead of multiple slightly-different profiles oscillating around an average profile shape and was observed when the IG waves were greater. The periodic enhancement of the IG waves (by the lack of a wave-maker with an active reflection compensation system in the flume) contributed to these oscillations.

- The dynamic equilibrium runs highlighted the fact that, as Masselink *et al.* (2006) had stated, the beachface cannot be considered in isolation from the surf zone: the changes induced by the IG waves in the upper-beach were seen to be linked to beach-profile changes in the surf and inner-shoaling zones, which were coupled to the hydrodynamics. Slow accretion of the beachface, when IG-wave height is minimal, results in a more reflective beachface, which contributes to a more energetic swash dynamics and to greater IG-wave reflection, thus promoting IG-wave growth. The accretion of the beachface is accompanied by an accretion just offshore of the breakpoint and by the definition of a more marked bar (due to the transport of sediment from the surf zone to the beachface and to the shoaling zone), increasing energy dissipation at the bar. This results in a less energetic swash zone and a less reflective beachface, which promotes IG-wave height decrease. When an IG-wave height minimum is reached, the slow accretion of the beachface can start again and the cycle continues.

- To avoid the effect of IG waves re-reflected at the wave maker, a series of runs with only two wave groups was conducted. The IG waves were then shown to be capable of influencing sediment transport, by two distinct mechanisms: (i) advection by IG-waves of sediment suspended by short-wave action, which is dependent on the IG-wave height and phasing with the short-wave groups and (ii) modulation of short-wave nonlinearities by IG-wave motion, both directly and indirectly, through water-depth modulation.

- The presence of a re-suspension maximum, where short-waves mobilize the sediment, which is then advected by the IG waves, as previously suggested by Aagaard & Greenwood (2008), was observed at the breakpoint position. When the modulation of the wave groups is higher, IG-wave velocities are larger and there are periods during which short waves are very small. In the absence of short-waves with positive skewness and asymmetry promoting onshore transport, the transport by the IG waves becomes important. Therefore, a certain modulation is necessary in order for the IG-wave transport to become significant relative to the

other sediment transport mechanisms (skewness and asymmetry of short waves, undertow). The greatest concentration of suspended sediment was observed near the end of each wave group. The greatest transport by the IG waves was observed for the wave condition which had the greatest negative velocities also near the end of each wave group. The phasing between the IG waves and short waves was thus shown to condition both the magnitude and direction of the sediment advected by the IG waves.

- The direction and magnitude of the sediment transport is always dependent on the initial beach profile: the same wave condition may promote offshore or onshore transport, depending on the relative importance of the different transport mechanisms, which depend also on the profile morphology, not only on the hydrodynamics.

5.2 Perspectives

5.2.1 Concerning GLOBEX data

The GLOBEX project provided an uncommon data set, especially in terms of velocity measurements, which are not very often available with such high resolution (in time and in space). This makes this data set ideal for analysing the evolution of the wave nonlinearities along the beach profile, for different wave conditions. The nonlinearities and IG-waves of the GLOBEX irregular-wave conditions have been extensively analysed (also by Rocha *et al.* (2013a); de Bakker *et al.* (2014); Ruju *et al.* (2014); among others) and are starting to be well understood. However, several issues rest to be clarified regarding the bichromatic wave conditions.

- The cause of the reformation of short-waves in the mid-surf zone, which does not happen for irregular waves.

- The variation of the incident IG-wave height in the surf zone: confirm if the mechanism proposed by Baldock (2012) can explain the marked decrease in IG-wave height after the breakpoint and explain the subsequent increase in the mid-surf zone.

- The generation of IG-waves by the varying-breakpoint mechanism. Even if the beach is a very gently-sloping one, there seems to be evidence of IG-wave generation by the varying-breakpoint mechanism, at least for the bichromatic waves. Since this may interfer with the propagation of the reflected IG waves

and the interaction between short and IG waves, this issue merits to be further investigated.

- The multiple skewness and asymmetry peaks of the bichromatic wave conditions. They seem to be related to short-wave breaking zones and the influence of IG-waves (correlation between short-waves and IG waves). A possible link between IG-wave minima and skewness and asymmetry maxima was observed, but further research is necessary for a more thorough understanding.

- The simulation of the bichromatic wave conditions with the SERR1D numerical model. Since the different nonlinearity peaks are not well explained, it was not possible to simulate them accurately with the SERR1D model, which can be improved if the origin of the different peaks is better understood.

Retrospectively on the choice of the wave conditions to be run, it would have been good to consider B3 wave condition with the same IG-wave period and greater modulation than B2, as it was done, but with the same short-wave energy as well. This would allow a more direct analysis of the influence of the IG-wave height on the nonlinearities.

5.2.2 Concerning the parameterization of nonlinearities

The Ruessink *et al.* (2012) parameterization was improved for the data presented in this work. To further validate this improvement, it should be applied to other data sets.

The improvement of the parameterization was reached through the change of only two of its parameters. Modifying the other parameters may bring further improvement, especially for the nonlinearity values in the end of the shoaling. This modification may probably be based on the NP_0 and γ as well.

If a large experimental or field data set with velocity measurements for wave conditions with different wave steepness, beach slope and spectral bandwidth is available, the modified expressions of Ruessink *et al.* (2012) parameters may be improved, by reducing the fitting error of B_{max} and $\psi_{(Ur=1)}$ to NP_0 and γ.

5.2.3 Concerning the LEGI experiments

The LEGI wave flume is a unique facility, which correctly represents many of the hydrodynamic and morphodynamic processes that exist in nature. However, it has still some technical limitations which limit the comprehension of certain processes.

- In the scope of this thesis, the first technical limitation was the lack of a wave-maker with an active reflection compensation system. This implied that IG waves

produced by the wave-maker that reflected back at the beach remained "trapped" in the flume, since they re-reflected back at the wave-maker, and so on, until the end of each experiment, when they finally dissipate. Therefore, the IG-wave height in the flume was constantly enhanced and the equilibrium profiles reached do not correspond to the equilibrium profiles that would be reached if the IG waves reflected at the beach were not re-reflected at the wave-maker (and which would be more directly comparable to nature). The evolution of the beach profile towards equilibrium was also more complex to study due to the constant enhancement of the IG waves, particularly for the wave condition with the largest modulation.

- The sediment transport rate can be deduced from the variation of the bed position between the beginning and the end of each run. However, the variation of the bed position during one run (which allows, for example, the following of the action of each short-wave or wave group) cannot be tracked with the optical bed profiler. A way to overcome this limitation is to use video imagery. Video imagery has the advantage of not influencing the flow (as typical instruments to measure velocity and sediment concentration do) and can be developed to detect the interface between the fluid and the bed and thus to follow the evolution of the bed position during the runs. Furthermore, it is possibly the only solution at the moment to make accurate velocity measurements in zones of high sediment suspension or very shallow water, which was also one of the limitations of this study that obliged the utilization of a numerical model to overcome the problem. Having accurate and simultaneous velocity measurements along the entire profile, and especially in the zones of greater sediment suspension (near the breakpoint and in the surf zone), would allow a better characterisation of the beach-profile evolution towards equilibrium. Furthermore, obtaining velocity measurements near the bed, particularly in the shoaling zone, would help further exploring the possibility of bed-load sediment transport by the IG waves.

- By running experiments of only two wave groups and comparing wave conditions with different modulation, the role of IG-wave phasing relatively to the short-wave groups and the short-wave sediment-suspension events was investigated and the importance of this phasing was underlined. To further confirm and extend the findings on this issue, sediment concentration measurements would be of great value. Measuring the velocity and concentration simultaneously and at the same locations would confirm the observed correlation between IG-wave motion and sediment transport, as well as the importance of the mentioned phasing.

Even within the referred technical limitations, other experiments similar to those

performed in the scope of this thesis can help increasing the current knowledge on IG-wave sediment transport. In this work, only three wave conditions were run in the LEGI wave flume. More wave conditions with the same short-wave energy and different degrees of modulation can further extend the present findings. Moreover, varying the period of the IG waves may help confirming the possible relation between the IG waves and the profile shape and, especially, the bar position.

5.2.4 General perspectives

The ultimate aim of being able of understanding wave nonlinearities and infragravity waves is to include their contribution in the prediction of the beach dynamics. For that purpose, some perspective work can be envisaged, based on the results obtained in this thesis.

The improved estimations of B and ψ parameters can be used, through Abreu *et al.* (2010) formulation, to provide a better estimation of the free-stream near-bed horizontal orbital motion. Many sand transport models evaluate the sediment transport as a function of the orbital velocity just above the wave boundary layer or of the bed shear stress (*e.g.* Meyer-Peter & Müller, 1948; Nielsen, 1992; Abreu *et al.*, 2013), which can also be obtained from the orbital velocity (*e.g.* Ribberink & Al-Salem, 1994; Nielsen, 2006). Hence, the new version provided of the parameterization of the velocity nonlinearities can be of further use to ameliorate current estimates of sediment transport. The data set of the LEGI wave-flume experiments can then used to validate the prediction of sediment transport.

The infragravity waves were also shown to influence sediment transport and thus their contribution must be included in sediment-transport models as well. Parameterizations of the sediment transport such as the one proposed by Mariño-Tapia *et al.* (2007) already include the influence of the infragravity-waves, through different terms of the near-bed velocity moments. However, the presence of infragravity waves is not condition enough for infragravity-wave-driven transport to exist: the phasing between the infragravity-waves and the moments of higher sediment suspension can condition both the magnitude and direction of sediment transport. Hence, the inclusion of a parameter related to this phasing in the parameterizations has to be envisaged. A potential approach may be similar to that of Dubarbier *et al.* (2015), which added an extra sediment-transport term to the two classical terms of bed-load and suspended-load fluxes to account for an acceleration-skewness (velocity asymmetry) induced transport. A new sediment-transport term can be imagined, which takes into account the IG-wave velocity magnitude and the phasing between IG waves and the short-wave groups (and the higher sediment-suspension events) and represents the transport by IG waves.

Bibliography

Aagaard, T. & Bryan, K. R. (2003). Observations of infragravity wave frequency selection. *Continental Shelf Research*, 23(10):1019–1034.

Aagaard, T. & Greenwood, B. (1994). Suspended sediment transport and the role of infragravity waves in a barred surf zone. *Marine Geology*, 118:23–48.

Aagaard, T. & Greenwood, B. (1995). Suspended sediment transport and morphological response on a dissipative beach. *Continental Shelf Research*, 15(9):1061–1086.

Aagaard, T. & Greenwood, B. (2008). Infragravity wave contribution to surf zone sediment transport - The role of advection. *Marine Geology*, 251:1–14.

Aagaard, T. & Hughes, M. (2006). Sediment suspension and turbulence in the swash zone of dissipative beaches. *Marine Geology*, 228:117–135.

Aagaard, T. & Jensen, S. G. (2013). Sediment concentration and vertical mixing under breaking waves. *Marine Geology*, 336(0):146–159.

Abdelrahman, S. M. & Thornton, E. B. (1987). Changes in the short wave amplitude and wave number due to the presence of infragravity waves. Dalrymple, I. R. A., *Coastal Hydrodynamics*.

Abreu, T. (2011). *Coastal sediment dynamics under asymmetric waves and currents: measurements and simulations*. PhD Thesis, Faculty of Sciences and Technology of the University of Coimbra.

Abreu, T., Figueiredo, F., & Silva, P. (2014). Influence of nonlinear waves on sandbar migrations using Monte Carlo simulations. In *EGU General Assembly Conference Abstracts*, 16 of *EGU General Assembly Conference Abstracts*, 3170 p.

Abreu, T., Michallet, H., Silva, P. A., Sancho, F., van der A, D. A., & Ruessink, B. G. (2013). Bed shear stress under skewed and asymmetric oscillatory flows. *Coastal Engineering*, 73(0):1–10.

Abreu, T., Silva, P., Sancho, F., & Temperville, A. (2010). Analytical approximate wave form for asymmetric waves. *Coastal Engineering*, 57:656–667.

Airy, G. (1845). *Tides and Waves: Extracted from the Encyclopaedia Metropolitana, Tom. V Pag. 241 - 396*. B. Fellowes.

Alsina, J. M., Cáceres, I., Brocchini, M., & Baldock, T. E. (2012). An experimental study on sediment transport and bed evolution under different swash zone morphological conditions. *Coastal Engineering*, 68(0):31–43.

Arcilla, A., Roelvink, J., O'Connor, B., Reniers, A., & Jiménez, J. (1994). The Delta Flume'93 Experiment. In *Coastal Dynamics '94*, pp: 488–502. ASCE.

Atkinson, A. & Baldock, T. E. (2016). A high-resolution sub-aerial and sub-aqueous laser based laboratory beach profile measurement system. *Coastal Engineering*, 107:28 – 33.

Bagnold, R. A. (1963). *Beach and nearshore processes - Part 1, Mechanics of marine sedimentation.*, 3 of *The sea - ideas and observations on progress in the study of the sea*. New York and London: Interscience Wiley, hill, m.n. edition.

Bailard, J. A. (1981). An energetics total load sediment transport model for a plane sloping beach. *Journal of Geophysical Research: Oceans*, 86(C11):10938–10954.

Baldock, T., Alsina, J., Caceres, I., Vicinanza, D., Contestabile, P., Power, H., & Sanchez-Arcilla, A. (2011). Large-scale experiments on beach profile evolution and surf and swash zone sediment transport induced by long waves, wave groups and random waves. *Coastal Engineering*, 58:214–227.

Baldock, T., Manoonvoravong, P., & Pham, K. (2010). Sediment transport and beach morphodynamics induced by free long waves, bound long waves and wave groups. *Coastal Engineering*, 57:898–916.

Baldock, T. & Simmonds, D. (1999). Separation of incident and reflected waves over sloping bathymetry. *Coastal Engineering*, 38(3):167 – 176.

Baldock, T. E. (2012). Dissipation of incident forced long waves in the surf zone - Implications for the concept of bound wave release at short wave breaking. *Coastal Engineering*, 60(0):276–285.

Baldock, T. E., Baird, A. J., Horn, D. P., & Mason, T. (2001). Measurements and modeling of swash-induced pressure gradients in the surface layers of a sand beach. *Journal of Geophysical Research: Oceans*, 106(C2):2653–2666.

Baldock, T. E., Huntley, D. A., Bird, P. A. D., O'Hare, T., & Bullock, G. N. (2000). Breakpoint generated surf beat induced by bichromatic wave groups. *Coastal Engineering*, 39(2):213–242.

Battjes, J., Bakkenes, H., Janssen, T., & van Dongeren, A. (2004). Shoaling of subharmonic gravity waves. *Journal of Geophysical Research: Oceans*, 109(C2):1978 – 2012.

Beach, R. & Sternberg, R. (1991). Infragravity driven suspended sediment transport in the swash, inner and outer-surf zone. In Kraus, G. & Kriebel, *Coastal Sediments*, pp: 114–128.

Beach, R. A. & Sternberg, R. W. (1988). Suspended sediment transport in the surf zone: Response to cross-shore infragravity motion. *Marine Geology*, 80(1):61–79.

Berni, C. (2011). *Processus de mobilisation et de transport de sédiments dans la zone de déferlement*. PhD Thesis, Université Joseph Fourier, Laboratoire des Écoulements Géophysiques et Industriels.

Berni, C., Barthélemy, E., & Michallet, H. (2013). Surf zone cross-shore boundary layer velocity asymmetry and skewness: An experimental study on a mobile bed. *Journal of Geophysical Research: Oceans*, 118:1–13.

Biésel, F. (1952). Équations générales au second ordre de la houle irrégulière. *Houille Blanche*, 5:371–376.

Boussinesq, J. (1872). Théorie des ondes et des remous qui se propagent le long d'un canal rectangulaire horizontal, en communiquant au liquide contenu dans ce canal des vitesses sensiblement pareilles de la surface au fond. *Journal de Mathématiques Pures et Appliquées*, 17(2):55–108.

Bowen, A. J. (1980). Simple models of nearshore sedimentation: beach profiles and longshore bars. Canada, G. S. o., *Coastline Of Canada, Littoral Processes And Shore Morphology*, 80-10, pp: 1–11.

Brunn, P. (1954). Coast Erosion and the Development of Beach Profiles. Technical Report No. 44, Beach Erosion Board, U.S. Army Corps of Engineers.

Calantoni, J. & Puleo, J. (2006). Role of pressure gradients in sheet flow of coarse sediments under sawtooth waves. *Journal of Geophysical Research*, 111.

Cienfuegos, R., Barthélemy, E., & Bonneton, P. (2006). A fourth-order compact finite volume scheme for fully nonlinear and weakly dispersive Boussinesq-type equations.

Part I: Model development and analysis. *International Journal for Numerical Methods in Fluids*, 51:1217–1253.

Cienfuegos, R., Barthélemy, E., & Bonneton, P. (2007). A fourth order compact finite volume scheme for fully nonlinear and weakly dispersive Boussinesq-type equations. Part II: Boundary conditions and validation. *International Journal for Numerical Methods in Fluids*, 53:1423–1455.

Cienfuegos, R., Duarte, L., Suarez, L., & Catalán, P. (2011). Numerical computation of infragravity wave dynamics and velocity profiles using a fully nonlinear Boussinesq model. *Coastal Engineering Proceedings*, 1(32):48.

Cienfuegos, R., Duarte, L., Suarez, L., & Catalán, P. A. (2010). Numerical computation of infragravity wave dynamics and velocity profiles using a fully nonlinear boussinesq model. In Lynett, J. M. S. & Patrick, *32nd Conference on Coastal Engineering*.

Cointe, R. & Tulin, M. P. (1994). A theory of steady breakers. *Journal of Fluid Mechanics*, 276:1–20.

Cowen, E., Sou, I., Liu, P., & Raubenheimer, B. (2003). Particle imagery velocimetry within a laboratory generated swash zone. *Journal of Engineering Mechanics*, 129(10):1119–1129.

Dally, W. R. (1987). Longshore bar formation. In *Coastal Sediments '87: Proceedings of a Specialty Conference on Advances in Understanding of Coastal Sediment Processes*.

Dalrymple, R. & Thompson, W. (1976). Study of equilibrium beach profiles. In *Proceedings 15th International Conference on Coastal Engineering*, 1 (15), pp: 1277–1296.

de Bakker, A., Herbers, T., Smit, P., Tissier, M., & Ruessink, B. G. (2015a). Nonlinear Infragravity-Wave Interactions on a Gently Sloping Laboratory Beach. *Journal of Physical Oceanography*, 45:589–605.

de Bakker, A., Tissier, M., & Ruessink, B. (2015b). Beach steepness effects on nonlinear infragravity-wave interactions: A numerical study. *Journal of Geophysical Research: Oceans*, in press p.

de Bakker, A. T. M., Tissier, M. F. S., & Ruessink, B. G. (2014). Shoreline dissipation of infragravity waves. *Continental Shelf Research*, 72:73–82.

Dean, R. (1977). *Equilibrium Beach Profiles: U.S. Atlantic and Gulf Coasts*. Ocean Engineering Report. Center for Apllied Coastal Research.

Dean, R. & Dalrymple, R. (1991). *Water Wave Mechanics for Engineers and Scientists*. Advanced series on ocean engineering. World Scientific.

Dean, R. & Dalrymple, R. (2002). *Coastal Processes with Engineering Applications*. Cambridge University Press, 487 p.

Dean, R. G. (1973). Heuristic models of sand transport in the surf zone. In *First Australian Conference on Coastal Engineering*, pp: 215–221, Sydney N. S. W. Institution of Engineers, Australia.

Dibajnia, M., Moriya, T., & Watanabe, A. (2001). A representative wave model for estimation of nearhore local transport rate. *Coastal Engineering Journal*, 43(1):1–38.

Didenkulova, I. & Soomere, T. (2011). Formation of two-section cross-shore profile under joint influence of random short waves and groups of long waves. *Marine Geology*, 289:29–33.

Doering, J. C. & Bowen, A. J. (1987). Skewness in the nearshore zone: A comparison of estimates from Marsh-McBirney current meters and colocated pressure sensors. *Journal of Geophysical Research: Oceans*, 92(C12):13173–13183.

Doering, J. C. & Bowen, A. J. (1995). Parametrization of orbital velocity asymmetries of shoaling and breaking waves using bispectral analysis. *Coastal Engineering*, 26:15–33.

Dohmen-Janssen, C., Kroekenstoel, D. F., Hassan, W. N., & Ribberink, J. S. (2002). Phase lags in oscillatory sheet flow: experiments and bed load modelling. *Coastal Engineering*, 46(1):61 – 87.

Dong, G., Chen, H., & Ma, Y. (2014). Parameterization of nonlinear shallow water waves over sloping bottoms. *Coastal Engineering*, 94(0):23–32.

Dong, G., Ma, X., Perlin, M., Ma, Y., Yu, B., & Wang, G. (2009). Experimental study of long wave generation on sloping bottoms. *Coastal Engineering*, 56(1):82–89.

Drake, T. & Calantoni, J. (2001). Discrete particle model for sheet low sediment transport in the nearshore. *Journal of Geophysical Research*, 106:19,859 – 19,868.

Dubarbier, B., Castelle, B., Marieu, V., & Ruessink, G. (2015). Process-based modeling of cross-shore sandbar behavior. *Coastal Engineering*, 95(0):35 – 50.

Elfrink, B. & Baldock, T. (2002). Hydrodynamics and sediment transport in the swash zone: a review and perspectives. *Coastal Engineering*, 45:149–167.

Elfrink, B., Hanes, D. M., & Ruessink, B. G. (2006). Parameterization and simulation of near bed orbital velocities under irregular waves in shallow water. *Coastal Engineering*, 53(11):915–927.

Elgar, S., Gallagher, E. L., & Guza, R. T. (2001). Nearshore sandbar migration. *Journal of Geophysical Research: Oceans*, 106(C6):11623–11627.

Elgar, S. & Guza, R. (1985). Observations of bispectra of shoaling surface gravity waves. *Journal of Fluid Mechanics*, 161:425–448.

Elgar, S., Guza, R., & Freilich, M. (1988). Eulerian measurements of horizontal accelerations in shoaling gravity waves. *Journal of Geophysical Research*, 93(C8):9261–9269.

Fernández-Mora, A., Calvete, D., Falqués, A., & de Swart, H. E. (2015). Onshore sandbar migration in the surf zone: New insights into the wave-induced sediment transport mechanisms. *Geophysical Research Letters*, 42(8):2869–2877.

Filipot, J.-F. (2015). Investigation of the bottom slope dependence of the nonlinear wave evolution toward breaking using SWASH. *Journal of Coastal Research*, 0(0):000–000.

Foster, D. L., Bowen, A. J., Holman, R. A., & Natoo, P. (2006). Field evidence of pressure gradient induced incipient motion. *Journal of Geophysical Research: Oceans*, 111(C5). C05004.

Frigaard, P. & Brorsen, M. (1995). A time-domain method for separating incident and reflected irregular waves. *Coastal Engineering*, 24(3-4):205–215.

Grant, W. D. & Madsen, O. S. (1979). Combined wave and current interaction with a rough bottom. *Journal of Geophysical Research: Oceans*, 84(C4):1797–1808.

Grasso, F. (2009). *Modélisation physique de la dynamique hydro-sédimentaire des plages*. PhD Thesis, Université Joseph Fourier, Laboratoire des Écoulements Géophysiques et Industriels.

Grasso, F., Michallet, H., & Barthélemy, E. (2011). Sediment transport associated with morphological beach changes forced by irregular asymmetric, skewed waves. *Journal of Geophysical Research: Oceans*, 116(C3):C03020.

Grasso, F., Michallet, H., Barthélemy, E., & Certain (2009a). Physical modeling of intermediate cross-shore beach morphology: transients and equilibrium states. *Journal of Geophysical Research: Oceans*, 114(C9):1978–2012.

Grasso, F., Michallet, H., Certain, R., & Barthélemy, E. (2009b). Experimental flume simulation of sandbar dynamics. *Journal of Coastal Research*, SI 56:54–58.

Guedes, R. M. C., Bryan, K. R., & Coco, G. (2013). Observations of wave energy fluxes and swash motions on a low-sloping, dissipative beach. *Journal of Geophysical Research: Oceans*, 118(7):3651–3669.

Guza, R. T. & Thornton, E. (1985). Velocity moments in nearshore. *J. of Waterway, Port Coast. Ocean Eng.*, 111(2):235–256.

Guza, R. T. & Thornton, E. B. (1982). Swash Oscillations on a Natural Beach. *Journal of Geophysical Research*, 87:483–491.

Guza, R. T., Thornton, E. B., & Holman, R. A. (1984). Swash on steep and shallow beaches. In *19th Int. Conf. on Coastal Engineering*, pp: 708–723.

Hardisty, J. (1986). A morphodynamic model for beach gradients. *Earth Surface Processes and Landforms*, 11(3):327–333.

Henderson, S. M. & Bowen, A. J. (2002). Observations of surf beat forcing and dissipation. *Journal of Geophysical Research*, 107(C11):3193.

Henderson, S. M., Guza, R., Elgar, S., Herbers, T., & Bowen, A. J. (2006). Nonlinear generation and loss of infragravity wave energy. *Journal of Geophysical Research*, 111.

Herbers, T., Elgar, S., & Guza, R. (1995). Generation and propagation of infragravity waves. *Journal of Geophysical Research*, 100(C12):24863–24872.

Herbers, T. H. C., Elgar, S., & Guza, R. T. (1994). Infragravity-Frequency (0.005-0.05 Hz) Motions on the Shelf. Part I: Forced Waves. *Journal of Physical Oceanography*, 24(5):917–927.

Hsu, T.-J. & Hanes, D. (2004). Effects of wave shape on sheet flow sediment transport. *Journal of Geophysical Research*, 109.

Hughes, S. A. (1993). *Physical models and laboratory techniques in coastal engineering*. Singapore : World Scientific. Includes bibliographical references and indexes.

Huntley, D. A., Guza, R. T., & Bowen, A. J. (1977). Universal Form for Shoreline Run-up Spectra. *Journal of Geophysical Research-Oceans and Atmospheres*, 82(18):2577–2581. gr.

Inch, K., Masselink, G., Puleo, J. A., Russell, P., & Conley, D. C. (2015). Vertical structure of near-bed cross-shore flow velocities in the swash zone of a dissipative beach. *Continental Shelf Research*.

IPCC (2014). Climate Change 2014: Synthesis Report. Contribution of Working Groups I, II and III to the Fifth Assessment Report of the Intergovernmental Panel on Climate Change. Technical report, Core Writing Team, R.K. Pachauri and L.A. Meyer (eds.)]. IPCC, Geneva, Switzerland, 151 pp.

Iribarren Cavanilles, R. & Casto Nogales, M. (1949). Protection des ports. Technical report, PIANC.

Janssen, T. T., Battjes, J. A., & van Dongeren, A. R. (2003). Long waves induced by short-wave groups over a sloping bottom. *Journal of Geophysical Research: Oceans*, 108(C8):3252.

Kennedy, A., Chen, Q., Kirby, J., & Dalrymple, R. (2000). Boussinesq modeling of wave transformation, breaking, and runup. Part I: 1D. *Journal of Waterway, Port, Coastal and Ocean Engineering*, 126(1):39–47.

Komar, P. (1976). *Beach processes and sedimentation*. Prentice-Hall, Inc., Englewood Cliffs, New Jersey.

Korteweg, D. J. & deVries, G. (1895). On the change of form of long waves advancing in a rectangular channel, and on a new type of long stationary waves. *Philosophical Magazine*, 39(5):422–443.

Kuriyama, Y. (2009). Numerical model for bar migration at Hasaki, Japan. In *Proceedings of Coastal Dynamics*, 9. World Scientific.

List, J. H. (1991). Wave groupiness variations in the nearshore. *Coastal Engineering*, 15(5-6):475–496.

Longuet-Higgins, M. & Stewart, R. (1962). Radiation stress and mass transport in gravity waves with applications to "surf-beats". *Journal of Fluid Mechanics*, 8:565–583.

Longuet-Higgins, M. & Stewart, R. (1964). Radiation stress in water waves: A physical discussion with applications. *Deep Sea Research*, 11:529–563.

Longuet-Higgins, M. S. (1953). Mass Transport in Water Waves. *Philosophical Transactions of the Royal Society of London A: Mathematical, Physical and Engineering Sciences*, 245(903):535–581.

Mariño-Tapia, I., Russell, P., O'Hare, T., Davidson, M., & Huntley, D. A. (2007). Cross-shore sediment transport on natural beaches and its relation to sandbar migration patterns: 1. Field observations and derivation of a transport parameterization. *Journal of Geophysical Research*, 112.

Masselink, G. (1995). Group bound long waves as a source of infragravity energy in the surf zone. *Continental Shelf Research*, 15(13):1525–1547.

Masselink, G., Evans, D., Hughes, M. G., & Russell, P. (2005). Suspended sediment transport in the swash zone of a dissipative beach. *Marine Geology*, 216(3):169–189.

Masselink, G., Kroon, A., & Davidson-Arnott, R. G. D. (2006). Morphodynamics of intertidal bars in wave-dominated coastal settings - A review. *Geomorphology*, 73:33–49.

Masselink, G. & Puleo, J. (2006). Swash-zone morphodynamics. *Continental Shelf Research*, 26:661–680.

Meyer-Peter, E. & Müller, R. (1948). Formulas for bed-load transport. Technical report, Report from the 2nd Meeting of the International Association for Hydraulic Structures Research, Stockholm, Sweden. IAHR.

Michallet, H., Cienfuegos, R., Barthélemy, E., & Grasso, F. (2011). Kinematics of waves propagating and breaking on a barred beach. *European Journal of Mechanics B/Fluids*, 30(6):624–634.

Michallet, H., Grasso, F., & Barthélemy, E. (2007). Long waves and beach profile evolutions. *Journal of Coastal Research*, SI50:221–225.

Michallet, H., Ruessink, G., Rocha, M. V. L., De Bakker, A., Van Der A, D. A., Ruju, A., Silva, P. A., Sénéchal, N., Marieu, V., Tissier, M., Almar, R., Abreu, T., Birrien, F., Vignal, L., Barthelemy, E., Mouazé, D., Cienfuegos, R., & Wellens, P. (2014). GLOBEX: Wave dynamics on a shallow sloping beach. In *HYDRALAB IV Joint User Meeting, Lisbon, July 2014*, Lisbon, Portugal.

Mori, N., Suzuki, T., & Kakuno, S. (2007). Noise of Acoustic Doppler Velocimeter Data in Bubbly Flows. *Journal of Engineering Mechanics*, 133(1):122–125.

Munk, W. (1949). Surf beats. *EOS Transactions*, 30:849–854.

Nielsen, P. (1992). *Coastal boundary layers and sediment transport.* World Scientific, Singapore, 324 p.

Nielsen, P. (2006). Sheet flow sediment transport under waves with acceleration skewness and boundary layer streaming. *Coastal Engineering*, 53(9):749 – 758.

Norheim, C. A., Herbers, T. H. C., & Elgar, S. (1998). Nonlinear Evolution of Surface Wave Spectra on a Beach. *Journal of Physical Oceanography*, 28(7):1534–1551.

Osborne, P. & Greenwood, B. (1992a). Frequency dependent cross-shore suspended sediment transport. 2. A barred shoreface. *Marine Geology*, 106:25–51.

Osborne, P. D. & Greenwood, B. (1992b). Frequency dependent cross-shore suspended sediment transport. 1. A non-barred shoreface. *Marine Geology*, 106:1–24.

Petti, M. & Longo, S. (2001). Turbulence experiments in the swash zone. *Coastal Engineering*, 43:1–24.

Prel, P., Michallet, H., & Barthélemy, E. (2011). Flume experiments on wave non-linear interactions effects on beach morphodynamics. *Journal of Coastal Research*, SI 64:2053–2057.

Puleo, J. A., Beach, R. A., Holman, R. A., & Allen, J. S. (2000). Swash zone sediment suspension and transport and the importance of bore-generated turbulence. *Journal of Geophysical Research: Oceans*, 105(C7):17021–17044.

Puleo, J. A., Holland, K. T., Plant, N. G., Slinn, D. N., & Hanes, D. M. (2003). Fluid acceleration effects on suspended sediment transport in the swash zone. *Journal of Geophysical Research: Oceans*, 108(C11). 3350.

Puleo, J. A., Lanckriet, T., & Wang, P. (2012). Near bed cross-shore velocity profiles, bed shear stress and friction on the foreshore of a microtidal beach. *Coastal Engineering*, 68(0):6–16.

Raubenheimer, B., Elgar, S., & Guza, R. T. (2004). Observations of swash zone velocities: A note on friction coefficients. *J. Geophys. Res.*, 109(C1):C01027.

Raubenheimer, B., Guza, R. T., & Elgar, S. (1996). Wave transformation across the inner surf zone. *Journal of Geophysical Research: Oceans*, 101(C11):25589–25597.

Ribberink, J., Dohmen-Janssen, C., Hanes, D., McLean, S., & Vicent, C. (2000). Near-bed sand transport mechanisms under waves, a large-scale flume experiment (Sistex99). In *Coastal Engineering 2000: Proceedings of the Twenty-First Coastal*

Engineering International Conference, July 16-21, 2000 in Sydney, Australia, pp: 3263–3276. Am. Soc. of Civ. Eng., Reston, Va.

Ribberink, J. S. & Al-Salem, A. A. (1994). Sediment transport in oscillatory boundary layers in cases of rippled beds and sheet flow. *J. Geophys. Res.*, 99(C6):12707–12727.

Rocha, M., Silva, P., Michallet, H., Abreu, T., & Barthélemy, E. (2013a). Nonlinearities of short and long waves across the shoaling, surf and swash zones: large-scale physical model results. In *Proc. 7th Int. Conf. on Coastal Dynamics*, pp: 1329–1340.

Rocha, M., Silva, P. A., Michallet, H., Abreu, T., Moura, D., & Fortes, C. (2013b). Parameterizations of wave nonlinearity from local wave parameters: a comparison with field data. *Journal of Coastal Research*, SI65:374–379.

Roelvink, J. & Stive, M. (1989). Bar-generating cross-shore flow mechanisms on a beach. *Journal of Geophysical Research*, 94(C4):4785–4800.

Ruessink, B., Kleinhans, M., & van den Beukel, P. (1998a). Observations of swash under highly dissipative conditions. *Journal Geophysical Research*, 103:3111–3118.

Ruessink, B. G., Houwman, K. T., & Hoekstra, P. (1998b). The systematic contribution of transporting mechanisms to the cross-shore sediment transport in water depths of 3 to 9 m. *Marine Geology*, 152(4):295–324.

Ruessink, B. G., Michallet, H., Abreu, T., Sancho, F., Van der A, D. A., Van der Werf, J. J., & Silva, P. A. (2011). Observations of velocities, sand concentrations, and fluxes under velocity-asymmetric oscillatory flows. *J. Geophys. Res.*, 116(C3):C03004.

Ruessink, B. G., Michallet, H., Bonneton, P., Mouazé, D., Lara, J., Silva, P., & Wellens, P. (2013). GLOBEX: Wave dynamics on a gently sloping laboratory beach. In *Coastal Dynamics*, pp: 1351–1362.

Ruessink, B. G., Ramaekers, G., & van Rijn, L. C. (2012). On the parameterization of the free-stream non-linear wave orbital motion in nearshore morphodynamic models. *Coastal Engineering*, 65(0):56–63.

Ruju, A., Lara, J. L., & Losada, I. J. (2012). Radiation stress and low-frequency energy balance within the surf zone: A numerical approach. *Coastal Engineering*, 68(0):44–55.

Ruju, A., Lara, J. L., & Losada, I. J. (2014). Numerical analysis of run-up oscillations under dissipative conditions. *Coastal Engineering*, 86(0):45–56.

Russell, P. & Huntley, D. A. (1999). A Cross-Shore Transport "Shape Function" for High Energy Beaches. *Journal of Coastal Research*, 15(1):198–205.

Russell, P. E. (1993). Mechanisms for beach erosion during storms. *Continental Shelf Research*, 13(11):1243 – 1265.

Schaffer, H. A. (1993). Infragravity waves induced by short-wave groups. *Journal of Fluid Mechanics*, 247:551–588.

Schäffer, H. A. (1996). Second-order wavemaker theory for irregular waves. *Ocean Engineering*, 23(1):47 – 88.

Sheremet, A., Guza, R. T., Elgar, S., & Herbers, T. H. C. (2002). Observations of nearshore infragravity waves: Seaward and shoreward propagating components. *Journal of Geophysical Research: Oceans*, 107(C8):10–1–10–10.

Short, A. D. (1975). Multiple offshore bars and standing waves. *Journal of Geophysical Research*, 80(27):3838–3840.

Short, A. D. & Woodroffe, C. D. (2009). *The coast of Australia / Andrew D. Short and Colin D. Woodroffe*. Cambridge University Press Melbourne.

Silva, P. A., Abreu, T., van der A, D., Sancho, F., Ruessink, B., van der Werf, J., & J.S., R. (2011). Sediment transport in nonlinear skewed oscillatory flows: Transkew experiments. *Journal of Hydraulic Research*, 49(1):72–80.

Sénéchal, N., Bonneton, P., & Dupuis, H. (2001). Field observations of irregular wave transformation in the surf zone. Engineers, A. S. o. C., *Coastal Dynamics '01*, pp: 62–71.

Sénéchal, N., Coco, G., Bryan, K. R., & Holman, R. A. (2011). Wave runup during extreme storm conditions. *Journal of Geophysical Research: Oceans*, 116(C7):n/a–n/a. C07032.

Soulsby, R. (1997). *Dynamics of Marine Sands: A Manual for Practical Applications*. Telford.

Stive, M. (1986). A model for cross-shore sediment transport. *Coastal Engineering Proceedings*, 1(20).

Stive, M. J., Aarninkhof, S. G., Hamm, L., Hanson, H., Larson, M., Wijnberg, K., Nicholls, R. J., & Capobianco, M. (2002). Variability of shore and shoreline evolution. *Coastal Engineering*, 47(2):211 – 235. Shore Nourishment in Europe.

Stokes, G. (1847). On the theory of oscillatory waves. *Transactions of the Cambridge Philosophical Society*, 8:441–455.

Svendsen, I. & Madsen, P. A. (1978). Wave characteristics in the surf zone. In *16th International Conference on Coastal Engineering*, 1, pp: 520–539. ASCE.

Swart, D. (1974). A schematization of onshore-offshore transport. *Coastal Engineering Proceedings*, 1(14).

Symonds, G., Huntley, D., & Bowen, A. J. (1982). Two-dimensional surf beat: long wave generation by a time-varying breakpoint. *Journal of Geophysical Research*, 87(C1):492–498.

Thornton, E., Dalrymple, R., Drake, T., Gallagher, E., Guza, R., Hay, A., Holman, R., Kaihatu, J., Lippmann, T., & Ozkan-Haller, T. (2000). State of nearshore processes research: II. Technical Report NPS-OC-00-001, Naval Postgraduate School, Monterey.

Thornton, E. & Guza, R. T. (1983). Transformation of wave height distribution. *J. Geophys. Res.*, 88(C10).

Ting, F. C. & Kirby, J. T. (1994). Observation of undertow and turbulence in a laboratory surf zone. *Coastal Engineering*, 24(1–2):51 – 80.

Turner, I. L., Russell, P. E., & Butt, T. (2008). Measurement of wave-by-wave bed-levels in the swash zone. *Coastal Engineering*, 55(12):1237–1242.

U.S. Army Corps of Engineers, Washington, D. (2002). *Coastal Engineering Manual*, Engineer Manual 1110-2-1100.

van der A, D., O'Donoghue, T., & Ribberink, J. (2010). Measurements of sheet flow transport in acceleration-skewed oscillatory flow and comparison with practical formulations. *Coastal Engineering*, 57(3):331–342.

van der A, D. A., Mouazé, D., Vignal, L., Silva, P. A., Abreu, T., Barthélemy, Elemy, E., & Michallet, H. (2013). Wave boundary layer dynamics on a low sloping laboratory beach. In *7th International Conference on Coastal Dynamics*, pp: 1741 – 1752, Arcachon, France.

van Dongeren, A. (1997). Quasi 3-D modeling of nearshore hydrodynamics. Technical report, Delaware University Newark Center for Applied Coastal Research.

van Dongeren, A., Battjes, J., Janssen, T., van Noorloos, J., Steenhauer, K., Steenbergen, G., & Reniers, A. (2007). Shoaling and shoreline dissipation of low-frequency waves. *Journal of Geophysical Research*, 112:C02011.

van Noorloos, J. (2003). Energy transfer between short wave groups and bound long waves on a plane slope. Msc, Delft University of Technology.

Vicinanza, D., Baldock, T., Contestabile, P., Alsina, J., Cáceres, I., Brocchini, M., Conley, D., Andersen, T. L., Frigaard, P., & Ciavola, P. (2011). Swash zone response under various wave regimes. *Journal of Hydraulic Research*, 49:55–63.

Voulgaris, G. & Trowbridge, J. H. (1998). Evaluation of the Acoustic Doppler Velocimeter (ADV) for Turbulence Measurements. *Journal of Atmospheric and Oceanic Technology*, 15(1):272–289.

Wells, D. R. (1967). Beach equilibrium and second-order wave theory. *Journal of Geophysical Research*, 72(2):497–504.

Wright, L. & Short, A. (1984). Morphodynamic variability of surf zones and beaches: A synthesis. *Marine Geology*, 56(1–4):93 – 118.

Appendix A

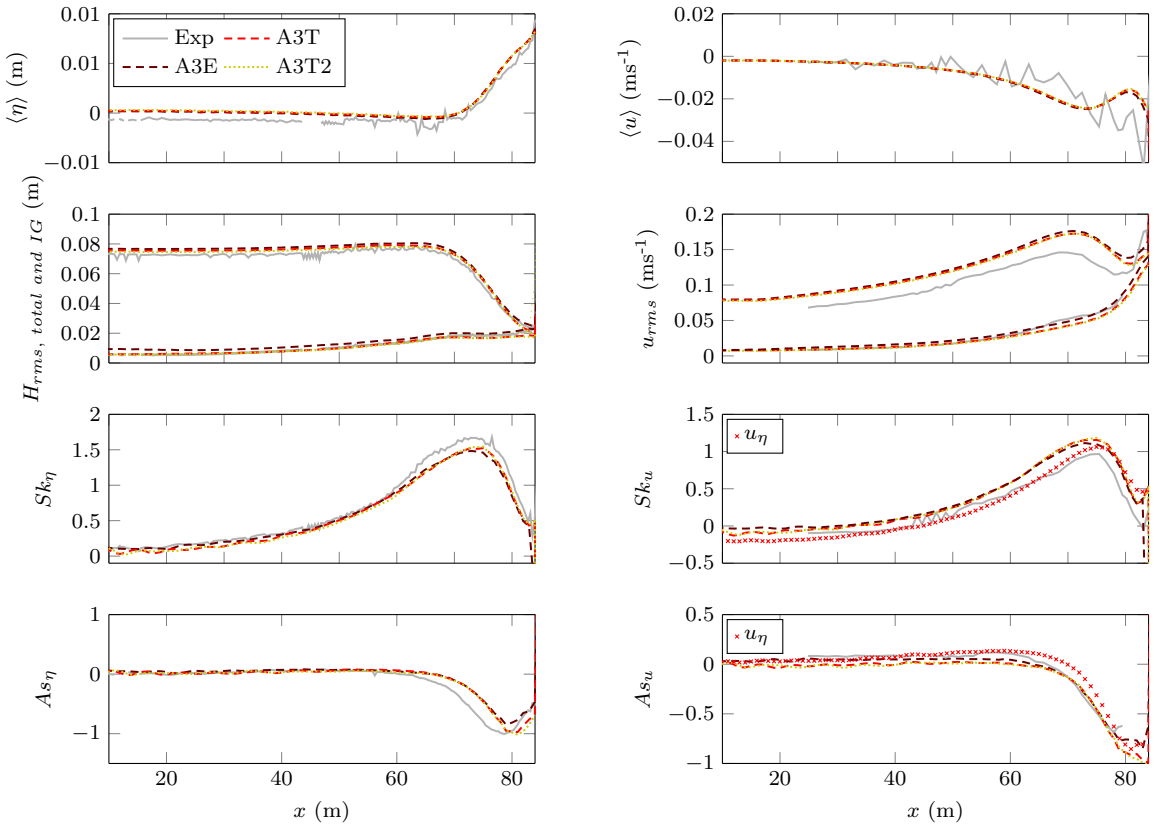

Figure A.1: Evolution of free-surface elevation and cross-shore velocity statistics along the cross-shore profile for A3. Grey line - experimental data; dark red - A3E; red - A3T; yellow - A3T2.

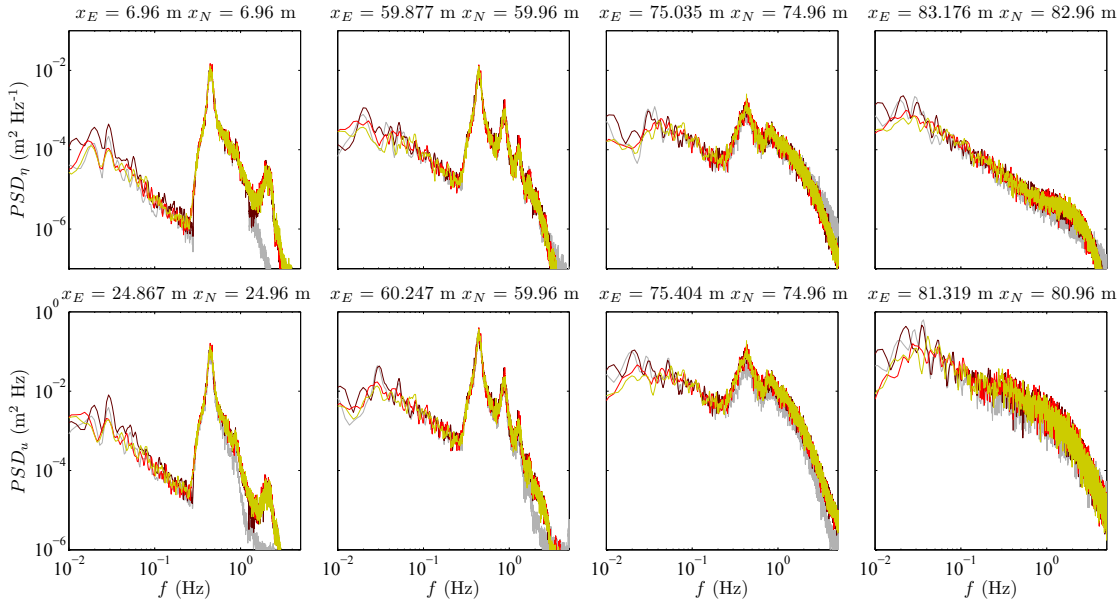

Figure A.2: Spectra of free-surface elevation (top) and cross-shore velocity (bottom) at four different cross-shore positions for A3. Grey line - experimental data; dark red - A3E; red - A3T; yellow - A3T2. The red dots in Sk_u and As_u figures were calculated from the velocity time series obtained from A3T free-surface elevation time series, with the u_η method (see subsection 3.2.5).

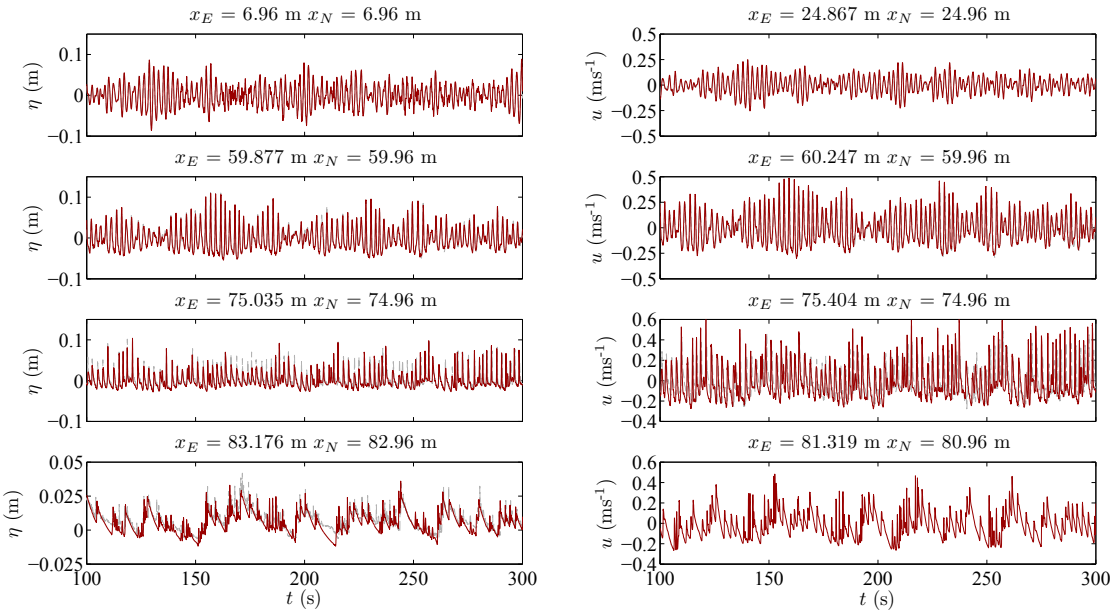

Figure A.3: Time series of free-surface elevation and cross-shore velocity spectra at four different cross-shore positions for A3 condition. Grey line - experimental data; dark red - A3E. Note: Since A3 is an irregular wave condition, the spectra of theoretic and experimental input conditions is the same, but not the time series and thus A3T and A3T2 time series are not compared to A3E.

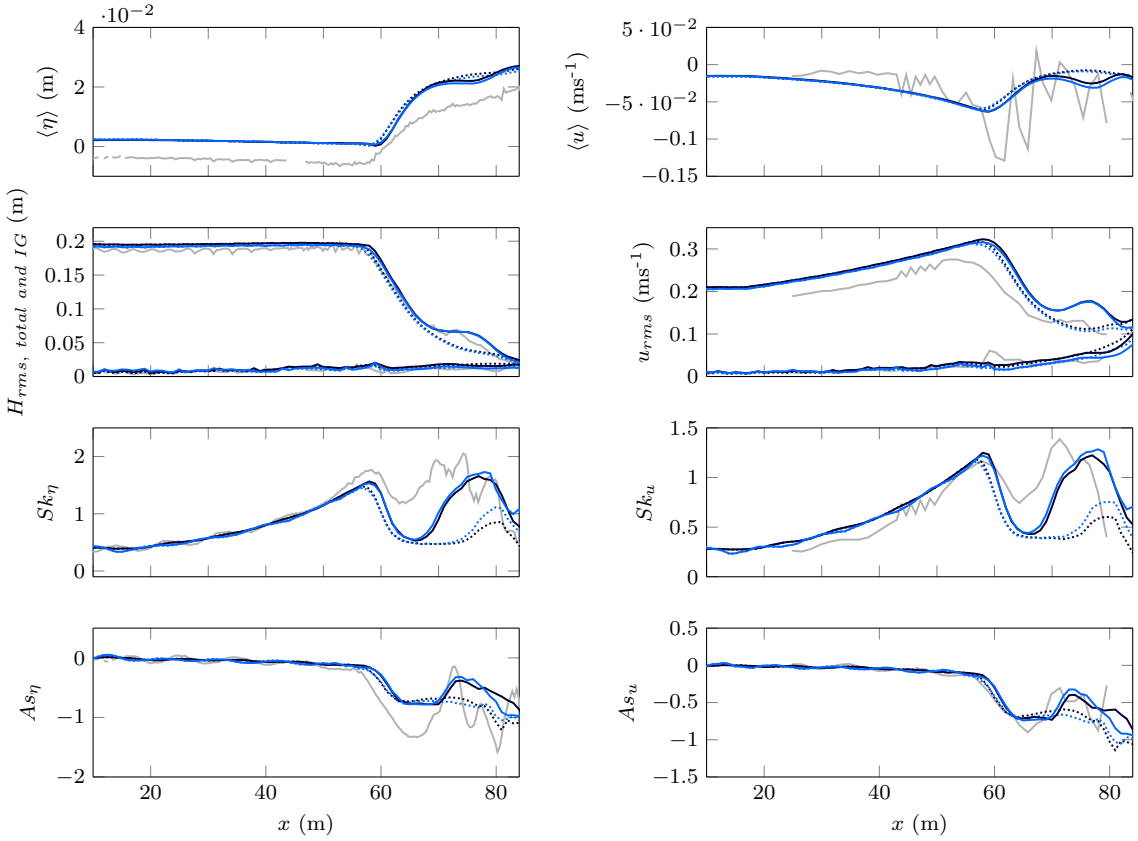

Figure A.4: Evolution of free-surface elevation and cross-shore velocity statistics along the cross-shore profile for B1. Grey markers - experimental data; dark blue - B1E; blue - B1T. Dotted lines: simulations ran with A set of breaking parameters; full lines: $\phi_b = 27°$ and $\phi_f = 9°$.

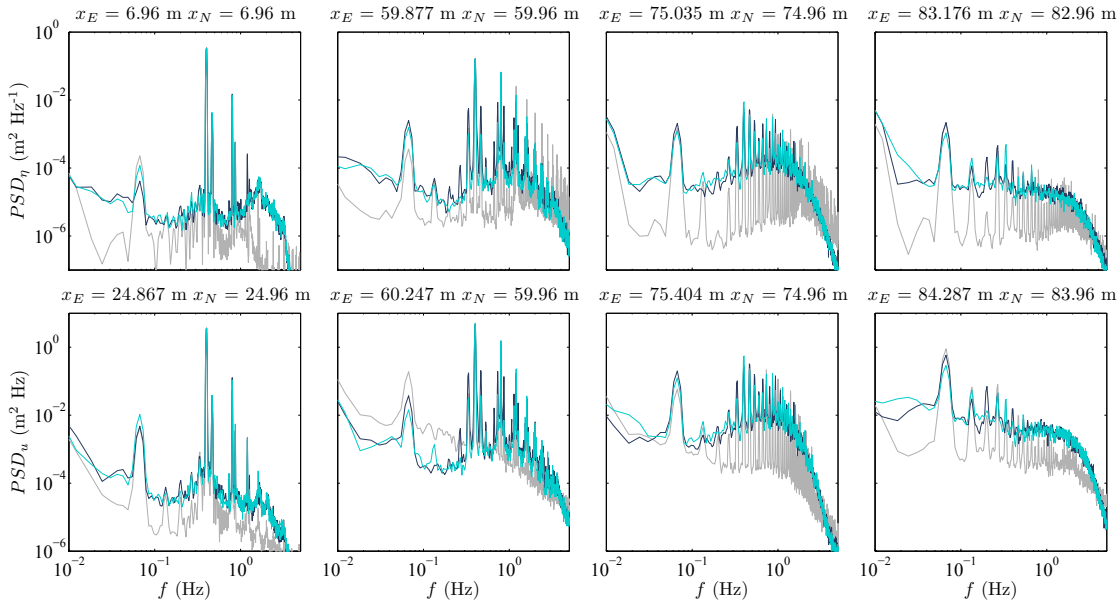

Figure A.5: Spectra of free-surface elevation (top) and cross-shore velocity (bottom) at four different cross-shore positions for B1 (with $\phi_b = 27^\circ$ and $\phi_f = 9^\circ$). Grey line - experimental data; dark blue - B1E; blue - B1T.

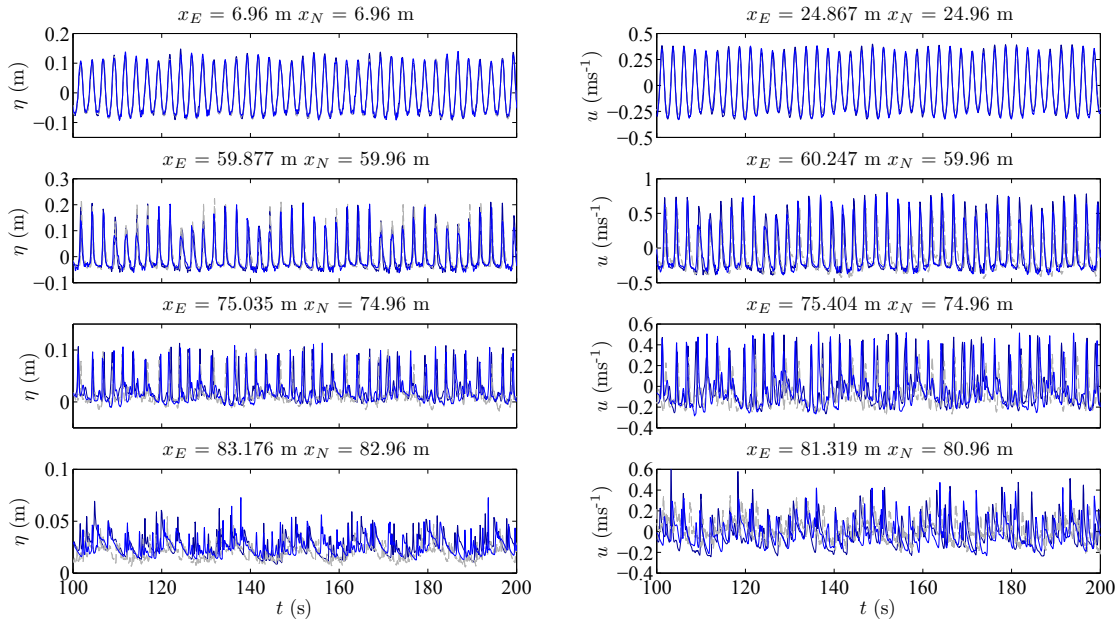

Figure A.6: Time series of free-surface elevation and cross-shore velocity spectra at four different cross-shore positions for B1 (with $\phi_b = 27^\circ$ and $\phi_f = 9^\circ$). Grey line - experimental data; dark blue - B1E; blue - B1T.

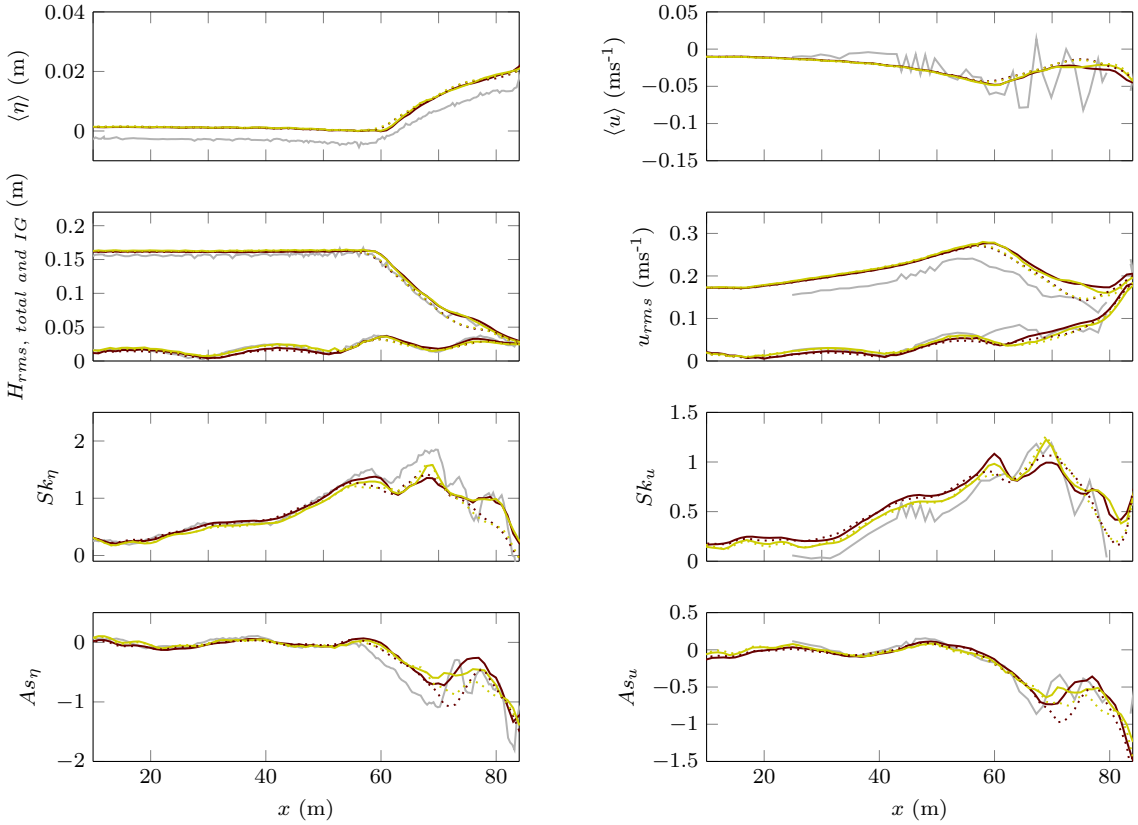

Figure A.7: Evolution of free-surface elevation and cross-shore velocity statistics along the cross-shore profile for B3 (with $\phi_b = 27^\circ$ and $\phi_f = 9^\circ$). Grey markers - experimental data; dark red - B3E; yellow - B3T.

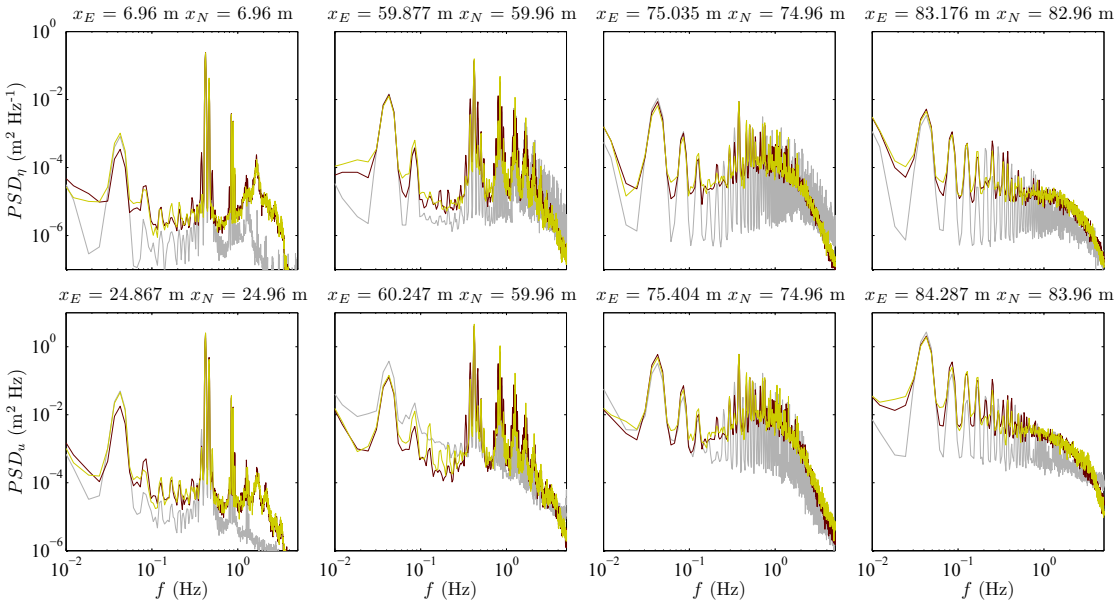

Figure A.8: Spectra of free-surface elevation (top) and cross-shore velocity (bottom) at four different cross-shore positions for B3. Grey line - experimental data; dark red - B3E; yellow - B3T. Dotted lines: simulations ran with A set of breaking parameters; full lines: $\phi_b = 27^\circ$ and $\phi_f = 9^\circ$.

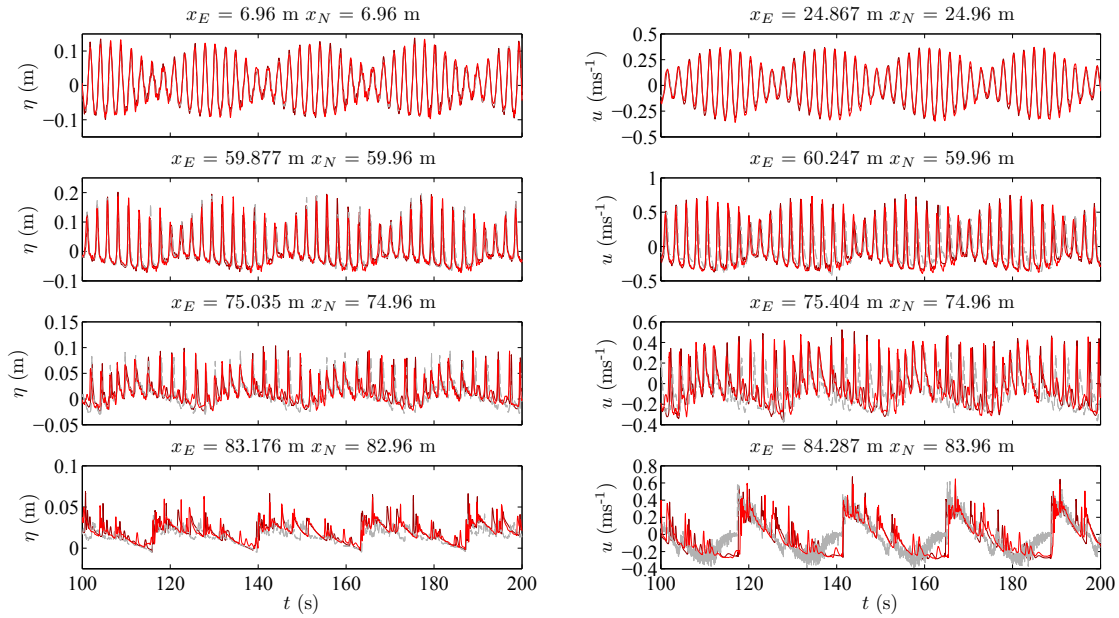

Figure A.9: Time series of free-surface elevation and cross-shore velocity spectra at four different cross-shore positions for B3 (with $\phi_b = 27^\circ$ and $\phi_f = 9^\circ$). Grey line - experimental data; dark red - B3E; yellow - B3T.

Appendix B

The following pages present a summary of the experiments carried out in the LEGI wave flume that were analysed in the scope of this thesis. For a correct interpretation of each column:

- column 1 - number of the experimental run;
- column 2 - wave condition
  C1: XB1001_syntS96H93, C2: XB1001_syntS96H93_C, C3: XB1003_syntS96H93.
  C1g: XB1001_syntS96H93_2gp, C2g: XB1001_syntS96H93_C_2gp,
  C3g: XB1003_syntS96H93_2gp.
  IG1: XB1001_LW, IG2: XB1001_LWX2,
  IG3: XB1001_LWX3, IG4: XB1001_LWX4.
  The wave conditions with _2gp in the name correspond to time series of only two wave groups; all the others correspond to time series of 20 min. These time series were repeated as wished for each experiment.)
- column 3 - pair of profiles measured at the end of each experiment;
- column 4 - duration of the wave condition;
- column 5 - cross-shore position of the twelve wave gauges during the run;
- column 6 - cross-shore and vertical (relatively to the mean water level) position(s) of the ADV (ADV1 stands for the side-looking ADV Nortek Vectrino +);
- column 7 - other measurements performed during the experiments that are not analysed in the scope of this thesis;
- column 8 - general observations concerning each experiment.

Exp.	Wave cond.	Final profile	Duration	x_{wg} (m)	x, z_{ADV1} (m, cm)	Other meas.	Observations
27	C1	1025 1026	20 min	2.01, 6, 9, 12, 15, 17, 19, 21.005, 22, 23, 24, 25	-	-	Great beach changes.
28	C1	1027 1028	20 min	2.01, 6, 9, 12, 15, 17, 19, 21.005, 22, 23, 24, 25	-	Optical profiler	Beach-face-oscillation runs (milder beach-face-slope of final profile).
29	C1	1029 1030	20 min	2.01, 6, 9, 12, 15, 17, 19, 21.005, 22, 23, 24, 25	-	Optical profiler	Beach-face-oscillation runs (steeper beach-face-slope of final profile).
30	C1	1031 1032	20 min	2.01, 6, 9, 12, 15, 17, 19, 21.005, 22, 23, 24, 25	-	Optical profiler	Beach-face-oscillation runs (milder beach-face-slope of final profile).
31	C1	1033 1034	20 min	2.01, 6, 9, 12, 15, 17, 19, 21.005, 22, 23, 24, 25	-	Optical profiler	Beach-face-oscillation runs (steeper beach-face-slope of final profile).
34	C1	1038 1040	20 min	2.01, 6, 9, 12, 15, 17, 19, 21.005, 22, 23, 24, 25	23, -4	Optical profiler	Beach-face-oscillation runs (milder beach-face-slope of final profile).
35	C1	1041 1042	20 min	2.01 6, 9, 12, 15, 17, 19, 21.005, 22, 23, 24, 25	23, -4	Optical profiler	Beach-face-oscillation runs (steeper beach-face-slope of final profile).
36	C1	1045	20 min	2.01, 6, 9, 12, 15, 17, 19, 21.005, 22, 23, 24, 25	23, -4	Optical profiler	Beach-face-oscillation runs (milder beach-face-slope of final profile).
38	C1	1047 1048	2h40	2.01, 6, 9, 12, 15, 17, 19, 21.005, 22, 23, 24, 25	23, -4	Optical profiler	Beach-face-oscillation runs (milder beach-face-slope of final profile).
39	IG1	1049 1050	60 min	2.01, 6, 9, 12, 15, 17, 19, 21.005, 22, 23, 24, 25	23, -4	max and min run-up positions	No beach changes.
40	C1	1051 1052	20 min	2.01, 6, 9, 12, 15, 17, 19, 21.005, 22, 23, 24, 25	23, -4	-	Smaller changes of the beach-face slope.
41	IG1	1053 1054	60 min	2.01, 6, 9, 12, 15, 17, 19, 21.005, 22, 23, 24, 25	23, -4	-	No beach changes.
42	C1	1055 1056	20 min	2.01, 6, 9, 12, 15, 17, 19, 21.005, 22, 23, 24, 25	22, -4	-	Smaller changes of the beach-face slope.
43	C1	1059 1060	3 h	2.01, 10.5, 16.5, 18, 20, 20.6, 21.3, 22.5, 23.4, 24.45, 24.80, 25.15	22.5, -3.6	Optical profiler	Beach-face oscillations stop, bar starts migrating onshore.
44	C1	1061 1062	5 h	2.01, 10.5, 16.5, 18, 20, 20.6, 21.3, 22.5, 23.4, 24.45, 24.80, 25.15	20.6, [-9.8, -15, -20, -19,	Optical profiler	Bar onshore migration. Velocity measurements at different heights.
45	C1	1063 1064	5 h	2.01, 10.5, 16.5, 18, 20, 20.6, 21.3, 22.5, 23.4, 24.45, 24.80, 25.15	-18, -17, -16, -14, -12, -8, -6, -13]	Optical profiler	Bar onshore migration.
46	C1	1065 1066	5 h	2.01, 10.5, 16.5, 18, 20, 20.6, 21.3, 22.5, 23.4, 24.45, 24.80, 25.15	21.3, -6	Optical profiler	Bar onshore migration. Velocity measurements at different heights.
47	C1	1067 1068	2 h	2.01, 4, 7.6, 10, 13.65, 21, 21.66, 22.16, 23, 23.8, 24.3, 24.65	22.5, [-4.5, -2.7, -4]	Optical profiler	Near C1 equilibrium. Velocity measurements at different heights.
48	C1	1069 1070	60 min	2.01, 5, 8.3, 15, 21, 22, 22.50, 23, 23.397, 24, 24.5, 25	21.66, [-7, -15, -14, -13, -12, -11, -10, -9, -8, -6, -5, -4]	Optical profiler	C1 equilibrium. Velocity measurements at different heights.
49	IG1	1071 1072	20 min	2.01, 5, 8.3, 15, 21, 22, 22.50, 23, 23.397, 24, 24.5, 25	21, [-10, -15, -18, -17,-10]	Optical profiler	No beach changes.
50	IG2	1073 1074	20 min	2.01, 5, 8.3, 15, 21, 22, 22.50, 23, 23.397, 24, 24.5, 25	22.5, -4	Optical profiler	No beach changes.
51	IG3	1075 1076	20 min	2.01, 5, 8.3, 15, 21, 22, 22.50, 23, 23.397, 24, 24.5, 25	22.5, -4	Optical profiler	No significant beach changes.
52	IG4	1077 1078	20 min	2.01, 5, 8.3, 15, 21, 22, 22.50, 23, 23.397, 24, 24.5, 25	22.5, -4	Optical profiler	Localised (at the bar) small beach changes.
53	C1	1079	4 h	2.01, 5, 8.3, 15, 21, 22,	22.5, -4	Optical	C1 equilibrium beach profile.

		1080		22.50, 23, 23.397, 24, 24.5, 25		profiler	
54	C2	1081 1082	4 h	2.01, 5, 8.3, 15, 21, 22, 22.50, 23, 23.397, 24, 24.5, 25	22, -5	Optical profiler	Evolution towards C2 equilibrium beach profile.
55	C2	1083 1084	2 h	2.01, 5.6, 16.5, 20, 21.65, 22, 22.5, 23, 23.397, 24, 24.5, 25	22, -5	Optical profiler	Evolution towards C2 equilibrium beach profile. Velocity measurements at different heights.
56	C2	1085 1086	5 h	2.01, 10.5, 14.5, 18, 21.3, 21.8, 22.3, 22.8, 23.3, 23.8, 24.3, 24.8	21.65, [-5, -7, -9, -11, -12]	Optical profiler	C2 equilibrium beach profile.
57	C2	-	40 min	2.01, 10.5, 14.5, 18, 21.3, 21.8,22.3, 22.8, 23.3, 23.8, 24.3, 24.8	-	-	C2 equilibrium beach profile.
58	C2	1087 1088	40 min	2.01, 4, 6, 18, 21.3, 21.8, 22.3, 22.8, 23.3, 23.8, 24.3, 24.8	2.01, -10	-	C2 equilibrium beach profile.
59	C2	1089 1090	40 min	2.01, 4, 6, 18, 21.3, 21.8, 22.3, 22.8, 23.3, 23.8, 24.3, 24.8	2.01, -7	-	C2 equilibrium beach profile.
60	CA	1091 1092	60 min	2.01, 4, 6, 18, 21.3, 21.8, 22.3, 22.8, 23.3, 23.8, 24.3, 24.8	2.01, -7	-	Test run for the possibility of modifying the signal generated at the wave-maker taking into account reflected IG waves.
61	CA	1093 1094	60 min	2.01, 4, 6, 18, 21.3, 21.8, 22.3, 22.8, 23.3, 23.8, 24.3, 24.8	2.01, -7	Optical profiler	Test run for the possibility of modifying the signal generated at the wave-maker taking into account reflected IG waves.
62	CA	1095 1096	60 min	2.01, 4, 6, 18, 21.3, 21.8, 22.3, 22.8, 23.3, 23.8, 24.3, 24.8	4, -8	Optical profiler	Test run for the possibility of modifying the signal generated at the wave-maker taking into account reflected IG waves.
63	CA	1097 1098	3 h	2.01, 4, 6, 18, 21.3, 21.8, 22.3, 22.8, 23.3, 23.8, 24.3, 24.8	4, -8	Optical profiler	Test run for the possibility of modifying the signal generated at the wave-maker taking into account reflected IG waves.
64	CA	1099 1100	3 h	2.01, 4, 6, 18, 21.3, 21.8, 22.3, 22.8, 23.3, 23.8, 24.3, 24.8	4, -6	Optical profiler	Wave gauge calibration.
65	CA	1101 1102	2 h	2.01, 4, 6, 18, 21.3, 21.8, 22.3, 22.8, 23.3, 23.8, 24.3, 24.8	4, -9	-	Test run for the possibility of modifying the signal generated at the wave-maker taking into account reflected IG waves.
66	C1	1103 1104	40 min	2.01, 4, 6, 18, 21.3, 21.8, 22.3, 22.8, 23.3, 23.8, 24.3, 24.8	4, -8	-	Test run for the possibility of modifying the signal generated at the wave-maker taking into account reflected IG waves.
67	C1	1105 1106	20 min	2.01, 4, 6, 18, 21.3, 21.8, 22.3, 22.8, 23.3, 23.8, 24.3, 24.8	-	-	Evolution towards C1 equilibrium beach profile.
68	C1	1107 1108	3 h	2.01, 4, 6, 18, 21.3, 21.8, 22.3, 22.8, 23.3, 23.8, 24.3, 24.8	-	-	Evolution towards C1 equilibrium beach profile.
69	C1	1109 1110	3 h	2.01, 4, 6, 18, 21.3, 21.8, 22.3, 22.8, 23.3, 23.8, 24.3, 24.8	4, -8	-	Evolution towards C1 equilibrium beach profile.
71	C1	1111 1112	3 h	2.01, 4, 6, 18, 21.3, 21.8, 22.3, 22.8, 23.3, 23.8, 24.3, 24.8	4, -8	ADVP	Evolution towards C1 equilibrium beach profile.
72	C1	1113 1114	3 h	2.01, 4, 6, 18, 21.3, 21.8, 22.3, 22.8, 23.3, 23.8, 24.3, 24.8	4, -8	ADVP Pressure gauges	Evolution towards C1 equilibrium beach profile.
73	C1	1115 1116	1h20	9, 12, 17, 18.5, 20.3, 20.95, 22.03, 22.48, 22.95, 24.03, 24.6, 25.3	6, -8	ADVP	Evolution towards C1 equilibrium beach profile. Wave gauge calibration.
74	C1	1117 1118	5h20	9, 12, 17, 18.5, 20.3, 20.95, 22.03, 22.48, 22.95, 24.03, 24.6, 25.3	[9, 12], -8	Pressure gauges Video	C1 equilibrium beach profile. Velocity measurements at different cross-shore positions.
75	C1	1119	2h20	9, 11, 14, 16, 18.5, 19.1,	[17, 18.5,	ADVP	C1 equilibrium beach profile. Velocity

		1120		21.306, 22.48, 22.95, 24.03, 24.6, 25.3	20.3, 20.95, 22.03, 22.03], [-8, -8, -8, -8, -5, -5]	Pressure gauges Vector	measurements at different cross-shore positions.
76	C1	1121 1122	2h20	9, 15, 17.65, 19.1, 19.66, 20.6, 21.306, 21.64, 22.95, 23.65, 24.6, 25.3	[11, 14, 16], -8	ADVP Pressure gauges Vector	C1 equilibrium beach profile. Velocity measurements at different cross-shore positions.
77	C1	1123 1124	2 h	9, 15, 17.65, 19.1, 19.66, 20.6, 21.320, 21.64, 22.95, 23.65, 24.6, 25.3	[15, 17.65, 19.1, 19.66], -8	Optical profiler ADVP Vector	C1 equilibrium beach profile. Velocity measurements at different cross-shore positions.
78	C1	1125 1126	2 h	9, 15, 17.65, 19.1, 19.66, 20.6, 21.320, 21.64, 22.95, 23.65, 24.6, 25.3	[22.95, 21.64], [-3.5, -8]	ADVP Vector	C1 equilibrium beach profile. Velocity measurements along different cross-shore positions.
79	C1g	1127 1128	2 h	9, 15, 17.65, 19.1, 19.66, 20.6, 21.31, 21.9, 22.95, 24.02, 24.6, 25.3	21.64, -8	Optical profiler ADVP Vector Video	C1 equilibrium beach profile.
80	C1g	1129 1130	60 min	9, 15, 17.65, 19.1, 19.66, 20.6, 21.31, 21.9, 22.95, 24.02, 24.6, 25.3	21.9, [-5, -1]	Optical profiler ADVP Vector Video	C1 equilibrium beach profile. Velocity measurement at two different heights.
81	C1g	1133 1134	30 min	9, 15, 17.65, 19.1, 19.66, 20.6, 21.31, 21.9, 22.95, 24.02, 24.6, 25.3	21.9, -5	ADVP Vector	C1equilibrium beach profile.
82	C1g	1135 1136	4 h	9, 15, 17.65, 19.1, 19.66, 20.6, 21.31, 21.9, 22.95, 24.02, 24.6, 25.3	-	ADVP Vector	Beach profile was modified before this run, retrieving C1 equilibrium profile. Wave gauge calibration.
83	C1g	1137 1138	27.2 s	9, 15, 18.5, 20.4, 21.31, 21.65, 22.16, 22.66, 23.33, 23.89, 24.45, 25	21.9, -5	-	C1 equilibrium beach profile.
84	C1g	1139 1140	27.2 s	9, 15, 18.5, 20.4, 21.31, 21.65, 22.16, 22.66, 23.33, 23.89, 24.45, 25	21.65, -8	ADVP	First run of two wave groups of C1.
85	C1g	1141 1142	27.2 s	9, 15, 18.5, 20.4, 21.31, 21.65, 22.16, 22.66, 23.33, 23.89, 24.45, 25	21.65, -8	ADVP	Start of accretion offshore of the breakpoint, erosion and deepening of a trough onshore of the breakpoint: definition of a bar.
86	C1g	1143 1144	27.2 s	9, 15, 18.5, 20.4, 21.31, 21.65, 22.16, 22.66, 23.33, 23.89, 24.45, 25	21.65, -6	-	Continuing previous tendency.
87	C1g	1145 1146	27.2 s	9, 15, 18.5, 20.4, 21.31, 21.65, 22.16, 22.66, 23.33, 23.89, 24.45, 25	21.65, -5	ADVP	Continuing previous tendency.
88	C1g	1147 1148	27.2 s	9, 15, 18.5, 20.4, 21.31, 21.65, 22.16, 22.66, 23.33, 23.89, 24.45, 25	21.65, -6	ADVP	Continuing previous tendency.
89	C1g	1149 1150	27.2 s	9, 15, 18.5, 20.4, 21.31, 21.65, 22.16, 22.66, 23.33, 23.89, 24.45, 25	22.66, -5	ADVP	Continuing previous tendency.
90	C1g	1151 1152	27.2 s	9, 15, 18.5, 20.4, 21.31, 21.65, 22.16, 22.66, 23.33, 23.89, 24.45, 25	22.66, -4	ADVP	Continuing previous tendency.
91	C1g	1153 1154	27.2 s	9, 15, 18.5, 20.4, 21.31, 21.65, 22.16, 22.66, 23.33, 23.89, 24.45, 25	22.66, -4	-	Continuing previous tendency.
92	C1g	1155 1156	27.2 s	9, 15, 18.5, 20.4, 21.31, 21.65, 22.16, 22.66, 23.33, 23.89, 24.45, 25	22.66, -4	ADVP	Continuing previous tendency.
93	IG1g	-	27.2 s	9, 15, 18.5, 20.4, 21.31,	22.66, -4	-	Continuing previous tendency.

				21.65, 22.16, 22.66, 23.33, 23.89, 24.45, 25			
94	IG2g	1157 1158	27.2 s	9, 15, 18.5, 20.4, 21.31, 21.65, 22.16, 22.66, 23.33, 23.89, 24.45, 25	22.66, -4	-	Testing infragravity-wave influence with only two wave groups.
95	C2g	1159 1160	27.2 s	9, 15, 18.5, 20.4, 21.31, 21.65, 22.16, 22.66, 23.33, 23.89, 24.45, 25	22.66, -4	Vector	No beach changes.
96	C2g	1161 1162	27.2 s	9, 15, 18.5, 20.4, 21.31, 21.65, 22.16, 22.66, 23.33, 23.89, 24.45, 25	22.66, -4	Vector	Testing infragravity-wave influence with only two wave groups. No beach changes.
97	C2g	1163 1164	27.2 s	9, 15, 18.5, 20.4, 21.31, 21.65, 22.16, 22.66, 23.33, 23.89, 24.45, 25	22.66, -4	Vector	First run of two wave groups of C2. Small accretion of the bar trough.
98	C2g	1165 1166	27.2 s	9, 15, 18.5, 20.4, 21.31, 21.65, 22.16, 22.66, 23.33, 23.89, 24.45, 25	22.16, -4	Vector	Small accretion of the bar trough.
99	C2g	1167 1168	27.2 s	9, 15, 18.5, 20.4, 21.31, 21.65, 22.16, 22.66, 23.33, 23.89, 24.45, 25	21.65, -4	Vector	No significant beach changes.
100	C2g	1169 1170	27.2 s	9, 15, 18.5, 20.4, 21.31, 21.65, 22.16, 22.66, 23.33, 23.89, 24.45, 25	21.65, -6	-	No significant beach changes.
101	C2g	1171 1172	27.2 s	9, 15, 18.5, 20.4, 21.31, 21.65, 22.16, 22.66, 23.33, 23.89, 24.45, 25	20.4, -10	Vector	No significant beach changes.
102	C2g	1173 1174	27.2 s	9, 15, 18.5, 20.4, 21.31, 21.65, 22.16, 22.66, 23.33, 23.89, 24.45, 25	20.4, -10	Vector	No significant beach changes.
103	C2g	1175 1176	27.2 s	9, 15, 18.5, 20.4, 21.31, 21.65, 22.16, 22.66, 23.33, 23.89, 24.45, 25	22.16, -5	Vector	No significant beach changes.
104	C2g	1177 1178	27.2 s	9, 15, 18.5, 20.4, 21.31, 21.65, 22.16, 22.66, 23.33, 23.89, 24.45, 25	22.16, -5	Vector	No significant beach changes.
105	C2g	1179 1180	27.2 s	9, 15, 18.5, 20.4, 21.31, 21.65, 22.16, 22.66, 23.33, 23.89, 24.45, 25	23.33, -4	Vector	No significant beach changes.
106	C1g	1181 1182	27.2 s	9, 15, 18.5, 20.4, 21.31, 21.65, 22.16, 22.66, 23.33, 23.89, 24.45, 25	23.33, -4	-	No significant beach changes.
107	C1g	1183 1184	27.2 s	9, 15, 18.5, 20.4, 21.31, 21.65, 22.16, 22.66, 23.33, 23.89, 24.45, 25	23.33, -4	-	No significant beach changes.
108	C1g	-	27.2 s	9, 15, 18.5, 20.4, 21.31, 21.65, 22.16, 22.66, 23.33, 23.89, 24.45, 25	23.33, -4	ADVP Vector	-
109	C1g	1185 1186	27.2 s	9, 15, 18.5, 20.4, 21.31, 21.65, 22.16, 22.66, 23.33, 23.89, 24.45, 25	20.4, -10	ADVP Vector	-
110	C2g	1187 1188	27.2 s	9, 15, 18.5, 20.4, 21.31, 21.65, 22.16, 22.66, 23.33, 23.89, 24.45, 25	20.4, -10	ADVP Vector	-
111	IG3g	1189 1190	27.2 s	9, 15, 18.5, 20.4, 21.31, 21.65, 22.16, 22.66, 23.33, 23.89, 24.45, 25	20.4, -10	ADV Vector	-
112	C2g	1191 1192	27.2 s	9, 15, 18.5, 20.4, 21.31, 21.65, 22.16, 22.66, 23.33, 23.89, 24.45, 25	23.33, -4	ADVP Vector	-
113	C1g	1193 1194	27.2 s	9, 15, 18.5, 20.4, 21.31, 21.65, 22.16, 22.66, 23.33, 23.89, 24.45, 25	23.33, -4	ADVP Vector	Testing infragravity-wave influence with only two wave groups. No significant beach changes.
114	C2g	1195	27.2 s	9, 15, 18.5, 20.4, 21.31,	20.4, -10	ADVP	-

		1196		21.65, 22.16, 22.66, 23.33, 23.89, 24.45, 25		Vector	
115	C1g	1199 1200	2 h	9, 15, 18.5, 20, 21.31, 21.65, 22.16, 22.66, 23.33, 23.89, 24.45, 25	21.65, -6	ADVP Vector Video	-
116	C2g	1201 1202	1 h	9, 15, 18.5, 20, 21.31, 21.65, 22.16, 22.66, 23.33, 23.89, 24.45, 25	20, -25	ADVP Vector Video	-
117	C2g	1205 1206	2 h	9, 15, 18.5, 20, 21.31, 21.65, 22.16, 22.66, 23.33, 23.89, 24.45, 25	20.0, -25	ADVP Vector	-
118	C2g	1209 1210	4 h	9, 15, 18.5, 20, 21.31, 21.65, 22.16, 22.66, 23.33, 23.89, 24.45, 25	20.0, -25	ADVP Vector	-
119	C2g	1217 1218	3h30	9, 15, 18.5, 20, 21.31, 21.65, 22.16, 22.66, 23.33, 23.89, 24.45, 25	20.0, -25	ADVP Vector	-
120	C2g	1219 1220	27.2 s	9, 15, 18.5, 20.4, 21.31, 21.65, 22.16, 22.66, 23.33, 23.89, 24.45, 25	[15, 18.5], [-23, -18.5]	ADVP Vector	-
121	C2g	1221 1222	27.2 s	9, 15, 18.5, 20.4, 21.31, 21.65, 22.16, 22.66, 23.33, 23.89, 24.45, 25	20.4, -10	ADVP Vector	Velocity measurements at different cross-shore positions.
122	C2g	1223 1224	27.2 s	9, 15, 18.5, 20.4, 21.31, 21.65, 22.16, 22.66, 23.33, 23.89, 24.45, 25	20.4, -10	ADVP Vector	Very good velocity measurements just outside the breakpoint.
123	C1g	1225 1226	27.2 s	9, 15, 18.5, 20.4, 21.31, 21.65, 22.16, 22.66, 23.33, 23.89, 24.45, 25	20.4, -10	ADVP Vector	Very good velocity measurements just outside the breakpoint.
124	C1g	1227 1228	27.2 s	9, 15, 18.5, 20.4, 21.31, 21.65, 22.16, 22.66, 23.33, 23.89, 24.45, 25	20.4, -10	ADVP Vector	Very good velocity measurements just outside the breakpoint.
125	C1g	1229 1230	27.2 s	9, 15, 18.5, 20.4, 21.31, 21.65, 22.16, 22.66, 23.33, 23.89, 24.45, 25	20.4, -10	ADVP Vector	Very good velocity measurements just outside the breakpoint.
126	C3g	1231 1232	27.2 s	9, 15, 18.5, 20.4, 21.31, 21.65, 22.16, 22.66, 23.33, 23.89, 24.45, 25	20.4, -10	ADVP Vector	Very good velocity measurements just outside the breakpoint.
127	C3g	1233 1234	27.2 s	9, 15, 18.5, 20.4, 21.31, 21.65, 22.16, 22.66, 23.33, 23.89, 24.45, 25	20.4, -10	ADVP Vector	Very good velocity measurements just outside the breakpoint.
128	C3g	1235 1236	27.2 s	9, 15, 18.5, 20.4, 21.31, 21.65, 22.16, 22.66, 23.33, 23.89, 24.45, 25	20.4, -10	ADVP Vector	New wave condition. Very good velocity measurements just outside the breakpoint.
129	C3g	1237 1238	1 h	9, 15, 18.5, 20.4, 21.31, 21.65, 22.16, 22.66, 23.33, 23.89, 24.45, 25	20.4, -10	ADVP Vector	Very good velocity measurements just outside the breakpoint.
130	C2g	1239 1240	27.2 s	9, 15, 18.5, 20.4, 21.31, 21.65, 22.16, 22.66, 23.33, 23.89, 24.45, 25	20.4, -10	ADVP Vector	Very goodvelocity measurements just outside the breakpoint.
131	C2g	1241 1242	27.2 s	9, 15, 18.5, 20.4, 21.31, 21.65, 22.16, 22.66, 23.33, 23.89, 24.45, 25	20.4, -10	ADVP Vector	C3 equilibrium beach profile. Very good velocity measurements just outside the breakpoint.
132	C2g	1243 1244	27.2 s	9, 15, 18.5, 20.4, 21.31, 21.65, 22.16, 22.66, 23.33, 23.89, 24.45, 25	20.4, -10	ADVP Vector	Very good velocity measurements just outside the breakpoint.
133	C2g	1245 1246	1 h	9, 15, 18.5, 20.4, 21.31, 21.65, 22.16, 22.66, 23.33, 23.89, 24.45, 25	20.4, -10	ADVP Vector	Very good velocity measurements just outside the breakpoint.
134	C3g	1247 1248	27.2 s	9, 15, 18.5, 20.4, 21.31, 21.65, 22.16, 22.66, 23.33, 23.89, 24.45, 25	20.4, -10	ADVP	Very good velocity measurements just outside the breakpoint.
135	C3g	1249	27.2 s	9, 15, 18.5, 20.4, 21.31,	20.4, -10	ADVP	C2 equilibrium beach profile. Very good

		1250		21.65, 22.16, 22.66, 23.33, 23.89, 24.45, 25			velocity measurements just outside the breakpoint.
136	C2g	1251 1252	27.2 s	2.01, 6, 9, 12, 15, 17, 19, 21.005, 22, 23, 24, 25	20.4, -10	ADVP	Very good velocity measurements just outside the breakpoint.
137	C2g	1253 1254	27.2 s	2.01, 6, 9, 12, 15, 17, 19, 21.005, 22, 23, 24, 25	20.4, -10	ADVP	Very good velocity measurements just outside the breakpoint.